Magnetism in Multiferroics and Low Dimensional Metal-Organic Complexes

Shuo Han

School of Physics and Astronomy

Queen Mary, University of London

Supervior: Dr. Alan Drew

Submitted in partial fulfillment of the requirements of

the Degree of Doctor of Philosophy

28 September 2016

To my Family

Statement of originality

I, Shuo Han, confirm that the research included within this thesis is my own work or that where it has been carried out in collaboration with, or supported by others, that this is duly acknowledged below and my contribution indicated. Previously published material is also acknowledged below.

I attest that I have exercised reasonable care to ensure that the work is original, and does not to the best of my knowledge break any UK law, infringe any third partys copyright or other Intellectual Property Right, or contain any confidential material.

I accept that the College has the right to use plagiarism detection software to check the electronic version of the thesis.

I confirm that this thesis has not been previously submitted for the award of a degree by this or any other university.

The copyright of this thesis rests with the author and no quotation from it or information derived from it may be published without the prior written consent of the author.

Signature:

Date:

Acknowledgment

Firstly, I would like to thank my supervisor, Dr. Alan Drew, for his patience guidance and excellent supervision to my Ph.D studies. He offers enormous support and sound advice. He always has lots of enthusiastic ideas. I learn not only the research skills but also the enthusiasm of research from him.

I would also like to acknowledge my secondary supervisor, Prof. William Gillin, for his support to my project, especially for his help with the thin film deposition work in my first and second year. Also a big thank you to Mr. Geoff Gannaway and Dr. Ken Scott for their great help with my experimental work in the laboratory.

I would also like to thank my collaborators Mr. Yinshan Meng, Prof. Bingwu Wang, Prof. Zheming Wang and Prof. Song Gao at Peking University for their great support of the sample preparations and also useful discussions. Dr. Houssny Bouyanfif from Universit*é* de Picardie Jules Verne, who prepared thin film $BiFeO_3$ samples for the GISANS measurement. Special thanks to Prof. Leander Schulz from Sichuan University for his great support to my research. Many thanks to Dr. Francis Pratt, Dr. Peter Baker, Dr. Sarah Roger from ISIS and Dr. Sean Giblin from Cardiff University, for their great help on μSR and GISANS experiments as well as some extremely useful discussions.

Special thanks to my colleagues in the condensed matter physics group in the department of physics at Queen Mary, University of London. A big thank you to Dr. Anthony Phillips, who offers great support to my project. Also I am grateful to Dr. Hongtao Zhang, Dr. Carlos Aristizabal, Miss Ke Wang, Mr. Viswanatha Mohandoss, Miss Helen Duncan and Miss Serena Maugeri for their great discussions and invaluable

suggestions during my Ph.D.

Thanks Chinese scholarship council and Queen Mary, University of London for funding. Finally, on a personal note, I would like to thank my parents and friends and Mr. Cheng Li for helping and supporting me throughout the years of my study. I would like to thank all of my friends for their support, friendship and guidance.

Abstract

Multiferroics and magnetic metal-organic complexes are candidates for sophisticated applications in the future. In this thesis, the magnetism in $BiFeO_3$ (a multiferroic material with an incommensurate spin cycloidal structure), copper guanidiniam formate (a multiferroic metal-organic complex with a one-dimensional magnetic structure) and CP*-RE-COT (a series of "zero-dimensional" single molecule magnets) are discussed.

A radio-frequency plasma sputtering thin film deposition system and a ferroelectric characterisation system were developed for the study of $BiFeO_3$ epitaxial thin films. A large leakage current was observed in $BiFeO_3$ thin films, which hindered the investigations on the ferroelectric properties and magnetoelectric coupling in them. An evidence of the spin cycloid in a $BiFeO_3$ thin film was observed by grazing-incidence small angle neutron scattering.

The magnetism of a multiferroic metal-organic complex with a one-dimensional magnetic chain, $[C(NH_2)_3][Cu(HCOO)_3]$, was studied by magnetometry and muon spin spectroscopy. A spin-canted antiferromagnetic order and critical phenomenon in this material were investigated. It was shown that this material possessed an 3D Heisenberg long-range order below 4.6K. The one-dimensional magnetic chain was also studied by muon spin spectroscopy. The correlation length was measured with a field dependence of $\xi \sim H^{-1}$.

Magnetisation relaxations of a series of single molecule magnets CP*-RE-COT (COT = $C_8H_8^-$, CP* = $C_5Me_5^-$), which show "zero-dimensional" magnetism, were studied using an AC magnetometer and muon spin spectroscopy. Three possible relaxation

pathways, including a quantum tunnelling process and two Orbach relaxation processes, were suggested by the relaxation behaviour. The suppression of the quantum tunnelling effect resulting from the entanglement of the ground states, which probably arises from the exchange interactions in CP*-RE-COT, was also observed with a 1000 Oe applied magnetic field. Data that were consistent with long-range magnetic ordering was observed in CP*-Dy-COT, which would be the first ever report of long-range magnetic order in a single ion magnet.

Contents

1 Introduction **27**

2 Magnetism in Multiferroic and Low-dimensional Magnetic Materials 31

2.1 Multiferroic Materials 33

2.1.1 Magnetoelectric coupling in multiferroics 34

2.1.2 Traditional inorganic multiferroics: transition metal oxides . . . 36

2.1.3 Multiferroic metal-organic frameworks (MOFs) 39

2.2 Low-dimensional Magnetism in Organic Complexes 41

2.2.1 Molecular magnets 41

2.2.2 One-dimensional antiferromagnetic chain 43

2.2.3 Single molecule magnets 48

2.3 Summary 70

3 Experimental Techniques **71**

3.1 Muon Spin Rotation, Relaxation and Resonance 71

3.1.1 Introduction to μSR 72

3.1.2 Muon polarisation functions in magnetic materials 80

3.1.3 Probing spin fluctuations in magnets 93

3.1.4 Critical phenomenon studied by μSR 98

3.2 Complementary Techniques 100

3.2.1 Magnetic susceptibility measurements 101

3.2.2 Magnetic neutron scattering 105

4 $BiFeO_3$ Epitaxial Film Deposition and Characterisation 111

4.1 Introduction to $BiFeO_3$ . . . 113

4.2 $BiFeO_3$ Epitaxial Thin Film Deposition . . . 123

4.2.1 Epitaxial thin film deposition by RF plasma sputtering . . . 123

4.2.2 Deposition system development . . . 127

4.3 Results . . . 129

4.3.1 Thin film deposition . . . 130

4.3.2 Characterisations of $BiFeO_3$ thin films . . . 132

4.4 Conclusion . . . 143

5 Multiferroic Metal-Organic Framework CuGF 145

5.1 Introduction to Copper Guanidinium Formate . . . 147

5.2 Structure . . . 148

5.3 Experimental Details . . . 149

5.4 Magnetism in CuGF . . . 151

5.4.1 Three dimensional long-range magnetic order . . . 151

5.4.2 Critical exponents . . . 160

5.4.3 One-dimensional magnetism in CuGF . . . 166

5.5 Magnetoelectric Coupling . . . 173

5.6 Discussion and Conclusion . . . 177

6 Single Molecule Magnets - CP*-RE-COT 179

6.1 Introduction to A Series of Single-Ion Magnets CP*-RE-COT . . . 181

6.2 Magnetisation Relaxations in CP*-RE-COT . . . 184

6.2.1 Experiment details . . . 184

6.2.2 AC susceptibility measurements on magnetisation relaxations in CP*-RE-COT . . . 186

6.2.3 ZF μSR measurements of magnetisation relaxations in CP*-RE-COT . . . 190

6.2.4 Long-range magnetic ordering in CP*-Dy-COT 193
6.2.5 Magnetisation relaxations and relaxation mechanism in CP*-Dy-COT 198
6.2.6 Longitudinal field dependence of the magnetisation relaxation in CP*-RE-COT 201
6.3 Conclusion 205

7 Conclusion and Future Work **207**

List of Figures

2.1 Classification of typical multiferroic oxides. The largest purple circle represents all insulating oxides. Among them, there are electrically polarisable materials (green ellipse), which include the ferroelectric as a subset (green circle) and magnetically polarisable materials (orange ellipse) with a subset of ferromagnetic materials (red circle). According to the definition, multiferroic materials correspond to the intersection between the orange and red circles. Magnetoelectric coupling, shown by the blue solid circle, shows the interplay between magnetism and electricity [24]. 38

2.2 The magnetoelectric coupling in $[(CH_3)_2NH_2]Fe(HCOO)_3$. (a) Dielectric constants as a function of temperature with different applied magnetic fields. The magnetic fields were applied along the same direction ([012]) along the crystal. (b) Magnetisation as a function of temperature measured with and without an electric field. The electric field was applied also along the [012] direction of the crystal during cooling process and was removed before starting the measurements during warming [57]. . . 40

2.3 Magnetic correlation length ξ, magnetic susceptibility χ and heat capacity C of a 1D Heisenberg antiferromagnetic chain [82]. 46

2.4 (a) Chemical structure of the magnetic core of a Mn_{12}-acetate molecule with four inner spin-down Mn^{4+} (green) and 8 spin-up Mn^{3+} (red) [108]. (b) Structure of a Mn_{12}-acetate molecule viewed along the *c*-axis with large pink balls representing the inner Mn, large red balls referring to outer Mn atoms, medium blue balls highlighting the position of O atoms, small yellow balls representing C atoms and small black balls to be H. The spins point up and down along the *c*-axis [109]. 51

2.5 (a) The temperature dependence of magnetisation measurements along the *c*-axis of Mn_{12}-acetate by ZFC and with a 100 Oe direct current (DC) FC [7]. (b) Hysteresis loops of Mn_{12}-acetate measured along the *c*-axis at 2.2 (solid circle) and 2.8 K (circle) [7]. (c) The field dependence of the magnetisation of Mn_{12}-acetate field-oriented crystals at six different temperatures [105]. (d) The field dependence of the magnetisation of a Mn_{12}-acetate single crystal. The measurement was performed along the *c*-axis (magnetic easy axis) [104]. 53

2.6 (a) Temperature dependence of the imaginary part of the magnetic susceptibility of a Mn_{12}-acetate powder sample measured at zero DC field [32]. (b) The temperature dependence of the relaxation time of Mn_{12}-acetate. Solid circles are data from the decay of magnetisation and open circles are data from AC susceptibility measurement [7]. (c) The relaxation rate as a function of magnetic field along the *c*-axis at 5 K. Dots are magnetisation data from Ref. [104] and full line is from the theoretical model from Ref. [112]. 55

2.7 The structure of $[Pc_2Ln]^-$ [21]. 57

2.8 (a) AC susceptibilities of the Tb complex (polycrystalline powder). Open symbols are data for the pure Tb complex and solid marks are data for the diluted sample (20% concentration). χ'_M, χ''_M and χ_M are in-phase-AC, out-of-phase-AC and DC molar magnetic susceptibilities, respectively [21]. (b) AC susceptibilities of the Dy complex (polycrystalline powder). Open symbols are data for the pure Dy complex and solid marks are data for the diluted sample (20% concentration) [21]. (c) Magnetic hysteresis of the diluted Tb (2% concentration) complex (powder) at 1.7 K [123]. (d) Magnetic hysteresis of the diluted Dy (2% concentration) complex (powder) at 1.7 K [123]. 58

2.9 (a) The magnetisation relaxation time τ vs. T^{-1} of $[Cp_2Dy(\mu\text{-bta})]_2$ under $H = 0$ Oe and $H = 1000$ Oe. The open symbols are for AC susceptibility data collected with a fixed frequency and varying temperatures while the solid marks are for data measured the other way around. Quantum tunnelling was directly measured by the linear AC susceptibility technique [124]. (b) Hysteresis loops of the diluted Tb complex (2% concentration, single crystal) with different field scan rates. The measurements were performed at 0.04 K with an applied field parallel to the magnetic easy axis [101]. (c) Details in low field region of (b) [101]. 60

2.10 The electronic levels of a Dy ion with the influence of the electronic repulsion, spin-orbit coupling and crystal field effects leading to the zero-field splitting of the energy levels in lanthanide Dy [134]. 64

2.11 Double well model of the schematic energy levels including zero-field splitting based on a cluster-based SMM. The blue arrows and yellow arrows show the thermal-activated relaxation and the quantum tunnelling process, respectively [135]. 65

2.12 Illustrations of the direct, quantum tunnelling, Raman and Orbach magnetisation relaxation processes. 67

2.13 (a) Logarithm of the magnetisation relaxation rate vs. the inverse temperature determined with AC susceptibility measurements on pure (triangles) and diluted (2% concentration) (circles) of the Tb complex [123]. (b) Logarithm of the magnetisation relaxation rate vs. the inverse temperature in the Dy complex (triangles are data for pure material and circles are data for diluted (2% concentration) material) [123]. (c) Muon and ^{1}H spin-lattice relaxation rates (NMR), exhibiting a relationship with the spin fluctuation rate that will be introduced in the next chapter, vs. inverse temperature for $[Pc_2Tb]^0$ and $[Pc_2Dy]^0$ complexes. Solid lines here are fit to the Orbach model [139]. (d) The temperature dependence of the correlation time for spin fluctuation rates of $[Pc_2Tb]^0$ under zero field and 1000 Oe measured with μSR. Inset shows $[Pc_2Dy]^0$ data but in a temperature range of 50 K to 250 K [140]. 68

3.1 (a) Spatial emission of the positron as a function of the emitted angle with different kinetic energies. (b) Configuration of the μSR experiment. In the case of applying an external magnetic field, the transverse field (TF) is perpendicular to the muon spin and the longitudinal field (LF) is parallel to the muon spin. 76

3.2 (a) The illustration shows that a muon usually sits at the interstitial position in a magnetic material. The green ball is the μ^+. (b) Muon precession around a local field. 80

3.3 A schematic representation of the three contributions to B_{dip} in a μSR experiment: the green square is the muon site and the black dots represent magnetic moments within the Lorentz sphere (denoted by the white sphere). 81

3.4 Schematic diagrams (left) showing how a muon interacts with a transverse field and measured signal (right) with blue solid curve, red solid curve and green dashed curve showing the counts from the backward detector, forward detector and their average, respectively. At $t = 0$, a muon (continuous beam) or muons (pulsed beam) are implanted into the sample sitting between the backward and forward detectors and the count is zero at $t = 0$ s. One moment later, sufficiently short that the muon spin direction is not changes by precession, relaxation or the like, the positrons corresponding to the muon spin pointing towards the backward detector are emitted. The asymmetry between the backward and forward detectors reach the maximum value in the experiment, which is defined as the initial asymmetry. At time $t = \pi/2\gamma_\mu B$, muon spins precess by $\pi/2$. The counts in the forward and backward detectors are nearly the same and $A(t)$ becomes zero. At $t = \pi/\gamma_\mu B$, muon spins precess through π resulting higher counts in the forward detector (to be continued). 83

3.5 (continued) Schematic diagrams showing how a muon interacts with a transverse field and measured signal (right) with blue solid curve, red solid curve and green dashed curve showing the counts from the backward detector, forward detector and their average, respectively. At $t = 3\pi/2\gamma_\mu B$, muon spins rotate by $3\pi/2$ giving a similar reading in the detectors on both sides again. Finally, at $t = 2\pi/\gamma_\mu B$, muon spins rotate back to zero degree completing a period of spin rotation. 84

3.6 (left) A schematic diagram showing how a muon interacts with a longitudinal field B_{long}. All the muon spins are aligned in the applied field. Nearly all emitted positrons point to the backward detector. (right) The muon polarisation function is a constant with time. 85

3.7 In a magnetically ordered material (taking a peroveskite crystal as an example as shown on the left), (a) one magnetically equivalent muon site, which is noted with a green ball in the crystal structure) has a single Larmor precession signal, which results in one cosine polarisation function as shown on the right. (b) N muon sites (two sites here noted with green and purple balls) can give rise to N Larmor precessions and the muon polarisation function is the combination of N cosine functions. 86

3.8 The Kubo-Toyabe function with several different external longitudinal fields with an internal field width to be $\gamma_\mu \Delta = 0.15$ MHz [142]. 90

3.9 (a) Zero-field muon polarisation functions $P(t)$ as a function of an asymmetry parameter arising from the short-range spin correlations in the system. Details can be founded in Ref. [13]. The inset shows that in the presence of a short-range spin correlation, the muon spin polarisation function can be approximated by Gaussian damped oscillations. The parameter Δ/B_0 correlates with the short-range correlation length of the sample [143]. (b) Parameter Δ/B_0 as a function of the correlation length in a simple case where the muons sit on the octahedral site of a face-centred-cubic lattice (lattice parameter is a) with ferromagnetic order [143]. 92

3.10 (a) Red curves are spectra of dynamic Kubo-Toyabe polarisation functions with different $R = \nu/\Delta$ ratio. Black curves are exponential relaxation functions, which can be used to describe dynamic Kubo-Toyabe function when $R \geq 5$. (b) The dynamic Kubo-Toyabe polarisation function with different applied longitudinal fields when $R = 2$ [147]. 96

3.11 The Debye relaxation model shows the evolution of AC susceptibility as a function of the AC field frequency. The dynamics in the sample results in the decline of χ' and a peak in χ'' at $\omega\tau = 1$. 105

3.12 (a) The geometry of neutron scattering experiments [153]. (b) The condition for Bragg scattering based on the scattering vector ($\vec{Q} = \vec{k}\text{-}\vec{k'}$) and the fulfilled condition $\left|\vec{Q}\right| = 2\left|\vec{k}\right|\sin(\frac{1}{2}\theta)$. 106

3.13 The geometry of a GISANS experiment with which a spin cycloidal structure lying in-plane of a $BiFeO_3$ thin film can be measured. 109

4.1 The crystal structure of $BiFeO_3$ in a hexagonal base. The FeO_6 octahedra are highly distorted and rotated along the $[001]_{\text{hex}}$ (or $[111]_{\text{c}}$) of the crystal. Due to the $6s$ lone pair electrons of the Bi, the Bi ion has a displacement from the centrosymmetric position, which allows the ferroelectric distortion along the $[001]_{\text{hex}}$ (or $[111]_{\text{c}}$) threefold axis [170]. 114

4.2 (a) The hexagonal lattice of $BiFeO_3$ (only iron and oxygen ions are shown). The arrows indicate the Fe^{3+} moment and the spin cycloid is roughly indicated [155]. (b) The schematic representation of the 62 nm spin cycloid in $BiFeO_3$. The blue and green arrows are canted antiferromagnetic spins with a cycloidal structure. The total moment, represented by the purple arrows, averages out resulting in a zero net magnetisation in $BiFeO_3$ [184]. 118

4.3 (a) Magnetoelectric effects in $BiFeO_3$ at low fields. P is proportional to H^2 (quadratic magnetoelectric coupling). Above $B_c = 200$ kOe, P is linearly dependent on H (linear magnetoelectric coupling) [15]. (b) Once the cycloid is destroyed, the small canted magnetic moment is recovered. Zero-field magnetisation yields a small net magnetisation of 0.3 emu/g [15, 157]. 121

4.4 (a) Magnetisation properties of a $(111)_c$ $BiFeO_3$ film and corresponding crystal. Weak ferromagnetism recovers in the thin film [158]. (b) The magnetic phase diagram of strained $BiFeO_3$ thin films. When compressive strain is bigger than 1.7% and tensile strain is bigger than 0.5% (blue columns), spin cycloid can be destroyed; if a moderate compressive strain is applied (pink column), $BiFeO_3$ thin film has a bulk-like spin cycloidal structure propagating along the $[1\bar{1}0]_c$ direction; with moderate tensile strain (yellow column), the propagation vector of the spin cycloid in a $BiFeO_3$ thin film change its direction towards $[110]_c$ [166]. 122

4.5 An illustration of the RF sputtering system: target ions are bombarded by energetic ions from plasma, such as Ar plasma, and then ejected to the substrate. The whole RF circuit is powered by an RF power supply with a fixed frequency of 13.56 MHz and the impedance is tuned with an external matching circuit. 125

4.6 (a) An illustration of the cross-section of the deposition system. (b) the overview of the real system. (c) An internal view of the deposition chamber. (d) The substrate heater attached to the top plate. 128

4.7 The temperature of the substrate position (a thermocouple was mounted to the position where the substrate usually sits) when the setting temperature was 690 °C. The inset shows the temperature at the position of the sputter gun in the deposition chamber under a typical deposition pressure. The cooling system keeps the sputter gun area at a reasonable temperature. 130

4.8 An example of the $BiFeO_3$ film on a glass substrate deposited using the conditions discussed in the text. 131

4.9 An illustration of the polarisation measurement system. A computer was used to control the experimental setup and to acquire the data. Details of the equipment are discussed in the text. 134

4.10 (a) Dielectric polarisation of a non-ferroelectric material. (b) Electric polarisation of a ferroelectric material. 136
4.11 (a) A screenshot of the "PE" hysteresis of a standard 2 kΩ resistor. P on the y-axis is polarisation × area (not known in the packed resistor) and has a unit of Column. The x-axis E is the applied voltage instead of the electric field as the thickness of the resistor is also unknown. (b) The "PE" hysteresis of a 1 μF ceramic capacitor. P is polarisation × device area and E is the voltage as the area and the thickness of the purchased capacitor are also unknown. 137
4.12 (a) A sample holder used to test a $BiFeO_3$ thin film sample in the PE measurement system. (b) An illustration of how the sample was mounted and how contacts were made during the measurement using the sample holder in (a). 137
4.13 (a) The current density in the $BiFeO_3$ thin film sample as a function of temperature. (b) The measured PE hysteresis based on a large leakage current shown in (a). (c) The first three IV tests on the $BiFeO_3$ film. . 138
4.14 XRD characterisation on (a) the 900 nm BFO film on a STO substrate; (b) the 300 nm BFO film on a STO substrate. They are $(111)_c$ oriented epitaxial films. This data is provided by Dr.Houssny Bouyanfif. 140
4.15 GISANS data of (a) the 300 nm (111)-oriented $BiFeO_3$ film measured at 300 K; (b) the cross-section of the lines in (a), where the red and black curves correspond to the red and black lines in (a); (c) the 900 nm (111)-oriented film measured at 123 K; (d) the cross-section of the lines in (c); (e) the 900 nm (111)-oriented film measured at 300 K; (f) the cross-section of the lines in (e). 142

5.1 (a) The structure of CuGF. (b) Side view of the crystal structure showing the oxygen octahedra connected by the formate. (c) The Cu chain along the c-axis. (d) The ab-plane showing that the Cu-O bonds have long (l), medium (m) and short (s) lengths due to the Jahn-Teller distortion. (e) Atomic structure of a $C(NH_2)_3$ (left) and Cu(CHOO) (right) unit [54]. 148

5.2 (a) The FC/ZFC magnetisation measurement of polycrystalline CuGF with an applied field $H = 10$ Oe. The inset shows details of the FC/ZFC data below 4.5 K. (b) χ and $1/\chi$ of the CuGF polycrystalline sample with an applied field $H = 5000$ Oe. (c) The magnetic susceptibility of polycrystalline CuGF with $H = 200$ Oe and 20000 Oe. The inset gives details of the susceptibility data below 10 K. (d) χ and $1/\chi$ of the CuGF single crystal with an applied field $H = 5000$ Oe, which is parallel to the c-axis of the crystal. 152

5.3 (a) The μSR spectrum at 300 mK: the grey symbols are the raw data and the blue curve is the fit with a χ^2 of 1.108. (b) The μSR spectra at 4.2 K, below the Néel temperature (4.6 K). (c) The residual of the 4.2 K data. (d) The relaxation rate as a function of temperature of the sixth relaxation term. (e) The frequencies of the five oscillations as a function of temperature. The critical behaviour is fitted with a power law and the fit is shown by the solid curves with a χ^2 of 1.256. (f) The relaxation rates of the five relaxed oscillations below the Néel temperature. 154

5.4 The Fourier transform of the spectrum measured at 0.3 K. 155

5.5 (a) The LF μSR spectra at 2.5 K for different applied longitudinal fields: the grey symbols correspond to the raw data, the blue curves are the fit ($\chi^2 = 1.081$ (1 Oe), 1.184 (100 Oe), 1.016 (1000Oe)), showing that all five oscillations and the sixth relaxation term can be quenched under a high LF field. (b) Muon polarisation as a function of the applied longitudinal field. The muon polarisation is completely decoupled from the internal magnetic field at about 750 Oe. 158

5.6 The transverse field (50 Oe) muon spin rotation measurement also exhibits a phase transition at 4.55 K. (a) The TF μSR spectrum at 4.3 K, where the grey symbols are the measured data and the blue line is the fit ($\chi^2 = 1.205$). (b) The total muon spin asymmetry decreases with the temperature decreasing below the Néel temperature. (c) The relaxation rate shifts as a function of temperature. (d) The measured field shifts as the temperature goes up. 159

5.7 The critical exponent β obtained from fits to the magnetisation data (4.2 K to 4.6 K) measured using a SQUID. The fit has the quality $\chi^2 = 1.075$ and $\beta = 0.353$. 162

5.8 (a) The critical exponent γ obtained from fits to the the DC magnetic susceptibility data (4.2 K to 4.6 K) measured under a 50 Oe applied field (fit quality $\chi^2 = 0.998$ (γ), 1.001 (γ')). (b) The critical exponent γ determined by fitting the μSR data (4.2 K to 4.6 K) with an applied 50 Oe transverse field ($\chi^2 = 1.048$). γ and γ' from both techniques are found to have different signs and the values do not agree with the theory. 163

5.9 The dynamic muon spin relaxation critical behaviour of f_5. The relaxation rate as a function of temperature clearly diverges at the Néel temperature. The inset shows the fitting of the dynamic critical exponent ν, which is fitted to be 0.574 ($\pm$ 0.016) with a fit quality $\chi^2 =$ 0.988. 165

5.10 The ZF μSR spectra at (a) 6 K, (b) 25 K and (c) 150 K. A static Kubo-Toyabe function and an exponential relaxation are fitted to the data (χ^2 = 1.091 (6 K), 1.115 (25K), 1.351 (150K)). The raw data and the fitting are shown by the grey symbols and blue curves, respectively. (d) The residual analysis on a typical μSR data above the Néel temperature (25 K). (e) The width of the dipole field distribution Δ and the relaxation rate λ_G as a function of temperature ($T > T_N$). 167

5.11 (a) The longitudinal field muon spin relaxation measurement shows that the internal field can be decoupled with LF > 50 Oe at 20 K. The grey symbols are raw data, blue curves are the fitting and red curves show the model of static Kubo-Toyabe function with an applied magnetic field. (b) The field dependence of the Gaussian field variance Δ at different temperatures. 169

5.12 The fraction of the oscillatory term of the muons sitting near the formate. The inset shows the details near the transition temperature. 171

5.13 The Δ_{osc}/B_0 ratio as a function of temperature is shown by the blue solid circles. The model based on a simple temperature correlation length treatment and Δ/B vs. correlation length relationship discussed in Section 3.1.2 is shown by the blue curve. The inset is a simple temperature correlation length treatment that diverges at the Néel temperature due to the phase transition. 172

5.14 The correlation length at 20 K as a function of the applied magnetic field using a power law as a fit function shown by the blue solid line (χ^2 = 0.971). The correlation length is in an arbitrary unit because the data is based on a model that describes short-range correlations in ferromagnetic materials. This approach may not be very precise for a CuGF 1D chain but the trend can be qualitatively reproduced. 173

5.15 (a) The temperature dependence of the *ab*-plane magnetisation along the [110] direction with and without applied electric fields along *c*-axis. The inset shows an enlarged view at low temperatures. (b) The dielectric constant along [110] as a function of temperature. The inset shows the M-H loop along [110] at 2 K. (c) The electric polarisation (left) and the reciprocal of magnetic susceptibility (right) along the *c*-axis as a function of temperature. The straight solid line is a fit to the Curie-Weiss law. The inset shows the measurement configuration [58]. 174

5.16 (a) Five muon precession frequencies as a function of the applied electric field. (b 1-5) The shift of the five oscillation frequencies at 0.7 K as a function of the applied electrical field. (c) The relaxation rate of the sixth Gaussian term as a function of the applied electric field. (d 1-5) Relaxation rates of the five damped oscillations as a function of electric field. There seems to be a small kink or feature centred around zero electric field (the region between the two dashed lines). These data were measured at a fixed temperature of 0.7 K and error bars are all included but some of them are too small to show up. 176

6.1 (a) The molecular structure of CP*-RE-COT, where the pink balls represent the lanthanide atom, orange balls represent carbon atoms and hydrogen atoms are not shown. Blue dash lines are connections between the lanthanide and the centre of the CP* and the COT rings. The angle between these two lines is defined as the bending angle α. (b) The disorder of the COT ring in CP*-RE-COT. Green ring corresponds to the staggered conformer and the orange ring corresponds to the eclipsed conformer compared with the CP* represented by grey ring. The molecular structure was reported by Ref. [103]. 181

6.2 (a) Interactions between molecules of CP*-RE-COT within the *ac*-plane of the crystal. The edge to face π-π stacking interactions between COT rings are shown by the blue dashed lines and the C-H$\cdots\pi$ interactions between the CP* and the COT rings are shown by the green dashed lines. (b) Details of the two interaction types in the CP*-RE-COT *ac*-plane for the eclipsed (golden) and staggered (green) COT conformers. The interactions relevant to eclipsed and staggered conformers are also represented by the golden and green dashed lines. The blue dashed lines are interactions between these two conformers [103]. 183

6.3 The magnetisation relaxation time of the Dy (5% concentration in CP*-Y-COT), Ho and Er compounds at low temperatures. The relaxation time in the quantum regime varies by several orders of magnitude from the Dy to the Er compounds [103]. 186

6.4 (a) AC susceptibility measurements of the pure Dy complex. (b) χ'' as a function of AC field frequency for the 5% CP*-Dy-COT doped in CP*-Y-COT without an applied DC field [103]. (c) The magnetisation relaxation time of CP*-$Y_{0.95}Dy_{0.05}$-COT at 0, 100 Oe and 6 kOe from 2 to 4.5 K [103]. (d) χ'' for the Er complex exhibits two relaxation processes [121]. 188

6.5 (a) Typical μSR spectra of CP*-Dy-COT at different temperatures with three fitted exponential relaxations. The normalised least square were $\chi^2 = 1.012$ (2 K), 1.006 (40 K) and 0.999 (100 K). Data are shown by the solid circles and the fit is shown by the curve with the same colour. The inset shows the zoom-in of the data up to 50 ns. (b) The residual analysis of the 100 K data. 192

6.6 The muon spin relaxation rates of the first and second relaxation components λ_1 and λ_2 as a function of temperature under zero field measured with the EMU (square symbols) and GPS (circle symbols) spectrometers. 192

6.7 (a) μSR spectra and fit of CP*-Dy-COT under zero magnetic field at 0.02 K (fit quality $\chi^2 = 1.058$). The inset shows the same spectrum up to 9 μs (fit quality $\chi^2 = 0.996$). (b) The residual analysis on the data at 0.02 K. (c) ZF μSR spectrum at 0.8 K (fit quality $\chi^2 = 1.020$). (d) LF μSR spectra with a 300 Oe applied longitudinal field driven from zero field and with a 300 Oe field after having been driven to 20 kOe at 0.02 K (fit quality $\chi^2 = 1.076$ for 300 Oe before 20 kOe and $\chi^2 = 1.094$ for 300 Oe after 20 kOe). The grey symbols represent the raw data and the black curves are for the fit to Eq.6.5. 195

6.8 The calculated zero-field magnetisation relaxation time ($\tau = 1/\nu$) corresponding to two conformers (τ_1 for the eclipsed conformer and τ_2 for the staggered conformer) in the structure from 2 K to room temperature. The red and blue symbols are data points and curves are fit to Eq.6.6 (fit quality $\chi^2 = 0.966$ (τ_1), 0.945 (τ_2)). 198

6.9 (a) The electronic structure of CP*-Dy-COT calculated by Jiang in Ref. [103]. (b) Various magnetisation relaxation pathways in the Dy complex. 200

6.10 (a) The field dependence of the muon spin relaxation rate λ_1 at 30, 100, 125, 150, 250 and 315 K. (b) The field dependence of the muon spin relaxation rate λ_2 at 30, 100, 125, 150, 250 and 315 K. (c) Comparison of μSR spectra at zero field and using a longitudinal field of 1000 Oe at 250 K (with fit quality $\chi^2 = 1.196$ (0 Oe), 1.142 (1000 Oe)). 202

6.11 (a) The field dependence of the muon spin relaxation rate λ_1 of the Tm compound at different temperatures. (b) The muon spin relaxation rate λ_1 as a function of field of the Tb compound at different temperatures. 203

6.12 AC susceptibility data of CP*-RE-COT. The peaks near 1000 Oe also appear using this instrument. (a) The AC susceptibility data for the Tm complex at 2.5 K. (b) The AC susceptibility data for the Dy complex at 2.5 K. 203

6.13 The field dependence of χ'' for pure CP*-Dy-COT and CP*-$Dy_{0.05}Y_{0.95}$-COT employing an AC field amplitude of 3 Oe and a frequency of 360 Hz. The inset shows the same data as the main figure but with an emphasis on the maximum near 1000 Oe. 204

List of Tables

2.1 Some well known multiferroic materials. 38

3.1 The properties of a positive muon (μ^+) compared with an electron and a proton, where m_e and e are the mass and the charge of an electron. . 73

3.2 Definition of critical exponents. T_c is the critical temperature (could be the Néel temperature for antiferromagnets or the Curie temperature for ferromagnets). C is the heat capacity. ξ is the correlation length. χ is the susceptibility of the order parameter. Ψ is the order parameter and the function $\langle\psi(0)\phi(\mathrm{r})\rangle$ is the correlation function. 98

4.1 Details of different techniques used to investigate the anomaly at around 200 K in $BiFeO_3$. 120

4.2 Relationship between deposition conditions and film thickness. 131

5.1 Details of the fit parameters. P_i, A_F, A_G, A_{BG}, f_i and φ_i are parameters from the fitting function Eq.5.2. 156

5.2 Theoretical and experimental values of critical exponents β, ν and γ. . 160

6.1 Crystallographic data of CP*-RE-COT from Ref. [103]. Data were taken at 293 K. 182

6.2 Details of the fit parameters for the 0.8 K data. 196

6.3 Fit parameters using Eq.6.6 for CP*-Dy-COT. 199

Chapter 1

Introduction

Magnetism plays an important role in human history. This phenomenon started to attract peoples' attention even in ancient times. Dating back to 600 B.C., the magnetic properties in lodestones were described by Greek philosophers. From about 1000 A.D., human beings started to take the advantage of magnetic properties of materials. Since the first application of magnetism in the magnetic compass, a large amount of magnetic devices have been developed, which had great impacts on science, technology and the whole society. Magnetic materials are widely used in daily life, including motors for utilizing electric power, the magnetic resonance imaging for medical imaging and particularly information storage in everyday electronic devices.

The increasing demands on high-density data storage and super computing devices attract profound research interests in new functional magnetic materials. Multiferroics, which show the interplay between magnetism and ferroelectricity within a single material, is one of the most appealing candidates for more sophisticated applications in the future [1]. Even though bringing the magnetism and ferroelectricity together in a material is difficult [2], strong multiferroic couplings were observed in some multiferroic materials, such as $TbMnO_3$ [3] and $TbMn_2O_5$ [4]. These observations motivated extensive researches into the multiferroic coupling mechanism and new materials exploration.

Recently, magnetic metal-organic complexes have attracted considerable attention.

Consisting of networks of metals linked by organic frameworks, these hybrid systems benefit from both organic and inorganic components in their structures [5]. Their extended structures with coordination bonds, which offer exchange paths to the magnetic moment carriers, can be tuned to adjust the interlayer coupling, magnetic anisotropy and the exchange interaction [5]. Consequently, the magnetic and electric properties and even magnetic dimensionality can be tuned by designing different organic frameworks connecting the magnetic ions [5]. These make metal-organic complexes promising magnetic materials.

The magnetic dimensionality in metal-organic complexes can be tuned by varying the organic building blocks [6–9]. This makes these hybrid materials scientifically interesting as low-dimensional magnetic structures could provide experimental data to validate theoretical models of many fundamental problems in magnetism [10–12].

In this thesis, magnetism in multiferroics and low-dimensional metal-organic complexes will be discussed. A multiferroic material, $BiFeO_3$, with a spin cycloidal structure; a multiferroic metal-organic complex, copper guanidinium formate, with a quasi-one dimensional magnetic chain; and a series of single molecule magnets CP*-RE-COT were chosen for the study. The outline of this thesis is as follows:

- Chapter 2: prior to the detailed discussion on the three systems studied in this work, basic principles of multiferroics and low-dimensional metal-organic complexes and literature on these systems are reviewed in Chapter 2. The multiferroic coupling mechanism in multiferroics is discussed followed by the introduction to multiferroic metal-organic frameworks. Basic concepts and typical examples of low-dimensional magnetic structures, including one-dimensional magnetic chain and "zero-dimensional" single molecule magnets are discussed in detail.

- Chapter 3: this chapter provides a survey of the experimental techniques used to investigate the interested magnetic systems in this thesis. Muon spin rotation, relaxation and resonance (μSR), which is the main technique, is discussed first.

The basics of this technique and methods to investigate the magnetic structure and spin dynamics using muon spin spectroscopy are introduced. Moreover, a brief discussion on the complementary techniques follows, including magnetometry and magnetic neutron scattering.

- Chapter 4: it contains the work to attempt to investigate the magnetoelectric coupling and spin cycloid in $BiFeO_3$ epitaxial thin films. The developments of both thin film deposition and characterisation systems are included followed by the measurements on the ferroelectricity and spin cycloid in $BiFeO_3$ thin films. Some technical problems, which hindered the investigations on this material, are also discussed.

- Chapter 5: main results in this thesis are discussed in Chapter 5 and Chapter 6. In Chapter 5, results of a multiferroic and quasi one-dimensional magnetic system, $[C(NH_2)_3][Cu(HCOO)_3]$, are presented. Studies on the long-range magnetic order, critical phenomenon, one-dimensional magnetic chain and magnetoelectric coupling in this material are included. Particularly, it is shown that the μSR technique, which is normally believed to be not able to measure short-range magnetic correlations [13], can sense the correlations in the one-dimensional magnetic chain.

- Chapter 6: from AC susceptibility and μSR measurements, magnetism in a series of single molecule magnets, CP*-RE-COT (RE = lanthanide metals) is discussed. Behaviour indicating long-range magnetic order is detected in CP*-Dy-COT, and if true, it is the first reported long-range magnetic ordering in a single-ion magnet. Moreover, by studying the spin dynamics in these compounds using an AC magnetometer and the μSR technique, the magnetisation relaxation behaviour in CP*-RE-COT series is characterised and the relaxation mechanism is discussed.

- Chapter 7: finally results of this work are summarised. Open issues and possible future work are discussed. It is proposed that 1. the comprehensive study on the

spin cycloid in $BiFeO_3$ thin films; 2. investigating the difference between different one-dimensional chains with varying metal-organic structures; 3. completing the investigations on the whole series of single molecule magnets studied in this work, need more efforts in the future.

With the main objective of this work being understanding the magnetism in multiferroics and low-dimensional hybrid magnets, exotic magnetic structures, including the spin cycloid in $BiFeO_3$, the one-dimensional magnetic chain in $[C(NH_2)_3][Cu(HCOO)_3]$ and "zero-dimensional" single molecule magnets CP^*-RE-COT, are studied. This is of great importance to not only explore these promising materials for future applications but also understand fundamental problems in physics.

Chapter 2

Magnetism in Multiferroic and Low-dimensional Magnetic Materials

Increasing demands on high density storage and super computing devices have attracted great attention to new functional magnetic materials [1,5,14,15]. Traditional oxide materials with multifunctional properties, such as multiferroic oxides, have received intense research interest in the past few decades [1,14]. A multiferroic material possesses more than one ferroic property, including ferroelectricity, ferromagnetism, ferroelasticity and ferrotoroidicity. The coexistence of these ferroic orders enables high susceptibility to multiple external perturbations [1]. On the other hand, a large amount of organic magnetic systems have emerged, which can be tuned to have certain magnetic and electric properties [16–19] as well as the desired dimensionality of their magnetic structures [16,20,21]. These multifunctional or hybrid magnetic systems have great potential applications, such as high-density data storage [15,22,23], quantum computing [24,25], bio-embedded devices [26] and sensors [27,28].

To date, one of the most studied and appealing subclass of multiferroics is so-called "magnetoelectric multiferroics" where the magnetic and electric dipole ordering co-

exist [1]. The cross coupling between the ferromagnetic and ferroelectric orders offers an extra degree of freedom, which enables possibilities to create new devices such as multiple-state storages. However, few materials with this required coupling and hence the multiferroic property exist. Bringing ferroelectricity and magnetism together within one material seem to be in general rather challenging. [2].

Apart from more traditional oxide multiferroic materials, multiferroic metal-organic frameworks (MOFs) have recently received lot of attention. Multiferroic properties of these hybrid systems are designed and tuned by altering the organic frameworks connected to the magnetic ions in these systems [5]. Thus, metal-organic frameworks offer a novel and promising way to synthesize new materials with multiferroic properties. Moreover, the tunable magnetic interactions in MOFs also make it possible to control the dimensionality of these materials [6–9]. Isolated clusters [21, 29], 1D chains [16, 17] and 2D layers [20] have been realised in MOFs. However, multiferroic properties in these systems can only be achieved at low temperature [30]. Studying these systems and understanding their magnetic properties will result in a better material design and therefore enhanced multiferroic (and other) properties in the future.

Among organic magnetic materials, nano-scaled single molecule magnets are another system with promising potential since they can work as individual magnets and hence have potential applications, such as quantum computing [25], high-density data storage [23] and magnetic refrigeration [31]. Even though this area has been extensively studied since the first single molecule magnet was reported in 1991 [32], the working temperature and magnetic properties are still not suitable for future applications [30,33]. One of the main reasons for lack of development could be that structure-function relationships in single molecule magnets have not been comprehensively studied.

These multiferroic materials are also valuable media to investigate some interesting physics, such as low-dimensional magnetic structure in MOFs [10, 11], modulated spin structure in some of the multiferroic oxides [15] and quantum magnetisation [12] shown in molecular magnets. Therefore, it is of great importance to study the magnetism

in these systems with fascinating magnetic properties for future applications and for a better understanding of fundamental physics.

2.1 Multiferroic Materials

Multiferroic materials possessing more than one ferroic order within one material, show coupling between different ferroic orders [1]. They play an important role in technology applications as well as fundamental physics. In particular, multiferroics displaying both ferroelectricity and (anti)ferromagnetism are the focus of this work. In these so-called "magnetoelectric multiferroics", where an interplay between magnetism and electricity exists, the magnetoelectric coupling enables the control of the magnetic order with an external electric signal or vice versa [1].

The coupling between electricity and magnetism has been studied for nearly two centuries since Oersted observed the effects of a changing electric current on magnetic fields [34]. The connection of magnetism and electricity was then elegantly described by Maxwell's equations in 1862. The argument of the existence of magnetoelectric coupling within a certain type of materials was made by Pierre Curie in 1894 [35]. The idea of "multiferroic materials" was confirmed in 1950s. Dzyaloshinskii demonstrated with a thermodynamic theory that linear magnetoelectric coupling in the magnetically ordered crystals is possible [36]. Later in 1960, the linear relationship between magnetic and electric fields was experimentally observed in chromium oxide [37] demonstrating that the magnetoelectric coupling can exist in a real material.

Despite further intensive investigations of the "magnetoelectric multiferroics" (may be known as "ferroelectromagnets" in earlier literature), the number of the discovered "magnetoelectric multiferroics" was limited and magnetoelectric coupling was found to be very weak in the materials studied in those days. Then, this field lost its momentum until the 2000s when two experimental breakthroughs were reported: 1. a large polarisation in $BiFeO_3$ thin films in 2003 [38] and 2. a strong magnetoelectric coupling

in $TbMnO_3$ in the same year [3]. Since then, the research activities in the field of multiferroics have revived.

2.1.1 Magnetoelectric coupling in multiferroics

The magnetoelectric coupling in multiferroics facilitates the conversion between magnetic and electric field energies [1]. Therefore, it is possible to tune the electric polarisation using an applied magnetic field or to modify the magnetisation using an external electric field.

To describe magnetoelectric coupling, it is convenient to use terms in the free energy expansion. As the electric field $\vec{H}$ and magnetic field $\vec{E}$ are vectors, coupling parameters will be tensors. Landau theory describes magnetoelectric coupling by [39]:

$$\begin{aligned} F(\vec{E},\vec{H}) &= F_0 - P_i^s E_i - M_i^s H_i \\ &- \frac{1}{2}\varepsilon_0\varepsilon_{ij}E_iE_j - \frac{1}{2}\mu_0\mu_{ij}H_iH_j - \alpha_{ij}E_iH_j - \frac{1}{2}\beta_{ijk}E_iH_jH_k - \frac{1}{2}\gamma_{ijk}H_iE_jE_k - ... \end{aligned} \tag{2.1}$$

where F_0 is the free energy in the absence of fields. The second and third terms on the right (with a superscript of s) are spontaneous components related to electric polarisation and magnetisation, respectively, followed by the fourth and fifth terms describing the system's electric and magnetic responses to external electric (ε is permittivity of the system) and magnetic fields (μ is permeability of the system), respectively. The sixth term describes the linear magnetoelectric coupling with a coupling parameter α_{ij}. The last two terms are second order of non-linear magnetoelectric couplings in the system (β_{ijk} and γ_{ijk} are quadratic coupling constants). Higher orders of the expansion are not shown. The electric polarisation $\vec{P}$ and magnetisation $\vec{M}$ can then be described as Eq. 2.2 and Eq. 2.3, respectively:

$$P_i(\vec{E},\vec{H}) = -\frac{\partial F}{\partial E_i} = P_i^s + \frac{1}{2}\varepsilon_0\varepsilon_{ij}\left(E_j + E_k\right) + \alpha_{ij}H_j + \frac{1}{2}\beta_{ijk}H_jH_k + \frac{1}{2}\gamma_{ijk}H_i\left(E_j + E_k\right)... \tag{2.2}$$

$$M_i(\vec{E},\vec{H}) = -\frac{\partial F}{\partial H_i} = M_i^s + \frac{1}{2}\mu_0\mu_{ij}\left(H_j + H_k\right) + \alpha_{ij}E_i + \frac{1}{2}\beta_{ijk}E_i\left(H_j + H_k\right) + \frac{1}{2}\gamma_{ijk}E_jE_k... \tag{2.3}$$

It is clear from Eq. 2.2 and Eq. 2.3 that the coefficient α_{ij} provides information about the linear cross-coupling between $\vec{P}$ and the magnetic field, and between $\vec{M}$ and the electric field. Thus, α_{ij} can be used to describe the linear magnetoelectric coupling in materials. The coefficients in the tensors β and γ describe higher orders of the magnetoelectric coupling. These magnetoelectric coupling coefficients can be determined indirectly by measuring changes in magnetisation near the ferroelectric transition or changes in dielectric constant near the magnetic transition of a material.

Magnetism and ferroelectricity have different origins. Magnetism in a multiferroic material is normally due to strong correlations between electrons in transition metals. However, ferroelectricity in a material could have different origins. Possible driving mechanisms of ferroelectricity are:

- "Proper" ferroelectricity: in proper ferroelectrics, the primary order parameter is the ferroelectric distortion. A possible mechanism of ferroelectricity, which allows its coexistence with magnetism, is lone-pair driven ferroelectricity [40]. $BiFeO_3$, one of the materials this thesis focuses on, possesses ferroelectricity based on this mechanism. In its perovskite structure, the A-site Bi^{3+} has a $6s^2$ lone-pair electron, which causes the Bi $6p$ (empty) orbital to come energetically closer to the O $2p$ orbital. This leads to hybridisation of Bi $6p$ and O $2p$ orbitals and drives the off-centring of the cation towards the neighbouring anion resulting in a ferroelectric behaviour [40].

- "Improper" ferroelectricity: in improper ferroelectrics, the spontaneous polarisation is a secondary effect from a structural phase transition. A textbook example is the geometric ferroelectric hexagonal $YMnO_3$, in which a structural phase transition at about 1300 K provides the symmetry lowering by tilting of the MnO_5 bipyramids. This tilting mechanism gives rise to bipyramids. This tilting mecha-

nism gives rise to ferroelectricity [41]. Charge ordering can also induce ferroelectricity in a material. For example, in a charge-frustrated system like $LuFe_2O_4$, the polar arrangement of electrons on Fe^{3+} arises from the charge frustration in the triangular lattice. This charge arrangement then enables ferroelectricity in $LuFe_2O_4$ [42].

As stated, different multiferroic materials may have different ferroelectric mechanisms so that the origin of magnetoelectric coupling varies.

Depending on different physical mechanisms of electric polarisation, multiferroic materials are classified into two types. In Type I multiferroics, a structural phase transition (nonpolar-to-polar) enables the ferroelectricity at high temperatures, whereas the magnetic order occurs below a separate magnetic phase transition at lower temperatures. Thus, the ferromagnetic and ferroelectric orders coexist but have different origins in type I multiferroics. In type-II multiferroics, the ferroelectric order is induced by magnetism. Magnetic ordering lowers the symmetry group from a nonpolar phase to a polar magnetic phase thereby inducing improper ferroelectricity occurs. In this case, the magnetic and electric orders are correlated that magnetoelectric coupling in these multiferroics is usually found to be strong.

2.1.2 Traditional inorganic multiferroics: transition metal oxides

Even though they are fascinating materials, the number of the existing multiferroic materials showing ferroelectricity and (anti)ferromagnetism is limited [2]. The symmetry restriction is one of the reason that multiferroics rarely occur in nature. Out of 122 crystallographic point groups, there are only 13 point groups that allows the coexistence of magnetic and electric orders [43]. The 13 crystallographic point groups are 1, 2, $2'$, m, m', 3, $3m'$, 4, $4m'm'$, $m'm'2'$, $m'm2'$, 6 and $6m'm'$.

Hill [2] has shown an analysis on the scarcity of the coexistence of these two ferroic

orders based on transition-metal oxides, the class of materials to which most studied multiferroic materials belong. Ferroelectricity originating from the displacement of the negative and positive charge centres favours off-centring d^0 ions [44]. In most ferroelectrics, such as $BaTiO_3$, the hybridisation of the empty d orbitals of Ti ions with the p orbitals of the surrounding oxygen ions results in the displacement of the positive and negative charge centres. Magnetism on the other hand arises from the unpaired localised electrons, for example from the partially filled d orbitals in transition metals. The chemical and physical difference of the origin of magnetism and ferroelectricity finally drove this study to perovskite-like complex oxides, which comprise two transition metal cations and oxygen with a chemical structure of ABO_3 (A, B are transition metal ions). A detailed discussion can be found in Ref. [2]. In the case of these oxides, the localised transition metal electrons could possess magnetism in the system and, at the same time, the transition metal and oxygen bonds, which have an ionic-covalent nature, could provide a strong electric polarisation [1].

The classification of typical multiferroic oxides is shown in Fig. 2.1. The relationship between multiferroic materials and those with ferromagnetic and ferroelectric orders are present. It is clear that the "magnetoelectric multiferroics" are not common. Some of the most-studied multiferroics are shown in Table 2.1. Cr_2O_3 is the first experimentally discovered multiferroic material. A linear magnetoelectric coupling in Cr_2O_3 [37] and $GaFeO_3$ [45] was observed in the 1960s. $BiFeO_3$ [15] and $BiMnO_3$ [38] show a large polarisation and are very promising for future applications. $BiFeO_3$ is probably the only room-temperature multiferroic material [46]. $TbMnO_3$ [3] and $TbMn_2O_5$ [4], both are type II multiferroics, possess very strong magnetoelectric coupling. The discovery of magnetically induced ferroelectricity in these two materials may help to overcome the chemical incompatibility of magnetism and ferroelectricity discussed above and to find more multiferroic materials with high critical temperatures. For more details of these multiferroic materials, please consult the references shown in Table 2.1.

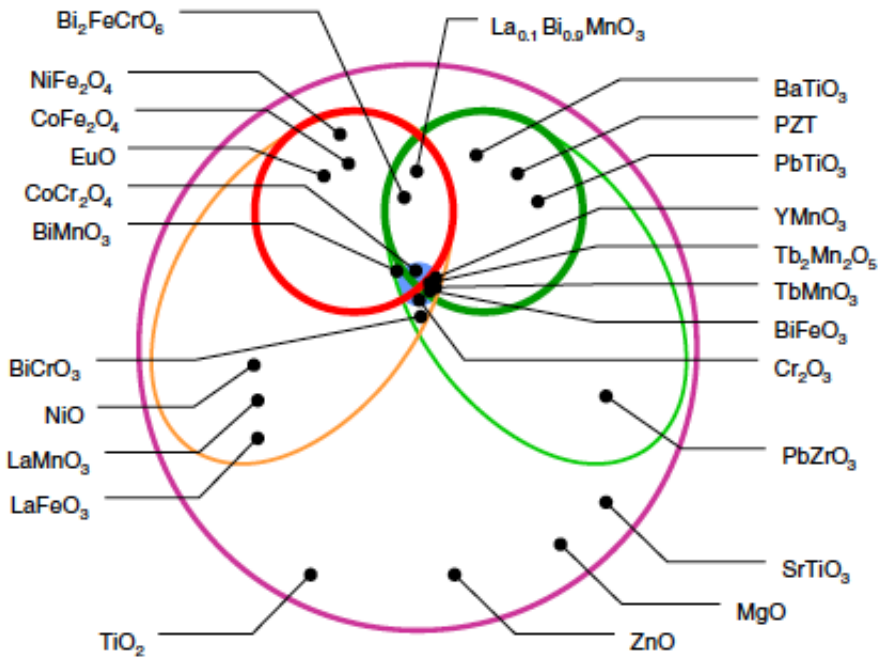

Figure 2.1: Classification of typical multiferroic oxides. The largest purple circle represents all insulating oxides. Among them, there are electrically polarisable materials (green ellipse), which include the ferroelectric as a subset (green circle) and magnetically polarisable materials (orange ellipse) with a subset of ferromagnetic materials (red circle). According to the definition, multiferroic materials correspond to the intersection between the orange and red circles. Magnetoelectric coupling, shown by the blue solid circle, shows the interplay between magnetism and electricity [24].

Table 2.1: Some well known multiferroic materials.

Materials	References
Cr_2O_3	Ref. [37]
$GaFeO_3$	Ref. [45]
$BiFeO_3$	Ref. [15]
$TbMnO_3$	Ref. [3]
$TbMn_2O_5$	Ref. [4]
$BiMnO_3$	Ref. [38]

2.1.3 Multiferroic metal-organic frameworks (MOFs)

As discussed earlier, only a few transition metal oxides show multiferroic properties. A lot of effort has been put in synthesizing new multiferroics with considerable magnetoelectric coupling. MOFs are hybrid crystalline compounds consisting of networks of metals framed by organic linkers. Therefore, MOFs have promising properties that benefit from both organic and inorganic components in their structures [5]. Combining the magnetism of metals and ferroelectricity enabled by the structural distortion of organic frameworks, MOFs offer a new avenue to build single-phase multiferroic materials. Moreover, it is also possible to tune or to control the multiferroic properties of these MOFs by controlling the magnetic coupling and structure distortions using different possible starting building blocks including both metal ions and organic templates [5].

Apart from traditional inorganic multiferroic oxides, MOFs are a new class of multiferroics. The first MOF was reported in 1995 [47]. Since then these nanoporous materials have been widely investigated due to potential applications, such as gas storage [48], gas separation [49], catalysis [50], biomedical imaging [26] and solar energy harvesting [51]. More recently, ferroelectricity or (anti)ferromagnetism was realised in some ABX_3 perovskite structured MOFs [5, 52]. In 2009, the first multiferroic MOF, $[(CH_3)_2NH_2]M(HCOO)_3$ (M = Mn, Fe, Co, Ni), possessing both magnetic and ferroelectric orders was reported by Jain *etal.* [16]. This work also demonstrated that multiferroic properties could be realised in MOFs by using metal-hydrogen bonds in the design. However, since then only a few multiferroic MOFs have been synthesized: $[C(NH_2)_3]Cu(HCOO)_3$ was reported in 2009 [17]; $(NH_4)[M(HCOO)_3]$(M = Mn, Fe, Co, Ni, Zn) was reported in 2011 [18]; $[NH_2(CH_3)_2][Fe^{III}Fe^{II}$-$(HCOO)_6]$ was reported in 2012 [19] and $[C(NH_2)_3]Cr(HCOO)_3$ was predicted by DFT calculation to be multiferroic in 2013 [53].

Even though multiferroic MOFs have been investigated for years, the magnetoelectric coupling, which is the most important property in these materials was only reported very recently. In 2011, the magnetoelectric coupling in $[C(NH_2)_3]Cu(HCOO)_3$

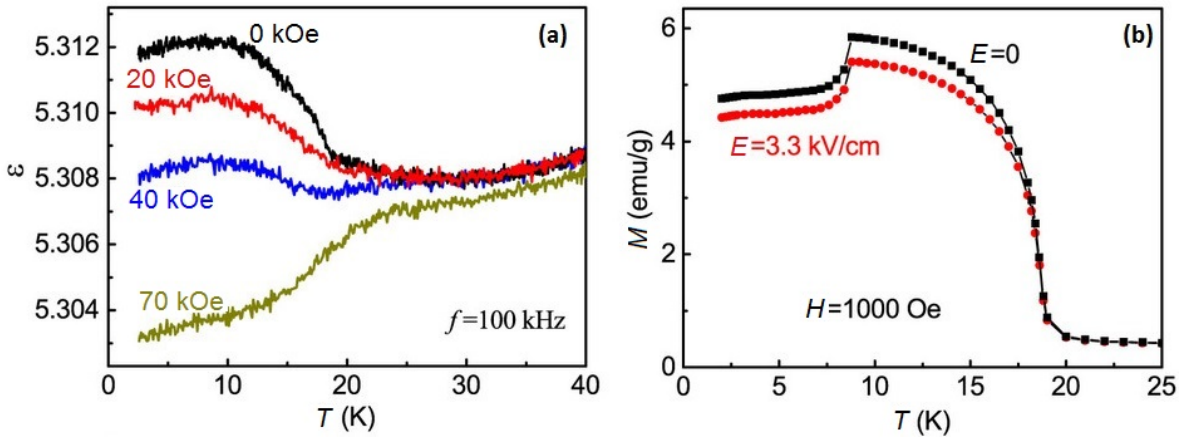

Figure 2.2: The magnetoelectric coupling in $[(CH_3)_2NH_2]Fe(HCOO)_3$. (a) Dielectric constants as a function of temperature with different applied magnetic fields. The magnetic fields were applied along the same direction ([012]) along the crystal. (b) Magnetisation as a function of temperature measured with and without an electric field. The electric field was applied also along the [012] direction of the crystal during cooling process and was removed before starting the measurements during warming [57].

was theoretically shown by ab-initio simulation [54]. The magnetic control of ferroelectricity [55] and the electric control of the magnetic order [56] in MOFs were observed in 2010 and 2014, respectively. Finally in 2014, a cross coupling between magnetic and ferroelectric orders was firstly found in $[(CH_3)_2NH_2]Fe(HCOO)_3$ by Tian [57] followed by the observation of strong cross coupling in $[C(NH_2)_3]Cu(HCOO)_3$ [58]. In $[(CH_3)_2NH_2]Fe(HCOO)_3$, as can be seen in Fig. 2.2 (a), the dielectric constant was suppressed by an external magnetic field while in Fig. 2.2 (b) the magnetisation was apparently lower with a positively poled electric field below the Néel temperature [57]. This provides a clear evidence of strong cross coupling between magnetic and ferroelectric orders in $[(CH_3)_2NH_2]Fe(HCOO)_3$.

Multiferroic MOFs have been achieved and provide a promising path to create new multiferroic systems. However, their multiferroic properties are only shown for temperatures much lower than room temperature [5,16–18,52]. Finding MOFs with multiferroic properties at higher temperatures is one of the main goals of the scientific community asking for the design of new multiferroic MOFs.

2.2 Low-dimensional Magnetism in Organic Complexes

In magnetic MOFs, low-dimensional magnetism exists, which has received much attention in the past decade [5, 6, 8, 9, 20, 59–70]. These crystalline hybrid materials, containing inorganic and organic components, possess extended structures with coordination bonds that can be used to tune interlayer coupling, magnetic anisotropy and the exchange interaction between the transition metal sites. Indeed, if the metal sites are linked by short ligands (such as oxygen anion, cyanide, and oxalate) to form infinite 1D chains and 2D or 3D arrays, there is a structural basis for tunable magnetic interactions [5, 8, 9, 20, 64–68]. In particular the dimensionality of the magnetic interaction and the sign of the magnetic coupling itself can be tuned [6]. For example, isolated clusters [7, 16, 68], 1D magnetic chains [8, 66, 67] and 2D magnetic layers [9, 20] (that often exhibit magnetic anisotropy of the coupling along different dimensions), can be achieved by carefully selecting the specific combination of co-ligands and short ligands.

This thesis focuses on one-dimensional magnetic chain and single molecule magnets ("zero-dimensional"). Therefore, these two systems will be discussed in more detail in following sections.

2.2.1 Molecular magnets

It has long been desired to produce pure organic magnets. Compared with traditional inorganic magnetic materials, organic magnets have interesting physical properties and often have good tunability [71]. Building units of organic magnets are molecules instead of atoms (magnetic elements) so that they are usually called molecular magnets.

The richness of organic carbon chemistry allows many adjustments to the molecular structures of molecular magnets so that their properties can be tuned [71]. A lot of attempts have been made to design pure organic magnets. Organic materials with unpaired electrons (radicals) are not rare but to assemble crystalline structures with

them and to align their spins are not straightforward. Only a limited number of pure organic magnets have been synthesized, such as ferromagnets based on nitronyl nitroxide radicals with a Curie temperature of 1 K and sulfur based radicals showing weak ferromagnetism below 36 K [71].

As it is difficult to produce pure organic magnets, transition metals and lanthanides are introduced in molecule-based magnets [71]. In these hybrid magnets, metals provide magnetic moments and organic blocks mediate interactions between metal ions. By changing organic blocks, interaction pathways vary so that magnetic properties of the system can be tuned [5]. This strategy has produced many molecular magnets with promising properties. Molecular magnets involved in this thesis are all hybrid organic magnetic materials.

In hybrid molecular magnets, magnetic interactions and dipolar interactions between metal ions are essential interactions that determine the magnetic properties [5]. Organic bridges between metal ions provide superexchange pathways that enables exchange interactions. Whereas, metal ions can also interact via dipole-dipole interaction without mediating orbitals [71]. Similar to traditional bulk magnets, molecular magnets can be magnetically ordered and have spontaneous magnetisation when interactions mentioned above are stronger than thermal agitations.

Moreover, by using different organic bridges along different directions, magnetic interactions between metal ions can also be limited to certain dimensions [6–9]. Therefore, the dimensionality of molecular magnets can also be tuned, which is fairly unique property. According to the number of directions along which infinite arrays of interacting magnetic centres exist, one-dimensional chains, two-dimensional layers, three-dimensional networks and even "zero-dimensional" systems with confinement along all directions can be designed.

2.2.2 One-dimensional antiferromagnetic chain

Dimensionality has important consequences for magnetism. For systems with nearest-neighbour exchange interactions, this is evident from simple topological considerations, because the number of magnetic ions with which each spin interacts directly is an important factor in stabilizing long-range order. The ideal 1D spin 1/2 antiferromagnet with only two nearest neighbours for each spin fails to develop long-range order. In a simple cubic 3D spin 1/2 antiferromagnet where there are six nearest neighbours for each spin, mean-field effects lead to long-range magnetic ordering and the Néel state is often an adequate approximation to the true ground state. The prototypical 1D system is the spin 1/2 Heisenberg antiferromagnetic chain, which has a long history dating back to the Ising model first reported in 1925 [72]. In 1964, Bonner and Fisher built on this model to describe the correlation function, heat capacity and magnetic susceptibility of 1D magnetic chains [73]. 1D chains started to be investigated experimentally in the 1970s, and examples are TMMC [74], $KCuF_3$ [75] and $CuCl_2{\cdot}2NC_5H_5$ [76]. Since then, extensive work has been carried out on many different systems. For detailed reviews on the one-dimensional magnetic structure, please consult Ref. [77, 78].

As discussed, in an ideal one-dimensional magnetic system, the spin only interacts with its nearest neighbours. According to the Bonner and Fisher model, linear magnetic chain systems were treated to be finite rings containing N ions (N is a finite number) [73]. In this case of an antiferromagnetic chain, the Hamiltonian describing the magnetic order is [79]:

$$H = -2J \sum_{i=1}^{N} \{S_i^z S_{i+1}^z + S_i^x S_{i+1}^x + S_i^y S_{i+1}^y\} - g\mu_B \sum_{i=1}^{N} \vec{H} \cdot \vec{S}_i, \tag{2.4}$$

with an antiferromagnetic ground state [79]:

$$E_0 = -\frac{1}{2} N|J| - \frac{1}{2} (N+1)\, g\mu_B H, \tag{2.5}$$

where S_i^{α} is the spin along the α direction, J is the exchange energy between these spins, N is the number of spins in the system and g and μ_B are the g-factor and the Bohr magneton, respectively. Then, the partition function of this system under zero field is [79]:

$$\begin{aligned} Z = \int \frac{\mathrm{d}\Omega_0}{4\pi} \int \frac{\mathrm{d}\Omega_1}{4\pi} \cdots \int \frac{\mathrm{d}\Omega_N}{4\pi} \exp\left(\frac{J}{2k_B T} \sum_{i=1}^{N} (\vec{s_i} \cdot \vec{s_{i-1}}) \right) \\ Z_N(T) = \left(\frac{2k_B T}{J} \sinh\left(\frac{J}{2k_B T} \right) \right)^N , \end{aligned} \tag{2.6}$$

where $d\Omega$ is the element solid angle for the vector $\vec{s_i}$ and k_B is the Boltzmann constant. Then, the magnetic internal energy U_N of a 1D antiferromagnetic system is [79]:

$$U_N = N k_B T - \frac{NJ}{2} \coth\left(\frac{J}{2k_B T} \right), \tag{2.7}$$

This internal energy increases slowly with increasing temperature. Therefore, by releasing entropy gradually, its heat capacity would show a broad peak instead of a sharp anomaly in the 3D magnetic transition case. The heat capacity C_N, in this case, is expressed by [79]:

$$C_N = N k_B - \frac{J^2}{4k_B^2 T^2} \sinh^2\left(\frac{J}{2k_B T} \right). \tag{2.8}$$

The numerical estimation based on a S = 1/2 Heisenberg antiferromagnetic chain was given by Ref. [73], showing the maximum position and the value of the broad peak in the heat capacity:

$$C_{Max} \sim 0.350 N k_B; \tag{2.9}$$

$$k_B T_{Max} = 0.962 |J| . \tag{2.10}$$

In terms of magnetic properties of the one-dimensional antiferromagnetic chain, the

spin pair correlation in this system was also described by Fisher [79]:

$$G_m = \langle S_n S_{n+m} \rangle = (-1)^{-m} s^2 \exp\left(-\kappa |m|\right), \tag{2.11}$$

with the inverse correlation length κ:

$$\kappa = -\log\left(\coth\left(\frac{2|J|\, s^2}{k_B T}\right) - \frac{k_B T}{2|J|\, s^2}\right), \tag{2.12}$$

As shown in Eq. 2.12, the correlation length of a one-dimensional antiferromagnetic system diverges at zero temperature and decreases as the temperature increases. Using the fluctuation relation, the magnetic susceptibility of a S = 1/2 system under zero field is related to the magnetic correlation length by [79]:

$$\chi(T) = \frac{g^2 \mu_B^2}{4 k_B T} \sum_{i=0}^{N} \sum_{j=0}^{N} \langle s_i^z s_j^z \rangle, \tag{2.13}$$

which can be derived to be [79]:

$$\chi = \frac{N g^2 \mu_B^2}{12 k_B T} \frac{1 + G_m(\kappa)}{1 - G_m(\kappa)} \tag{2.14}$$

where G_m is the correlation function and κ is described in Eq. 2.12. The magnetic susceptibility of the 1D antiferromagnet calculated here also shows a broad peak at the position:

$$k_B T_{Max} = 1.282 |J|, \tag{2.15}$$

with a peak value:

$$\chi_{Max} \sim 0.07346 \frac{g^2 \mu_B^2}{|J|}. \tag{2.16}$$

This broad peak is considered to be a signature of a one-dimensional antiferromagnetic structure in susceptibility measurements. The numerical solution and modification of the temperature dependence of the magnetic susceptibility was then calculated to

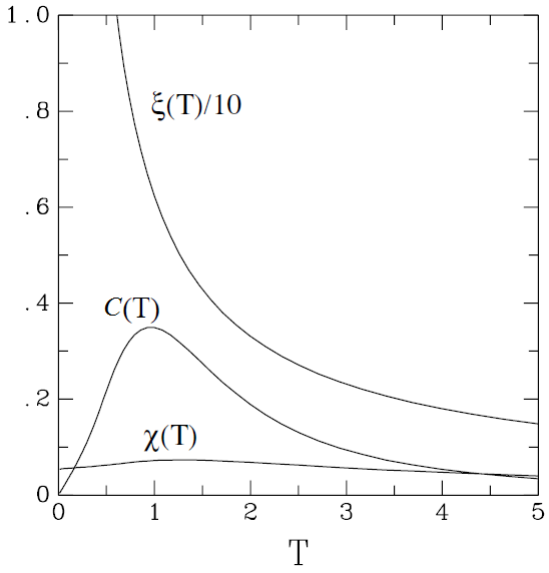

Figure 2.3: Magnetic correlation length ξ, magnetic susceptibility χ and heat capacity C of a 1D Heisenberg antiferromagnetic chain [82].

be [80, 81]:

$$\chi_{chain} = \frac{Ng^2\mu_B^2}{k_B T} \frac{0.25 + 0.074975x + 0.075235x^2}{1.0 + 0.9931x + 0.172135x^2 + 0.757825x^3}, \tag{2.17}$$

where χ_{chain} is the magnetic susceptibility and x is defined as:

$$x = \frac{|J|}{k_B T}. \tag{2.18}$$

This is for an ideal antiferromagnetic one-dimensional chain system so that the interchain exchange energy is neglected. If taking the interchain exchange energy, which is not negligible in a real one-dimensional system, into account, the modification is shown below [81]:

$$\chi = \frac{\chi_{chain}}{1 - \frac{2zJ'}{Ng^2\mu_B^2}\chi_{chain}}, \tag{2.19}$$

where z is the number of the nearest neighbours of the metal ions.

The theoretical magnetic internal energy, correlation function, heat capacity and susceptibility of a one-dimensional magnetic chain have been discussed and these quan-

tities as a function of temperature are shown in Fig. 2.3. Among these properties, the magnetic susceptibility and heat capacity are often used to characterise one-dimensional systems and to measure the exchange energies within the systems according to Eq. 2.8, Eq. 2.17 and Eq. 2.19. Pure one-dimensional magnetic systems do not support long-range magnetic order at a finite temperature as it is very easy to destroy the magnetic chain by breaking it at one point to allow spins to point to different directions at different sides of this breaking point [83]. Thus, a short-range correlation, which exists at a temperature that is higher than the exchange energy along the magnetic chain, is a key characterisation of a one-dimensional magnetic system.

In addition to the magnetisation investigations on one-dimensional magnetic systems as discussed above, neutron scattering techniques have been used to investigate one-dimensional magnetic chains. Neutron scattering, which can give an instantaneous picture of the magnetic system, is a powerful tool to study magnetic structures, spin interactions and excitations in one-dimensional magnetic chains directly. Many quasi-one-dimensional magnetic systems, such as $KCuF_3$ [84], $CsNiF_3$ [77] and $NiTa_2O_6$ [85], were investigated using elastic and inelastic neutron scattering to understand the magnetic structures, spin waves and magnetic correlation lengths.

With extensive research into MOFs in the past decade, many real one-dimensional magnetic chain systems have been reported among these new hybrid materials. However, only a relatively small number of studies are based on neutron scattering studies [86–94]. This may be explained by two reasons: 1. it is difficult to synthesize reasonable quantities of deuterated compounds, which are needed for neutron experiments as ^{1}H has a large inelastic neutron scattering length which contributes to background rather than constructive interference cross-section whereas ^{2}H has a reasonable elastic scattering length. A useful signal may not be detected if non-deuterated materials are used; 2. magnetic contributions to the total neutron scattering are weak in these materials [94]. Other techniques, such as electron paramagnetic resonance (EPR) [16, 95] and muon spin spectroscopy [96], have been utilised to study these hybrid one-dimensional

systems. Reports based on EPR and μSR measurements mainly focus on phase transitions [16, 95, 96] and spin dynamics [96] in one-dimensional magnetic chains.

2.2.3 Single molecule magnets

Molecular magnets also offer a new path to study magnetic properties. Using organic building blocks allow them to have many advantages over traditional metallic or metal oxide magnets, for example low density, transparency and electrical insulation [71]. As discussed in the previous section, their properties, particularly dimensionality, can be tuned by varying the organic building blocks.

Introduction to single molecule magnets

Single molecule magnets (SMMs), in which every single molecule shows spontaneous magnetisation, have very weak interactions between molecules. Every molecule can be viewed as an isolated magnet. These materials with single magnetic domains perform as a collection of giant magnetic moments, which work similarly to the spin centres in paramagnetic materials [30]. They can be magnetised by external magnetic fields but with a larger magnetic susceptibility.

With the existence of very strong magnetic anisotropy in these nano-scaled materials, the magnetic moment ideally has two stable orientations antiparallel with each other and separated by an energy barrier [30]. Even though every single-domain unit performs like a giant magnetic moment, the individual spins can also flip randomly owing to thermal or magnetic field perturbations. This is very similar to the magnetisation relaxation in superparamagnetic materials [30], in which spins on every single nanoparticle relax with the help of external perturbations. Louis Néel investigated the magnetic anisotropy and magnetisation relaxations in superparamagnetic materials in 1949 [97]. The models and approaches he developed can also be used to describe the magnetisation relaxations in SMMs. The Néel relaxation phenomenon and the zero-field

relaxation is described by the Néel-Arrhenius equation [97, 98]:

$$\tau_{N\acute{e}el} = \tau_0 \exp\left(\frac{KV}{k_B T}\right), \tag{2.20}$$

where $\tau_{N\acute{e}el}$ is the average time for the magnetisation of the single-domain unit randomly flipping as a result of thermal fluctuations. τ_0 is the relaxation constant, which is called "attempt time" with a typical value between 0.1 and 1 ns and is a characteristic parameter. K is the magnetic anisotropy energy density. V is its volume and T is the temperature. KV is then the energy barrier associated with the magnetisation moving from its initial easy axis direction, through a hard plane, to the opposite easy axis direction. It is clear that a large energy barrier is necessary to keep the magnetisation of the single-domain unit. Thus, the magnetisation relaxation rate is a crucial criterion of a good SMM.

Another important parameter that characterises SMMs is the blocking temperature. It is defined as a temperature below which the magnetic state of the material is "blocked". In Néel's original paper, blocking temperature T_B was also defined [97, 98]:

$$T_B = \frac{KV}{k_B \ln\left(\frac{\tau_m}{\tau_0}\right)}, \tag{2.21}$$

where τ_m is the measurement time. It is easy to understand that when $\tau_{N\acute{e}el} < \tau_m$, the spin of the single-domain unit will flip during the measurement time and the measured magnetisation will be averaged to be zero. In contrast, when $\tau_{N\acute{e}el} > \tau_m$, the instantaneous magnetisation will be maintained as there is not enough time for the spin to flip during the measurement time. It is worth mentioning that T_B, even though it can characterise the performance of an SMM, can vary in different measurements. By increasing the frequency of the instrument, meaning that the measurement is fast and τ_m is small, one can increase the apparent T_B of an SMM material.

Therefore, unlike traditional magnets, the magnetic hysteresis in SMMs does not re-

quire long-range magnetic ordering in these materials. Even in the paramagnetic state of SMMs, the magnetic hysteresis was reported [99–103]. When the system has a large overall magnetic anisotropy, the magnetisation relaxation time τ in this particular material will be long [30]. If the magnetisation relaxation is slower than the measurement window, the magnetisation relaxation is not able to be detected by the instrument. Thus, every molecule, viewed as an isolated magnet, can "memorise" its magnetisation and this results in a magnetic hysteresis phenomenon in the paramagnetic state.

SMMs are also great media for understanding quantum magnetisation. Some theoretically predicted phenomena were observed in SMMs. For example, macroscopic quantum tunnelling of magnetisation was observed in an SMM, Mn_{12}-acetate cluster [104, 105]. Moreover, in 1999, the interference of the quantum spin phase (Berry phase) was observed in another SMM, a Fe_8 cluster [12]. Hence, SMMs are valuable mesoscopic systems, which could provide experimental data for validating physical models of quantum size effects in magnetism.

Two types of single molecule magnets

To form an SMM, a high-spin molecule, which has a high number of spins, is needed. These high-spin systems can be achieved by two methods: putting magnetic ions together to form a magnetic cluster or using a single high-spin ion such as a lanthanide ion in a molecule [30, 106]. Hence, there are broadly two types of SMMs, namely cluster-based SMMs and single ion magnets (SIMs). By choosing organic building blocks carefully, the magnetic ions (clusters) in SMMs can be far apart from each other so that the magnetic exchange energy is very small and only very weak dipolar interactions between these organic blocks exist [106]. Therefore, every single molecule can be viewed as an isolated magnetic system or a nanomagnet.

The first reported SMM is $[Mn_{12}O_{12}(CH_3COO)_{16}(H_2O)_4]\cdot 2CH_3COOH\cdot 4H_2O$ (Mn_{12}-acetate), a cluster-based molecule magnet. Its magnetic properties were firstly investigated and the magnetic ground state was reported to be S = 14 [107]. In 1991, D.

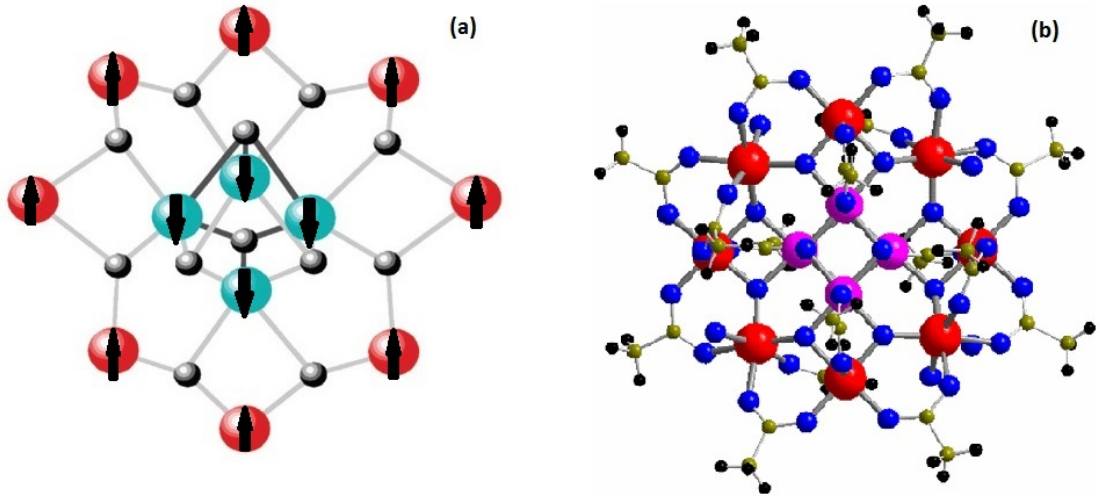

Figure 2.4: (a) Chemical structure of the magnetic core of a Mn_{12}-acetate molecule with four inner spin-down Mn^{4+} (green) and 8 spin-up Mn^{3+} (red) [108]. (b) Structure of a Mn_{12}-acetate molecule viewed along the *c*-axis with large pink balls representing the inner Mn, large red balls referring to outer Mn atoms, medium blue balls highlighting the position of O atoms, small yellow balls representing C atoms and small black balls to be H. The spins point up and down along the *c*-axis [109].

Gatteschi and R. Sessoli carried out EPR measurements on Mn_{12}-acetate and discovered a paramagnetic behaviour with a magnetic ground state S = 10 [32]. Since then, not only Mn_{12}-acetate but also other cluster-based SMMs have been extensively studied.

The structure of Mn_{12}-acetate is shown in Fig. 2.4. The magnetic core of the Mn_{12} cluster is formed by a Mn^{4+} (S = 3/2) tetrahedron surrounded by eight Mn^{3+} (S = 2) ions. These Mn ions are coupled by exchange through oxygen bridges and the four inner ions and eight outer ions possess opposite spin directions [110] so that the total spin S = 10. There are four water and two acetic acid molecules, which are not directly bound to the Mn_{12} core in the Mn_{12}-acetate molecule. The acetic acid molecules located between two adjacent Mn_{12} cores have interactions with the acetate ligands via hydrogen bonds and are also disordered. This disorder results in Jahn-Teller distortions of Mn^{3+} sites [111], which is the most important contribution to the magnetic anisotropy in Mn_{12}-acetate.

Without showing long-range magnetic order, a bifurcation in field-cool (FC)/zero-field-cool (ZFC) magnetisation measurements and magnetic hysteresis effects were ob-

served in Mn_{12}-acetate [7]. Fig. 2.5 (a) shows the temperature dependence of the magnetisation, which was measured along the c-axis of a Mn_{12}-acetate crystal. The FC and ZFC curves separate below $T_B = 3$ K. A magnetic hysteresis was also observed below this blocking temperature, as shown in Fig. 2.5 (b). Unlike an ordered magnetic material, this magnetic hysteresis does not come from the movement of magnetic domain walls. Instead, it depends on every single molecule in the system. When the magnetisation relaxation is slower than the measurement window, every single magnetic unit can "memorise" its magnetisation and this gives rise to the magnetic hysteresis. The hysteresis loop also shows a temperature dependence as the magnetisation relaxation rate changes with temperatures, as shown in Fig. 2.5 (b) and (d). With a faster relaxation at a higher temperature, it is easier to break the "memory" of the magnetic system so that the hysteresis loop becomes narrower. These results proved that Mn_{12}-acetate has a bistable magnetic state at low temperatures and every single molecule of it worked as a traditional ferromagnet.

Hysteresis loops shown in Fig. 2.5 (b) are very similar to those of magnetically ordered materials. However, the data quality of this measurement was not ideal (the applied field step was large) to fully understand the magnetic hysteresis in Mn_{12}-acetate. In 1996, Friedman [105] and Thomas [104] measured magnetic hysteresis curves of Mn_{12}-acetate more carefully and observed the quantum tunnelling in this material. As shown in Fig. 2.5 (c), Friedman observed steps at regular intervals of magnetic field in the hysteresis loop of field-oriented Mn_{12}-acetate crystals (powder sample oriented using DC fields). Clearer steps in the hysteresis loop were then reported in the same year by Thomas [104] on a single crystal sample, as shown in Fig. 2.5 (d). In the flat regions, the magnetisation relaxation time is longer than the measurement time so that the magnetisation saturated. In the steep regions of the steps, the relaxation time is smaller than the measurement time window resulting in the change of the magnetisation. This means that the magnetisation relaxation rate increase significantly with some certain magnetic fields, because the ground state is lifted by the applied field to match a certain

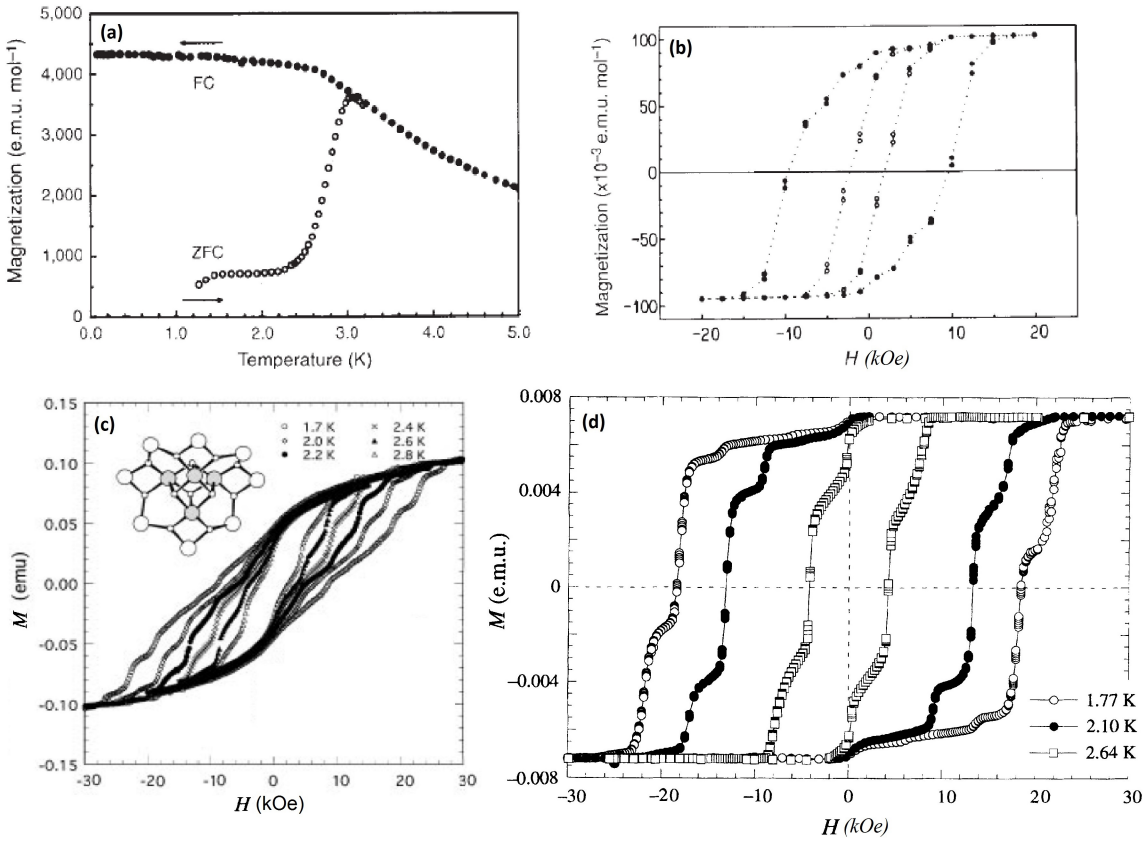

Figure 2.5: (a) The temperature dependence of magnetisation measurements along the c-axis of Mn_{12}-acetate by ZFC and with a 100 Oe direct current (DC) FC [7]. (b) Hysteresis loops of Mn_{12}-acetate measured along the c-axis at 2.2 (solid circle) and 2.8 K (circle) [7]. (c) The field dependence of the magnetisation of Mn_{12}-acetate field-oriented crystals at six different temperatures [105]. (d) The field dependence of the magnetisation of a Mn_{12}-acetate single crystal. The measurement was performed along the c-axis (magnetic easy axis) [104].

excited state resulting in quantum tunnelling between these two states. Thus, the steps in the hysteresis loop is a signature of quantum tunnelling in Mn_{12}-acetate.

The existence of magnetic hysteresis loops is usually a confirmation of the slow magnetisation relaxation in SMMs as the hysteresis can only be recorded when the relaxation time is longer than the measurement time. Mn_{12}-acetate is the first SMM in which slow magnetisation relaxation was detected. It was found that the alternating current (AC) susceptibility of Mn_{12}-acetate had a frequency dependence [32], as shown in Fig. 2.6 (a). The temperature at which the maximum in χ'' occurs is frequency dependent. These data indicate a frequency dependent freezing temperature of the magnetisation. This is a signature of slow magnetisation relaxation as the relaxation time is longer than the time window of a traditional AC susceptibility measurement (> 0.1 ms). The relaxation time can be calculated from the decay of the magnetisation and AC susceptibility shown in Fig. 2.6 (b). It exhibits an exponential decay as a function of temperature. By fitting the decay curve, the efficient anisotropy energy barrier (U_{eff}) and the relaxation time constant (τ_0) can be calculated. They are U_{eff} = 61 K and $\tau_0 = 210$ ns [7]. The field dependence of the relaxation rate seems to have a resonance-like shape [104], as shown in Fig. 2.6 (c). As discussed in Fig. 2.5 (d), the magnetic hysteresis in SMMs exhibits a stair-like shape due to spin tunnelling induced by the magnetic anisotropy in the system. When quantum tunnelling occurs, the magnetisation relaxation rate increases resulting in a sharp decrease of the relaxation time τ, as shown in Fig. 2.6 (c). This resonance-like relaxation time also confirms the existence of spin quantum tunnelling in Mn_{12}-acetate.

Apart from Mn_{12}-acetate, the most studied cluster-based SMM, there are many other cluster-based SMMs that have been synthesized in the past three decades, such as other Mn-core-based [113, 114], Fe_8 [115] and Fe_4 [116] based SMMs. However, the blocking temperature and the relaxation time are difficult to improve in cluster-based SMMs as to increase the anisotropy energy barriers is challenging (the barrier of existing clusters are all less than 100 K) [30].

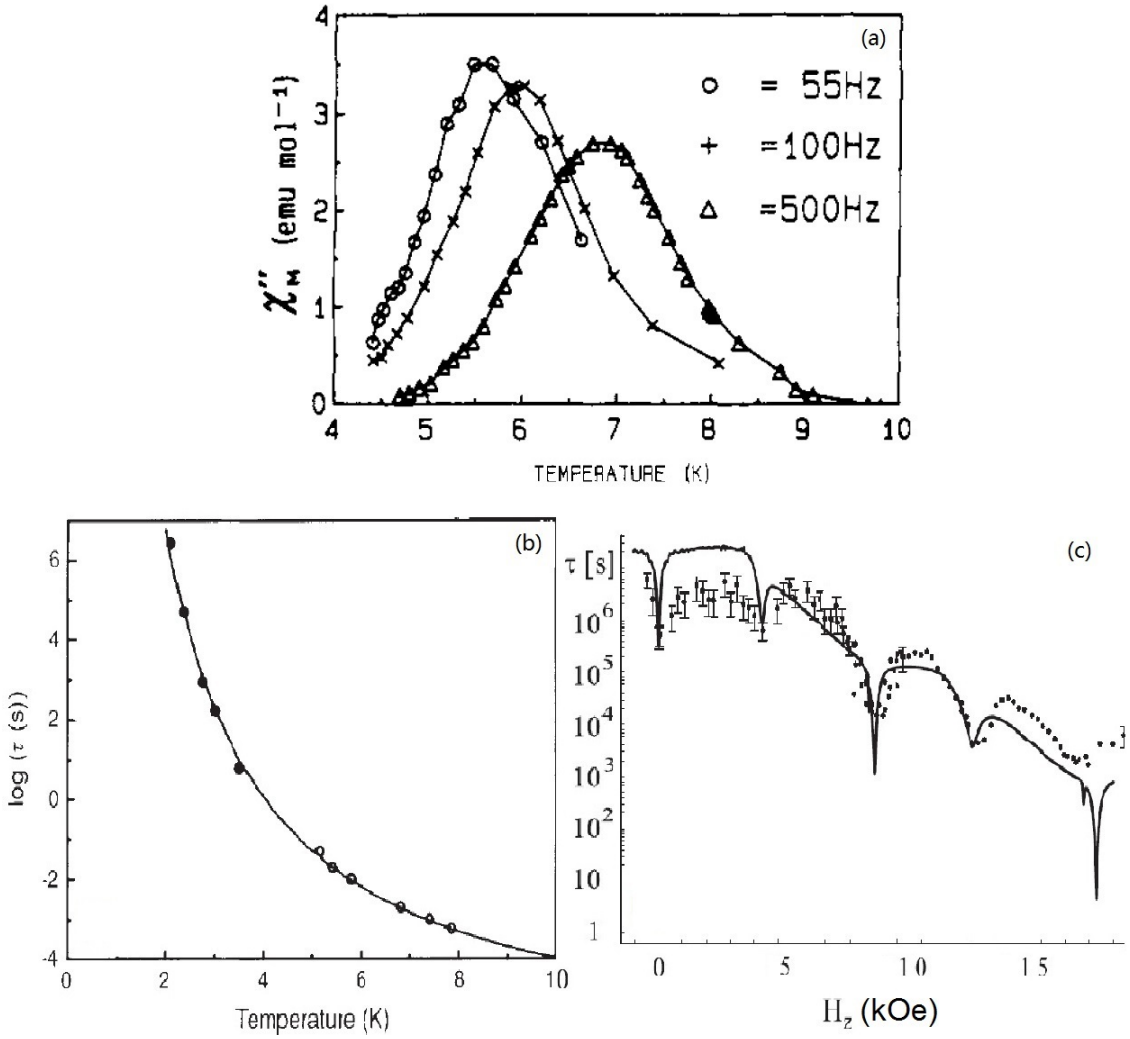

Figure 2.6: (a) Temperature dependence of the imaginary part of the magnetic susceptibility of a Mn_{12}-acetate powder sample measured at zero DC field [32]. (b) The temperature dependence of the relaxation time of Mn_{12}-acetate. Solid circles are data from the decay of magnetisation and open circles are data from AC susceptibility measurement [7]. (c) The relaxation rate as a function of magnetic field along the *c*-axis at 5 K. Dots are magnetisation data from Ref. [104] and full line is from the theoretical model from Ref. [112].

To form a single molecule magnet, a high-spin ground state and large uniaxial anisotropy are required. With an uniaxial magnetic anisotropy, the magnetisation of every single molecule has a preferential orientation that forms the magnetic easy axis of the magnet. Thus, increasing the magnetic anisotropy is the key to improve the performance of an SMM [103]. Uniaxial anisotropy in a system usually has three sources: magnetocrystalline anisotropy, magnetoelastic anisotropy and exchange anisotropy [117]. In SMMs, where exchange and magnetoelastic effects are usually not present, the main contribution to the uniaxial anisotropy is the magnetocrystalline one, which mainly owes to the coupling between the orbital motion of electrons and crystal fields in the system. Therefore, the strong spin-orbit coupling of the paramagnetic ions used to form SMMs, including transition metals for the cluster-based SMMs and lanthanides for SIMs, and its coupling with crystal fields makes strong uniaxial anisotropy possible in these systems. An S = 83/2 Mn_{19}-cored cluster SMM has been synthesized but the anisotropy energy barrier was still quite low [118]. This suggests that simply increasing the spin ground state is not enough to improve the performance of an SMM. Therefore, great attempts have been made to synthesize SMMs with high-spin lanthanide ions as the high-spin lanthanides usually have a larger magnetic anisotropy compared with the transition metal cluster-based SMMs [119–122]. This is because the spin-orbit coupling in lanthanide ions is stronger as the crystal field interaction leading to the unquenched orbital moments, which is quenched in $3d$ metal ions resulting from the crystal field interactions.

The overall uniaxial anisotropy of SMMs which is crucial to improving blocking temperatures is normally small and difficult to control due to the complexity of coupling between individual paramagnetic centres in SMMs [103]. This complexity obstructs the determination of the underlying mechanisms that govern the anisotropy and zero-field splitting properties of SMMs. As a result, it is useful to study SMMs with only one spin carrier to reduce the dimensionality to understand the nature of their electronic structures.

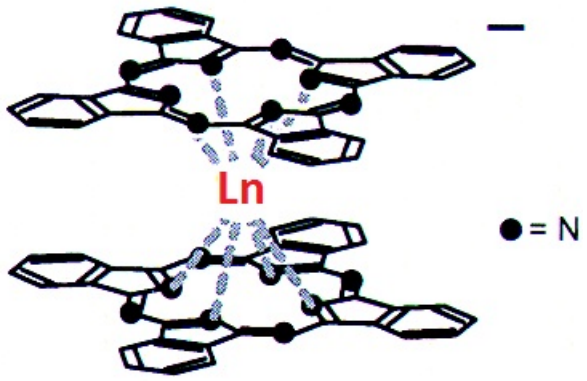

Figure 2.7: The structure of $[Pc_2Ln]^-$ [21].

The first SIM was reported in 2003. Phthalocyanine double-decker complexes, $[Pc_2Ln]^- \cdot TBA^+$ (Ln = Tb, Dy, Ho, Er, TM or Yb; Pc = dianion of phthalocyanine; $TBA^+ = N(C_4H_9)_4^+$) were synthesized and Tb and Dy complexes were found to behave similar to SMMs showing slow magnetisation relaxations [21]. Since then, more and more SIMs systems, such as $[ErW_{10}O_{36}]_9^-$ polyanion in 2008 [119], $U(Ph_2BPz_2)_3$ in 2009 [120], $[Dy(acac)_3(H_2O)_2]$ in 2010 [29], Cp*-Ln-COT in 2011 [121], were synthesized and extensively studied.

$[Pc_2Ln]$ series of complexes are the most studied SIMs systems. $[Pc_2Ln]^-$ has a symmetric structure with a lanthanide ion sandwiched by two phthalocyanine compounds, as shown in Fig. 2.7. In this series of SIMs, the slow magnetisation relaxation and magnetic hysteresis were observed in the Tb and Dy complexes [21, 100]. As shown in Fig. 2.8 (a) and (b), AC susceptibilities of both pure samples and diluted samples are frequency dependent, which is a sign of slow magnetisation relaxation as discussed above. Magnetic hysteresis in these two complexes were also measured by Ishikawa in 2004 [123]. Fig. 2.8 (c) and (d) show hysteresis loops of diluted samples measured at 1.7 K. They are very different from the hysteresis of Mn_{12}-acetate. In this case, the magnetisation decreases sharply in the region $|H| < 1000$ Oe. This indicates that the relaxation in this region is much faster than in the higher $|H|$ region [123]. This fast relaxation at around zero external field was also observed in other SIMs [29, 119]. In

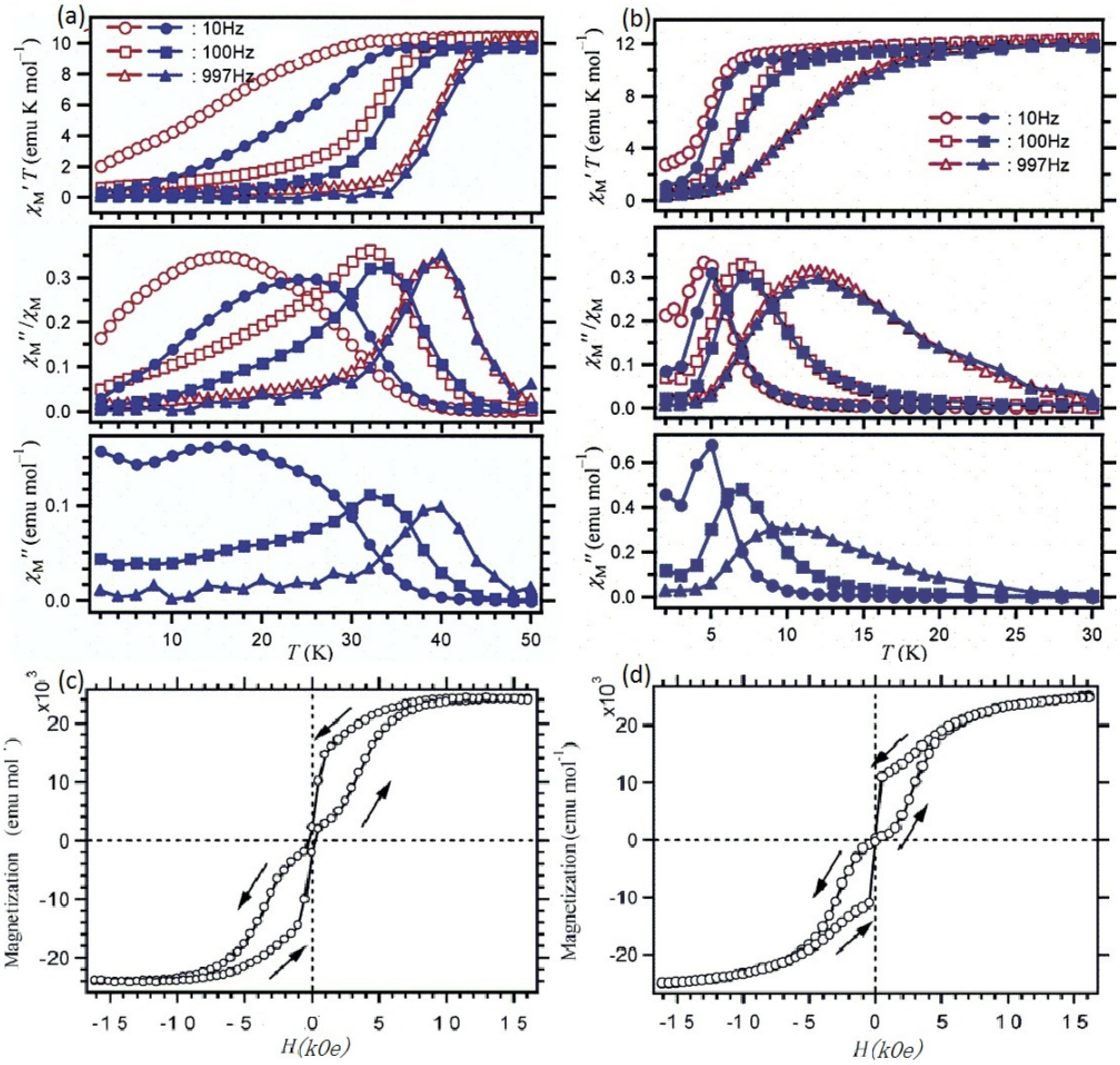

Figure 2.8: (a) AC susceptibilities of the Tb complex (polycrystalline powder). Open symbols are data for the pure Tb complex and solid marks are data for the diluted sample (20% concentration). χ_M', χ_M'' and χ_M are in-phase-AC, out-of-phase-AC and DC molar magnetic susceptibilities, respectively [21]. (b) AC susceptibilities of the Dy complex (polycrystalline powder). Open symbols are data for the pure Dy complex and solid marks are data for the diluted sample (20% concentration) [21]. (c) Magnetic hysteresis of the diluted Tb (2% concentration) complex (powder) at 1.7 K [123]. (d) Magnetic hysteresis of the diluted Dy (2% concentration) complex (powder) at 1.7 K [123].

Ref. [29] and Ref. [103], similar butterfly-like hysteresis loops were also observed in other SIMs systems. This fast relaxation under zero field was explained to be a consequence of quantum tunnelling between the two ground states [29]. This quantum tunnelling effect under zero field was also directly measured by AC susceptibility [29, 103, 124]. Fig. 2.9 (a) shows the first measurement employing a linear AC susceptibility technique based on an SIM $[Cp_2Dy(\mu\text{-bta})]_2$ [124]. It demonstrates the relaxation arising from quantum tunnelling between two ground states is fast under a zero external magnetic field and the magnetic field can quench this fast relaxation.

The magnetic hysteresis loops in SIMs are quite different from those of cluster-based SMMs. Quantum tunnelling is allowed between different substates when they coincide with each other under a certain external applied magnetic field. This quantum tunnelling process that involves excited states is normally called thermally assisted quantum tunnelling. In cluster-based SMMs, the energy difference between different substates is equivalent to a magnetic field strength of several hundred or thousand Oersted. This is much smaller than that in SIMs where the equivalent of approximately 10^5 or even 10^6 Oersted are required. Therefore, thermally assisted quantum tunnelling is often easy to be observed in cluster-based SMMs while in lanthanide-based SIMs the maximally possible applied external magnetic field in a common magnetometer is not enough to allow the thermally assisted quantum tunnelling. When quantum tunnelling occurs, the magnetisation relaxation is much faster and the step structure in the hysteresis loop will be present. So usually stair-like hysteresis loops are observed in cluster-based SMMs while butterfly-shaped hysteresis loops showing zero-field fast relaxations are obtained in lanthanide-based SIMs. However, in 2005, a staircase-like hysteresis loop similar to the one of Mn_{12}-acetate, was observed in an SIM system at $T < 1$ K. When changing the field scan rate in a single crystal sample at 0.04 K, staircase-like hysteresis loops were reported in diluted $[Pc_2Tb]^- \cdot TBA^+$ and $[Pc_2Dy]^- \cdot TBA^+$. Fig. 2.9 (b) and (c) show the magnetic hysteresis of a single crystal Tb complex. The hysteresis curve of the Dy complex is very similar to that of the Tb complex and

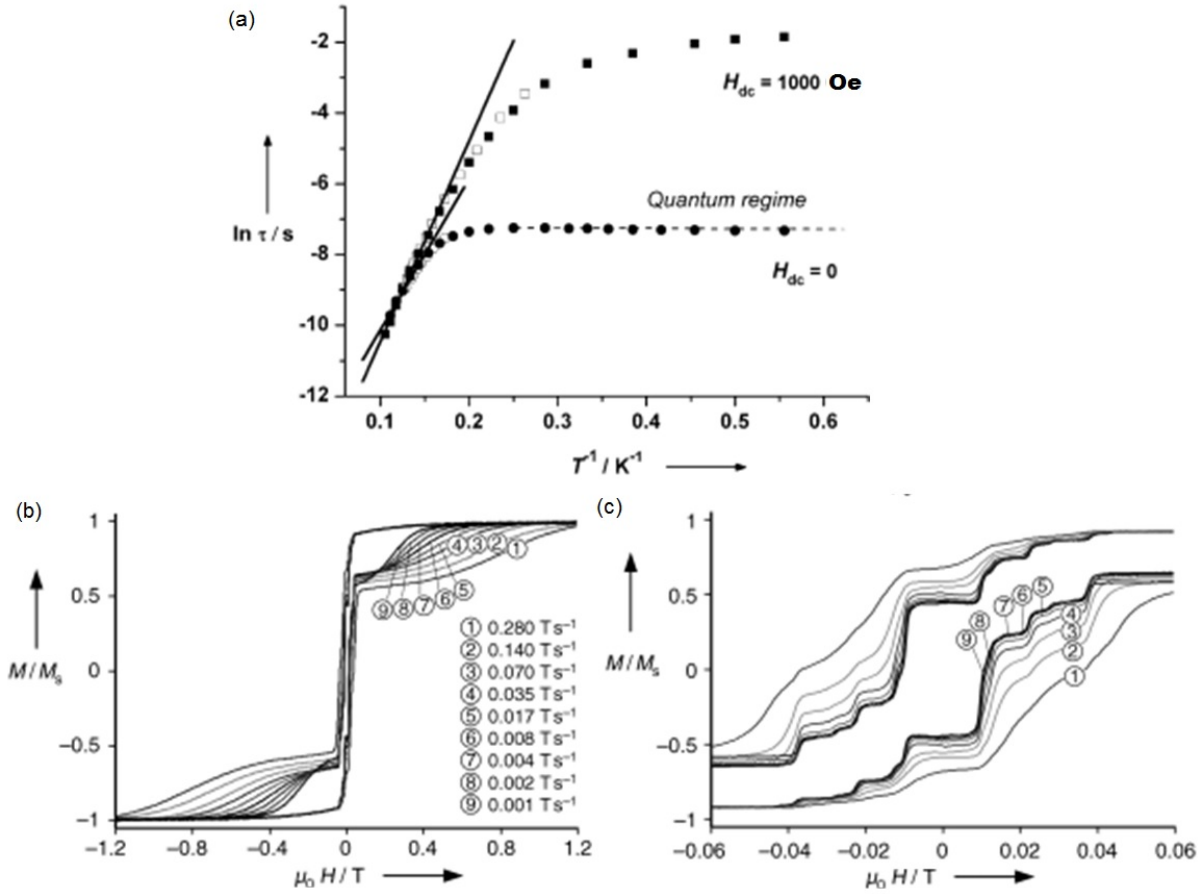

Figure 2.9: (a) The magnetisation relaxation time τ vs. T^{-1} of $[Cp_2Dy(\mu\text{-bta})]_2$ under $H = 0$ Oe and $H = 1000$ Oe. The open symbols are for AC susceptibility data collected with a fixed frequency and varying temperatures while the solid marks are for data measured the other way around. Quantum tunnelling was directly measured by the linear AC susceptibility technique [124]. (b) Hysteresis loops of the diluted Tb complex (2% concentration, single crystal) with different field scan rates. The measurements were performed at 0.04 K with an applied field parallel to the magnetic easy axis [101]. (c) Details in low field region of (b) [101].

can be found in Ref. [101]. The quantum process in this case cannot be tunnelling between different excited states. This is because that it requires a magnetic field that is several orders of magnitude larger to enable the tunnelling between different excited states in lanthanide-based SIM systems. This stair-like hysteresis loop is a result of the resonant quantum tunnelling between entangled states of the electron and nuclear spin systems [101]. It is worth mentioning that this staircase-like hysteresis has not been observed in any non-symmetric lanthanide-based SIMs, as the mix between excited states and ground states is relatively high. The relaxation due to zero-field quantum tunnelling is fast [29, 103]. Thus, it is difficult to measure small steps resulting from nuclear-spin-driven quantum tunnelling.

Long-range magnetic ordering in SMMs

By engineering ligands around the paramagnetic centres in SMMs, the intermolecular interactions can be very weak so that every molecule in the system can be treated as being isolated from each other. In the ideal case when there are no interactions between the molecules, long-range magnetic order is not supported. In practice, however, there are weak interactions between the molecules that when the system is cooled to a temperature that is smaller than the exchange or dipolar energy between the molecules, long-range magnetic order may be observed. It is also worth mentioning even though long-range magnetic ordering in SMMs is not common, the intracluster exchange coupling can be strong to enable spins of the paramagnetic ions to achieve an ordered state inside a cluster [125].

Long-range magnetic ordering has been reported in several SMM systems, both theoretically and experimentally. In 2001, long-range ferromagnetic order in an Fe_8-cored SMM was theoretically predicted to as a result of dipolar interactions below $T \sim 130$ mK by calculation [126]. Then in 2004, long-range magnetic ordering was experimentally reported in a Mn_4 cluster-based SMM with an anomaly in the heat capacity measurements at 0.21 K [127]. Similarly in Mn_{12}-acetate [128–130], Mn_6 cluster

[131] and Fe_{17} cluster [132], long-range magnetic ordering due to dipolar interactions between molecules has also been observed.

In lanthanide-based SIMs, however, long-range magnetic order has never been reported. Considering that the intermolecular interactions is not zero in SIMs, long-range magnetic order may be detected in the future. The reason for the lack of reports of long-range magnetic order in SIMs is probably related to measurements conditions: the measurements carried out on those systems most likely did not reach sufficiently low temperature to investigate the ordering state.

Magnetisation relaxations in single molecule magnets

The magnetic blocking temperature and magnetisation relaxation are crucial properties of an SMM. As discussed in the previous section, all the existing SMMs are still not capable for industrial applications - the blocking temperatures are not high enough and the magnetisation relaxations are too fast at room temperature.

In cluster-based SMM systems, strong crystal field effects cause the zero-field splitting of the spin energy levels, which removes the degeneracy of the S multiplet. This can be described by the Hamiltonian [133]:

$$\hat{H} = D_{xx}\hat{S}_x^2 + D_{yy}\hat{S}_y^2 + D_{zz}\hat{S}_z^2, \tag{2.22}$$

where D_{xx}, D_{yy} and D_{zz} are the zero-field splitting constants. When dealing with such a system, a zero-point is properly chosen to make $D_{xx} + D_{yy} + D_{zz} = 0$. The Hamiltonian can also be described by the spin operator, which shows the interaction between the crystal field and the spin [133]:

$$\begin{aligned} \hat{H} &= \sum_{k,q} B_k^q \hat{O}_k^q \\ &= B_2^0\hat{O}_2^0 + B_2^2\hat{O}_2^2 = B_2^0\left[3\hat{S}_z^2 - S(S+1)\right] + \frac{1}{2}B_2^2\left(\hat{S}_+^2 + \hat{S}_-^2\right), \end{aligned} \tag{2.23}$$

where O_k^q is the spin operator. As the two Hamiltonians should describe the same system and physics, a constant need to be added to Eq. 2.22:

$$\begin{aligned}\hat{H} &= D_{xx}\hat{S}_x^2 + D_{yy}\hat{S}_y^2 + D_{zz}\hat{S}_z^2 - \frac{1}{2}D_{zz}S \\ &= \frac{1}{2}\left(D_{xx}+D_{yy}\right)\left(\hat{S}_x^2+\hat{S}_y^2\right) + \frac{1}{2}\left(D_{xx}-D_{yy}\right)\left(\hat{S}_x^2-\hat{S}_y^2\right) + D_{zz}\hat{S}_z^2 \\ &= \frac{3}{2}D_{zz}\left[\hat{S}_z^2 - \frac{1}{3}S(S+1)\right] + \frac{1}{4}\left(D_{xx}-D_{yy}\right)\left(\hat{S}_+^2+\hat{S}_-^2\right).\end{aligned} \tag{2.24}$$

In the case of uniaxial symmetry, where $D_{xx} = D_{yy}$, the Hamiltonian can be written as: [133]:

$$\begin{aligned}\hat{H} &= \frac{3}{2}D_{zz}\left[\hat{S}_z^2 - \frac{1}{3}S(S+1)\right] \\ &= D\left(\hat{S}_z^2 - \frac{1}{3}S\left(S+1\right)\right),\end{aligned} \tag{2.25}$$

where $D = \frac{3}{2}D_{zz}$. Then, the energy eigenstates will be [133]:

$$E_{M_s} = D\left(M_s^2 - \frac{1}{3}S(S+1)\right), \tag{2.26}$$

where M_s is the spin quantum number. It is clear that without an external magnetic field, energy levels in SMMs will split according to different M_s values. This is the result of electron-electron repulsion and the crystal field effect in the system.

Similarly in lanthanide-based SIMs systems, the crystal field interaction can also cause the energy level splitting [134]. However, different from transition metals, the spin-orbit coupling is much stronger in lanthanide ions thereby enhancing its important role in zero-field splitting. In lanthanide ions, the $4f$ electrons are well shielded by the outer $5s$ and $5d$ states and the $4f$ electrons have an angular variance leading to a much stronger spin-orbit coupling than in $3d$ transition metals, where the angular momentum is quenched by crystal fields. As a consequence, the energy level splitting in lanthanide ions is determined by electron repulsion (levels split $\sim 10^4$ cm^{-1}), spin-orbit coupling (levels split 10^3 to 10^4 cm^{-1}) and crystal field interactions (levels split $\sim 10^2$ cm^{-1}) [134]. The electronic structure of a Dy ion after including electronic

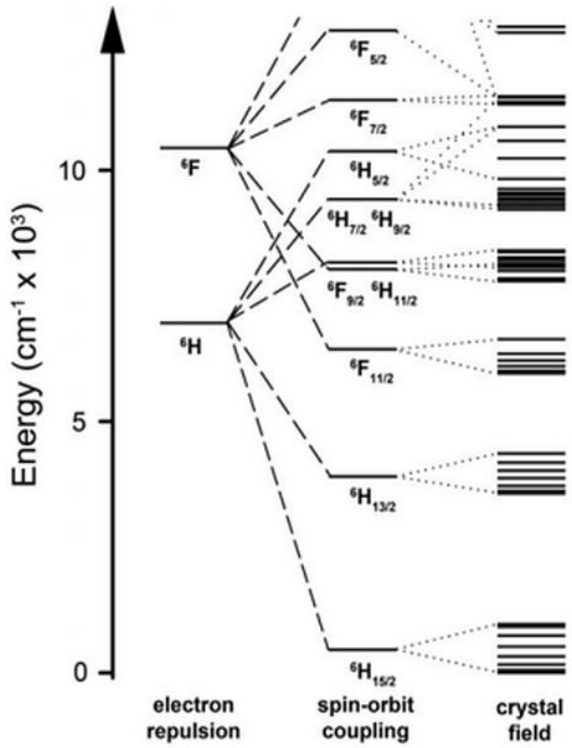

Figure 2.10: The electronic levels of a Dy ion with the influence of the electronic repulsion, spin-orbit coupling and crystal field effects leading to the zero-field splitting of the energy levels in lanthanide Dy [134].

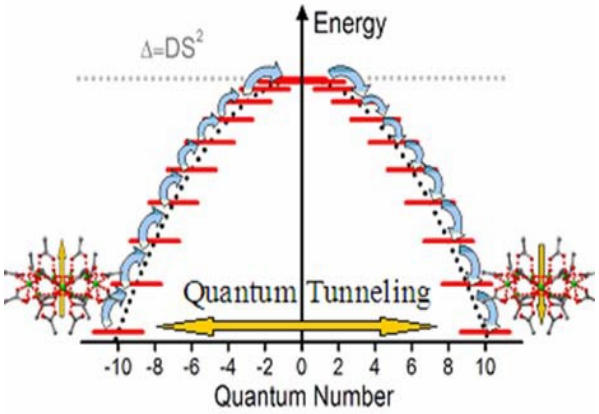

Figure 2.11: Double well model of the schematic energy levels including zero-field splitting based on a cluster-based SMM. The blue arrows and yellow arrows show the thermal-activated relaxation and the quantum tunnelling process, respectively [135].

repulsion, spin-orbit coupling and crystal field effects is shown in Fig. 2.10.

As discussed, even without an external field, all spin energy levels in SMMs have a zero-field splitting into degenerate pairs. This can be described by a double well model, as shown in Fig. 2.11 (taking a cluster-based system as an example). In the ideal case, the $\pm M_s$ levels are orthogonal and no mixing nor magnetisation relaxations between these two states is possible. When a small perturbation is induced in the Hamiltonian Eq. 2.25, the two degenerate states will mix with each other that the spin tunnelling between the two states is then possible, as shown in Fig. 2.11 (yellow arrows). The small perturbation can be provided by many sources, for example external magnetic fields and intermolecular interactions between molecules. Indeed, the tunnelling effects were observed in different SMM systems [29, 103–105, 112, 124].

At low temperatures only the two lowest degenerate levels are populated. With increasing temperature, other higher energy levels are also populated. Therefore, the thermally activated process enables magnetisation relaxations via these higher energy states as shown in Fig. 2.11 (blue arrows). In order to understand the thermally activated relaxation process here, the spin-lattice relaxation theory based on paramagnetic salts can be used [136]. Van Vleck suggested that the lattice vibrations had a significant effect on the spin-lattice relaxation. The two relaxations, the direct and the Raman

relaxations, were described [137]. Later in 1961, Orbach reported a new relaxation process, namely the Orbach process [136]. These three possible spin-lattice relaxation mechanisms are shown in Fig. 2.12 (a), (c) and (d), respectively.

As discussed above, the magnetisation can relax via thermal processes or quantum tunnelling in SMMs. Details of these relaxation processes are:

- Direct process: the direct process is a single-phonon process, where the magnetic ion flips to another energy level directly by absorbing or emitting the energy of one phonon as shown in Fig. 2.12 (a). This process is temperature and field dependent. Van Vleck proved that the spin-lattice relaxation rate had a form of AH^2T, where A is a relaxation constant [137].

- Quantum tunnelling process: this process occurs when two degenerate states mix with each other due to some small perturbation(s) such as intermolecular interactions. It can also happen when the energy of the lowest substates coincide with one of the excited states due to the Zeeman interaction. In theses two cases, the spin can tunnel between two energy states, as shown in Fig. 2.12 (b). It is worth mentioning that the latter case would be rare in lanthanide-based SIMs as energy barriers between the states are usually very large. 10^5 or even 10^6 Oersted of magnetic field would be needed to make the lowest and second lowest energy level to coincide. The relaxation rate of this process was experimentally proven to be $\frac{B_1}{1+B_2H^2}$ [138].

- Raman process: the Raman process involves a phonon with frequency ω_1. The absorption of the phonon causes an excitation of a magnetic ion to reach a virtual state. The magnetic ion then instantaneously decays by emitting a new phonon with a frequency of ω_2, as shown in Fig. 2.12 (c). This is a non-resonant process. The relaxation rate usually follows a temperature power law [137].

- Orbach process: similar to the Raman process, a phonon with a frequency of ω_1 is absorbed. But instead of be excited into a virtual state, the magnetic ion reaches

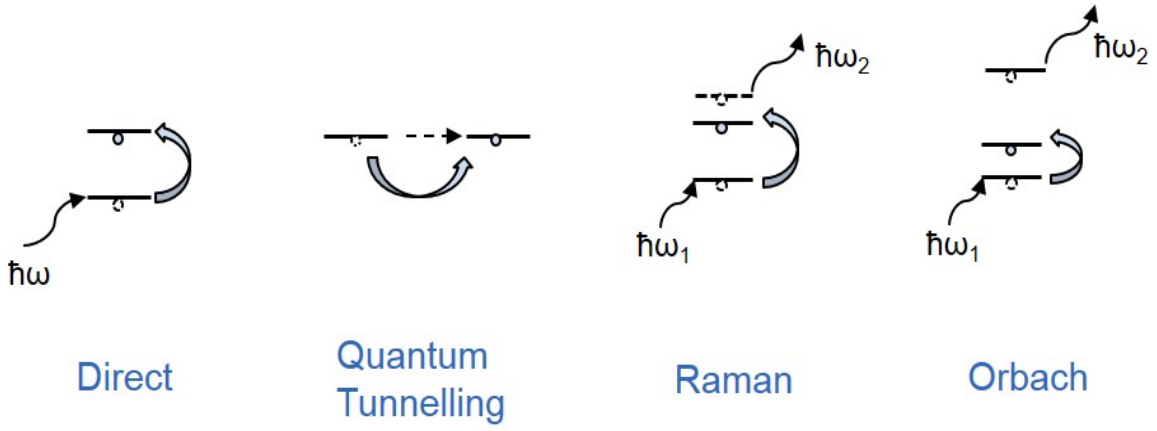

Figure 2.12: Illustrations of the direct, quantum tunnelling, Raman and Orbach magnetisation relaxation processes.

a real intermediate state and then decays to a lower state, as shown in Fig. 2.12 (d). Thus, it is a two phonon resonant process and its relaxation rate usually has the form $\exp(-\Delta E/k_BT)$ with ΔE being the energy barrier between the initial and final states [136].

Therefore, a simple expression of the direct, quantum tunnelling, Raman and Orbach processes is obtained [81, 136, 138]:

$$\tau^{-1} = ATH^2 + \frac{B_1}{1 + B_2H^2} + CT^n + \tau_0^{-1}\exp(\frac{-U_{eff}}{k_BT}), \tag{2.27}$$

where B_1, B_2, C and n are relaxation constants for each process. τ and τ_0 are relaxation times for any given temperature and $T = 0$ K. U_{eff} is an effective energy barrier which spin flipping needs to overcome due to thermal fluctuations. However, this relation is far from complete. Not all of the four processes will always occur at the same time in a material and all the coefficients are material dependent.

Magnetisation relaxations in SIMs are usually studied by AC susceptibility measurements. By studying the nature of the relaxation time, the relaxation mechanism can be understood. Let us take the most studied SIM, $[Pc_2Ln]^-$ series, as an example. As shown in Fig. 2.13 (a), the logarithm of the reverse relaxation time of the Tb

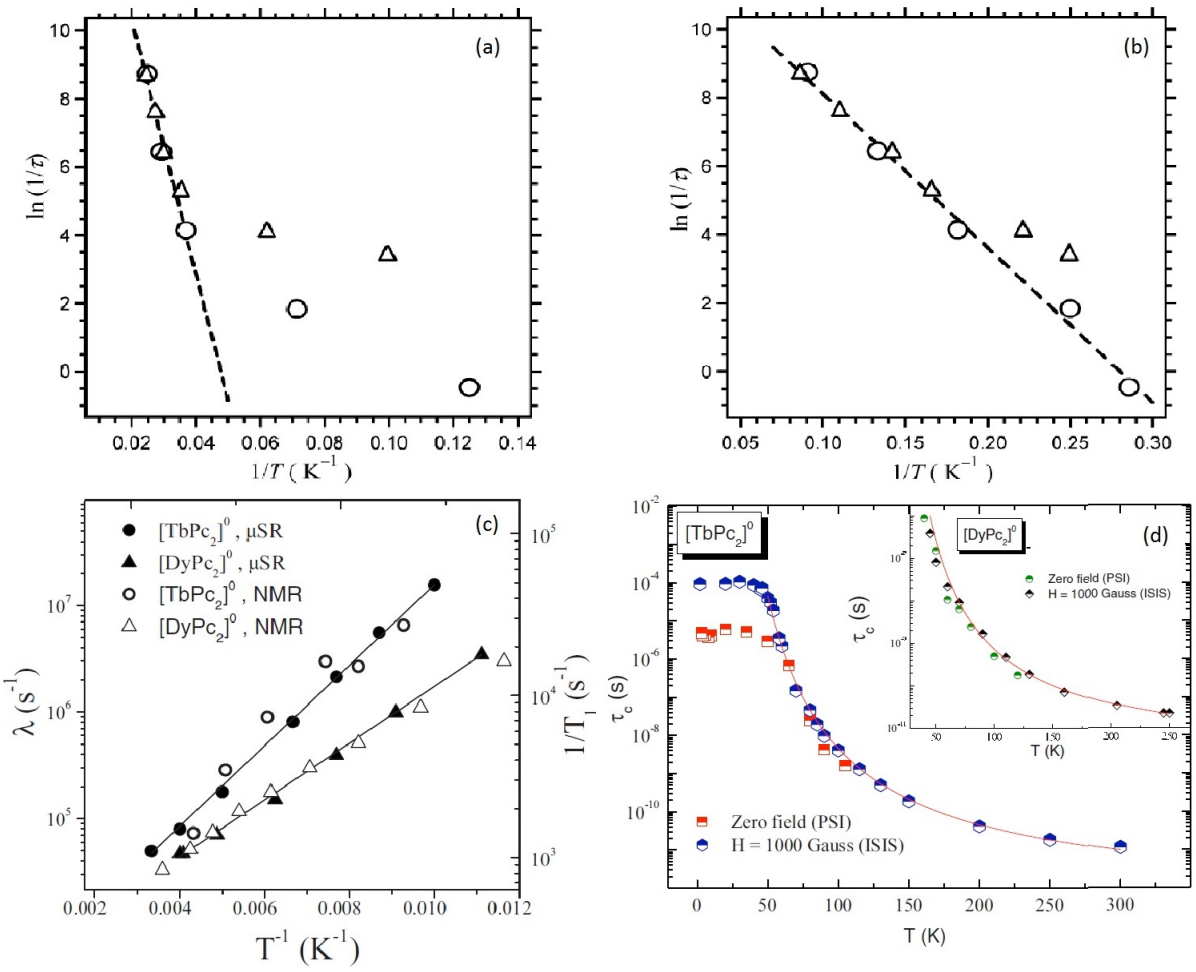

Figure 2.13: (a) Logarithm of the magnetisation relaxation rate vs. the inverse temperature determined with AC susceptibility measurements on pure (triangles) and diluted (2% concentration) (circles) of the Tb complex [123]. (b) Logarithm of the magnetisation relaxation rate vs. the inverse temperature in the Dy complex (triangles are data for pure material and circles are data for diluted (2% concentration) material) [123]. (c) Muon and ^{1}H spin-lattice relaxation rates (NMR), exhibiting a relationship with the spin fluctuation rate that will be introduced in the next chapter, vs. inverse temperature for $[Pc_2Tb]^0$ and $[Pc_2Dy]^0$ complexes. Solid lines here are fit to the Orbach model [139]. (d) The temperature dependence of the correlation time for spin fluctuation rates of $[Pc_2Tb]^0$ under zero field and 1000 Oe measured with μSR. Inset shows $[Pc_2Dy]^0$ data but in a temperature range of 50 K to 250 K [140].

complex vs. inverse temperature ranging from 3 to 30 K is found to be linear. This indicates that the relaxation path is dominated by the two-phonon Orbach process in this temperature range. In the case of the Dy complex shown in Fig. 2.13 (b), it is clear that the relaxation is also governed by the Orbach process between 2 and 25 K. However, at low temperatures (below 25 K), the relaxation time of the Tb complex shifts away from the Orbach relaxation model and the difference between the diluted and pure samples indicates that either the direct or Raman process dominates below 25 K in the Tb complex [123]. By fitting the data with the Orbach model, the effective energy barriers in these two materials are 32.2 meV for Tb and 3.8 meV for Dy, both in agreement with the electronic structure.

At high temperatures, magnetisation relaxations, which are usually dominated by the thermal process (Orbach and Raman), are usually very fast. In this temperature regime, nuclear magnetic resonance (NMR) and muon spin spectroscopy which have higher frequency responses than traditional AC susceptibility measurements are utilised to investigate fast magnetisation relaxations in SMMs as they offer higher probing frequencies. Fig. 2.13 (c) and (d) show NMR and μSR measurements on $[Pc_2Ln]^0$ series [139, 140], which are slightly different from the $[Pc_2Ln]^-$ discussed above. They are $[Pc_2Ln]^-$ systems, oxidised involved one electron. The magnetisation relaxation in both Tb and Dy complexes were very fast at high temperatures. It is clear that the Tb compound shows a fast temperature independent relaxation above 50 K and a field dependent quantum tunnelling relaxation below 50 K. Moreover, the relaxation time above 60 K in Fig. 2.13 (d) can also be described by the Orbach relaxation model and the first and second excited states were involved in the relaxation process. As NMR and μSR techniques can measure fast relaxations, magnetisation relaxations in SMMs can be investigated from very low temperature (< 1 K) up to room temperature. This is helpful to understand relaxation pathways and to measure electronic structures experimentally in SMMs.

2.3 Summary

In this chapter, basic principles of multiferroics and low-dimensional metal-organic complexes were reviewed. The background of both traditional oxide inorganic multiferroics and multiferroic MOFs was introduced. The magnetoelectric coupling and structure-property relationship in multiferroics are essential to understand these materials and provide important information for new material design.

Basic concepts of low-dimensional magnetic structures were discussed in detail. The Bonner and Fisher model describes the behaviour of heat capacity, magnetic susceptibility and magnetic correlation function in a 1D Heisenberg antiferromagnetic chain. With this model, the 1D magnetic chain can be characterised by measuring its magnetic properties. Single molecule magnets, which are "zero-dimensional" magnets, were also reviewed. The principles and properties of typical SMMs were introduced. Magnetic hysteresis and slow magnetisation behaviour was observed in SMMs without showing long-range magnetic order.

The magnetoelectric coupling in some multiferroics is complicated and the structure-property relationship in multiferroic MOFs has not been well studied. Moreover, the working temperature and magnetic properties of low-dimensional molecular magnets are still not suitable for future applications. Therefore, the magnetic structures and properties of the room temperature multiferroic material - $BiFeO_3$, multiferroic low-dimensional magnetic MOF - copper guanidinium formate and a series of single molecule magnets - CP^*-RE-COT will be studied in this thesis. Thus, a better understanding of these systems can be gained and more information of how to optimise their properties would be obtained.

Chapter 3

Experimental Techniques

In this thesis, the magnetic structure and spin dynamics in multiferroic $BiFeO_3$ epitaxial thin films and low-dimensional magnets are discussed. Apart from commonly used techniques to characterise magnetic materials and thin films, such as X-ray diffraction (XRD) and atomic force microscopy (AFM), muon spin rotation, relaxation and resonance, magnetic susceptibility measurements and neutron scattering are the main techniques employed for this thesis. Therefore, details of these three techniques will be discussed in this chapter.

3.1 Muon Spin Rotation, Relaxation and Resonance

The muon spin rotation, relaxation and resonance technique involves the implanting of positive muons into materials, where they probe their environment at a microscopic level. The time evolution of muon spin polarisation provides information about the local magnetic environment and the physical and chemical properties of a material. Unlike the resonance-based NMR and EPR techniques, the "R" in μSR stands for either rotation, relaxation or resonance. When the muon spin experiences a Larmor precession around a DC magnetic field, μSR is referred to as muon spin rotation. When the muon senses dynamics in the material, its spin can relax towards an equilibrium

direction, i.e. the muon spin ensemble, which was 100% spin polarised at the beginning of the experiment, tends to relax towards an unpolarised muon spin ensemble. In the case of muon spin resonance, more complex dynamics dictated by the addition of short radio frequency pulses or intrinsic resonance are involved, such as the muon-electron level crossing. This technique was utilised in the past few decades to investigate the properties of magnetic materials, superconductors and soft materials.

3.1.1 Introduction to μSR

The muon, which belongs to a family of elementary particles known as leptons, is a spin $\frac{1}{2}$ particle with a magnetic moment of $m_\mu = 3.18\mu_p$ ($\mu_p = 1.4106\times10^{-26}$ JT^{-1}, μ_p is the proton magneton). Thus, it can act as a sensitive local magnetometer when it is implanted into a material - it can probe the local magnetic field at its site and its precession provides a way to measure the local field precisely. A muon has a negative charge but an antimuon, which has a positive charge, is normally used in μSR experiments. A positively charged muon is like a proton but it is only about one-ninth of a proton's mass. In this case, a muon can behave like a light proton isotope in a material. Moreover, it can pick up an electron to form a muonium, which can interact with materials in a similar manner to hydrogen. In some certain semiconductors, the muonium sits at an interstitial site that would give information about the carrier lifetime. Or it can chemically bond to certain materials to create a radical, thereby providing information about the chemical bonding in materials. Moreover, a muon is also an unstable particle with a lifetime of 2.2 μs and decays into a positron and two neutrinos. The spin direction of the muon at time of the decay is linked to the emission distribution of the positrons. By detecting the emission direction of the positron, the direction of the muon spin at the decay time can be obtained. Thus, the muon's spin polarisation at time of the decay can be measured. The properties of a positive muon particle are listed in Table 3.1.

Even though muons exist in nature as cosmic rays, particle accelerators are needed

Table 3.1: The properties of a positive muon (μ^+) compared with an electron and a proton, where m_e and e are the mass and the charge of an electron.

Properties	Muon	Electron	Proton
Mass	207 m_e = 105.7 MeV/c^2	m_e = 0.51 MeV/c^2	1836 m_e = 938 MeV/c^2
Moment	3.18μ_p = 4.49×10^{-26} JT^{-1}	657μ_p = 9.27×10^{-24} JT^{-1}	μ_p = 1.41×10^{-26} JT^{-1}
Charge	e	-e	e
Spin	1/2	1/2	1/2
Gyromagnetic ratio (MHz/T)	135.5	-28025	42.6
Lifetime	2.2 μs	4.6×10^{26} years	$\sim$10^{32} years

to produce high intensity spin polarised muons for experiments in condensed matter physics where a high counting rate is necessary. By directing an accelerated proton beam to a production target, pions are produced [141]:

$$p + p \rightarrow p + n + \pi^+, \tag{3.1}$$

or

$$p + n \rightarrow n + n + \pi^+. \tag{3.2}$$

The produced pions have different momenta. Different types of μ^+ beams can be chosen for μSR measurements, including a high-energy, low-energy or surface beam. Most of μSR experiments (including all of the μSR experiments in this thesis) use surface muons (momentum = 29.8 MeV/c, kinetic energy = 4.2 MeV). After the pions are obtained, positive muons are created via a two-body decay of the pions that possess a lifetime of 26 ns [141]:

$$\pi^+ \rightarrow \mu^+ + \nu_\mu. \tag{3.3}$$

To obey the conservation of momentum, the muon's and the neutrino's momenta must

be of equal magnitude and opposite to one another as the pions that are used are at rest in the case of the surface muons. Therefore, both the neutrino and the μ^+ are ejected with their spins antiparallel to their momenta as a result of the conservation of spin. Therefore, the produced muon beam is nearly 100% spin-polarised.

Once muons are produced, they are directed to the sample by a series of focusing and steering magnets and the spin polarisation of muons is maintained during the transport process (the muon spin direction changes on average only 15 mrad [142]). Then, muons are implanted into the sample with an energy of 4.2 MeV and a 0.1 to 1 mm penetration depth. The kinetic energy of the implanted muons is then reduced to a few keV within hundreds of picoseconds as a consequence of the inelastic scattering by the sample. Sitting in the sample, these muons then temporally form neutral muonium by continuously "catching" and "losing" electrons. During this process, muon spins and electron spins in the "temporary muonium" are coupled by hyperfine interactions resulting in the overall change of the directions of muon spins. The energy of muons then reduces to hundreds of eV within a picosecond [142]. Finally, the "temporary muonium" collides with the surrounding atoms or molecules in the sample and continuously loses energy before coming to rest. In this process, the "temporary muonium" can dissociate into an unbound muon by losing an electron or remain as a hydrogen-like muonium.

As discussed, a muon decays with a lifetime of 2.2 μs. The decay of the muon is a three-body process, in which a muon decays into a positron and two neutrinos as a result of the lepton number conservation:

$$\mu^+ \rightarrow e^+ + \nu_e + \overline{\nu}_\mu. \tag{3.4}$$

Among the three particles, the positron is detected in μSR experiments by scintillators with photomultiplier tubes or solid state detectors such as avalanche photodiodes. In this three-body decay, the energy of the emitted positron has an angular dependence and this angular dependence correlates with the distribution of the energy between the three

bodies involved. Fortunately, this decay is mediated by the weak interaction so parity conservation is violated and the momentum of the emitted positron is preferentially along the decaying muon spin direction. According to the theory of the weak interaction, the probability W for a positron to be emitted at a angle of θ to the direction of the muon spin is [143]:

$$W(\theta) \propto [1 + a(\epsilon)\cos\theta], \tag{3.5}$$

where $a(\epsilon)$ is the asymmetry factor of the emitted positron expressed as $(2\epsilon - 1)/(3 - 2\epsilon)$, ϵ=E/E_{max}, which is the reduced kinetic energy of the positron normalised to the maximum kinetic energy of a positron E_{max}. The maximum energy of the positron is observed when the two neutrinos in the three body decay recoil against the positron. Hence the corresponding maximum energy is [144]:

$$E_{max} = \frac{1}{2} m_\mu c^2 = 52.7\,\mathrm{MeV}. \tag{3.6}$$

The energy distribution of the emitted positrons can be described by $2\epsilon^2(3-2\epsilon)$. Therefore, the spatial emission distribution of the positron can be expressed as [142]:

$$W(\theta) = [1 + a(\epsilon)\cos\theta]2\epsilon^2(3 - 2\epsilon). \tag{3.7}$$

This spatial distribution is shown in Fig. 3.1 (a). Thus, a positron that has the maximum kinetic energy means an asymmetry factor $a = 1$. If taking all the positrons with different energies into account, the average asymmetry factor, calculated by integration over the whole energy range, is $\overline{a} = 1/3$.

In a real μSR experiment, the positron detector arrays are placed around the sample to monitor the time and angle dependence of the emitted positrons. There are different configurations of the detectors. The simplest configuration involves two detector arrays: one forward (F) and one backward (B) referring to the initial muon spin direction (or to the muons momenta in some cases, which is opposite to the muon spin direction as

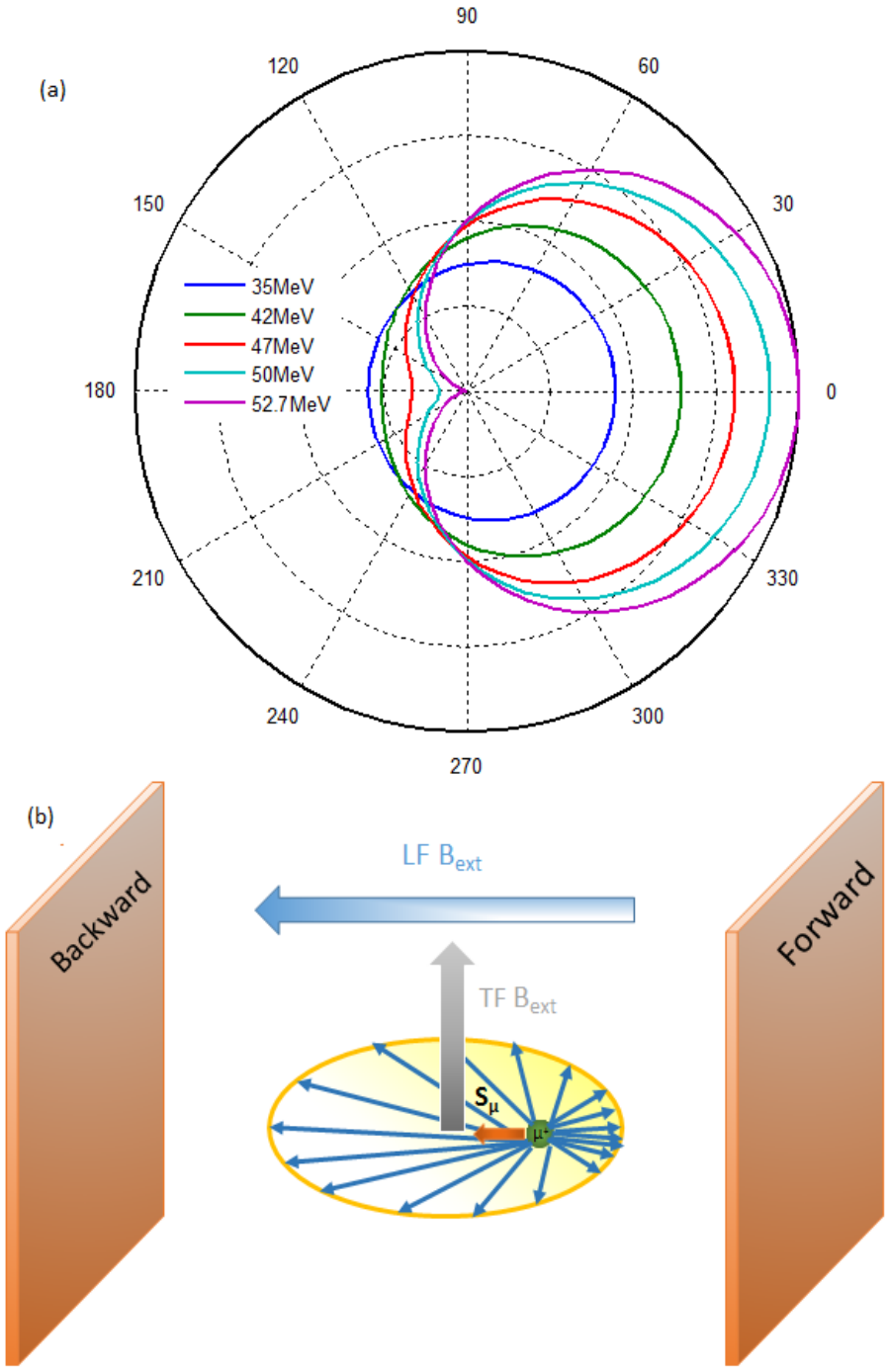

Figure 3.1: (a) Spatial emission of the positron as a function of the emitted angle with different kinetic energies. (b) Configuration of the μSR experiment. In the case of applying an external magnetic field, the transverse field (TF) is perpendicular to the muon spin and the longitudinal field (LF) is parallel to the muon spin.

discussed earlier), as shown in Fig. 3.1 (b). The number of events, N, as a function of time is measured by the detectors. The number of events at the forward (N_F) and backward (N_B) detectors are [142]:

$$N_F(t) = BG_F + N_F^0 \exp\left(-t/\tau_\mu\right)\left(1 - A_0 P(t)\right) \tag{3.8}$$

and

$$N_B(t) = BG_B + N_B^0 \exp\left(-t/\tau_\mu\right)\left(1 + A_0 P(t)\right), \tag{3.9}$$

respectively, where the BG term is the background contribution from, for example, the cosmic muons and the electronic noise of the detectors. The N^0 term is the initial number of events recorded. τ_μ is muon lifetime (2.2 μs). A_0 is the initial asymmetry of the emitted positron, which is 1/3 as discussed above. $P(t)$ is the muon polarisation function. A_0 is in practice smaller than 1/3 due to various factors, such as the limited coverage of the detectors, positrons stopping in the sample and magnetic field affecting the positron emission, etc. A typical A_0 in μSR experiments is less than 25%. The experimental quantity that is of interest is the asymmetry defined as:

$$A(t) = \frac{N_B - \alpha N_F}{N_B + \alpha N_F}, \tag{3.10}$$

where α is a constant which is determined by the inequivalence between the forward and backward detectors and the relative position of the sample. In the ideal case, forward and backward detectors have the same efficiency and are symmetric with respect to the sample. In this ideal geometry, α is simply 1. In a real experiment, α can be determined with a transverse field measurement, which will be discussed in the next section. When the background problems are removed, the measured asymmetry correlates with the muon spin polarisation $P(t)$ by:

$$A(t) = A_0 P(t). \tag{3.11}$$

Therefore, the muon polarisation can be measured, which provides information about physical and chemical properties of the sample.

There are four main muon facilities for μSR experiments in the world. Japan Proton Accelerator Research Complex (J-PARC) in Japan and ISIS in the UK, which are based on synchrotrons and are pulsed muon sources. The other two are TRIUMF in Canada and Paul Scherrer Institute (PSI) in Switzerland, which are based on cyclotrons and are quasi-continuous sources of muons. At PSI, protons accelerated in a 590 MeV ring cyclotron are guided to a pyrolytic graphite target to generate a quasi-continuous muon beam. At ISIS, protons are accelerated in an 800 MeV synchrotron at a working frequency of 100 Hz, and the produced muons appear in form of a double pulse structure with a frequency of 50 Hz.

In a continuous source, by controlling the beam slits, the overall rate of muons per second can be tuned. If the slits are too small, there will not be sufficient usable muons for the measurement. If they get too large, the possibility of double incidence, which will be vetoed, increases. As a consequence, the usable counting rate decreases. Therefore, there should be a balance between the overall rate of muons and the vetoed events resulting from double incidence. The beam slits should be properly controlled such that any further increase will reach a stage that the rate of the double incidence increase is the same as the rate of increase in muons. In practice, for the 10 μs measurement window settings, the overall rate of muons should be controlled to be about 30,000 - 35,000 muons per second. In the case of a usable counting, there is only one event being measured. The requirement of only one muon being implanted results in a low counting rate. In a typical experiment, only around 10 - 20% of the positron decays are actually detected (and not vetoed), so the actual useable rate for a standard experiment in a continuous source is about 10 - 15 million events per hour. In this case, the resolution is only limited by method of positron detection; for example, dispersion in the detector electronics or cables. Taking the GPS spectrometer in PSI as an example, which was used in this project, the time resolution is 130 ps. In addition, a continuous muon

source also has a high background. This is because that the positron detectors are on for a significant amount of time such that the possibility of charged particles hitting the detectors during the long counting time is high. Take 10 μs measuring time with a typical muon incoming rate of 30,000 per second as an example. The average time between muons is 33 μs so that the detectors should be on for 10 μs over 33 μs (30% of the time). Compared to a 50 Hz pulsed muon source, if the measurement window is 30 μs within a single pulse (0.02 s), the detectors only need to be on 0.15% (30 μs/0.02s) of the time. So a continuous source will have 200 times the background from cosmic rays than a pulsed source. In summary, the continuous muon source usually has a better time resolution but the counting rate and the background in an experiment are not ideal.

On the other hand, a pulsed muon source has a much higher counting rate as a bunch muons hit the sample within a single pulse. The overall rate of muons can reach up to 300 million muons per hour. All of the events within a pulse are counted and the counting rate of the pulsed muon source is only limited by the detector. The detector always has limitations on the speed with which it can respond. If the muon incoming rate is too high, multiple positrons may hit the detector within a short period of time that the detector cannot distinguish them and only counts once resulting in the missing of events. Thus, there is a deadtime, during which further decays are missed. This deadtime determined by the intrinsic time response of the detector restricts the counting rate of a pulsed muon source. Moreover, the detector are only activated after the incoming pulse so that the counting from other charged particles can be limited resulting in a low background signal. However, the resolution of a pulsed muon source is limited by the width of the pulse. The muon pulse width is roughly 100 ns. It is determined by the width of the proton pulse (a 70 - 80 ns inverse parabola) convoluted with the pion half life of 26 ns (exponential lifetime). The 100 ns muon pulse width limits the frequency response of a pulse muon source to be about 10 MHz or a little higher.

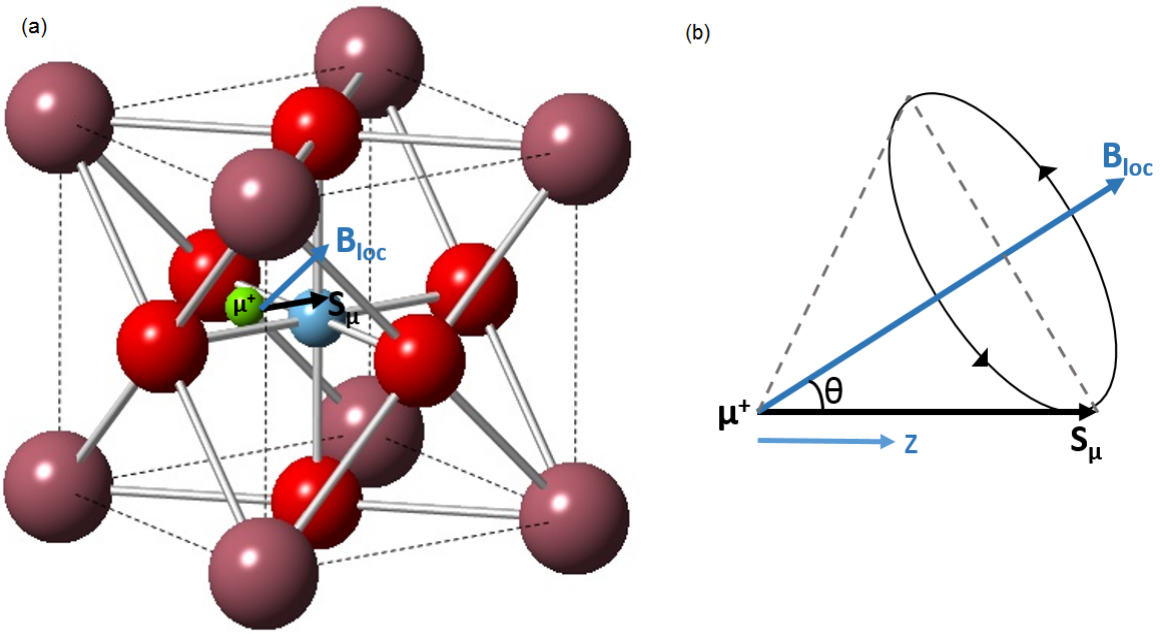

Figure 3.2: (a) The illustration shows that a muon usually sits at the interstitial position in a magnetic material. The green ball is the μ^+. (b) Muon precession around a local field.

3.1.2 Muon polarisation functions in magnetic materials

In this work, the μSR technique is only used to study the magnetism in materials. Thus, only the applications of μSR on magnetic materials will be discussed in this section. In a μSR experiment, the implanted muons will sit at an interstitial position in the sample, as shown in Fig. 3.2 (a), probably close to an anion as a muon possesses a positive charge. When a local field B_{loc} exists, the spins of these muons will experience a Larmor precession, as shown in Fig. 3.2 (b). The Larmor frequency is determined by the magnitude of the local field B_{loc}:

$$\omega = \gamma_\mu B_{loc}, \tag{3.12}$$

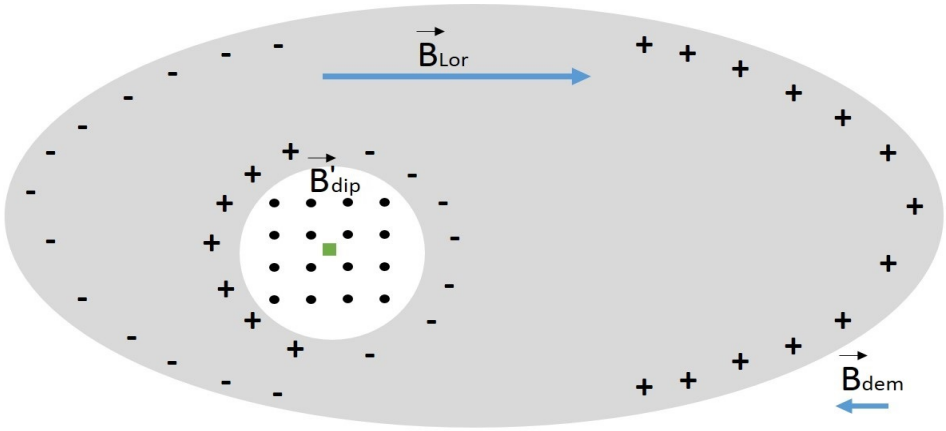

Figure 3.3: A schematic representation of the three contributions to B_{dip} in a μSR experiment: the green square is the muon site and the black dots represent magnetic moments within the Lorentz sphere (denoted by the white sphere).

where γ_μ is the gyromagnetic ratio of the muon (135.5 MHz/T, see Table 3.1). The local field B_{loc} in a magnet at a muon site consists of there contributions [143]:

$$\vec{B}_{loc} = \vec{B}_{ext} + \vec{B}_{dip} + \vec{B}_{hyp}, \tag{3.13}$$

where $\vec{B}_{ext}$ and $\vec{B}_{dip}$ are the applied magnetic field and the dipolar field in the sample, respectively. $\vec{B}_{dip}$ includes $\vec{B}'_{dip}$, which is the dipole field inside a sufficiently large Lorentz sphere centred at the muon site, the Lorentz field $\vec{B}_{Lor}$ and the demagnetisation field $\vec{B}_{dem}$ due to charges locating at the surface of the Lorentz sphere (a schematic representation of these contributions to $\vec{B}_{dip}$ is shown in Fig. 3.3). $\vec{B}_{hyp}$ is the hyperfine field for interactions between the muon and the localised magnetic moment near the muon site through the conduction electrons. In the case of insulators, where few conduction electrons exist, $\vec{B}_{hyp}$ is negligible. The measured local field is:

$$\vec{B}_{loc} = \vec{B}_{ext} + \vec{B}_{dip}. \tag{3.14}$$

Therefore, μSR can directly measure the local magnetic field in a material.

There are three experimental configurations in μSR experiments, namely zero-field (ZF) mode, transverse field (TF) mode and longitudinal field (LF) mode. In the ZF

mode, there is no applied magnetic field (or only a small applied magnetic field to compensate the Earth's field) in the measurement so that the local field measured in Eq. 3.14 is only $\vec{B}_{dip}$ in the sample. This mode is important to investigate the magnetism in a sample as the local internal magnetic field, spin dynamics and field distributions in the sample can be studied.

In the case of the TF mode, an external transverse field, B_{tran}, which is perpendicular to the initial muon spins, is applied. When the muon spin interacts with a transverse field B_{tran}, the muon spin precesses around the applied field. The muon spin precession gives rise to a cosine-like polarisation function of muons, as shown in Fig. 3.4 and 3.5. This is the ideal case for muons experiencing no interaction with the sample or when the applied transverse field is large enough that the influence from the sample is negligible. In practice, the precession frequency may be different from the applied transverse field due to 1. the internal field of the measured sample brings an extra component to the local field; 2. spin dynamics in the sample can result in a damped oscillation polarisation function. It is worth mentioning that TF measurements can also be used to estimate the α value mentioned above. With a reasonable applied transverse field, the cosine-form polarisation function should be a cosine function without any offset in the TF measurement. The polarisation function will have an offset when there is an inequivalence between the forward and backward detectors. By adjusting α, the zero-offset requirement can be achieved and the real α value can be estimated.

In the LF mode shown in Fig. 3.6 (left), B_{long} parallel to the initial muon spins is applied. This configuration is usually used to investigate spin dynamics in magnetic materials or charge carriers dynamics in polymers. In magnetic materials, the focus of this thesis, when a longitudinal field can decouple the muon spins from the internal magnetic moment, all the muon spins are aligned along the B_{long} direction. This will give rise to a straight line of the polarisation function in the static case, as shown in Fig. 3.6 (right). When a system with dynamic magnetism is investigated, even though muon spins still tend to align with B_{long}, they will experience a relaxation due to the

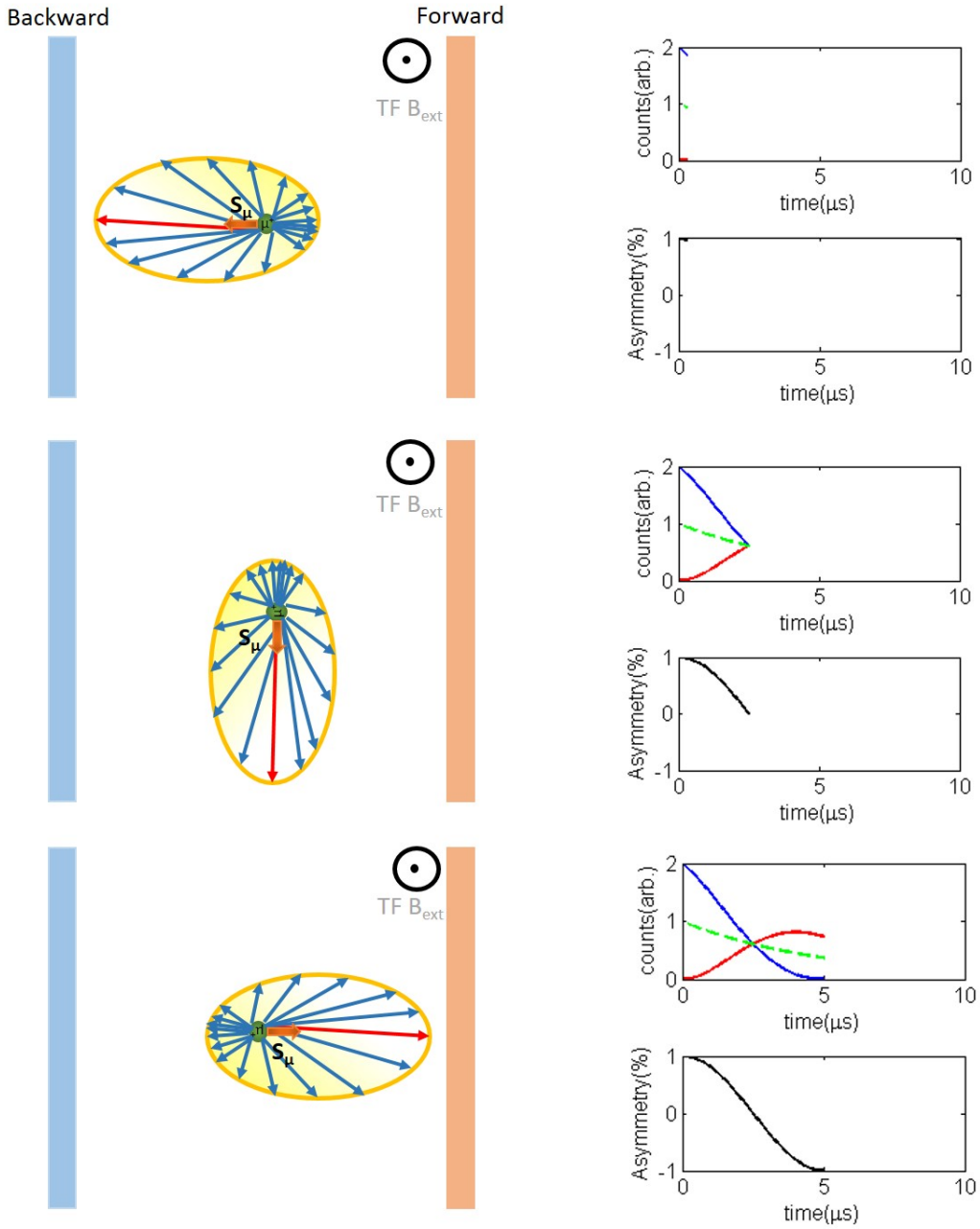

Figure 3.4: Schematic diagrams (left) showing how a muon interacts with a transverse field and measured signal (right) with blue solid curve, red solid curve and green dashed curve showing the counts from the backward detector, forward detector and their average, respectively. At $t = 0$, a muon (continuous beam) or muons (pulsed beam) are implanted into the sample sitting between the backward and forward detectors and the count is zero at $t = 0$ s. One moment later, sufficiently short that the muon spin direction is not changes by precession, relaxation or the like, the positrons corresponding to the muon spin pointing towards the backward detector are emitted. The asymmetry between the backward and forward detectors reach the maximum value in the experiment, which is defined as the initial asymmetry. At time $t = \pi/2\gamma_\mu B$, muon spins precess by $\pi/2$. The counts in the forward and backward detectors are nearly the same and $A(t)$ becomes zero. At $t = \pi/\gamma_\mu B$, muon spins precess through π resulting higher counts in the forward detector (to be continued).

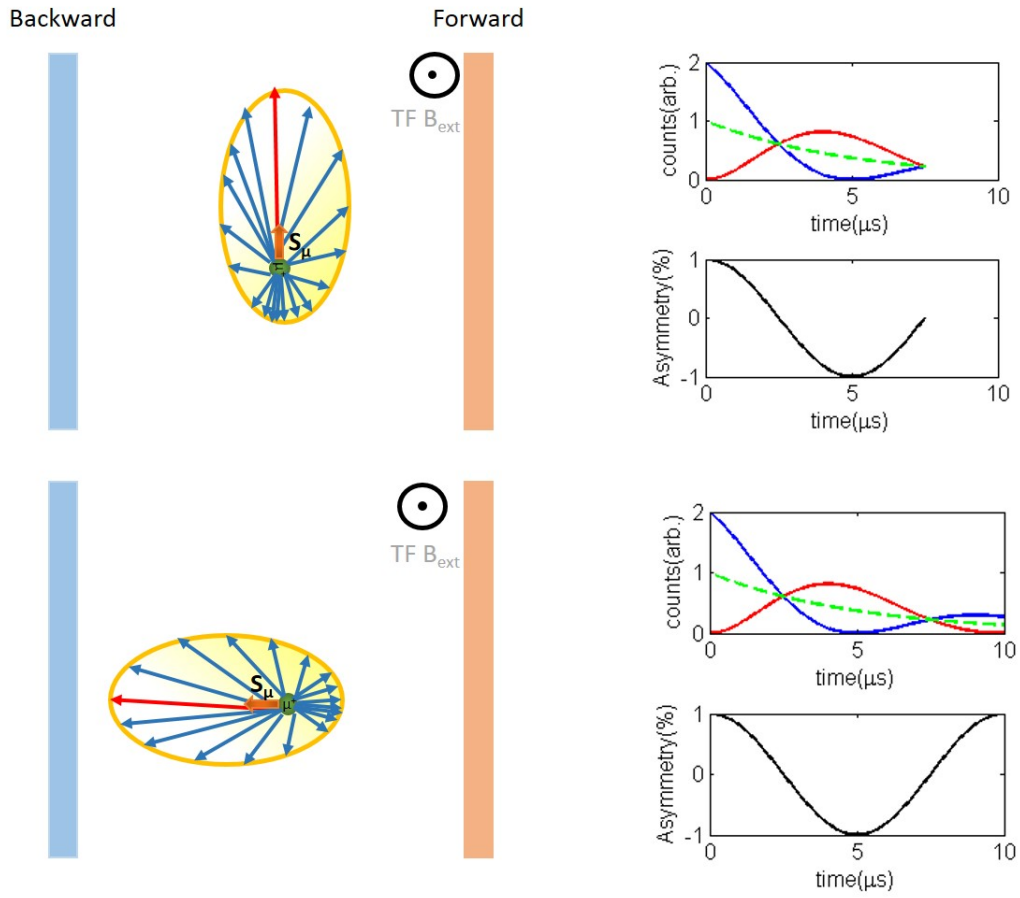

Figure 3.5: (continued) Schematic diagrams showing how a muon interacts with a transverse field and measured signal (right) with blue solid curve, red solid curve and green dashed curve showing the counts from the backward detector, forward detector and their average, respectively. At $t = 3\pi/2\gamma_\mu B$, muon spins rotate by $3\pi/2$ giving a similar reading in the detectors on both sides again. Finally, at $t = 2\pi/\gamma_\mu B$, muon spins rotate back to zero degree completing a period of spin rotation.

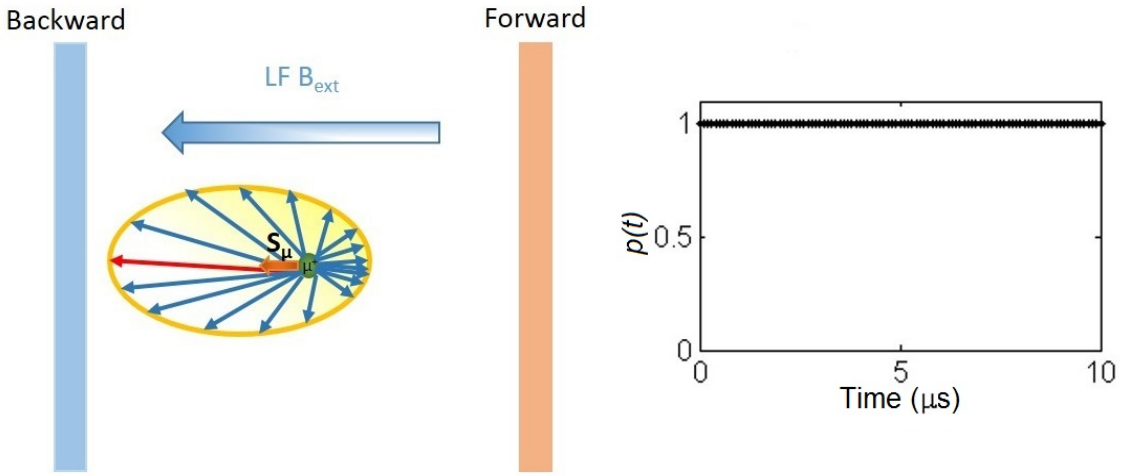

Figure 3.6: (left) A schematic diagram showing how a muon interacts with a longitudinal field B_{long}. All the muon spins are aligned in the applied field. Nearly all emitted positrons point to the backward detector. (right) The muon polarisation function is a constant with time.

dynamics including spin fluctuations and muon diffusion with the sample. This means that the muon spin relaxation can be used to investigate spin dynamics in the system.

In the long-range magnetic ordered state

As discussed above, muon spins will experience a Larmor precession in the presence of local magnetic fields. In the ordered state of a magnetic material, internal magnetic moments at the muon sites can be sensed thereby the long-range magnetic order can be studied by μSR. In a ZF measurement, two measured parameters, namely the local mean-field B_0 and its variance Δ, are essential to understand the magnetism in a sample.

When implanted into a sample, muons can sit at various positions depending on the sample. If muons sit in positions that are magnetically equivalent to each other (an example is shown in Fig. 3.7 (a)), they sense the same magnetic signal from the sample. However, if they sit in N non-equivalent magnetic sites (an example of two different muon sites ($N = 2$) is shown in Fig. 3.7 (b)), muons in the experiment will precess or relax according to N different internal fields.

Let us consider a simple case. When there is only one muon site and the internal

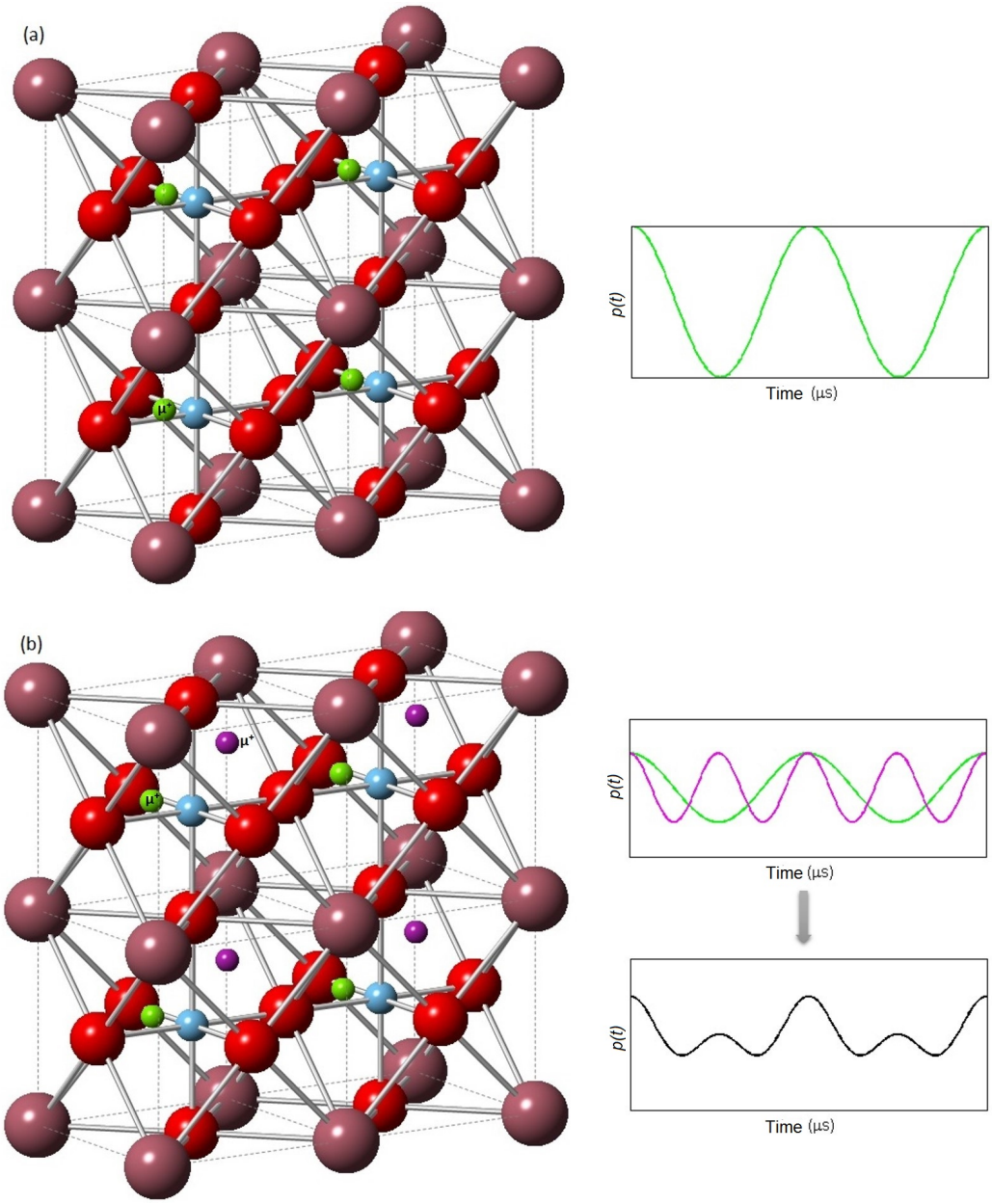

Figure 3.7: In a magnetically ordered material (taking a peroveskite crystal as an example as shown on the left), (a) one magnetically equivalent muon site, which is noted with a green ball in the crystal structure) has a single Larmor precession signal, which results in one cosine polarisation function as shown on the right. (b) N muon sites (two sites here noted with green and purple balls) can give rise to N Larmor precessions and the muon polarisation function is the combination of N cosine functions.

field has a narrow distribution, which means the sample has proper long-range magnetic order, muons will precess around the internal magnetic moment, as shown in Fig. 3.2. The polarisation function can then be expressed by [143]:

$$P_z(t) = \cos^2\theta + \sin^2\theta\cos(\gamma_\mu B_{loc} t), \tag{3.15}$$

where θ is the angle between the internal field and the spin direction of the muon ensemble. In a magnetic single crystal, θ can be any value depending on the orientation of the sample with respect to the muon spin direction. However, in a polycrystalline sample, all of the grains in the measured sample are randomly oriented. Therefore, the polarisation function assumes an average over all possible θ such that [143]:

$$P_z(t) = \frac{1}{3} + \frac{2}{3}\cos\left(\gamma_\mu B_{loc} t\right). \tag{3.16}$$

In both Eq. 3.15 and 3.16, the first term refers to muons sensing the internal field parallel to the muon spins and the second term represents muon precession around the internal field with a cosine form of the polarisation function. For a polycrystalline sample with a preferred orientation, Eq. 3.16 is no longer correct. The relative weights of oscillating and non-oscillating parts may vary.

The assumptions for Eq. 3.15 and 3.16 are: 1. there is only one single muon site in the sample; 2. the internal field distribution is narrow. In a realistic scenario, these assumptions are not always true. When there are N non-equivalent muon sites, the spins of muons sitting at different sites will precess according to the individual site's local magnetic field. Thus, the real polarisation function is a combination of Eq. 3.15 with N B_{loc} values. In the case where the internal field at the muon site is not narrow enough and has a Gaussian distribution with a field width of Δ_G, Eq. 3.15 is then

expressed as [143]:

$$P_z(t) = \cos^2\theta + \sin^2\theta \exp\left(-\frac{\gamma_\mu^2 \Delta_G^2 t^2}{2}\right) \cos\left(\gamma_\mu B_{loc} t\right). \tag{3.17}$$

Moreover, muons are very sensitive to weak dynamical environment. In a real magnetic system, magnetic dynamics are normally not negligible, especially near magnetic phase transitions. With the presence of dynamics, the field distribution at the muon site has a Lorentzian form rather than a Gaussian form as the muons relax according to (lose phase with each other) [143]:

$$P_z(t) = \cos^2\theta + \sin^2\theta \exp(-\gamma_\mu \Delta_L t) \cos(\gamma_\mu B_{loc} t). \tag{3.18}$$

In summary, the μSR technique can probe long-range magnetic order and magnetic dynamics. The oscillatory part in the polarisation function is a signature of the ordered magnetic state in materials, regardless of the nature of the ordering. As it is extremely sensitive to small spatially and temporally inhomogeneous magnetism, it is often used to study magnetic phase transitions, materials with weak magnetism and frustrated systems. It is worth mentioning that aside from the proper long-range magnetic order, μSR can detect short-range magnetic correlations, which will be discussed later, and incommensurate magnetic structures, not presented in this work.

Randomly oriented moments in the static case

If the magnetic moments in the measured material are randomly oriented, the local fields at the muon sites are usually Gaussian-distributed. When taking the field distribution into account, the polarisation function of Eq. 3.15 becomes [143]:

$$P_z(t) = \int \left(\cos^2\theta + \sin^2\theta \cos\left(\gamma_\mu B_{loc} t\right)\right) D_V\left(\vec{B}_{loc}\right) d^3\overrightarrow{B}_{loc}, \tag{3.19}$$

where $D_V\left(\vec{B}_{loc}\right) d^3\vec{B}_{loc}$ is the field distribution of the local field:

$$D_V\left(\vec{B}_{loc}\right) d^3\overrightarrow{B}_{loc} = \left(\frac{\gamma_\mu}{\sqrt{2\pi}}\right)^3 \exp\left(-\frac{\left(\gamma_\mu B_{loc}^X\right)^2}{2\Delta^2}\right) \exp\left(-\frac{\left(\gamma_\mu B_{loc}^Y\right)^2}{2\Delta^2}\right) \exp\left(-\frac{\left(\gamma_\mu B_{loc}^Z\right)^2}{2\Delta^2}\right) dB_{loc}^X dB_{loc}^Y dB_{loc}^Z. \tag{3.20}$$

Substituting Eq. 3.20 into Eq. 3.19 and averaging over the angle provides a polarisation function that can be written as [143]:

$$P_z(t) = \frac{1}{3} + \frac{2}{3}\left(1 - \gamma_\mu^2\Delta^2 t^2\right) \exp\left(-\frac{\gamma_\mu^2\Delta^2 t^2}{2}\right). \tag{3.21}$$

This is the famous Kubo-Toyabe polarisation function, where Δ represents the width of the Gaussian distribution of the internal field. This polarisation function describes the muons' behaviour in a sample with randomly oriented static magnetic moments. The spin dynamics in this case can also been taken into account by using the strong collision model. This will be later discussed in more detail in Section 3.1.3.

When a longitudinal field is applied, the Kubo-Toyabe function will take the form [142]:

$$P_z(t) = 1 - \frac{2\Delta^2}{B_{ext}^2}\left(1 - \cos\left(\gamma_\mu B_{ext} t\right) \exp\left(-\frac{\gamma_\mu^2\Delta^2 t^2}{2}\right)\right) + \frac{\gamma_\mu\Delta_4}{B_{ext}^3}\int_0^t \sin\left(\gamma_\mu B_{ext}\tau\right) \exp\left(-\frac{\gamma_\mu^2\Delta^2\tau^2}{2}\right) d\tau. \tag{3.22}$$

This function is plotted in Fig. 3.8 [142] for several B_{ext} values. It is clear that the zero-field Kubo-Toyabe function seems like a damped oscillation and recovers after a single minimum at the position $t = \sqrt{3}/\Delta$ to a plateau at a value of 1/3. The applied longitudinal field can totally decouple the muon spins from the internal field if the external field is of the same strength or stronger. With an applied LF, the 1/3 tail, as

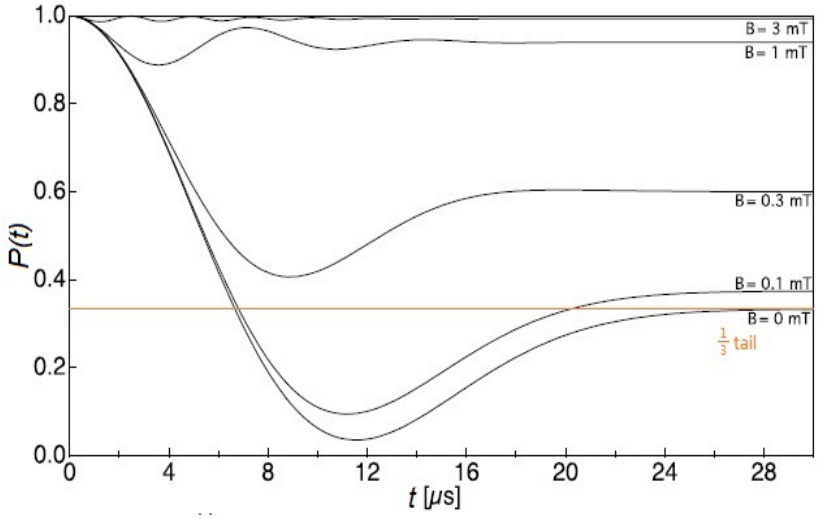

Figure 3.8: The Kubo-Toyabe function with several different external longitudinal fields with an internal field width to be $\gamma_\mu \Delta = 0.15$ MHz [142].

shown in Fig. 3.8, of the polarisation function is shifted towards higher values and the position of the minimum changes. Therefore, the LF measurement is usually conducted to check the spin dynamics as the muon spins could not been totally decoupled when LF is comparable with or larger than the internal field when dynamic processes exist. Moreover, if the field that the muons sense comes from the nuclear dipoles, the field width Δ should be temperature independent since the nuclear dipole field is not a function of temperature. This is an important clue to judge the origin of the magnetic field that the muons sense.

Short-range correlations

As discussed above, the appearance of the oscillation in the muon polarisation function is a signature of long-range magnetic order in the material. It was believed that muons cannot sense the short-range correlations, similar to many other microscopic characterisation techniques [13]. However, unlike traditional magnetisation measurements, where the entire sample is probed macroscopically, the microscopically probing muons should in principle be able to offer information about these correlations.

In 2008, Yaouanc first observed a coherent μSR precession for a magnetic material

with a correlation length of only 2.5 nm [145]. This kind of short-range correlation studied with μSR was also reported by Akiyama (2010) [146]. In 2013, Yaouanc described the influence of short-range correlations on μSR spectra in the slow dynamic limit [13]. It was shown that the ZF μSR spectra should be a Kubo-Toyabe-shaped damped oscillation when muons sense the short-range correlations in the system. Fig. 3.9 (a) shows the μSR spectra for different field asymmetry originating from the spin short-range correlations. It is clear that a shortening correlation length breaks the symmetry of the local field distribution. The minimum of the Kubo-Toyabe-like polarisation function becomes shallower and moves towards earlier times. Short-range correlations definitely have a great influence on μSR spectra. In Ref. [143], the muon polarisation function with incorporated short-range correlation is estimated to be a Gaussian-damped oscillation:

$$P(t) = \exp\left(-\gamma_\mu^2 \Delta^2 t^2/2\right) \cos\left(\gamma_\mu B_0 t\right). \tag{3.23}$$

This polarisation function is shown in Fig. 3.9 (a, inset). Comparing with the standard polarisation function shown in Fig. 3.9 (a), this damped oscillation approximation is able to describe the short-range correlation well and offers an easier way to determine the magnetic correlation length in a complex system.

After having shown that muons can sense the short-range correlations in magnetic materials, it is also possible but not straightforward to measure the correlation length with the μSR technique. The measurable parameter Δ, which is the local field width, can be translated into a function of the short-range correlation length [143]:

$$\Delta^2 = \left(\frac{\mu_0 m}{4\pi v_c}\right)^2 \sum_{i,i'} \hat{G}_{\vec{r}_i} \hat{G}_{\vec{r}'_i} \sum_{K \neq 0} C_K \left(i - i_\prime\right), \tag{3.24}$$

where m, v_c, r_i are the mass of the magnetic atom, the speed of light and the distance between the muon site and the magnetic ion, respectively. Each of the $\frac{\mu_0 m}{4\pi v_c}\hat{G}_{\vec{r}_i}$ term signifies the local field at the muon site with a tensor G consisting of dipolar and

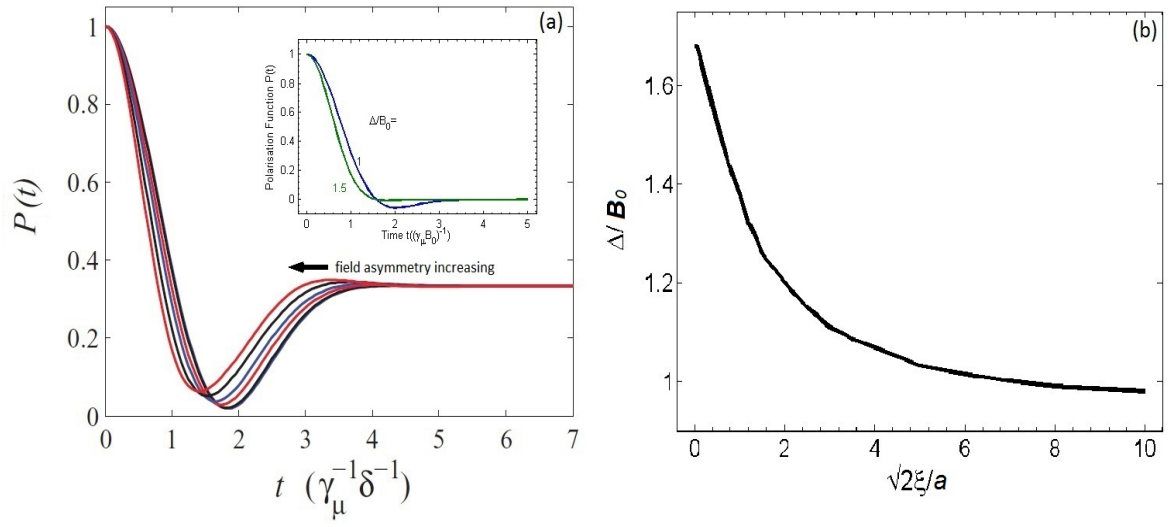

Figure 3.9: (a) Zero-field muon polarisation functions $P(t)$ as a function of an asymmetry parameter arising from the short-range spin correlations in the system. Details can be founded in Ref. [13]. The inset shows that in the presence of a short-range spin correlation, the muon spin polarisation function can be approximated by Gaussian damped oscillations. The parameter Δ/B_0 correlates with the short-range correlation length of the sample [143]. (b) Parameter Δ/B_0 as a function of the correlation length in a simple case where the muons sit on the octahedral site of a face-centred-cubic lattice (lattice parameter is a) with ferromagnetic order [143].

hyperfine field contributions depending on the crystal structure and where muon sites are. $C_K(i-i')$ is the correlation function of the short-range correlations. Eq. 3.24 shows that the short-range correlations can be measured qualitatively by the field distributions that the muons sense.

In principle, if the crystal structure and the muon sites are known, the G tensor in Eq. 3.24 and then the correlation function can be calculated from μSR measurements. However, the expression of the G tensor would be very difficult to determine in some real cases due to the complexity of the muon sites. In the most simple case, where muons sit on the octahedral site of a face-centred-cubic lattice with ferromagnetic order, the G tensor was calculated [143]. If we assume that the correlation function has an exponential form $\sum_{K\neq 0} C_K(i-i') = \exp(-r/\xi)$, the magnetic correlation length ξ can be calculated from the internal field distribution. Fig 3.9 (b) shows the ratio of the internal field width and the mean field (Δ/B_0) as a function of the spin correlation

length. A longer correlation length results in a smaller Δ/B_0 ratio which means that a larger local field B_0 or a sharper field distribution is present in the sample. For example, in the case of long-range magnetic order where the local field has a finite value (should be larger than the short-range correlation) and the field distribution is quite sharp, the Δ/B_0 ratio would be small and approach zero and the correlation length is infinite. Therefore, Δ/B_0 is a measure of the magnetic correlation length in μSR measurements.

3.1.3 Probing spin fluctuations in magnets

The μSR technique is a powerful tool to investigate dynamics in magnetic systems, including muon diffusions and spin fluctuations. As muon diffusion is not relevant to this thesis, this section will focus on how the μSR technique accesses information about spin fluctuations in magnetic materials.

As discussed before, the muon spin polarisation exhibits a form of relaxation, if dynamic processes are present. Both spin fluctuations and muon hopping lead to relaxations of the implanted muon spins. This is because the local field probed by the muons varies with time as a result of spin dynamics. To be more precise, all muon spins precess at a different frequency resulting in a complete loss of the coherent spin phase as time elapses. The relaxation has an exponential form when the spin fluctuation rate is high, but it evolves into a Gaussian-like function when the spin dynamics slow down. In this thesis, critical fluctuations in magnetic materials and spin flipping in single molecule magnets will be discussed. When studying spin dynamics in a magnetically ordered state, the spin fluctuations usually cause a relaxation of the oscillation signal: the polarisation function turns in to a relaxed oscillation. For the paramagnetic system, spin dynamics translate into different muon relaxation functions depending on the spin fluctuation rate.

If spin dynamics are present in the paramagnetic state, the Kubo-Toyabe function is no longer suitable to describe the muon spin relaxation. To understand the effect of spin fluctuations, strong collision approximation (SCA) is used. In this approximation,

the strong collision between the muon spins and the spins of the sample is assumed to happen at time t, when the direction of the local field changes after the occurrence of a strong collision. The probability of this collision is related to the spin fluctuation rate ν of the system by $\rho(\mathrm{t}) \propto \exp(-\nu t)$. After the collision, it is also assumed that the change of the field direction is totally random. If the static polarisation function is $p(t)$, after the collision at time t', the muon polarisation function still has the same shape as $p(t)$ but with a different starting polarisation of $p(t')$. Therefore, considering n collisions in total, the total polarisation function at time t will be the sum of the polarisation of all the muons:

$$P(t) = \sum_{n=0}^{\infty} p^{(n)}(t), \tag{3.25}$$

where $p^{(n)}(t)$ is the polarisation function after the nth collision. This polarisation function will still follow the manner of $p(t)$ but has a starting polarisation of $p^{(n-1)}(t_n)$. It is straightforward to obtain the polarisation function of muons that experience no collision:

$$p^{(0)}(t) = \exp(-\nu t)p(t). \tag{3.26}$$

For muons that only experience one collision at time t_1 and remain unchanged until time t, the polarisation function is:

$$p^{(1)}(t) = \nu \int_0^{\infty} p(t_1)\exp(-\nu t_1)p(t-t_1)\exp(-\nu(t-t_1))dt_1, \tag{3.27}$$

where $p(t_1)$ is the starting polarisation of the muons which only collide once. $p(t-t_1)$ is the polarisation function of the muons after the collision starting at time t_1. The probability of the muons that only experience one collision between t_1 and t can be expressed as $\nu\exp(t_1)\exp(t-t_1)dt_1$. Then, the higher terms can be successively written as:

$$p^{(n)}(t) = \nu \int_0^{\infty} p^{(0)}(t_n)p^{(n-1)}(t-t_n)dt_n. \tag{3.28}$$

Therefore, the total polarisation function of all the muons can be derived by summing

over all $p^{(n)}$ according to Eq. 3.26:

$$\begin{aligned} P(t) &= \sum_{n=0}^{\infty} p^{(n)}(t) = p^{(0)}(t) + \sum_{n=1}^{\infty} \nu \int_0^t p^{(0)}(t_n) p^{(n-1)}(t - t_n) dt_n \\ &= \exp(-\nu t)[p(t) + \nu \int_0^t p(t_1) p(t - t_1) dt_1] \\ &+ \nu^2 \int_0^t \int_0^{t_1} p(t_2) p(-t_1 - t_2) p(t - t_1 - t_2) dt_1 dt_2 + ... \end{aligned} \tag{3.29}$$

Executing the Laplace transformation on both sides of the above equation provides:

$$F(s) = \sum_{n=0}^{\infty} \nu^n f^{n+1}(s + \nu), \tag{3.30}$$

where $F(s)$ and $f(s)$ are the Laplace transformations of $P(t)$ and $p(t)$, respectively. If the expression of the static muon polarisation function $p(t)$ is known, it is possible to calculate the dynamic polarisation function using the SCA described above. For detailed discussion on SCA model in μSR, please consult Ref. [143].

In the paramagnetic state, muons sense randomly oriented nuclear moments. Thus, the static polarisation function $p(t)$ can be described by the static Kubo-Toyabe function (Eq. 3.21). Therefore, the expression of $P(t)$ can be evaluated by the numerical integral for any internal field distribution, including Gaussian or Lorentzian distributions. This has been reported in Ref. [147] and the result is called the dynamic Kubo-Toyabe function. The evolution of the dynamic Kubo-Toyabe function as a function of the spin fluctuation time in a zero applied field is shown in Fig. 3.10 (a).

However, the data analysis using the dynamic Kubo-Toyabe function is difficult. The data fitting usually takes a few minutes per solution on a modern computer. Fit algorithms employing multiple solutions per iteration can even take. Approximations were made depending on the spin fluctuation rate in the system in order to obtain easier polarisation functions for the data analysis.

- In the quasi-static limit: by studying the Laplace transformation in Eq. 3.30 in the limit of $(s + \nu)/(\gamma_\mu \Delta) \ll 1$, where the system's spin fluctuation rate ν is very

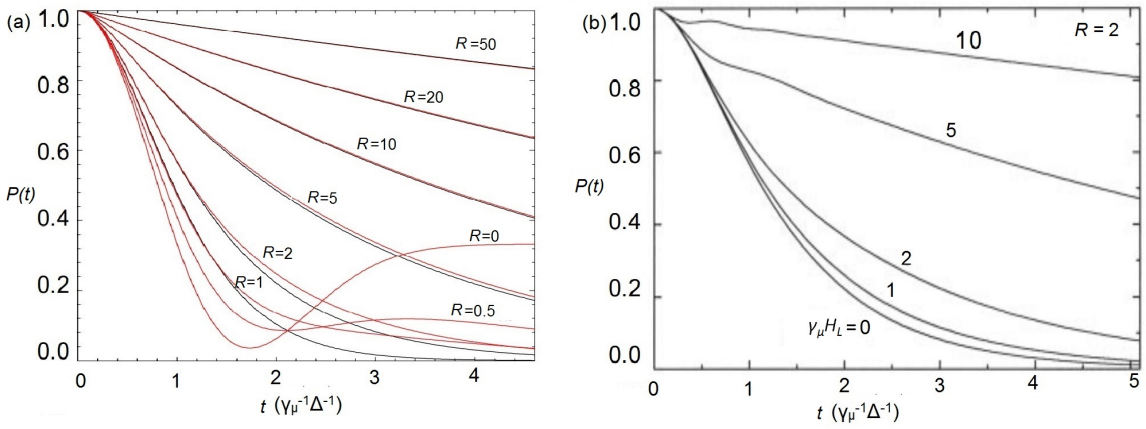

Figure 3.10: (a) Red curves are spectra of dynamic Kubo-Toyabe polarisation functions with different $R = \nu/\Delta$ ratio. Black curves are exponential relaxation functions, which can be used to describe dynamic Kubo-Toyabe function when $R \geq 5$. (b) The dynamic Kubo-Toyabe polarisation function with different applied longitudinal fields when $R = 2$ [147].

small, the polarisation function $P(t)$ simplifies according to D. de Reotier and A. Yaouanc [143]:

$$P(t) = \frac{1}{3}\exp\left(-\frac{2}{3}\nu t\right) + \frac{2}{3}\left(1-\gamma_\mu^2\Delta^2 t^2\right)\exp\left(-\frac{\gamma_\mu^2\Delta^2 t^2}{2}\right). \tag{3.31}$$

By comparing this function with the static Kubo-Toyabe function in Eq. 3.21, it is obvious that only the 1/3 tail of the static Kubo-Toyabe function relaxes. This relaxing tail can also be seen in Fig. 3.10 (a). The relaxation of the 1/3 tail has an exponential form with a characteristic relaxation rate λ_μ. This relaxation rate is related to the spin fluctuation rate ν in the system by:

$$\lambda_\mu = \frac{2}{3}\nu. \tag{3.32}$$

- In the intermediate limit: when spin dynamics is faster and we can write $(s + \nu)/(\gamma_\mu\Delta)>1$, the Abragam formula from a NMR theory was found to be a good approximation for the enveloping function of the dynamic Kubo-Toyabe function. The field distribution term Δ^2 in the Abragam formula has to be substituted by

$2\Delta^2$ as there are two components of $\vec{B}_{loc}$ perpendicular to the muon spin. The polarisation function that describes the spin fluctuation in the intermediate limit is [143, 148]:

$$P(t) = \exp\left(-\frac{2\Delta^2 t}{\nu^2}\left(\exp\left(-\nu t\right) - 1 + \nu t\right)\right). \tag{3.33}$$

- In the fast limit: when spin dynamics in the system are fast, it is reasonable to assume that $\nu/(\gamma_\mu \Delta) \gg 1$ and Eq. 3.33 becomes:

$$P(t) = \exp\left(-\frac{2\gamma_\mu^2 \Delta^2}{\nu} t\right). \tag{3.34}$$

This muon relaxation function has an exponential form with a muon relaxation rate $\lambda_\mu = \frac{2\Delta^2}{\nu}$. It can be seen from Fig. 3.10 (a) that when the spin fluctuation is fast (roughly $\nu > 5\Delta$), an exponential relaxation is a good approximation of the dynamic Kubo-Toyabe function. When a longitudinal field is applied, the muon relaxation rate λ_μ is modified to [143]:

$$\lambda_\mu = \frac{2\Delta^2 \tau}{1 + \gamma_\mu^2 H_L^2 \tau^2}, \tag{3.35}$$

where $\tau = 1/\nu$ is the fluctuation time of the system and H_L is the external applied longitudinal field. The field dependence of the dynamic Kubo-Toyabe in this fast limit is shown in Fig. 3.10 (b). The applied longitudinal field can push the polarisation function towards higher values but the spin fluctuations cannot be completely quenched by a large longitudinal field.

In summary, spin fluctuations in a system can be sensed by muons and the method to describe the spin fluctuations is shown above. In the case of single molecule magnets, muons will relax according to the relaxation functions depending on different spin fluctuation limits. When considering the critical fluctuations in the magnetically ordered states, the dynamic processes will give rise to a dephasing of the Larmor precession around the internal fields.

Table 3.2: Definition of critical exponents. T_c is the critical temperature (could be the Néel temperature for antiferromagnets or the Curie temperature for ferromagnets). C is the heat capacity. ξ is the correlation length. χ is the susceptibility of the order parameter. Ψ is the order parameter and the function $\langle\psi(0)\phi(\mathrm{r})\rangle$ is the correlation function.

Temperature	Exponents	Definitions	Quantities described
$T<T_c$	α'	$C \sim (1\text{-}\frac{T}{T_c})^{-\alpha'}$	Heat capacity
	β	$\Psi \sim (1\text{-}\frac{T}{T_c})^{\beta}$	Order Parameter
	ν'	$\xi \sim (1\text{-}\frac{T}{T_c})^{-\nu'}$	Correlation length
	γ'	$\chi \sim (\frac{T}{T_c}\text{-}1)^{-\gamma'}$	Susceptibility
$T>T_c$	α	$C \sim (\frac{T}{T_c}\text{-}1)^{-\alpha}$	Heat capacity
	ν	$\xi \sim (\frac{T}{T_c}\text{-}1)^{-\nu}$	Correlation length
	γ	$\chi \sim (\frac{T}{T_c}\text{-}1)^{-\gamma}$	Susceptibility
$T = T_c$	δ	$H \sim \Psi^{\delta}$	Field evolution of the order parameter
	η	$\langle\psi(0)\phi(\mathrm{r})\rangle \sim r^{-d+2-\eta}$	Correlation function

3.1.4 Critical phenomenon studied by μSR

It is established that the critical temperature, where a phase transition occurs, is associated with scale invariant rules. That means the physical parameters, i.e. order parameter and the correlation length, have a certain configuration near the critical temperature. They follow a power law, which is a typical scale-invariant mathematical function [149]. In theory, the critical exponents are calculated from the specific free energy in the system.

Critical exponents describing the behaviour of different physical parameters during the phase transition, are defined both below and above the critical temperature. The definition of exponents in the ordered phase, disordered phase and at the critical point is listed in Table 3.2. These critical exponents are universal and only depend on the dimension, spin dimension and the range of interaction in the system. They do not depend on the detail of the individual system [149]. For example, critical exponents for a 3D Heisenberg antiferromagnet and a 3D Heisenberg ferromagnet are identical.

In general, the prime exponents have the same values as those above the critical temperature, mathematically $\alpha = \alpha'$, $\nu = \nu'$ and $\gamma = \gamma'$. However, there are some anisotropic systems, such as low-dimensional magnetic systems, which may have different critical exponents below and above the critical temperature. Otherwise, there are other scaling laws between these critical exponents listed in Eq. 3.36 to 3.39.

$$\alpha + 2\beta + \gamma = 2, \tag{3.36}$$

$$\beta(\delta - 1) = \gamma, \tag{3.37}$$

$$\nu(2 - \eta) = \gamma, \tag{3.38}$$

$$2 - \alpha = \nu d, \tag{3.39}$$

where d is the dimension of the system.

Among all these critical exponents, the ones related to the order parameter, susceptibility and magnetic correlation length, namely β, γ (γ') and ν (ν'), can be measured with the μSR technique. Mouns, working as a local probe, can measure the order parameter as well as the dynamics in a magnetic material. They measure a sum of dipolar fields from all of the spins in the system at a specific site. In a ferromagnet, the sum of the measured local field corresponds to the magnetisation in the material, which is the order parameter of a ferromagnet. However, in an antiferromagnet, the net magnetisation is no longer the order parameter as it is not macroscopic. The magnetic susceptibility is not the order parameter susceptibility, either. There is no field that can be in one direction for one spin and in the opposite direction for its neighbours. Thus, the exponents β and γ in an antiferromagnet cannot be obtained by simply measuring net magnetisation or magnetic susceptibility of the system. The order parameter for an antiferromagnet is the staggered magnetisation [150], which is defined as:

$$\vec{M}_{staggered} = \sum_i (-1)^i \vec{s}_i, \tag{3.40}$$

where $\vec{s}_i$ is the spin at site i. Muons, being a local probe, are sensitive to the staggered magnetisation in an antiferromanget. The internal field measured by muons grows as it is cooled, as a result of the order parameter, just like the internal field of a ferromagnet grows as it cools (resulting in a net magnetisation). Therefore, the order parameter and its susceptibility can be measured by the μSR technique.

The exponent β, which is determined from the temperature evolution of the order parameter can be determined with the muon oscillation frequency as a function of temperature. The local magnetic field B_{local} correlates with the order parameter Φ (net magnetisation for a ferromagnet and staggered magnetisation for an antiferromagnet) by $B_{local} \sim \Phi$. Then the local field $B_{local} = \gamma_\mu f_{osc} \sim (1\text{-}\frac{T}{T_c})^\beta$ [151]. The critical exponent γ, which corresponds to the critical behaviour of the susceptibility, can also be studied with the muon spin rotation technique. In a magnetic material, the local susceptibility, which can be measured with the TF μSR technique, shows the behaviour of the order parameter susceptibility (staggered susceptibility). Therefore, γ can be determined by evaluating the field shift: $\chi \sim \frac{B}{H}\text{-}1 \sim \frac{f(T)}{f(0)}\text{-}1 \sim (\frac{T}{T_N}\text{-}1)^{-\gamma}$ [151]. A dynamic critical phenomenon can also be investigated by μSR. The longitudinal muon spin relaxation is sensitive to spin dynamics as discussed in the previous section. The spin fluctuation rate λ is a measure of the spin correlation time τ, which diverges according to the following proportionality: $\lambda \sim \tau \sim (\frac{T-T_N}{T})^{-\nu}$ [151].

Since the μSR technique is very sensitive to local magnetic properties, the critical exponents determined with μSR may give extra information about the magnetic system. Investigations on the critical exponents of many different magnetic system using the μSR technique have been reported. For further details, please consult Ref. [151, 152].

3.2 Complementary Techniques

In this thesis, the magnetism in multiferromagnetic and low-dimensional magnetic materials are mainly investigated by the μSR technique. In addition to μSR, various of

other complementary characterisation techniques, such as XRD, AFM, magnetometry and neutron scattering were used. In this section, the magnetometer and grazing-incident small angle neutron scattering (GISANS) are discussed in detail.

3.2.1 Magnetic susceptibility measurements

Magnetometry is a very common technique to characterise the magnetic properties of a magnetic material. In a measurement, the magnetisation, DC susceptibility and AC susceptibility can be measured. Considering that the principle and experimental setup of this measurement are well known, only general basics of this technique and the particular method to measure magnetisation relaxations in single molecule magnets will be addressed in this section.

Introduction to DC and AC susceptibility measurements

In this work, DC and AC susceptibility measurements are used to characterise the magnetism and magnetisation dynamics of the investigated materials. In a DC susceptibility measurement, the equilibrium value of the volume magnetic susceptibility is measured. The sample is magnetised by a constant applied magnetic field and its magnetic moment is measured by force (Faraday's scale), torque (Guoy's scale) or induction (induction method or the Superconducting Quantum Interference Device (SQUID)) techniques. In this work, the DC susceptibility measurements were performed with the Vibrating Sample Magnetometer (VSM) of a Physical Properties Measurement System (PPMS) or with a SQUID. The AC susceptibility was measured with an AC Measurement System (ACMS) of a PPMS.

In an inductive measurement, the sample should be kept moving relative to the pickup coils. The SQUID consists of two Josephson junctions and the change of the magnetic field due to the moment of the sample will generate an induced current in the SQUID. During the measurement, the sample is transported across a superconducting pick-up loop and the output voltage is recorded as a function of the sample position.

Whereas, in the VSM, the sample is moved continuously in an oscillating linear motion up and down through a coil at a certain frequency. With a lock-in amplifier the desired signal is filtered and amplified.

In contrast to DC susceptibility measurements, AC susceptibility measurements provide information about magnetisation dynamics in a material as the induced magnetic moment is time dependent. In the ACMS, there is an AC coil set that provides an alternating field and a detection coil set that generates the signal from the induction from the sample. These coil sets are concentric within the superconducting DC magnet of the PPMS. During an AC measurement, a small AC magnetic field with a certain frequency plus a static DC field is applied to the sample. The field of the time-dependent magnetic moment due to the AC field will induce an AC current in the pickup coil. There is no need for a continuously moving of the sample. The detection component of the AC magnetometer is configured to detect a frequency band, usually 10 Hz to 10 kHz (frequency response for the majority of the commercial available measurement systems), which sometimes is a limitation for the measurements of magnetisation dynamics.

The measured AC susceptibility, unlike DC susceptibility, has a complex value that consists of an in-phase or real part and an out-of-phase or imaginary part. The magnetic field that is applied in the AC susceptibility measurement can be expressed as:

$$\vec{H}_{AC}(t) = \vec{H}_0 + \vec{h}\cos(\omega t) + i\vec{h}\sin(\omega t), \tag{3.41}$$

where $\vec{H}_0$ is the applied DC field, $\vec{h}$ is the AC field and $\omega = 2\pi f$, where f is the frequency of the applied AC field. The measured magnetisation is time dependent and may have a different phase with the applied AC field. Therefore, the measured AC magnetisation can be described as:

$$\vec{M}_{AC}(t) = \vec{M}_0 + \vec{m}\cos(\omega t - \theta) + i\vec{m}\sin(\omega t - \theta), \tag{3.42}$$

where $\vec{M}_0$ is the magnetisation related to the DC field and θ is the phase difference

between the measured signal and the AC field. Then the AC susceptibility can easily be derived by Eq. 3.41 and Eq. 3.42:

$$\chi_{AC} = \frac{d\overrightarrow{M}}{d\overrightarrow{H}} = \frac{me^{i(\omega t-\theta)}}{he^{i\omega t}} = \frac{m}{h}e^{-i\theta} = \frac{m}{h}\cos\theta - i\frac{m}{h}\sin\theta. \tag{3.43}$$

Here the real (χ') and imaginary (χ'') parts of χ_{AC} are:

$$\begin{aligned} \chi' &= \frac{\vec{m}}{\vec{h}}\cos\theta = \chi\cos\theta, \\ \chi'' &= \frac{\vec{m}}{\vec{h}}\sin\theta = \chi\sin\theta. \end{aligned} \tag{3.44}$$

Here χ' indicates the magnetic dispersion and χ'' represents the magnetic absorption in a material. An absorption coefficient θ is defined as:

$$\theta = \arctan\left(\frac{\chi'}{\chi''}\right). \tag{3.45}$$

This coefficient describes the phase difference of the induced magnetic moment lags behind the applied AC field. As χ' and χ'' describe the magnetic dispersion and energy absorption in the sample, changes of χ' and a non-zero value of χ'' indicate dynamic magnetism. Thus, AC susceptibility measurements are often used to study the magnetic dynamics. Typical examples include the irreversibility in spin-glasses or domain wall movements in magnets and magnetic phase transitions since the AC susceptibility signal is very sensitive to thermal dynamic phase changes.

AC susceptibility measurements accessing magnetic relaxations in SMMs

As discussed, if there are magnetic dynamics in a system, the imaginary component of the AC susceptibility χ'' will be non-zero. If there is no slow magnetisation relaxation behaviour in a single molecule magnet, which is an important case in this thesis, it will behave like a paramagnetic material and no phase shift between the induced magnetic moment and the applied AC field is observed. Therefore, θ is zero and $\chi' = m/h$ is the

same as the DC susceptibility value, while $\chi'' = 0$. If slow magnetisation is present below the blocking temperature T_B, θ will be non-zero as the induced AC moment lags behind the applied AC field due to the relative long magnetic relaxation time. Therefore, a peak in χ'' will appear, which is the signature of slow magnetisation relaxation in single molecule magnets.

According to Debye relaxation model, the dynamic susceptibility can be expressed as:

$$\chi(\omega) = \chi_S + \frac{\chi_T - \chi_S}{1 + i\omega\tau}, \tag{3.46}$$

where χ_T and χ_S are the isothermal and adiabatic susceptibility. In this equation, the isothermal susceptibility χ_S is the susceptibility measured at a fixed temperature and is usually a static susceptibility. The adiabatic susceptibility is the dynamic susceptibility for an isolated system in the limit of an infinitely slowly increasing field. According to this equation, the real and imaginary parts of AC susceptibility are:

$$\begin{aligned} \chi' &= \Re[\chi(\omega)] = \chi_S + \frac{\chi_T - \chi_S}{1 - \omega^2\tau^2}, \\ \chi'' &= \Im[\chi(\omega)] = (\chi_T - \chi_S)\frac{\omega\tau}{1 - \omega^2\tau^2}. \end{aligned} \tag{3.47}$$

Fig. 3.11 shows the AC susceptibility as a function of $\omega\tau$ according to the Debye relaxation model. It is clear that, if magnetic fluctuations exist, χ' exhibits a decline while χ'' peaks at $\omega\tau$. Thus, at a certain frequency, χ'' will reach a maximum value at a certain temperature T, which means that the vibration of the AC field and the spin fluctuation in the sample achieve a "resonance". Thus, the magnetisation relaxation time $\tau_R = 1/2\pi f$, where f is the frequency of the AC field. Therefore, in a real experiment, the AC susceptibility of a single molecule magnet can be measured as a function of temperature and frequency. Then, the temperature dependence of the magnetisation relaxation time of a single molecule magnet can be determined as described above.

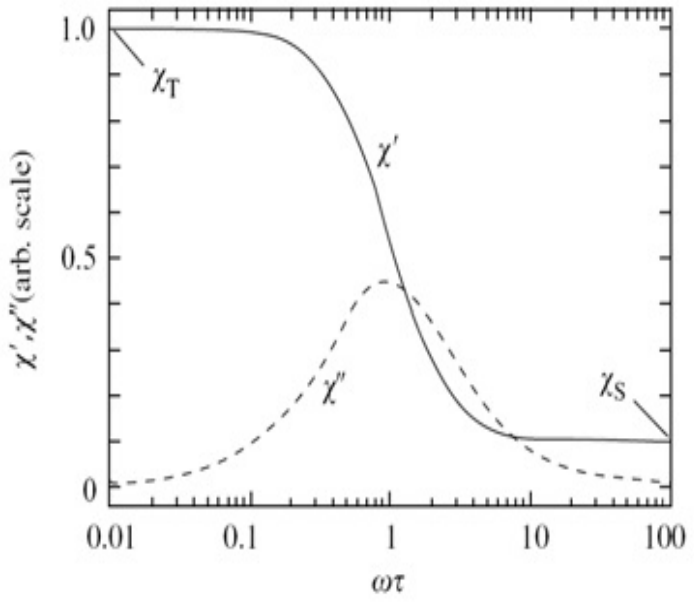

Figure 3.11: The Debye relaxation model shows the evolution of AC susceptibility as a function of the AC field frequency. The dynamics in the sample results in the decline of χ' and a peak in χ'' at $\omega\tau = 1$.

3.2.2 Magnetic neutron scattering

Neutron scattering is a very powerful and widely used tool to study the structures and properties of both inorganic and organic materials. Neutrons are subatomic particles with a mass of $m_n = 939$ MeV/c^2. A neutron has no electric charge but has spin 1/2. The neutrons used for scattering experiments are normally treated as waves with a wavelength of $\lambda = 2\pi/k_n$ (the de Broglie's relation), where k_n is the wave vector. Neutrons interact with atomic nuclei via the strong nuclear force as well as with magnetic moments via electromagnetic interactions as they carry spins. Hence, neutron scattering technique is often used to investigate the magnetic structures and electron spin fluctuations in materials. In this project, the magnetic neutron scattering technique was utilised to study the magnetic ordering in $BiFeO_3$.

In a neutron scattering experiment, the sample is placed in the neutron beam with a incident flux of $\Phi(k)$. Fig. 3.12 (a) shows the geometry of a neutron scattering experiment. The neutron's energy and momentum change after interaction with the

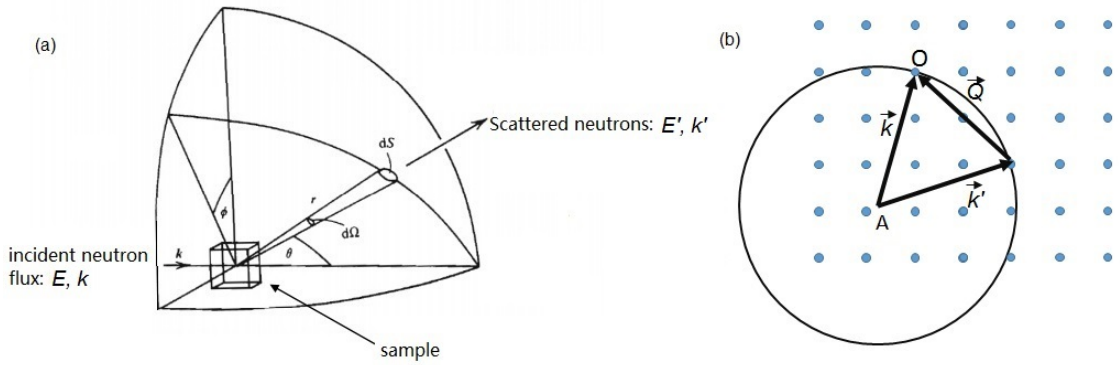

Figure 3.12: (a) The geometry of neutron scattering experiments [153]. (b) The condition for Bragg scattering based on the scattering vector ($\vec{Q} = \vec{k}$-$\vec{k'}$) and the fulfilled condition $\left|\vec{Q}\right| = 2\left|\vec{k}\right|\sin(\frac{1}{2}\theta)$.

sample:

$$\begin{aligned} \Delta\vec{P} &= \hbar\vec{Q} = \hbar(\vec{k} - \vec{k'}), \\ \Delta E &= \frac{\hbar^2}{2m_n}(k^2 - k'^2), \end{aligned} \tag{3.48}$$

where $\Delta\vec{P}$ and ΔE are the momentum and energy change of the neutron, respectively. $\hbar$ is the Planck constant. k and k' are incident and scattered wave vectors. Q is the scattering vector $\vec{Q} = \vec{k}$ - $\vec{k'}$. In elastic neutron scattering, there is no energy transfer thereby $\Delta E = 0$. The momentum transfer is described by the scattering vector, $\vec{Q}$ = k - k'. The obtained scattering function $\mathrm{S}(\vec{Q}, \omega)$ contains the desired structural information. In inelastic neutron scattering experiment, both energy and Q vector of the scattered neutron change, which gives information about dynamics in the system.

The interaction between neutrons and matter can be described by the neutron cross-section σ, which represents the effective area scattering potential for a passing neutron. If neutrons traverse this area, they experience the potential and are scattered isotropically. In the case of a single nucleus, the cross-section is:

$$\sigma = 4\pi b^2, \tag{3.49}$$

where b is the nuclear scattering length that is the effective range of the nuclear po-

tential. Considering a crystal, which is a periodically repeating array of atoms, the differential cross-section $\frac{d\sigma}{d\Omega}$ is [153]:

$$\frac{d\sigma}{d\Omega} = \left| \sum_{l} \exp\{i\vec{Q} \cdot \vec{l}\} \sum_{d} b_d \exp\{i\vec{Q} \cdot \vec{d}\} \right|^2 , \tag{3.50}$$

where the first term shows the periodicity of the crystal ($\vec{l} = n_1\vec{a} + n_2\vec{b} + n_3\vec{c}$, n_1, n_2, n_3 are coefficients and $\vec{a}$, $\vec{b}$, $\vec{c}$ are the unit vectors in the directions of the a, b, c axis of the crystal) and the second term is the sum of all atoms in a single unit cell. This cross-section can also be described by the Fourier transform of the potential function $\hat{V}(\vec{r})$ of the measured sample [153]:

$$\frac{d\sigma}{d\Omega} = (\frac{m_n}{2\pi\hbar^2})^2 \left| \langle \vec{k'} \left| \hat{V}(\vec{r}) \right| \vec{k} \rangle \right|^2 , \tag{3.51}$$

where m_n is the mass of a neutron. The potential energy $\hat{V}(\vec{r})$ here describes all the physics involved in the scattering process.

Coherent scattering will only occur if Bragg's law is satisfied, as shown in Fig. 3.12 (b):

$$\exp(i\vec{Q} \cdot \vec{l}) = 1 \tag{3.52}$$

for all the l. Now $\vec{Q} = \vec{\tau} = h\vec{a^*} + k\vec{b^*} + l\vec{c^*}$, where the $\vec{\tau} = h\vec{a^*} + k\vec{b^*} + l\vec{c^*}$ term describes the reciprocal lattice vector of the crystal. If we define d to be the distance between atoms in the real space, we can use the following equations: $\tau = \frac{2\pi}{d}n$ and k = $\frac{2\pi}{\lambda}$, so that $|\vec{\tau}| = \frac{2\pi}{d}n = \left|\vec{Q}\right| = 2\left|\vec{k}\right|\sin(\frac{1}{2}\theta)$. Finally, a simple equation $2d\sin(\frac{1}{2}\theta) = n\lambda$ can be obtained. This is the more familiar expression of Bragg's law.

The magnetic moment of the neutron interacts with the magnetic moments in the sample. The magnetic moment of a neutron can be expressed in terms of the Pauli matrix $\hat{\vec{\sigma}}$:

$$\hat{\vec{\mu}} = \mu_N \hat{\vec{\sigma}}, \tag{3.53}$$

where μ_N is the nuclear magneton. Therefore, neutrons interact with the magnetic induction $B(r)$ from the sample via $-\hat{\vec{\mu}} \cdot \vec{B}$ and the potential $\hat{V}(\vec{r})$ in Eq. 3.51 is modified to include a magnetic term $\hat{V_m}(\vec{r})$ [153]:

$$\hat{V_m}(\vec{r}) = -\mu_N \hat{\vec{\sigma}} \cdot \vec{B(r)}. \tag{3.54}$$

Then,

$$\begin{aligned} \left| \langle \vec{k'} \middle| \hat{V}(\vec{r}) \middle| \vec{k} \rangle \right| &= \left| \int V_m(\vec{r}) \exp(i\vec{Q} \cdot \vec{r}) \cdot d\vec{r} \right| \\ &= \left| \mu_N \int \exp(i\vec{Q} \cdot \vec{r}) \hat{\vec{\sigma}} \cdot \hat{\vec{B}}(r) \cdot dr \right| \\ &\sim \left| \int \exp(i\vec{Q} \cdot \vec{r}) \hat{\vec{M}}(r) \cdot dr \right| \sim \left| \vec{M}(\vec{Q}) \right|, \end{aligned} \tag{3.55}$$

where $M(\vec{Q})$ is the magnetisation of the measured system. According to Eq. 3.51, neutrons with a wave vector of $\vec{k}$ can only sense the magnetic moment that is perpendicular to the scattering vector $\vec{Q}$. Thus, the cross-section for magnetic scattering is [154]:

$$\frac{d\sigma_m}{d\Omega} \sim \langle \vec{M}^*_{\perp}(\vec{Q}) \rangle \langle \vec{M}_{\perp}(\vec{Q}) \rangle, \tag{3.56}$$

where $\vec{M}_{\perp}(\vec{Q})$ is the magnetisation that is perpendicular to the Q vector. This demonstrates that the magnetic neutron scattering can measure the magnetic correlations in the material.

In summary, by measuring the scattering function in an elastic neutron scattering experiment, information about the reciprocal lattice of the sample can be obtained and the crystal structure can be studied. As neutrons have spins that can interact with the magnetic moment in the sample, the magnetic structure can also be investigated by this technique.

Grazing-incidence small angle neutron scattering

Different experimental geometries in neutron experiments are designed to study different structures. These different scattering geometries can probe a variety of length scales

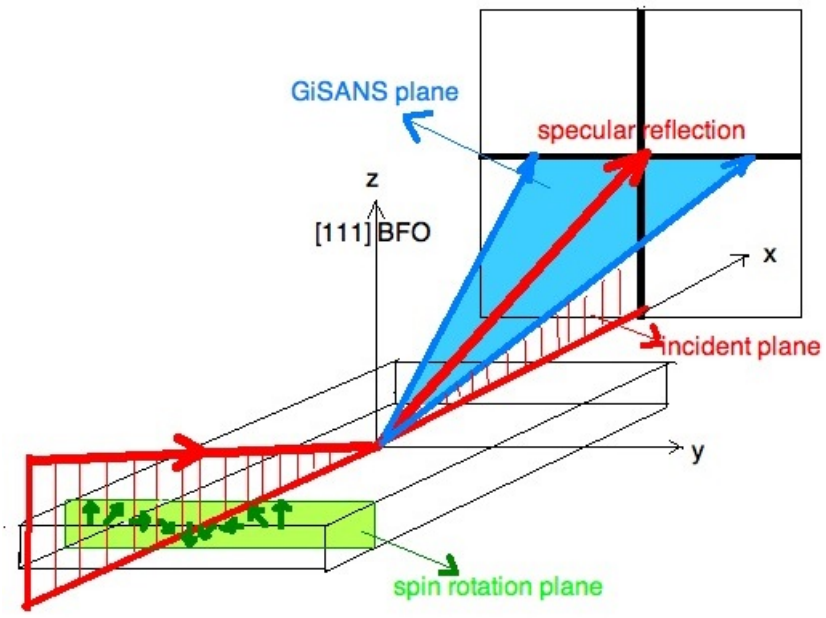

Figure 3.13: The geometry of a GISANS experiment with which a spin cycloidal structure lying in-plane of a $BiFeO_3$ thin film can be measured.

ξ. In this thesis, the spin cycloid with a period of 62 nm in (111)-oriented epitaxial thin film of $BiFeO_3$ is investigated. This structure has a very large length scale and is parallel to the film surface, as shown in Fig. 3.13. In order to study this large magnetic structure in a thin film surface, the GISANS technique was used.

Using grazing-incidence geometry, it is possible to distinguish three scattering geometries (shown in Fig. 3.13): specular reflection, scattering in the incidence plane and scattering perpendicular to the incidence plane (GISANS). Among them, GISANS probes in-plane features in the range 3 nm $< \xi <$ 100 nm, which is a perfect technique to study the incommensurate spin configuration in $BiFeO_3$ thin films.

The technique of GISANS is based on the propagation of an evanescent wave along the surface. When the grazing angle gets close to the critical edge, the evanescent neutron wave penetrates deeply into the sample and possibly but undesired also the substrate. As long as the grazing angle is smaller than the critical angle, the incident neutrons will be totally reflected. Therefore, the beam can only interact with the sample surface and detect large in-plane structures.

The geometry of the GISANS experiment to investigate the spin cycloid in (111) $BiFeO_3$ is shown in Fig. 3.13. The cycloid magnetic structure with a 62 nm length scale would give a signal of around $Q = 0.01$ Å^{-1}. This small Q value requires a long counting time to reduce the influence of noise. Details of the measurement will be discussed in the following chapter.

Chapter 4

$BiFeO_3$ Epitaxial Film Deposition and Characterisation

Among all multiferroic materials, $BiFeO_3$ is the most studied and exhibits ferroelectricity [38], antiferromagnetism [155] and the white-light photovoltaic effect [156] at room temperature. This makes it a very promising candidate for future applications. Interestingly, it has an incommensurate antiferromagnetic order making it an important model to study an incommensurate magnetic structure and multiferroic physics. The study of $BiFeO_3$ started in the 1960s. Limited by the poor crystal quality, early studies encountered many problems and no applicable devices were fabricated in the last century. The research interest of $BiFeO_3$ surged again after a large remnant polarisation in a $BiFeO_3$ thin film was discovered in 2003 [38].

Due to the incommensurate spin cycloid [155], the magnetoelectric coupling in $BiFeO_3$ is weak [15, 157]. This slows down the development of future applications based on this promising room-temperature multiferroic material. Moreover, the spin cycloid has never been directly observed in the $BiFeO_3$ thin film due to poor thin film quality [158]. As this spin cycloid directly affects the magnetic structure and the magnetoelectric coupling in $BiFeO_3$, it is of great importance to study it and to learn more about the interplay between the magnetic and ferroelectric ordering in the $BiFeO_3$ thin

film, in which form the applicable devices should be fabricated.

The existence of the incommensurate spin structure makes $BiFeO_3$ a very important material to understand multiferroic physics. Sosnowska and co-workers [155] firstly reported the incommensurate spin cycloidal structure in a $BiFeO_3$ single crystal in 1982. This cycloid was reported to have no spin reorientation from 4 K to room temperature based on investigations using neutron scattering [14]. However, anomalies were observed in Raman [159, 160], optical reflectivity [161], μSR [162], impedance and mechanical spectroscopy [163, 164] measurements in bulk $BiFeO_3$ at around 200 K. The anomaly exhibits a strong magnetoelastic coupling and a small coupling to polarisation. It has been suggested that this anomaly can be explained by the spin reorientation [159–161, 163, 164] or the spin-glass behaviour [165]. However, the origin of this anomaly is still controversially debated.

The spin cycloid plays an important role in the multiferroic properties of $BiFeO_3$. It averages out the linear magnetoelectric coupling and the weak ferromagnetism in $BiFeO_3$. Only higher orders of magnetoelectric coupling in $BiFeO_3$ are allowed [15,157]. In this case, a large external magnetic field ($\sim$ 200 kOe) is needed in order to break the spin cycloid structure and to achieve the linear magnetoelectric coupling in $BiFeO_3$. However, how this incommensurate magnetic structure varies with the magnetic field and electric field has not been reported yet.

The properties of $BiFeO_3$ single crystals have been extensively studied, whereas the properties of $BiFeO_3$ thin films have not been comprehensively investigated because epitaxially grown $BiFeO_3$ thin films of high quality are very difficult to fabricate. It was reported that the spin cycloid was destroyed by the epitaxial constraint in the $(111)_c$-oriented film [158]. Moreover, in 2013, an evidence of the spin cycloid in $BiFeO_3$ was discovered indirectly by engineering the strain in epitaxial thin films [166]. However, limited by the poor quality of films, spin cycloid has never been directly observed in $BiFeO_3$ thin films.

As the spin cycloid in $BiFeO_3$ directly modifies the magnetic structure and weakens

the magnetoelectric coupling of this multiferroic material, a thorough investigation of this incommensurate spin cycloidal structure and magnetoelectric coupling in relation to the spin cycloid in $BiFeO_3$ thin films is desperately needed. Therefore, in this project, the deposition of high-quality $BiFeO_3$ epitaxial thin films was proposed followed by characterisations of the spin cycloid. The incommensurate structure at around 200 K was also studied to explore the origin of the potential "transition". It was also proposed to study the evolution of the cycloid under external magnetic and electric fields as well as strain in order to obtain a better understanding of the cycloidal structure as well as the magnetoelectric coupling in $BiFeO_3$ thin films.

4.1 Introduction to $BiFeO_3$

$BiFeO_3$ is one of the most extensively studied multiferroic materials as it shows multiferroic properties at room temperature. It is known as a G-type antiferromagnet with a Néel temperature $T_N = 370$ °C [167]. Its ferroelectric ordering was firstly reported in 1970 [168] with a Curie temperature of $T_C = 820$ °C - 850 °C. In 2003, Wang reported a huge remnant polarisation in an epitaxial $BiFeO_3$ thin film, which is 15 times larger than that found in the bulk [38].

However, the magnetic moments in $BiFeO_3$ do not align perfectly antiparallel with each other as an antiferromagnet. They were reported to have an incommensurate spin cycloid [155]. The spin cycloid weakens the magnetoelectric coupling in $BiFeO_3$ [15,157]. In this section, the structure, magnetoelectric coupling and spin cycloid in $BiFeO_3$ will be reviewed.

Crystal structure

$BiFeO_3$, as shown in Fig. 4.1, belongs to the $R3c$ space group with the lattice parameter of $a_{\text{hex}} = 5.58$ Å and $c_{\text{hex}} = 13.87$ Å [169]. In many papers, the structure of $BiFeO_3$ is described in the pseudocubic frame to show that it has a distorted perovskite ABO_3

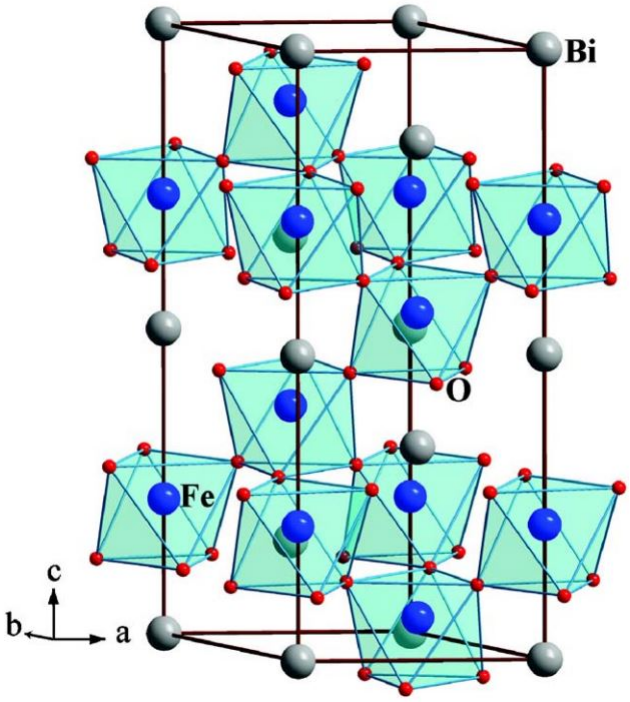

Figure 4.1: The crystal structure of $BiFeO_3$ in a hexagonal base. The FeO_6 octahedra are highly distorted and rotated along the $[001]_{hex}$ (or $[111]_c$) of the crystal. Due to the $6s$ lone pair electrons of the Bi, the Bi ion has a displacement from the centrosymmetric position, which allows the ferroelectric distortion along the $[001]_{hex}$ (or $[111]_c$) threefold axis [170].

structure. This means the $[111]_c$ is parallel to the $[001]_{hex}$ plane with a lattice parameter of $a_{rh} = 3.965$ Å and a rhombohedral angle of $\alpha_{rh} = 89.3°$ - $89.4°$ at room temperature [15]. As shown in Fig. 4.1, its rhombohedral symmetry can be derived from an ideal cubic perovskite ($Pm\bar{3}m$) by two types of distortions: the tilting of the FeO_6 octahedra along the $[111]_c$ direction and the displacement of the anion and cation leading to ferroelectricity in $BiFeO_3$.

The crystal structure of $BiFeO_3$ is very complicated in the higher temperature region (above room temperature). According to the most complete study of the $BiFeO_3$ phase diagram, it has three distinct solid phases above room temperature and below the melting point (960 °C) [171]: the rhombohedral α-phase below 830 °C (related to ferroelectric-paraelectric transition); an intermediate β-phase in the region of 830 - 925 °C; and a cubic γ-phase with a space group of $Pm\bar{3}m$ in the region of 925 -

933 °C before decomposition. The symmetry of the β phase is rather controversial. First-principle calculation has predicted that above T_c the structure changes into a tetragonal phase $I4/mcm$ [172]. However, an X-ray powder diffraction (XRPD) study revealed that the space group of $BiFeO_3$ is $C2/m$ [172] or $P2_1/\mathrm{m}$ above the critical temperature [173]. Neutron scattering measurements, which are more sensitive to the position of the oxygen, indicate that the β phase is orthorhombic with the space group $Pbnm$ [171].

Ferroelectricity

The $6s^2$ lone electron pairs of the Bi^{3+} ion result in Bi $6p$ orbitals coming energetically closer to the O $2p$ orbitals in $BiFeO_3$. The hybridisation between these two orbitals drives the Bi cation towards the neighbouring O anion leading to structural distortions in $BiFeO_3$ [170]. The relative displacement of the negative and positive charge centres in $BiFeO_3$ occurs along the $[111]_c$ direction, as shown in Fig. 4.1. Thus, a spontaneous polarisation is permitted along this threefold axis.

A bulk ferroelectricity only 6 $\mu C/cm^2$ in $BiFeO_3$ was firstly measured in 1970 [168]. The small value of the polarisation was limited by the large leakage current in the sample [38]. However, a large spontaneous polarisation was expected because of the large displacement of atoms from the centrosymmetric position in the $R3c$ space group. The ab initio calculation also agrees with the prediction that bulk $BiFeO_3$ can offer a large polarisation of up to 90 to 100 $\mu C/cm^2$ [174]. By improving the quality and reducing leakage currents, a larger polarisation was finally measured in a $BiFeO_3$ thin film (55 $\mu C/cm^2$) [38] and single crystals (100 $\mu C/cm^2$ in the [001] direction) [175] more than 30 years after the first reported polarisation measurement in a bulk sample.

However, ferroelectricity in $BiFeO_3$ thin films may be highly influenced by the strain introduced during the film fabrication. Even though the absolute value of the spontaneous polarisation in films with different strain remained constant [176], the polarisation axis was no longer along $[111]_c$ but rotated slightly away [177] in the presence of strain.

This is because that the strain in $BiFeO_3$ thin films can change the displacement of the negative and positive charge centres or the symmetry of the thin film [178, 179]. This then affects the ferroelectric properties in $BiFeO_3$ thin films. However, the piezoelectric constant of $BiFeO_3$ is small. Hence, the structural change is relatively small when the strain is induced in thin films. Thus, the change of ferroelectricity due to strain effects is not significant [15].

Another factor that complicates investigations on ferroelectricity in $BiFeO_3$ thin films is the large leakage current. The large leakage current in $BiFeO_3$ is normally a significant problem even in bulk samples. With a large leakage current, the polarised current is difficult to detect, and the ferroelectricity cannot be properly investigated. There are three possible leakage current mechanisms: interface-limited Schottky emission, bulk-limited ohmic (or space-charge-limited conduction) and bulk-limited Poole-Frenkel emission. In the case of the Schottky emission, the Fermi energy difference between $BiFeO_3$ and the contacting metal results in a current across the interface [180]. In contrast to the interface limited mechanism, leakage current can also have a bulk-limited source, which is formed by free carriers trapped by oxygen vacancies in $BiFeO_3$. With a small applied electric field, electrons can be injected and this will result in a drift current (Ohmic conduction). When more electrons are injected under a larger electric field, unbalanced space charges occur. As a consequence, the leakage current has a space-charge limited source [181]. At high temperatures, the thermal energy is sufficiently large to enable the so-called Poole-Frenkel emission in the material. Due to random thermal fluctuations, charges, which are trapped in localised states at low temperatures, start to hop between different trap centres. This could also be a source of the leakage current in $BiFeO_3$ [182]. In pure and high-quality bulk $BiFeO_3$, oxygen vacancies can be well controlled. The DC resistivity in a pure bulk $BiFeO_3$ can be as large as 10^{10} Ohm·cm at room temperature [183], which means that the leakage current in a high-quality bulk $BiFeO_3$ can be very small. However, it is more difficult to reduce defects, and oxygen vacancies are harder to control in thin films. As a result, the

leakage current problem in $BiFeO_3$ thin films is even worse than in the bulk material. In summary, mechanisms of the leakage current in $BiFeO_3$ thin films are complicated and normally depend on the thin film quality. High-quality thin films, which may have smaller leakage currents, are needed to lower the influence of the leakage current when measuring the electric polarisation in $BiFeO_3$ thin films.

Magnetic order in $BiFeO_3$

The antiferromagnetic order in $BiFeO_3$ was first detected with the neutron diffraction technique and was classified as G-type with a Néel temperature of 643 K [185]. Each Fe^{3+} parallel spin is surrounded by six antiparallel spins on the nearest iron atoms. However, the spins are not perfectly antiparallel. A spatial-modulated spin cycloidal structure with an incommensurable period of 620 Å was revealed in $BiFeO_3$ [155], as shown in Fig. 4.2 (a) and (b). The cycloid propagates along the $[110]_{\mathrm{hex}}$ or the $[10\bar{1}]_{\mathrm{c}}$ direction in bulk $BiFeO_3$ [155, 184].

It was believed that there is no structural or magnetic phase transition between room temperature and 4 K, and that the antiferromagnetic structure dose not change with temperature in this temperature range. Ref. [14] proved that there is no change of the time-averaged spin projection over the cycloid plane at low temperatures from the neutron diffraction measurement. Zalessky's group, however, revealed that the spin cycloid is distorted at low temperatures with a neutron spin echo study [186]. This disagreement between neutron diffraction and spin echo measurements may be explained by the dynamic sensitivity of the neutron spin echo technique [187]. In a neutron spin echo experiment, the Larmor precession of the neutrons' magnetic moment is used as an internal clock to record the transit of the individual neutrons through two large solenoids before and after the measured sample. It directly measures the real part of the intermediate scattering function, and it is used to study slow dynamics in materials. Therefore, a neutron spin echo experiment can often measure dynamic processes whereas a diffraction experiment cannot.

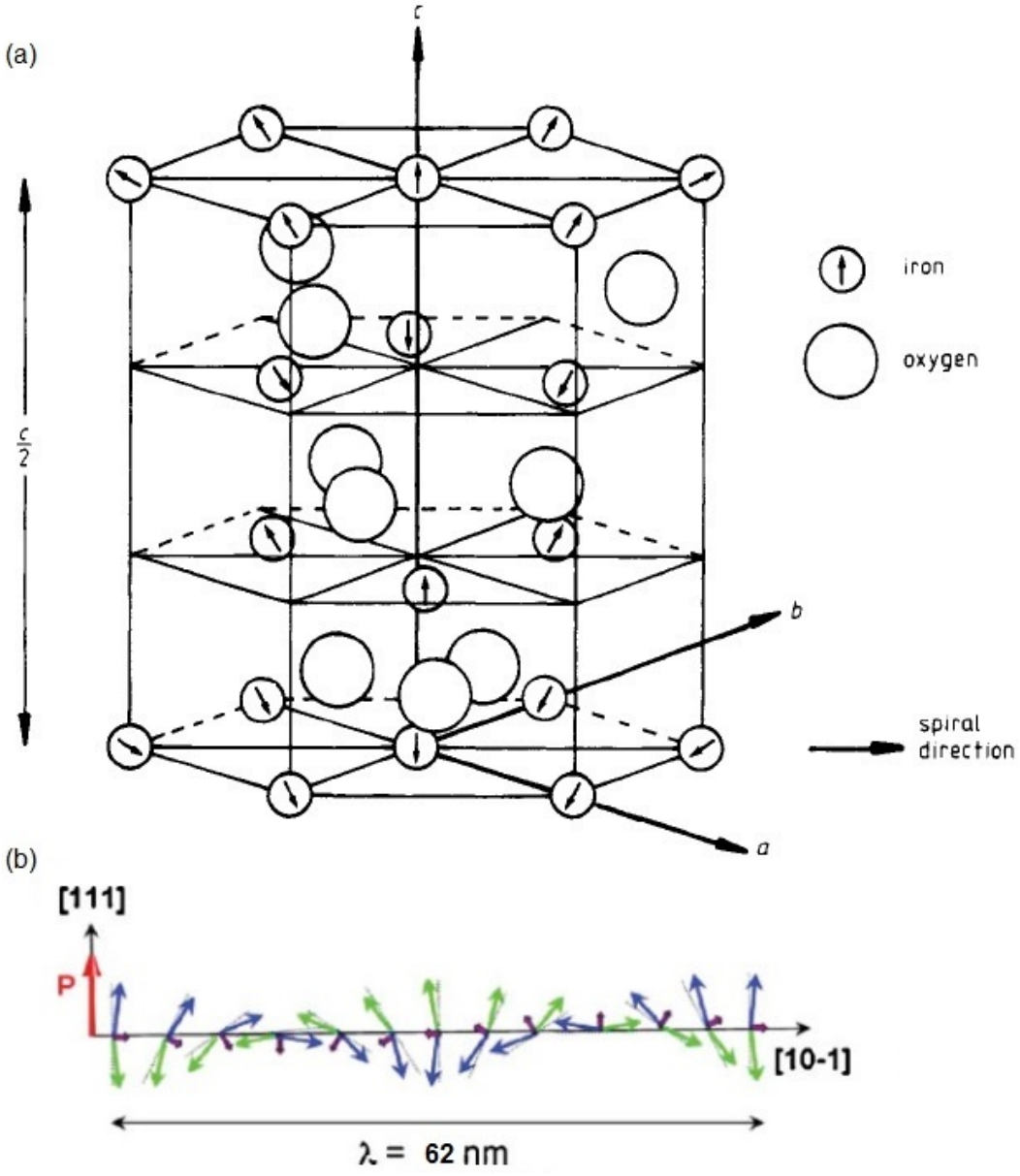

Figure 4.2: (a) The hexagonal lattice of $BiFeO_3$ (only iron and oxygen ions are shown). The arrows indicate the Fe^{3+} moment and the spin cycloid is roughly indicated [155]. (b) The schematic representation of the 62 nm spin cycloid in $BiFeO_3$. The blue and green arrows are canted antiferromagnetic spins with a cycloidal structure. The total moment, represented by the purple arrows, averages out resulting in a zero net magnetisation in $BiFeO_3$ [184].

However, two anomalies at 140 and 200 K were observed in the measurements of magnetisation, magnetic susceptibility, Raman spectroscopy, optical reflectivity, impedance and mechanical spectroscopy and muon spin spectroscopy. This can potentially be a sign of spin reorientation in $BiFeO_3$. The 140 K anomaly has already been interpreted as a surface phase transition [165]. However, the origin of the 200 K anomaly is still a controversial issue. It has been suggested to be a result of a spin reorientation [160,163,188] or a spin-glass behaviour [165]. All the reports on the anomaly in $BiFeO_3$ at around 200 K are listed in Table 4.1. This 200 K anomaly is clearly different from the 140 K transition: it has a strong magnetoelastic coupling and shows a change in spin dynamics. Even though neutron scattering data showed that there is no spin reorientation between 4 K and room temperature, other techniques do observe a dynamic or magnetoelectric process happening at around 200 K. This makes the "potential transition" at 200 K interesting and important to be understood in $BiFeO_3$.

Magnetoelectric coupling in $BiFeO_3$

At room temperature, $BiFeO_3$ crystallises in a polar group as a result of the tilted oxygen octahedra. This will also cause the canting of spins due to the Dzyaloshinskii-Moriya (DM) interaction. This DM interaction also leads to weak ferromagnetism. Apart from this homogeneous DM interaction, there is also an inhomogeneous coupling in $BiFeO_3$, which means that the ferroelectric polarisation couples to the gradients of magnetisation. This inhomogeneous coupling results in an inhomogeneous spin structure: the spin cycloid in $BiFeO_3$. This spin cycloid averages out the linear magnetoelectric coupling in $BiFeO_3$. Therefore, the linear coupling constant α_{ij} in Eq. 2.1 is zero and only higher orders of magnetoelectric coupling are allowed in $BiFeO_3$.

If a large external magnetic field is applied, the magnetoelectric coupling and ferromagnetism recovers (Fig. 4.3) [157]. The magnetisation and polarisation have a non-linear dependence on the magnetic field at low fields followed by transitions at a high magnetic field around 200 kOe, as shown in Fig. 4.3 (a) and (b). The linear magneto-

Table 4.1: Details of different techniques used to investigate the anomaly at around 200 K in $BiFeO_3$.

Technique	Temperature	Sample	Ref.	Phenomenon
Raman spectroscopy	200 K	$(001)_c$ single crystal	[188]	The one-magnon branch at 2.28 meV saw an increased intensity and narrowing FWHM at 200 K.
Raman spectroscopy	140 K - 200 K	Polycrystal	[160]	Raman spectra change in this temperature range.
Dynamic Mechanical Analysis	$\sim$ 230 K	Ceramic bars	[163]	A large peak occurred at 230 K in modulus losses and tan δ (a mechanical dissipative process).
Dielectric measurements	$\sim$ 200 K	Both ceramic and single crystal	[163]	The dielectric loss has a clear change at 230 K.
Magnetometry (FC/ZFC)	230 K	Polycrystalline thin film (263 nm)	[163]	The FC and ZFC data of the magnetisation measurement show a difference from below 230 K.
Ultrafast optical pump-probe spectroscopy	195 K	$(001)_c$ thin film (150 nm)	[161]	Spin dynamics change at 140 K and 200 K.
μSR	140 K - 230 K	Single crystal	[162]	Muon senses the internal field and spin dynamics change in this temperature range.

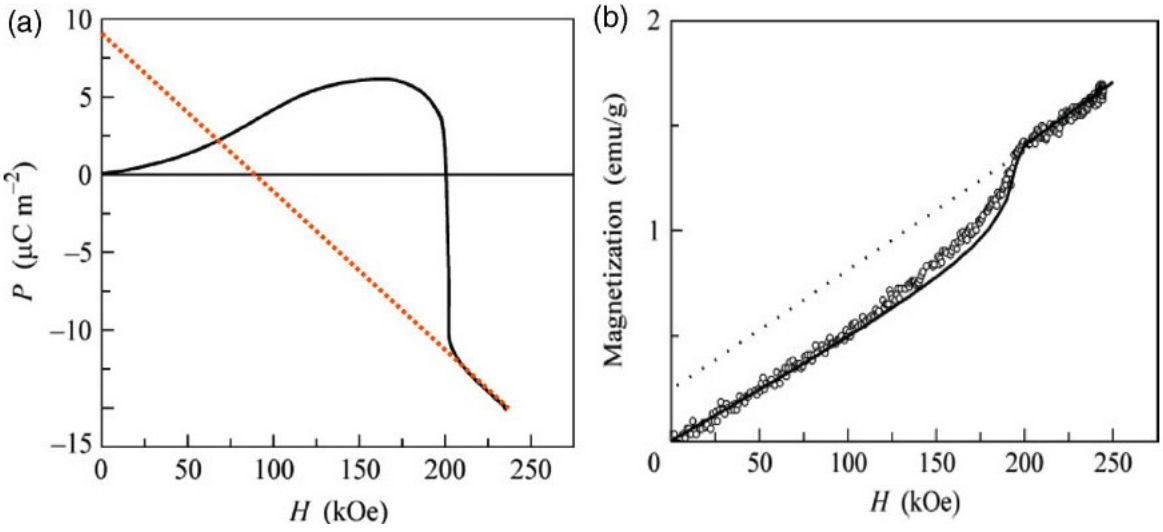

Figure 4.3: (a) Magnetoelectric effects in $BiFeO_3$ at low fields. P is proportional to H^2 (quadratic magnetoelectric coupling). Above $B_c = 200$ kOe, P is linearly dependent on H (linear magnetoelectric coupling) [15]. (b) Once the cycloid is destroyed, the small canted magnetic moment is recovered. Zero-field magnetisation yields a small net magnetisation of 0.3 emu/g [15, 157].

electric effect, which is prevented by the spin cycloid structure, appears when $H > 200$ kOe, as shown in Fig. 4.3 (a). This indicates that a high magnetic field can destroy the spin cycloid in $BiFeO_3$ [15]. Meanwhile, the remnant magnetisation arising from the canted spins also recovers at the same applied magnetic field, as shown in Fig. 4.3 (b). Therefore, the linear magnetoelectric coupling and weak ferromagnetism are both allowed if the spin cycloidal structure is destroyed by a large external magnetic field [15]. Moreover, at low fields, when the spin cycloid still exists, the magnetically induced polarisation is found to be proportional to the square of the external magnetic field (shown in Fig. 4.3 (a)). This confirms that only higher orders of the magnetoelectric coupling are allowed if the spin cycloid exists in $BiFeO_3$ [15].

Aside from a large applied magnetic field, epitaxial strain in $BiFeO_3$ thin films is also capable of destroying the spin cycloid. The latent antiferromagnetic component that is hindered by the cycloid was reported to be released in a $(111)_c$ $BiFeO_3$ thin film because of the epitaxial constraint within the structure [158] (shown in Fig. 4.4 (a)) [158]. The presence of an induced magnetisation at low magnetic fields, which

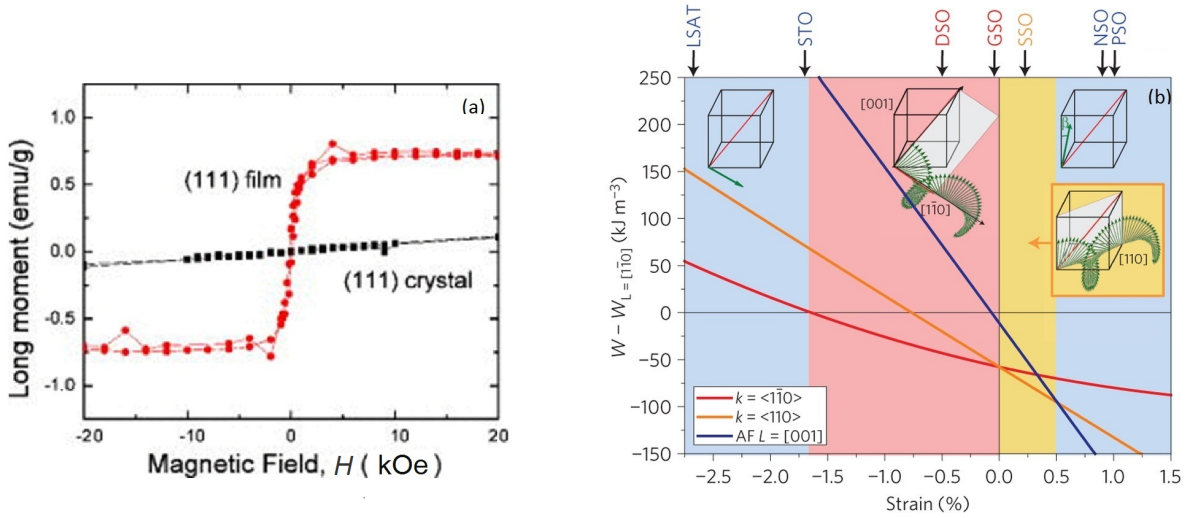

Figure 4.4: (a) Magnetisation properties of a $(111)_c$ $BiFeO_3$ film and corresponding crystal. Weak ferromagnetism recovers in the thin film [158]. (b) The magnetic phase diagram of strained $BiFeO_3$ thin films. When compressive strain is bigger than 1.7% and tensile strain is bigger than 0.5% (blue columns), spin cycloid can be destroyed; if a moderate compressive strain is applied (pink column), $BiFeO_3$ thin film has a bulk-like spin cycloidal structure propagating along the $[1\bar{1}0]_c$ direction; with moderate tensile strain (yellow column), the propagation vector of the spin cycloid in a $BiFeO_3$ thin film change its direction towards $[110]_c$ [166].

is somewhat close to that of a homogeneous antiferromagnetic spin state, implies a transition between cycloidal and homogeneous antiferromagnetic spin states with the existence of epitaxial strains in thin films.

According to a more recent report, the spin cycloid can be tuned by the epitaxial strain [166], as shown in Fig. 4.4 (b). With a high epitaxial strain (both tensile and compressive), the spin cycloid is found to be destroyed in the epitaxial $(001)_c$ orientated $BiFeO_3$ film and antiferromagnetism recovers. This is similar to the case given in Fig. 4.4 (a). However, when moderate strain was applied, the spin cycloid is still present. With moderate compressive strain, bulk-like spin cycloid along $[1\bar{1}0]_c$ is observed in the same oriented thin film structure. Whereas, for moderate tensile strain, spin cycloid still exists but the propagation vector is along $[110]_c$.

In summary, $BiFeO_3$ is a promising multiferroic material possessing both antiferromagnetism and ferroelectricity at room temperature. However, a spin cycloid in $BiFeO_3$ prevents a linear magnetoelectric coupling. Only a large external field ($H > 200$ kOe)

or epitaxial strain in thin films can suppress this spin cycloid. Whether this cycloidal structure has a spin reorientation below room temperature is still contentious as many techniques observe a magnetoelastic or spin dynamics related anomaly at around 200 K while a neutron diffraction experiment showed no spin reorientation between 4 K and room temperature. Moreover, this spin cycloid has not been well studied in $BiFeO_3$ thin films due to current low quality of the films.

4.2 $BiFeO_3$ Epitaxial Thin Film Deposition

A high-quality epitaxial thin film of $BiFeO_3$ is needed in order to investigate the spin cycloid in its thin film structure. Successful fabrication of epitaxial $BiFeO_3$ thin films with high quality were reported using pulse laser deposition (PLD) [166,189]. However, if the thin film thickness is less than 300 nm, the epitaxial strain is large, which may destroy the spin cycloid in $BiFeO_3$ [166]. Therefore, thicker films are needed as the strain effects on the layers far away from the film-substrate interface are smaller. However, films deposited using the PLD technique were usually not thick enough as the laser only ablates a small area of the target and the deposited film cannot grow thicker when this small area of the target becomes exhausted. In order to grow a thicker $BiFeO_3$ film, a radio-frequency (RF) magnetron sputtering deposition was therefore employed in the current project.

4.2.1 Epitaxial thin film deposition by RF plasma sputtering

In an epitaxial thin film growth, the atomic arrangement of the film matches that of the crystalline substrate. There are two types of epitaxy: homoepitaxy and heteroepitaxy. Homoepitaxy refers to the epitaxial growth where the film and substrate are the same material with the same crystal structure and orientation. Heteroepitaxy refers to the film growth where the film is a different material from the substrate. In this project, heteroepitaxial deposition was used as there was no available $BiFeO_3$ single crystal

substrates. The heteroepitaxy is more complex because the growth must accommodate compatibility issues between the film and substrate.

RF plasma sputtering with a substrate heating system was developed to fabricate epitaxial $BiFeO_3$ thin films. During the deposition process, the depositing temperature and the deposition rate can affect the quality of epitaxial films. It is essential to optimise the growth conditions. In addition, for the epitaxial growth of $BiFeO_3$, which is an oxide material, the oxygen partial pressure is also an essential factor, since it affects the concentration of the oxygen vacancies in the deposited films.

Deposition methods RF magnetron sputtering is employed to fabricate the epitaxial $BiFeO_3$ thin films. In the sputtering system, which is shown in Fig. 4.5, energetic ions from the plasma of a gaseous discharge bombard a target acting as the cathode of the discharge. Target atoms are ejected and impinged onto a substrate to form a coating on the substrate. Then, the charges travel to the grounded deposition chamber to complete the circuit. During the process, magnets in the sputter gun are utilized to confine the plasma in order to achieve an efficient bombardment. Magnetron sputtering employs a DC or RF supply depending on the conductivity of the target. If the target material is a conductor, a circuit is formed between the cathode and anode through the conducting target. However, if the target is an insulator such as $BiFeO_3$, an RF supply is required. In an RF circuit, the sign of the anode-cathode bias is varied at a high rate in order to prevent charge build up on the chamber surface.

Substrate choice The choice of the substrate is limited by various factors including the crystal symmetry, orientation and lattice mismatch. A similar crystal symmetry and the same orientation is required for the film to follow the pattern of the substrate and achieve a good epitaxy. For $BiFeO_3$ thin films, $SrTiO_3$ single crystal substrate, which has a similar perovskite structure, has been suggested to be a good substrate [190]. The lattice mismatch is defined as the difference between the lattice parameters of the film

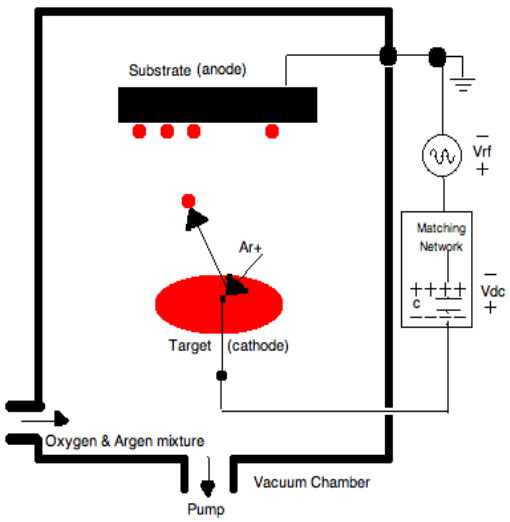

Figure 4.5: An illustration of the RF sputtering system: target ions are bombarded by energetic ions from plasma, such as Ar plasma, and then ejected to the substrate. The whole RF circuit is powered by an RF power supply with a fixed frequency of 13.56 MHz and the impedance is tuned with an external matching circuit.

material and the lattice parameters of the substrate material:

$$M = \left(a_f - a_s\right)/a_s, \tag{4.1}$$

where M is the lattice mismatch between the substrate and the film and a_f, a_s are the lattice parameter of the film and the lattice parameter of the substrate, respectively. For the $SrTiO_3$ substrate, its lattice parameter is 3.905 Å, which is very close to the pseudocubic lattice parameter of $BiFeO_3$ (3.965 Å). This means that the mismatch between the substrate and the film is only 1.5%, which is relative small compared to other substrate candidates whose $M > 2\%$ [166]. However, the high dielectric constant of $SrTiO_3$ may create difficulties when electric and magnetic measurements are carried out on the sample. Therefore, a conducting $SrRuO_3$ layer with a similar structure to both $BiFeO_3$ and $SrTiO_3$ with a lattice parameter of 3.93 Å was employed as a intermediate layer. This layer provides a smaller lattice mismatch (0.9%) and it can act as a buffer layer as well as an electrode during electrical property measurements.

Crystallisation temperature The deposition temperature has a direct effect on the epitaxy of the thin film. In general, it is more likely to achieve epitaxy with higher substrate temperatures. This can be explained by the higher mobility of the deposited atoms at the substrate surface at higher temperatures. $BiFeO_3$ thin films deposited by PLD were found to be well crystalline with the substrate temperature above 550 °C [190, 191]. It is also worth noting that $BiFeO_3$ decomposes and bismuth starts to escape when $T > 850$ °C. Therefore, it was preferable to keep the substrate temperature between 550 and 850 °C, so that substrate heating apparatus is needed to achieve a good crystallisation of $BiFeO_3$ films.

Gas pressure During the deposition of $BiFeO_3$ thin films, the total gas pressure and the oxygen partial pressure affect the epitaxy of the deposited films. Moreover, the total gas pressure in an RF sputtering system determines the mean free path of the plasma. With the increase of the gas pressure, the mobility of the particles will decrease near the substrate. Thus, in order to achieve high quality epitaxial films, a low gas pressure is needed. But with a low total gas pressure, the population of the energetic ions is small leading to a low deposition rate. Therefore, the gas atmosphere needs to be adjusted carefully to achieve a trade-off between the film quality and the deposition rate.

Considering the oxides deposition, oxygen partial pressure is also a very important parameter that needs to be considered. Oxygen helps $BiFeO_3$ to maintain its stoichiometry in the thin film during the deposition process. However, a high oxygen partial pressure can introduce extra Bi_2O_3 in a deposited film [192]. Wu [190] reported a successful fabrication of (111)-oriented $BiFeO_3$ films using a 10 mTorr deposition pressure with the ratio of $Ar : O_2 = 4 : 1$. This ratio was also employed in the deposition of $BiFeO_3$ films in this thesis.

4.2.2 Deposition system development

In this project, a vacuum chamber with a magnetron sputter gun, substrate heating apparatus, cooling systems, gas supplies and a gas analysis module was built for the deposition of $BiFeO_3$ thin film. An illustration of the system's cross-section and the real components are shown in Fig. 4.6. It is an RF magnetron sputtering system with the sputter gun sitting directly below the substrate. The sputter gun is connected to the RF power supply through a coaxial cable at the bottom. The distance between the sputter gun and the substrate can be varied from 5 to 20 cm by adjusting the position of the substrate heater, to which the substrate is attached. As shown in Fig. 4.6 (c), in addition to the bottom port for the sputter gun and top port for the heater plate, there are three ports at the sides of the chamber. Port 1 is for a window (the front window in Fig. 4.6 (b)) to monitor the plasma and deposition in the system. Port 2 is a small one and is connected to external argon and oxygen pipelines. The flow of the gases is controlled by needle valves. Port 3, which is the biggest port, is shared by a pumping system and a residual gas analyser (RGA), which is used to analyse the gas composition during the thin film deposition. In order to achieve this sharing, a T-piece with a valve is connected to it. The pumping station here helps to keep the chamber where the RGA sit in a reasonable pressure. There is a tiny hole on the valve, which allows some gas samples from the main chamber to reach the RGA when the total pressure in the chamber is much higher than the working pressure of the RGA ($\sim 10^{-5}$ mbar) during the RF sputtering process.

Before the deposition, the height of the heater was adjusted and the substrate was attached to the centre of the bottom stainless steel plate with carbon paste. Then, the whole system was pumped down by a pumping station connected to the top plate of the system to achieve a reasonable vacuum of $\sim 5 \times 10^{-6}$ mbar. Once a good vacuum was obtained, argon gas flew into the chamber several times and cycled for about 10 minutes in order to reduce the nitrogen and water and other contaminations in the chamber. Then, the total and oxygen partial pressure were carefully tuned to the right

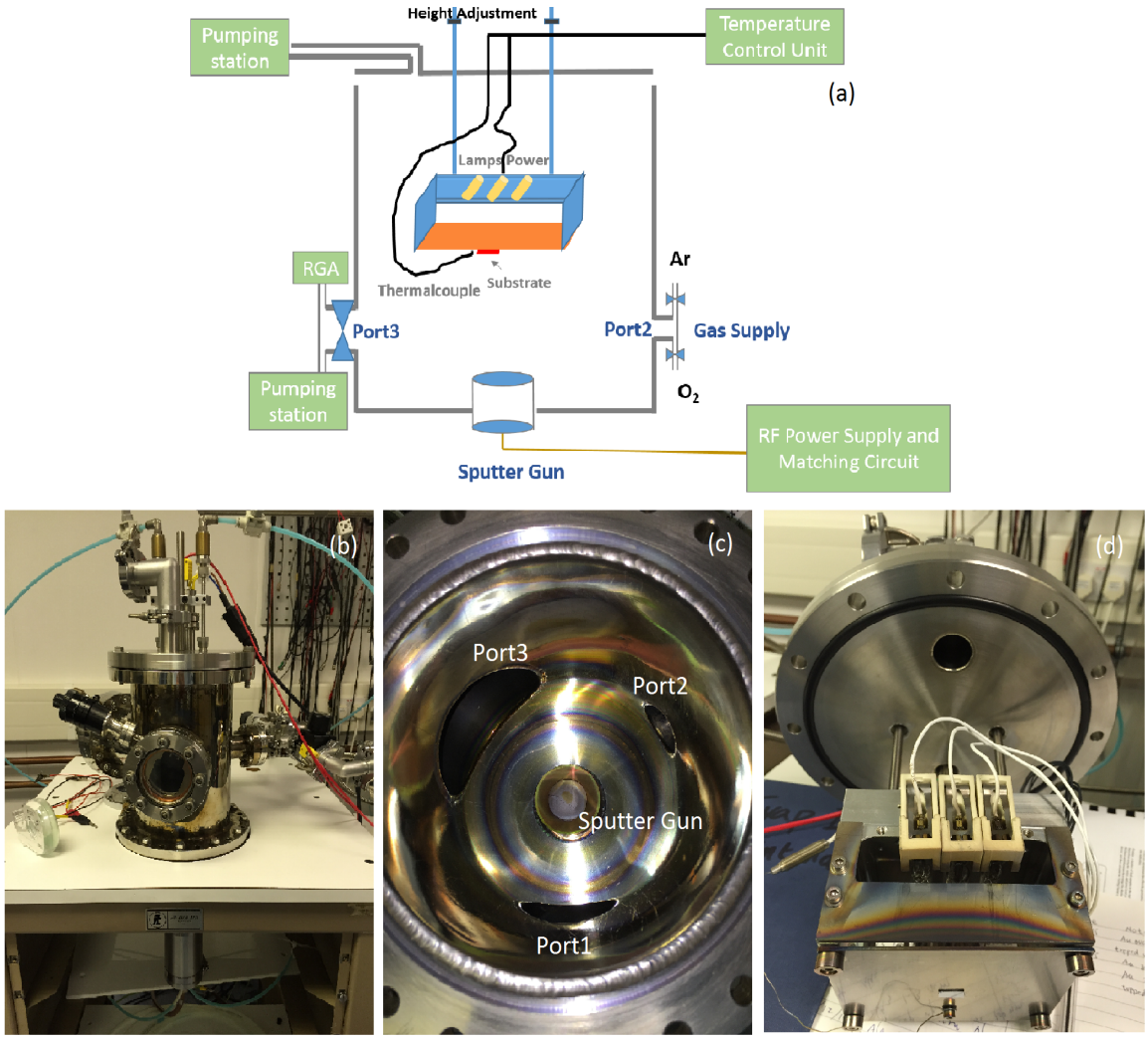

Figure 4.6: (a) An illustration of the cross-section of the deposition system. (b) the overview of the real system. (c) An internal view of the deposition chamber. (d) The substrate heater attached to the top plate.

conditions by adjusting the needle valves.

Halogen lamps were used to heat the bottom stainless steel plate, to which the substrate was directly attached. An illustration of the cross-section and the real apparatus are shown in Fig. 4.6 (a) and (d), respectively. A thermocouple was mounted at the edge of the substrate to monitor the temperature near the centre area. The performance of the heater was good and stable and can reach 690 °C within 3 minutes, as shown in Fig. 4.7. After reaching the set temperature, 10 minutes waiting time was set to allow the $SrTiO_3$ substrate to achieve the thermal equilibrium at the set temperature. During the whole deposition process, cooling water was flowing through the heating metal block to keep the whole chamber at a reasonable low temperature. This measure protects the sputter gun and electric circuits in the chamber from any potential damage. A test was conducted in a testing chamber to monitor the temperature in a position of 12 cm below the substrate, where the sputter gun should sit. It is shown in Fig. 4.7 (inset) that the temperature of the sputter gun was kept below 30 °C during the whole heating process (the substrate was heated to 690 °C, kept for 265 second and cooled below 200 °C, as shown in Fig. 4.7). It can cool the sputter gun area efficiently and keep the temperature sufficiently low to protect the gun from thermal damage.

4.3 Results

Once the deposition system was developed and tested, a lot of effort was put into epitaxial $BiFeO_3$ thin film deposition using this custom-built RF sputtering system. The deposited films were initially planned to be used for further characterisation of their multiferroic properties and the spin cycloid. However, a high-quality thin film could not be fabricated due to technical problems, which will be discussed later in this section.

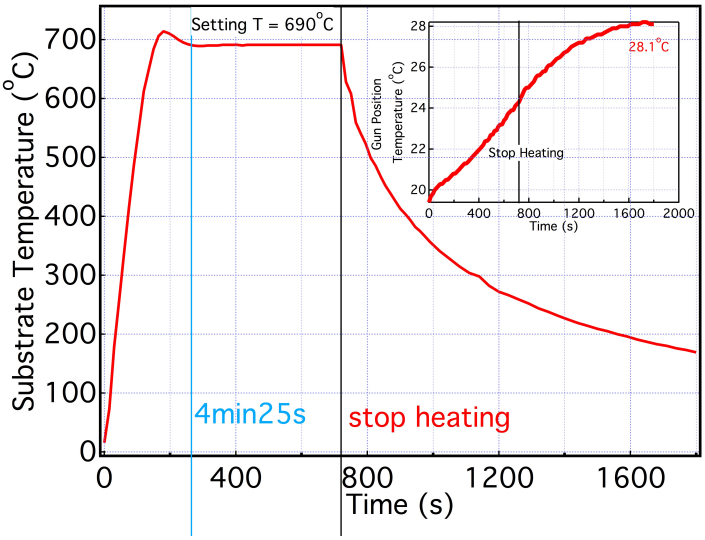

Figure 4.7: The temperature of the substrate position (a thermocouple was mounted to the position where the substrate usually sits) when the setting temperature was 690 °C. The inset shows the temperature at the position of the sputter gun in the deposition chamber under a typical deposition pressure. The cooling system keeps the sputter gun area at a reasonable temperature.

4.3.1 Thin film deposition

Films were firstly grown on glass substrates without substrate heating in order to investigate the relationship between the deposition conditions and the thickness of the films. This relationship is shown in Table 4.2. It is clear that a low total pressure and high RF power were helpful for obtaining thick films and the system adjustments were sufficiently good to grow a thick film of up to 750 nm or thicker. As discussed, it is important to use a relatively slow growth rate in order to achieve a good epitaxial film. Therefore, a trade-off between the growth time and the growth rate was apparent. An RF power of 50 W, a distance between substrate and sputter gun of 5 cm and $\sim$ 0.04 mbar total deposition pressure were chosen. A good gas ratio of O_2 : Ar = 1 : 4 [190] was used to sputter $BiFeO_3$ thin films and the gas composition was monitored by the RGA. A $BiFeO_3$ film on glass with a thickness of 450 nm grown under this condition is shown in Fig. 4.8. The growth rate of the films with a substrate-target distance higher than 7 cm is very small. These rates are not added to Table 4.2.

Table 4.2: Relationship between deposition conditions and film thickness.

RF Power (W)	P_{total} (mbar)	O_2 : Ar	Distance (cm)	Deposition Time (min)	Thickness (nm)	Growth Rate (nm/min)
50	0.048	1:3.8	7	10	55	5.5
50	0.045	1:4	7	10	55	5.5
50	0.035	Pure Ar	7	10	62	6.2
50	0.037	Pure Ar	7	15	90	6
50	0.042	1:3.8	5	15	150	10
50	0.035	1:4	5	60	750	12.5
80	0.037	1:4	5	10	400	40
50	0.038	1:5.8	5	15	180	12
80	0.040	1:4.1	5	10	380	38
80	0.050	1:4	5	15	420	28

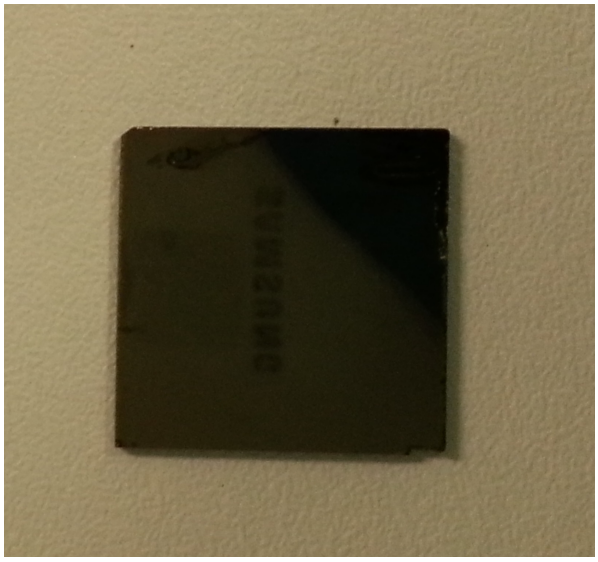

Figure 4.8: An example of the $BiFeO_3$ film on a glass substrate deposited using the conditions discussed in the text.

Even though the RF sputtering deposition system and the substrate heater work perfectly individually, they were found to be not compatible with each other during hot sputtering experiments. The distance between the electrodes of the lamps and the sputter gun was only about 10 cm, which means that they were very close in the system. After plasma was generated, it can easily travel into the heater and short-circuited the halogen lamps. Once the plasma shorted the current in the heater, the fuses in the protecting circuit and the fuse of the laboratory burnt as the circuit between the lamp electrodes and the grounded vacuum chamber was shorted. A possible solution would be shielding the electric circuit from plasma, which will include the rebuilding the substrate heater. This development have taken too much time for this PhD work. In order to continue the investigation on $BiFeO_3$, epitaxial thin films were then taken from the Bouyanfif's group in Universit*é* de Picardie Jules Verne. They fabricated $BiFeO_3$ epitaxial films with high quality deposited with a PLD system.

4.3.2 Characterisations of $BiFeO_3$ thin films

To characterise the ferroelectric properties of $BiFeO_3$ thin films, a ferroelectricity measurement system was built. This system was integrated into a superconducting magnet in a cryostat, which can provide a 70 kOe magnetic field and a temperature as low as 2 K. With this cryomagnetic system, the magnetic field evolution of the polarisation-electric field (PE) loop can be measured at different temperatures. Meanwhile, the spin cycloid was studied using the grazing-incident small angle neutron scattering.

Electric polarisation in $BiFeO_3$ thin films

Multiferroic properties was initially proposed to be investigated by measuring PE loops of $BiFeO_3$ thin films with applied magnetic fields. If an electric bias is applied to a ferroelectric sample, where the centres of the positive and negative charges are not the same, the polarisation will be aligned by the external electric field. When this external electric field changes, the direction of the electric polarisation would change resulting

in a charge transfer in the circuit. In an ideal case when the measured sample has no leakage current, this charge transfer in the sample can be obtained by integrating the measured polarised current through the sample, using [193]:

$$P(or\frac{C_p}{A}) = \int J_p dt, \tag{4.2}$$

where C_p is the moving charge in the circuit due to the spontaneous polarisation in a ferroelectric sample. The polarised current corresponding to the spontaneous polarisation alignment with an electric field is described by the current density J_p. P, A and t are the polarisation in the ferroelectric sample, the device area and the time, respectively. The measured current through the film has two origins, namely the polarised current (I_P) and the leakage current (I_L):

$$I_{measured} = I_L + I_P. \tag{4.3}$$

The big leakage current I_L in $BiFeO_3$ is the main obstacle for device applications. It is believed that the leakage current originates from the free carriers trapped by oxygen vacancies [194]. The value of the leakage current may vary with the films' quality as well as the working temperature and the applied electric field. Normally, the leakage current is expected to increase with the temperature because the mobility of the oxygen vacancies is higher at elevated temperatures. Therefore, it is important to measure the polarisation current at low temperatures in order to limit the influence of the leakage current in $BiFeO_3$ thin films.

According to this basic principle, a polarisation measurement system based on the method in Ref. [193], with a customised measuring script, was built. The schematic setup of the measurement is shown in Fig. 4.9. A two-channel 30 MHz Agilent 33500B waveform generator was used to generate a sine wave. Since the dielectric properties of $BiFeO_3$ thin films are frequency dependent [15], the frequency of the applied voltage was treated as an important parameter in the measurement. Then, the signal was

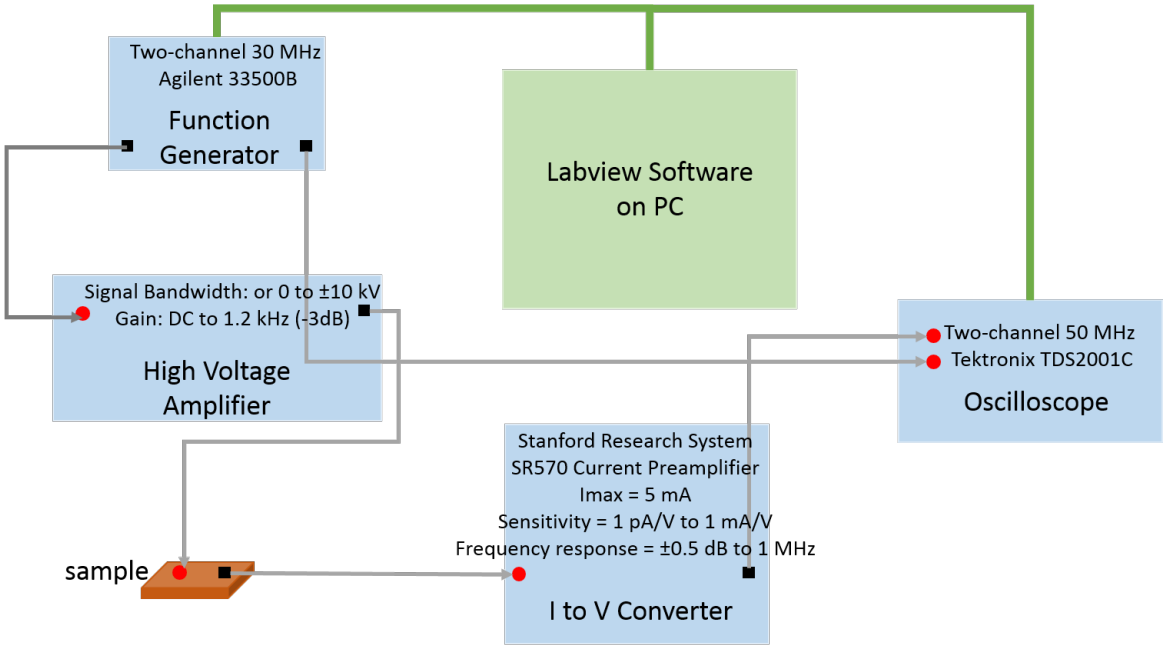

Figure 4.9: An illustration of the polarisation measurement system. A computer was used to control the experimental setup and to acquire the data. Details of the equipment are discussed in the text.

amplified by a Trek 610E high-voltage amplifier and then fed into the sample sitting in the cryomagnet. The current through the sample is then converted into a voltage by a Stanford Research System SR570 current-voltage converter and finally read by a Tektronix TD2001C oscilloscope. To acquire the data, a software was also developed using Labview. In the software, all pieces of equipment included in Fig. 4.9 were automatically controlled. The measured voltage from the oscilloscope was collected by the measuring script and the polarised current was then calculated (using the conversion ratio chosen in the SR570 current-voltage converter) and integrated to be the polarisation according to Eq. 4.2. This data acquisition process was automatically done in the software and can be shown on the software window and stored in the computer instantaneously.

When measuring the electric polarisation of a material, an external electric field E should be applied. With the external electric field, dipole moments in the material can be aligned nearly linearly proportional to the applied field. This is called the dielectric

polarisation, as shown in Fig.4.10 (a). In the case of a ferroelectric material, spontaneous polarisation can exist, be poled and switched by an external electric field. In polycrystalline and non-perfect single crystalline ferroelectrics, the ferroelectric grains are always split into many domains as a consequence of the complex set of the boundary conditions in the material. The application of an electric field will reduce or even remove domain walls. As shown in Fig. 4.10 (b), the switching of the domain walls in the material means that the polarisation in a ferroelectric material can be reversed by an external electric field and shows a hysterestic behaviour. If an applied electric field is sufficiently small to switch domains with non-preferable directions, the polarisation increases linearly with the field amplitude, as shown by the segment OM in Fig. 4.10 (b). With increasing field, the polarisation of domains with non-preferable directions starts to switch towards directions as close as possible to the direction of the applied electric field. Thus, the measured charge density is dramatically increased and the polarisation response in this region is strongly non-linear (segment MA). After all the domains are aligned (at the point A), the ferroelectric performs as a linear dielectric again, as shown in segment AB. When the field strength decreases, the polarisation of some domains will relax owing to thermal excitations resulting in a gradual decrease of the polarisation (segment BC). At zero field, many domains still keep their polarisation leading to a non-zero net polarisation in the material. A reversed field is needed to reach the zero-polarisation state (at the point N). A further increase of the reversed field will then result in a realignment of dipoles (segment ND) until it saturates at point D and become linearly again in the segment DE. Then, the reversed field strength is reduced to zero (segment DG) and reversed (segment GA) to complete the cycle. This polarisation hysteresis is a characteristic behaviour of a ferroelectric material.

Before measuring $BiFeO_3$ thin films, a standard resistor and capacitor were measured to test the reliability of the self-developed PE measurement system. Fig. 4.11 (a) and (b) show the PE behaviour of a resistor and a capacitor, respectively measured with this system with a sine-shaped applied AC voltage. For the PE behaviour of a resistor,

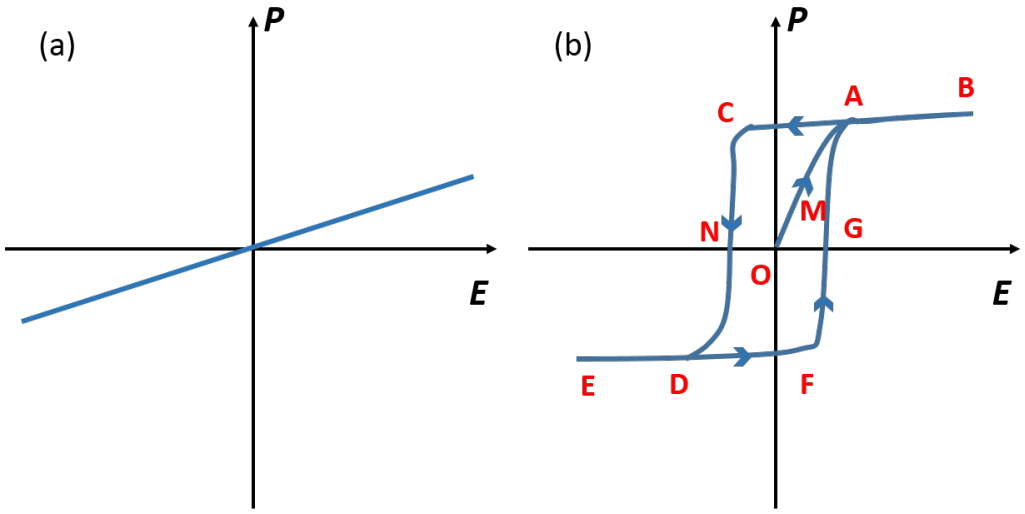

Figure 4.10: (a) Dielectric polarisation of a non-ferroelectric material. (b) Electric polarisation of a ferroelectric material.

it should be a circle (or ellipse) with the centre in the origin. The polarised current in an ideal resistor has the same phase as the applied voltage. We can write $P = \int J(t)dt = \int \frac{\sin(\omega t)dt}{RA} \sim$ -cos(ωt), where ω is the frequency of the applied voltage and $E \sim \sin(\omega t)$. In a measurement, as shown in Fig. 4.13 (a), the resistor had a circle-shaped PE loop, which is exactly what it should be. While in the case of an ideal capacitor, the polarisation behaves the same as the dielectric polarisation, as shown in Fig. 4.10 (a) and should follow a straight line. The ceramic capacitor measured in the experiment did not perform as an ideal capacitor, as shown in Fig. 4.13 (b). This may be caused by the small leakage current, which has the same phase as the applied voltage. In a non-ideal capacitor, this result is reasonable. In conclusion, the measurements based on a resistor and a capacitor were successful and demonstrated that the measurement system and software can work properly to measure the ferroelectric properties of a material.

For the polarisation measurement in the $BiFeO_3$ thin film, a film device was prepared with a $BiFeO_3$ (BFO)/$SrRuO_3$ (SRO)/$SrTiO_3$ (STO) structure by the Bouyanfif's group. Above the $BiFeO_3$ layer, an array of indium tin oxide (ITO), having a good conductivity and harder than most of metal contacts, was chosen as point cathodes. The ITO point contacts were 0.5 mm in diameter. The film was clipped down to the

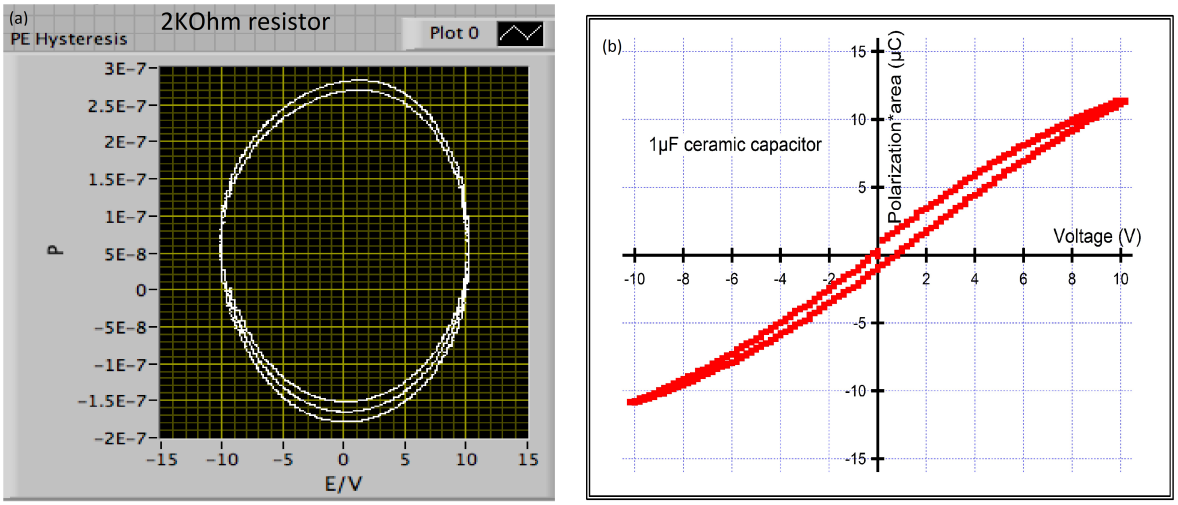

Figure 4.11: (a) A screenshot of the "PE" hysteresis of a standard 2 kΩ resistor. P on the y-axis is polarisation × area (not known in the packed resistor) and has a unit of Column. The x-axis E is the applied voltage instead of the electric field as the thickness of the resistor is also unknown. (b) The "PE" hysteresis of a 1 μF ceramic capacitor. P is polarisation × device area and E is the voltage as the area and the thickness of the purchased capacitor are also unknown.

sample holder of the cryomagnet (shown in Fig. 4.12(a)) by two copper contacts. One of the contacts was connected to the $SrRuO_3$ layer of the device and the other one was connected to the ITO point contact. Details of the sample mounting and connection is shown in Fig. 4.12 (b).

Before measuring the PE hysteresis loop, the current vs. voltage (IV) was measured on the a (001) $BiFeO_3$ film device in order to determine the conversion ratio

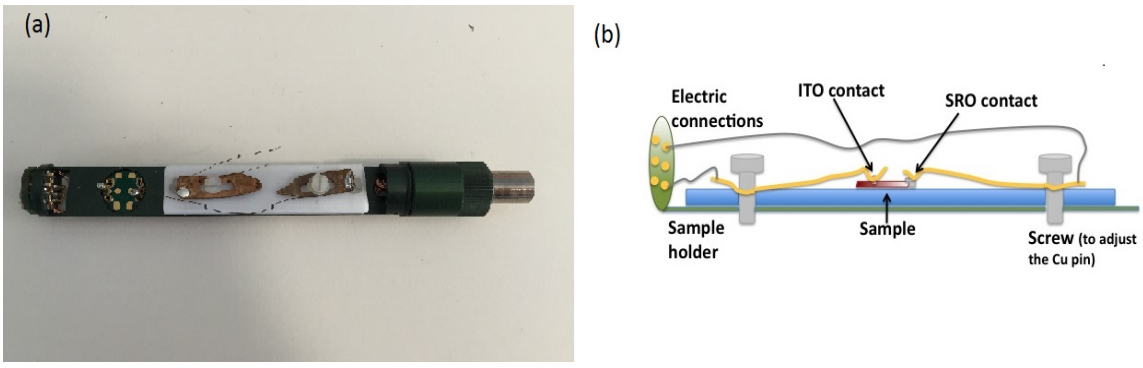

Figure 4.12: (a) A sample holder used to test a $BiFeO_3$ thin film sample in the PE measurement system. (b) An illustration of how the sample was mounted and how contacts were made during the measurement using the sample holder in (a).

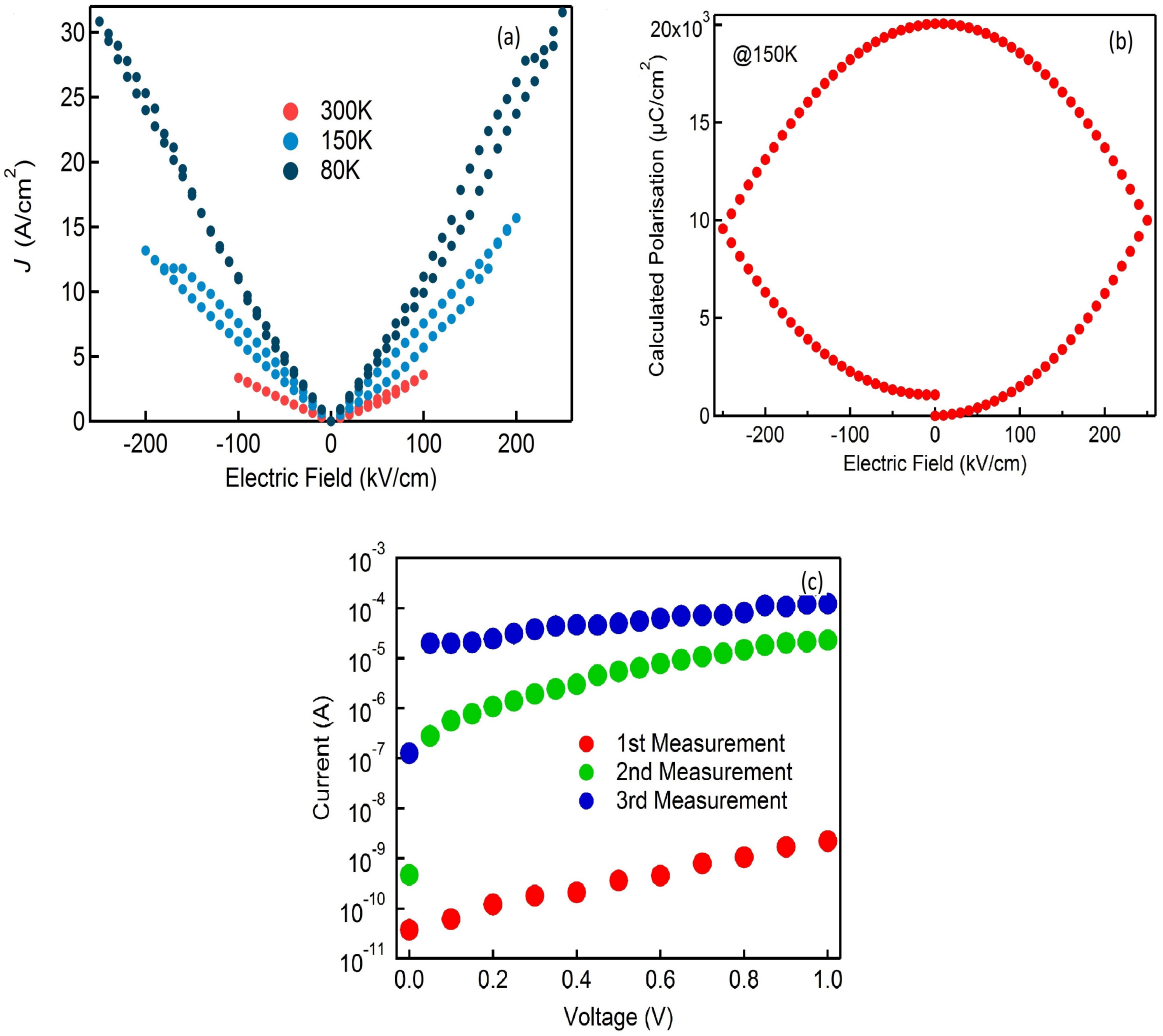

Figure 4.13: (a) The current density in the $BiFeO_3$ thin film sample as a function of temperature. (b) The measured PE hysteresis based on a large leakage current shown in (a). (c) The first three IV tests on the $BiFeO_3$ film.

of the current-voltage converter. As shown in Fig. 4.13 (a), the measured current is very large indicating that the film have a resistance of only several Ohm. The leakage current density in the measured sample is nearly six orders of magnitude larger than the reported leakage current density (6×10^{-6} A/cm^2 at 80K with a 250 kV/cm applied electric field) in a typical $BiFeO_3$ film [195]. This observation is not very sensible as pure $BiFeO_3$ should be an insulator. Also, the current becomes smaller with increasing temperature. This also contradicts the nature of the leakage current in $BiFeO_3$. Moreover, it is found that the charge builds up during the measurements, as shown in Fig. 4.13 (c). The first measurement of a fresh film has a reasonable small current. But in the following measurements, the current keeps increasing and can grow as much as six orders of magnitude, even when the voltage is reduced. It is likely that the film was broken down or burnt by the large leakage current and these measurements are not valid for the estimation of the polarisation in this $BiFeO_3$ thin film. However, the reason for this problem still needs to be investigated thoroughly and will be done in future work.

Therefore, the polarised current in this $BiFeO_3$ film cannot be measured properly with the existence of a large leakage current. One may be able to explain these data with the nature of the sample or the measurement. If the polarisation is calculated based on the current shown in Fig. 4.13 (a), then the calculated PE hysteresis loop is like a circle (shown in Fig. 4.13 (b)). With other words, it behaved more like a resistor instead of an expected ferroelectric-like hysteresis, indicating that I_P was only a small portion the total measured current. This also confirms that we measured the current through a conducting material, which is unlikely to be $BiFeO_3$.

Spin cycloid in $BiFeO_3$ thin films

As previously mentioned, $BiFeO_3$ is an antiferromagnetic material with an incommensurate spin cycloid along the $[10\bar{1}]_c$ direction. Due to the quality limitation of the thin film, this spin cycloid has not been directly observed. Therefore, this spin cycloid in

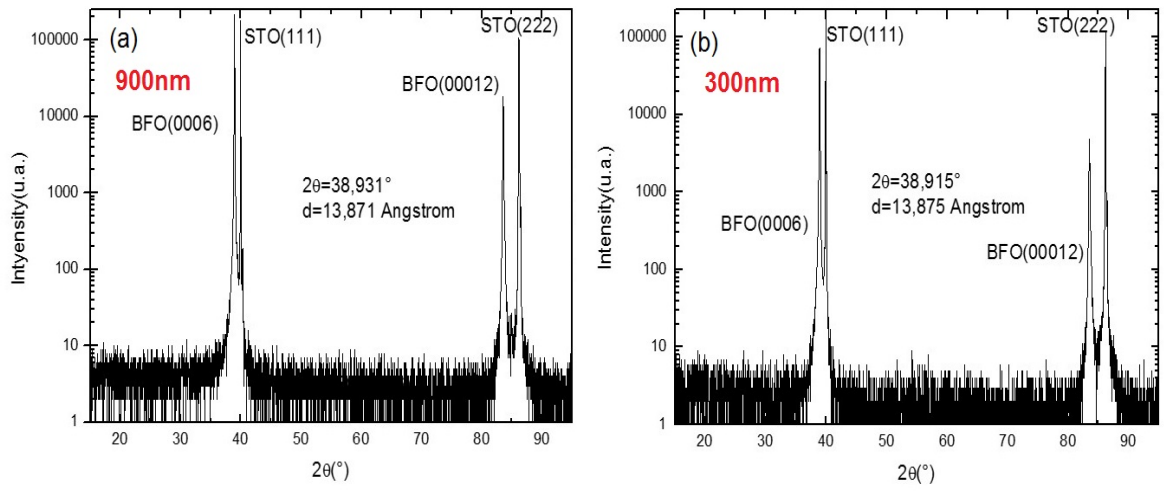

Figure 4.14: XRD characterisation on (a) the 900 nm BFO film on a STO substrate; (b) the 300 nm BFO film on a STO substrate. They are $(111)_c$ oriented epitaxial films. This data is provided by Dr. Houssny Bouyanfif.

the high-quality $BiFeO_3$ (111) thin films was investigated using the neutron scattering technique. As the spin cycloid, which is perpendicular to the $[111]_c$ direction, lies in-plane of the sample, the grazing-incidence small angle neutron scattering technique was utilised. This technique measures in-plane large-scaled structures. The experiment was carried out on the SANS2D spectrometer at ISIS using small angle scattering geometry. Two samples with thicknesses of 300 nm and 900 nm were measured.

The samples were deposited by the Bouyanfif's group using PLD on (111) single crystal $SrTiO_3$ substrates. Before the neutron scattering experiment, both samples were characterised using XRD, as shown in Fig. 4.14. It was confirmed that the 300 nm and very thick 900 nm $BiFeO_3$ films were $(111)_c$ oriented epitaxial thin films on STO substrates.

The (111)-orientated $BiFeO_3$ film was chosen for two reasons. First, the spin cycloid has a length of 62 nm. If the spin cycloid is perpendicular to the film surface, a significant number of this lengthscale is needed in order to support a cycloid, since epitaxial strain on the structure of the perovskite unit cell can induce a number of structural effects, such as polar cation shifts or rotation of the oxygen octahedra, that result in a significant modification to the spin cycloid or even its destruction [166, 196].

If the cycloidal structure lies in the plane of the thin film, it just needs to scale by the ratio of the cycloid radius, which is shorter than the lengthscale of a single lattice. Thus, using a film with the cycloid in the plane is more likely to maintain the spin cycloid in the $BiFeO_3$ film. Second, it was initially proposed to measure the evolution of the cycloid with applied electric fields. [111] is the polarisation easy axis in $BiFeO_3$. Therefore it is easier to measure the magnetoelectric coupling using this orientation.

As discussed in Chapter 3, the GISANS technique can be used to probe the lateral large magnetic structure. The spin cycloid, which lies in-plane of the $BiFeO_3$ film, should result in several diffraction peaks or a ring depending on the grain size and dynamics in the sample. The diffraction peaks or ring will have a Q value of $2\pi/62$ nm $= 0.01$ Å^{-1}, provided the cycloidal structure is present in the $BiFeO_3$ thin film and it has the same periodicity as in the bulk material.

Fig. 4.15 (a), (c) and (e) show the 2D neutron diffraction pattern for the 300 nm sample at 300 K, the 900 nm sample at 123 K and the same 900 nm sample at 300 K, respectively. The bright spot in the centre is the specular reflection point of the neutron beam. For the 900 nm sample, two wing-like spots near the specular reflection point at 123 K (Fig. 4.15 (c)) appear compared to the 300 nm sample (Fig. 4.15 (a)). Taking the cross-section of the spectrum at positions near (presented by the red line in the figure) and away (presented by the black line in the figure) the wings, it is clear that the spectrum of the 900 nm sample measured at 123 K has an obvious broadening (Fig. 4.15 (d)) compared with the spectrum of the 300 nm sample (Fig. 4.15 (b)). This broadening ends at $Q \sim 0.01$ Å^{-1}, which is the right Q for the 62 nm incommensurate cycloid. As reported, the strain in $BiFeO_3$ thin film relaxes with increasing thickness [176] thereby the spin cycloid is probably destroyed by strain in the 300 nm sample. The strain in the 900 nm sample is smaller and the cycloid appears. Moreover, the diffraction volume in the 300 nm sample is only 1/3 of the 900 nm sample. Judging from the weak signal from the 900 nm sample, it is also likely that the diffraction signal from the 300 nm was too weak to be observed during the limited counting time.

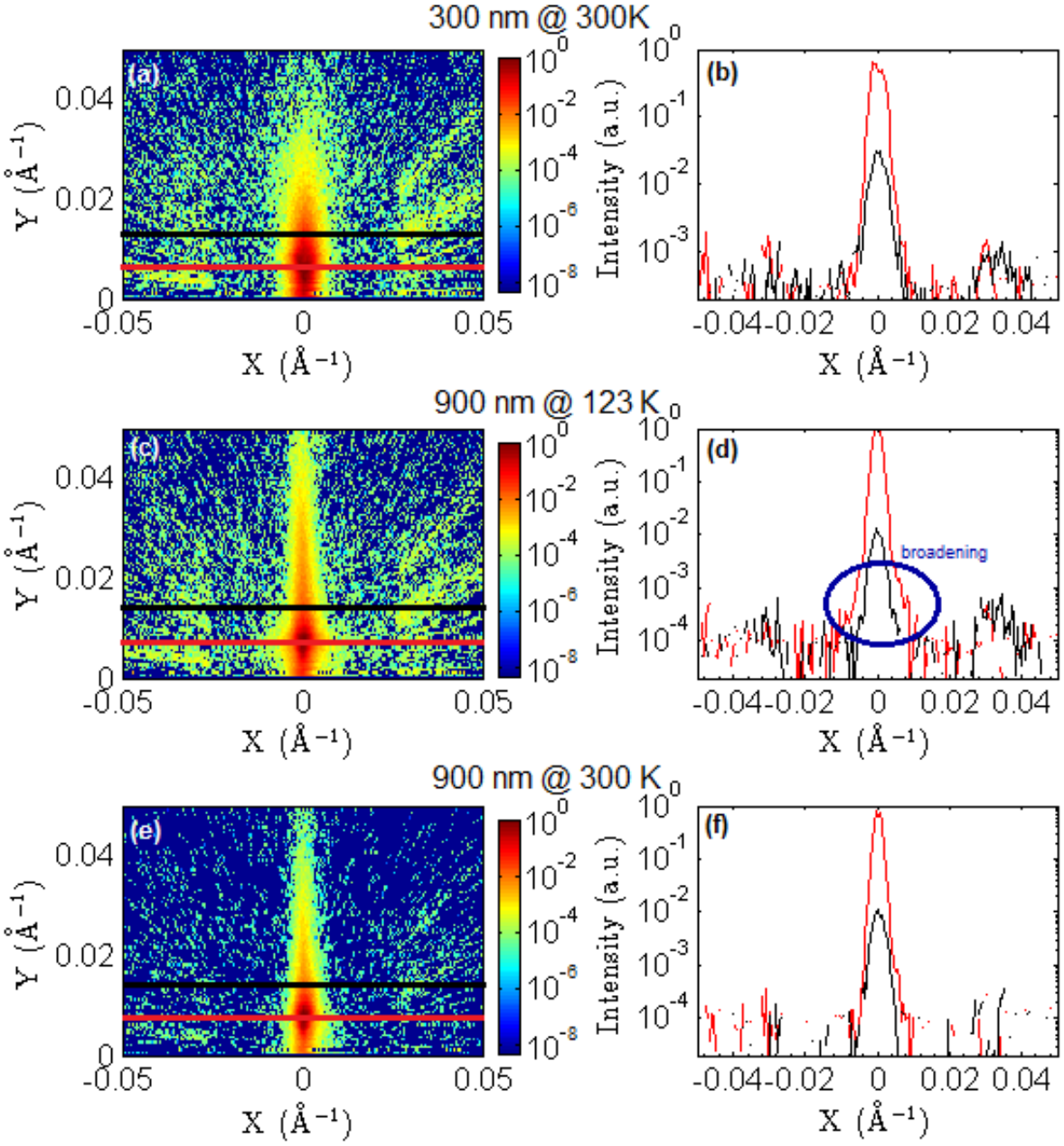

Figure 4.15: GISANS data of (a) the 300 nm (111)-oriented $BiFeO_3$ film measured at 300 K; (b) the cross-section of the lines in (a), where the red and black curves correspond to the red and black lines in (a); (c) the 900 nm (111)-oriented film measured at 123 K; (d) the cross-section of the lines in (c); (e) the 900 nm (111)-oriented film measured at 300 K; (f) the cross-section of the lines in (e).

When measuring the same 900 nm sample at a different temperature, as shown in Fig. 4.15 (c) and (e), the diffraction pattern is different. At 300 K, the wing-like feature is less significant. If the slices near and away from the central point are also taken from the 300 K spectrum, it is shown in Fig. 4.15 (f) that the broadening disappears at 300 K. This indicates that whatever causes the wing-like feature changes with temperature. Maybe the dynamics of the spin cycloid lower the intensity of the modulation peaks. Further investigations are still needed to understand the spin cycloid in $BiFeO_3$ thin films.

The data shown in Fig. 4.15 are noisy and the Q value corresponding to the 62 nm spin cycloid was very small. The data were collected using a large Q range but better statistics is needed in the Q near 0.01 $Å^{-1}$. Therefore, it is not reasonable to draw any solid conclusion based on the current data set. Future experiments using continuous neutron beams have been proposed. It would be ideal to measure the cycloid using a continuous neutron source with an instrument that is specialised in measuring large-scale magnetic structures. This would make it possible to use neutrons with a small range of Q near the interesting Q value and to count for longer time. Temperature dependent measurements as well as the electric field and film strain dependent measurements are also planned in the future.

4.4 Conclusion

This chapter discussed the unsolved problems related to the spin cycloidal structure in $BiFeO_3$ and effort of the $BiFeO_3$ thin film deposition and the characterisation. A working RF plasma thin film deposition system was built, but no epitaxial film could be produced due to a compatibility problem of the substrate heater. Further development of the deposition system is needed in the future. The automatic ferroelectric measurement system was also developed and worked properly. However, the measured $BiFeO_3$ thin films had a large leakage current, which broke down the films during the

measurement. More efforts are needed to reduce the leakage of the deposited thin films.

Characterisations of the spin cycloid in $BiFeO_3$ thin films were carried out by the grazing-incidence small angle neutron scattering. Two satellite peaks were observed at around $Q = 0.01$ Å^{-1}, which might correspond to the 62 nm cycloidal structure. However, the data were of low quality since the data were collected using a large Q range and the resolution at a small Q value was poor. Thus, no solid conclusion can be drawn. Further investigations using a more specialised instrument to utilise neutrons with a small range of Q just near the interested Q value are proposed in a further work.

If the leakage problem could be overcome, it would be interesting to continue the investigation of the spin cycloid as a function of electric field and epitaxial strain. How an electric field would affect the spin cycloid may provide more information about the magnetoelectric coupling in $BiFeO_3$. In Ref. [166], it was indicative that the properties of the spin cycloidal structure vary with epitaxial strain. A more direct measurement using neutron scattering could study how the spin cycloid is affected by the strain, thereby understanding more about the role of epitaxial strain in $BiFeO_3$ thin films.

In summary, the spin cycloid and magnetoelectric coupling in $BiFeO_3$ thin films were not properly investigated and the epitaxial thin film deposition also need further improvements. These are planned for the future.

Chapter 5

Multiferroic Metal-Organic Framework CuGF

Metal-organic frameworks are compounds containing metal ions or clusters linked by organic bridging ligands. They have been studied for their potential applications in fuel storage [48], gas purification [49], catalysis sensors [50] and novel magnetic materials [5]. Among these hybrid materials, the magnetic MOF belong to the branch of molecular magnets and is of central importance for this work. In magnetic MOFs, the central ions are often paramagnetic metals, in particular the first row of the transition metals. These metal ions act as magnetic moment carriers. The exchange interactions between the metal ions are realised via some organic bridging ligands. They act as connections between the metal ions providing exchange paths for the magnetic moments. Therefore, the structure and properties of MOFs can usually be adjusted by varying the organic bridging ligands [5].

Tunability makes MOF a great approach to produce new multiferroic materials, which are quite rare in nature. By modifying the organic frameworks, it is possible to create MOFs with both ferroelectricity and (anti)ferromagnetism. The first multiferroic MOF was reported in 2009. However, there have been just a few reports of multiferroic MOFs since then, including $[(CH_3)_2NH_2]M(HCOO)_3$ (M = Mn, Fe, Co, Ni) [16],

$[C(NH_2)_3]M(HCOO)_3$(M = Mn, Fe, Co, Ni, Cu, Zn) [17], $(NH_4)[M(HCOO)_3]$(M = Mn, Fe, Co, Ni, Zn) [18] and $[NH_2(CH_3)_2][Fe^{III}Fe^{II}(HCOO)_6]$ [19]. The magnetic phase transition temperatures of these reported multiferroic MOFs are far below room temperature. Hence, it is essential to study the magnetism in these systems to explore structure-property relations in order to find a way to improve the multiferroic properties in MOFs.

Even though the first multiferroic MOF was reported in 2009, the magnetoelectric coupling in these systems was not studied when this project began in 2011. $[C(NH_2)_3]$-$[Cu(HCOO)_3]$, called copper guanidinium formate (CuGF), was theoretically shown to exhibit magnetoelectric coupling in 2011 [54]. Therefore, this multiferroic MOF was chosen to study the magnetoelectric coupling. By understanding the magnetoelectric coupling mechanism in MOFs, more details of the structure-property coupling in the multiferroic MOFs should be obtained.

Moreover, the magnetic dimensionality of MOFs can also be controlled by tuning the exchange pathways provided by the organic bridges [6–9]. As the exchange interactions along all three dimensions can be easily controlled in MOFs, low-dimensional magnetic systems can be realised, which are expected to be excellent platforms to study low-dimensional magnetism and possibly quantum effects, such as quantum phase transitions in one-dimensional systems [10, 11] and the interference of the quantum spin phase in "zero"-dimensional systems [12]. Among them, one-dimensional magnetic systems have attracted much attention as they can be treated from a theoretical point of view much easier than two and three-dimensional systems [77]. It is a simplified model which can provide a better understanding on some complicated general theoretical problems [79].

Therefore, another reason why CuGF was chosen for this project was that it has a one-dimensional magnetic chain in its magnetic structure [17]. As the exchange energy along the copper chains is much stronger than the energy between the chains, it shows low-dimensional magnetic behaviour. To study the spin correlations and mag-

netic properties of the strong correlated low-dimensional chain in CuGF is helpful to understand low-dimensional magnetism and basic physics in magnetism.

In this chapter, the magnetic properties, one-dimensional magnetism and magnetoelectric coupling in CuGF will be discussed. Using zero-field μSR measurements, the phase transition and the critical phenomenon are studied. A method to study the one-dimensional magnetic correlation with the μSR technique will also be demonstrated in Section 5.4.3. Finally in Section 5.5, the magnetoelectric coupling in CuGF will be discussed.

5.1 Introduction to Copper Guanidinium Formate

Among magnetic MOFs, those with formate anions (HCOO-) have been less studied in comparison to others having short ligands such as cyanides, oxalates, acetates, etc. Among those MOFs, one family that possesses the general structure $[C(NH_2)_3]$-$[M^{II}(HCOO)_3]$ (M = Mn, Fe, Co, Ni, or Cu) has drawn much attention recently. Due to the Jahn-Teller distortion of the $3d^9$ electrons, the copper complex crystallises into a polar group [17]. This is important for its potential multiferroic properties, and indeed the ab initio calculation confirmed that the magnetism is coupled to the polarisation [54].

Due to the Jahn-Teller distortion, the magnetic structure of CuGF is non-trivial. The anionic Cu-formate framework consists of Cu-O chains connected by the bridging anti-anti formate ions through the short Cu-O formate bonds, which are in turn linked by the long Cu-O formate bonds. As a result, this material displays one-dimensional magnetism along the chain, as shown in Fig. 5.1 (c) [17].

CuGF exhibits three-dimensional spin-canted Heisenberg antiferromagnetism with a Néel temperature of 4.6 K [17]. Below the Néel temperature, a spin-canting antiferromagnetic structure was detected. Above the Néel temperature, a broad peak in magnetic susceptibility arising from one-dimensional antiferromagnetic chain was observed. The interchain exchange energy J = -5.4 K is much weaker than the intrachain

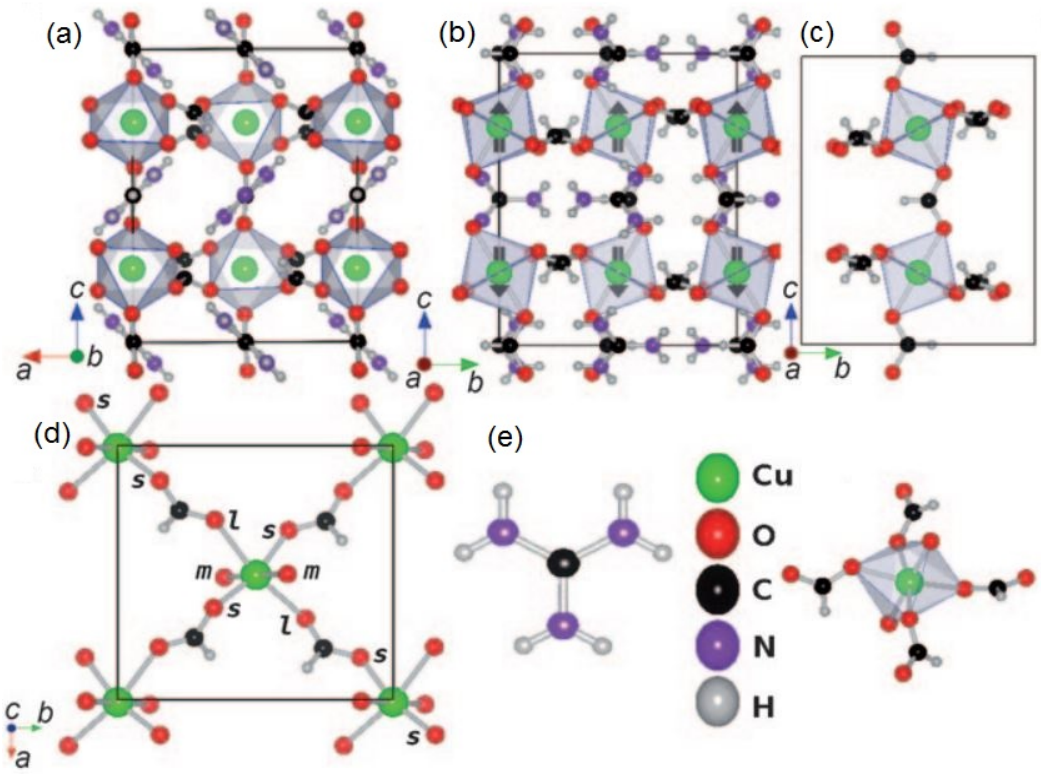

Figure 5.1: (a) The structure of CuGF. (b) Side view of the crystal structure showing the oxygen octahedra connected by the formate. (c) The Cu chain along the c-axis. (d) The ab-plane showing that the Cu-O bonds have long (l), medium (m) and short (s) lengths due to the Jahn-Teller distortion. (e) Atomic structure of a $C(NH_2)_3$ (left) and Cu(CHOO) (right) unit [54].

one J' = -47.3 K [17].

5.2 Structure

CuGF has a perovskite crystal structure in a $Pna2_1$ space group with anionic metal-formate frameworks of $[Cu(HCOO)_3]^-$ and Gua^+ cations located in the nearby cubic cavities. The copper ions are connected by the formate bridges. The structures of the $[Cu(HCOO)_3]^-$ and Gua^+ units are shown in Fig. 5.1 (e). The crystal of CuGF has an orthorhombic structure with the lattice parameters a = 8.5212(3) Å, b = 9.0321(3) Å and c = 11.3497(4) Å [17], as shown in Fig. 5.1 (a) and (b).

The copper ions in the system are connected with six neighbouring metals via the

Cu-O bonds and the oxygen octahedra are connected by the formate. As the Cu^{2+} here is a Jahn-Teller ion, it shows 2+2+2 stretched octahedral geometry, as shown in Fig. 5.1 (d). There are two short Cu-O bonds with a length of 1.97 Å and 1.99 Å, two medium bonds with lengths of 2.01 Å and 2.02 Å and two long Cu-O bonds with lengths of 2.37 Å and 2.39 Å, respectively [54]. Therefore, along the Cu-OCHO-Cu chains connected by short Cu-O bonds, as shown in Fig. 5.1 (c), the distance between the nearest cooper ions is shorter than those on the other two directions. The interchain Cu-Cu distance is 5.679 Å and the intrachain ones are 6.199 Å and 6.219 Å [17]. As a consequence, the exchange energy along these copper chains is much larger than the exchange energy between the chains.

The adjacent oxygen octahedra in CuGF are tilted and are not centrosymmetric, as shown in Fig. 5.1 (b). Hence, Dzyaloshinsky-Moriya interactions or antisymmetric exchange interactions exist in this system, which give rise to the canting of the spins in CuGF. The canting angle is 0.21° [17].

5.3 Experimental Details

In this work, powder samples were needed for the AC and DC magnetometry measurements and single crystal samples were prepared for both magnetometry and μSR measurements. The samples were synthesized with the slow solution evaporation method at room temperature. During the synthesis process, an aqueous solution (8 mL) containing formic acid (5.0 mmol), $[C(NH_2)_3]_2CO_3$ (2.1 mmol), and Cu-$(NO_3)_2{\cdot}6H_2O$ (0.40 mmol) was slowly evaporated. Blue crystals were harvested after four days. The synthesis details can be found in Ref. [17]. All the powder sample was synthesized by Prof. Zheming Wang at Peking University and the single crystals of CuGF were synthesized by Dr. Anthony. E. Phillips and Mr. Viswanathan Mohandoss at Queen Mary, University of London.

All the DC and AC measurements in Ref. [17] were performed on the powder and

single crystal samples. In μSR measurements, zero-field condition was employed for the magnetisation study longitudinal and transverse field measurements were carried out to investigate dynamics and field dependent properties in CuGF. The μSR measurements with applied electrical fields were also carried out to study the multiferroic properties of the sample.

DC and AC susceptibility were measured using a SQUID and the ACMS of a PPMS, respectively. Before measuring the polycrystalline sample, CuGF powder was finely ground before being loaded into the sample holder. For the single crystal sample, the alignment of the crystal orientation and the field direction of the equipment was checked carefully to make the *c*-axis of the sample aligned with the direction of the applied field before loading the sample. All measured samples were wrapped in paraffin films (diamagnetic, light and stretchable films giving low background and can seal samples firmly by stretching the films) to keep them sealed and fixed in a capsule. The capsule was then loaded into the centre of the sample stick, which was then placed to the SQUID or PPMS chamber. All the diamagnetic materials used in this process were measured individually before the experiments as background signals ($\chi_{capsule}$ = 1.8×10^{-8} emu/Oe and $\chi_{paraffin}$=6.47×10^{-10} emu/Oe/mg).

In μSR measurements, CuGF single crystals with the dimensions 5 mm $\times$ 3 mm $\times$ 1 mm each were carefully aligned into a crystal array and attached to a silver plate with the *c*-axis pointing out of the plate. The geometry was chosen such that the electric field is aligned with the magnetic easy axis in the experiments to investigate the multiferroic properties. The crystal array had an area of 25 mm $\times$ 25 mm and was big enough for μSR experiments. The silver plate, together with the crystal array was attached to the sample stick and loaded into a cryostat before the measurements. All the μSR data was analysed using the WIMDA program [197].

5.4 Magnetism in CuGF

CuGF is expected to have low-dimensional magnetic chains, which were indeed observed. A DC magnetic investigation on the powder sample was investigated by Gao's group in 2009 [17]. It was found that CuGF had spin-canted three dimensional antiferromagnetism below the Néel temperature of 4.6 K and showed the feature of one-dimensional antiferromagnetism above 4.6 K until about 100 K.

Moreover, a very narrow "hysteresis loop" was observed indicating possible magnetic ordering below 4.6 K [17]. The magnetisation increases sharply to 25 cm^3Gmol^{-1} at about 50 Oe. The continued increase of the magnetisation slows down and is nearly linear above 4 kOe. Below 20 Oe, the sharply increasing region is claimed to show a magnetic hysteresis loop [17]. However, the "hysteresis loop" follows an opposite route as it should be. Since the coercive field is very small ($\sim$ 7 Oe) and the magnet used for the measurement may not be capable to control such a small field and to measure the hysteresis loop precisely. Details of their research can be found in Ref. [17].

In this section, the magnetic properties and low-dimensional magnetism investigated with magnetometry and the μSR technique will be discussed. In particular, μSR, working as a local probe shows great power to study the magnetic phase transition and one-dimensional magnetism in this multiferroic MOF.

5.4.1 Three dimensional long-range magnetic order

Our magnetisation measurements on the single crystalline and polycrystalline samples also confirm that CuGF has a spin-canted antiferromagnetic order below 4.6 K. The FC/ZFC magnetisation data based on a polycrystalline sample (shown in Fig. 5.2 (a)) has a small bifurcation below 4.6 K and a spontaneous magnetisation of 25 cm^3Gmol^{-1} is observed. These results are consistent with the reported ones in Ref. [17]. The Néel temperature was determined to be 4.60 $\pm$ 0.02 K by determining the negative peak position of dM_{FC}/dT in the FC data. The susceptibility under 5 kOe was measured

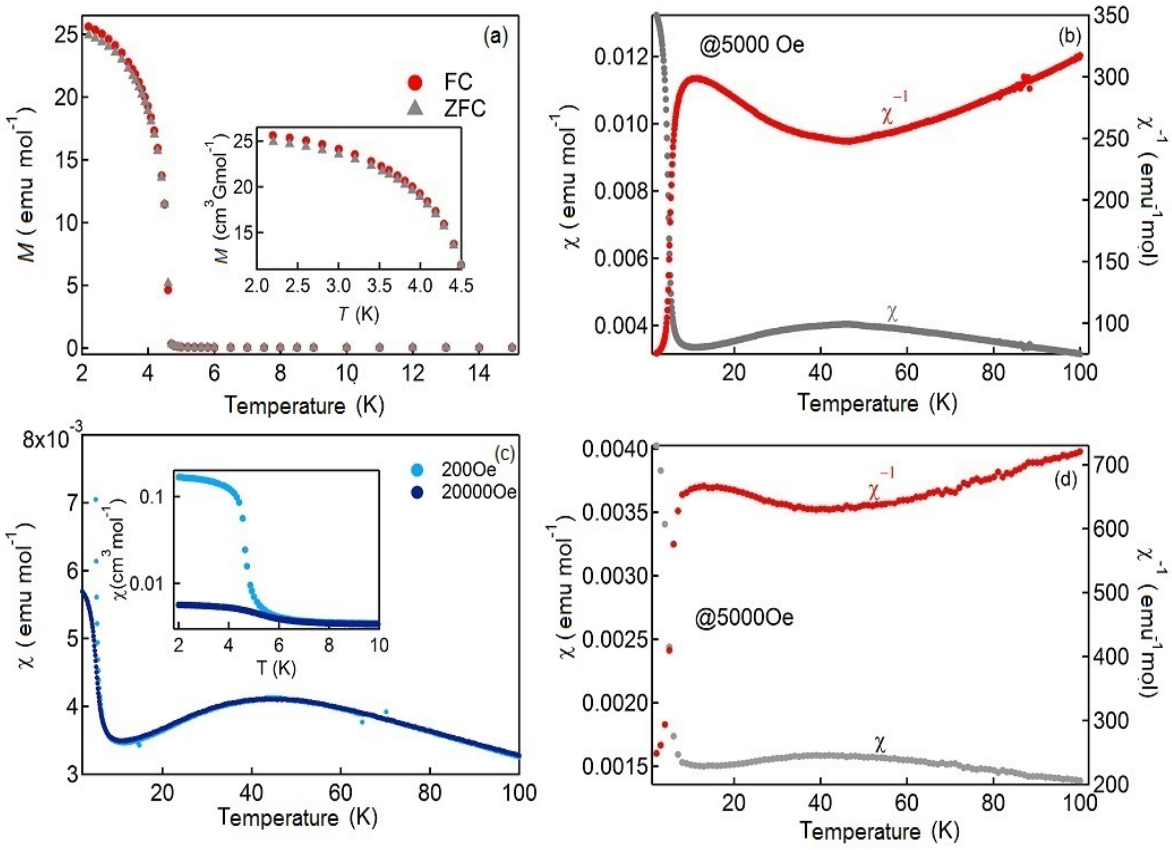

Figure 5.2: (a) The FC/ZFC magnetisation measurement of polycrystalline CuGF with an applied field $H = 10$ Oe. The inset shows details of the FC/ZFC data below 4.5 K. (b) χ and $1/\chi$ of the CuGF polycrystalline sample with an applied field $H = 5000$ Oe. (c) The magnetic susceptibility of polycrystalline CuGF with $H = 200$ Oe and 20000 Oe. The inset gives details of the susceptibility data below 10 K. (d) χ and $1/\chi$ of the CuGF single crystal with an applied field $H = 5000$ Oe, which is parallel to the c-axis of the crystal.

on the single crystalline (Fig. 5.2 (d)) and polycrystalline samples (Fig. 5.2 (b)). The DC susceptibility exhibits a steep increase below 6 K following by a broad peak around 45 K, which is a signature of the one-dimensional magnetism and will be discussed in the next section. The rapid increase of the susceptibility during cooling and the small bifurcation below 4.6 K indicate that antiferromagnetic CuGF has a spin-canted structure.

The susceptibility in the spin-canted antiferromagnetic CuGF, which looks like the

susceptibility of a ferromagnetic material, has three contributions:

$$\chi_{measured} = \chi_{AFM} + \chi_{chain} + \frac{M_{canted}}{H}. \tag{5.1}$$

As a result of the canted spins, ferrimagnetic sublattices exist in CuGF below the transition temperature. Therefore, the measured susceptibility has a contribution from the magnetisation owing to the canted moments (M_{canted}). The χ_{AFM} and χ_{chain} contributions arise from the antiferromagnetic order and the one-dimensional chain in the system, respectively. The susceptibility measurements of the polycrystalline (Fig. 5.2 (b)) and single crystal (Fig. 5.2 (d)) CuGF show the contributions from the spin-canting and low-dimensional terms. They have very similar features but the absolute values of χ in these two measurements were slightly different because the diamagnetic contribution in the measurement of the single crystal sample was likely not done properly. The diamagnetic contribution is complicated as too much paraffin film was used to secure and fix the small crystal in the measurement. In the polycrystalline and single crystal samples, the susceptibility χ increases sharply below the Néel temperature during cooling thereby representing the contribution from the magnetisation due to canted spins. A broad peak in the χ data at about 45 K and the non-paramagnetic $1/\chi$ behaviour ($1/\chi$ vs. T should be a straight line according to the Curie-Weiss law $\chi \sim \frac{C}{T-\theta}$, where C is the Curie constant and θ is the Weiss constant) indicate a low-dimensional magnetic contribution to the measured susceptibility above the Néel temperature. When a higher magnetic field is applied, as shown in Fig. 5.2 (c), the magnetic susceptibility is suppressed. The canted spins are aligned and saturated in a large magnetic fields. This behaviour was also reported in other spin-canted systems [198].

μSR experiments also confirm the three dimensional long-range magnetic order at low temperatures. Typical μSR spectra below the Néel temperature are shown in Fig. 5.3 (a) and (b). It is clear that a muon oscillation is observed below 4.6 K. The oscillatory signal owing to the muon precession around the local magnetic field is a clear

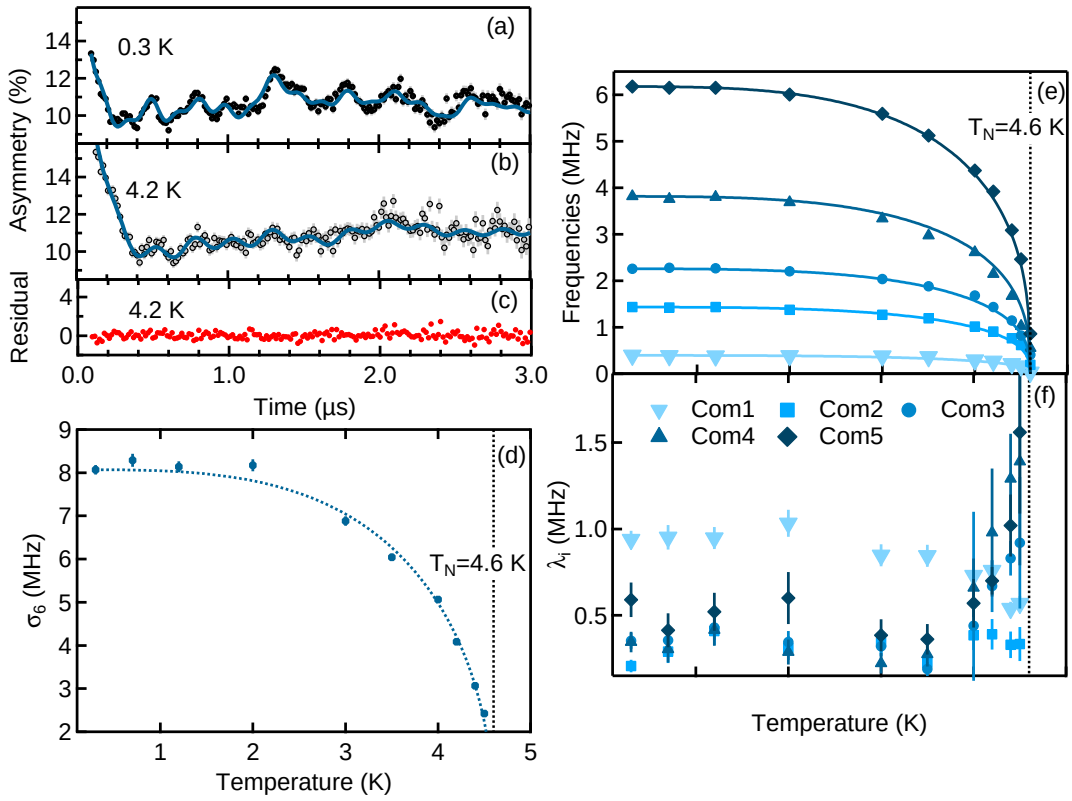

Figure 5.3: (a) The μSR spectrum at 300 mK: the grey symbols are the raw data and the blue curve is the fit with a χ^2 of 1.108. (b) The μSR spectra at 4.2 K, below the Néel temperature (4.6 K). (c) The residual of the 4.2 K data. (d) The relaxation rate as a function of temperature of the sixth relaxation term. (e) The frequencies of the five oscillations as a function of temperature. The critical behaviour is fitted with a power law and the fit is shown by the solid curves with a χ^2 of 1.256. (f) The relaxation rates of the five relaxed oscillations below the Néel temperature.

sign of the long-range magnetic order in CuGF. The oscillation, however, is in a very complicated form. The Fourier transform of the spectrum at the lowest temperature is calculated. There are four obvious peaks and one tiny peak in the frequency domain, as shown in Fig. 5.4. Some peaks in the frequency domain are not very obvious as they are suppressed by the relaxation signal (frequency = 0 MHz). The data were then fitted with five damped oscillations and a Gaussian relaxation below the Néel temperature:

$$A(t) = A_F[\sum_{i=1}^{n=5} P_i \exp(-\lambda_i t)\cos(2\pi f_i t + \varphi_i) + P_6 \exp(-(\sigma_6 t)^2)] + A_G \exp(-\lambda_G t) + A_{BG}, \tag{5.2}$$

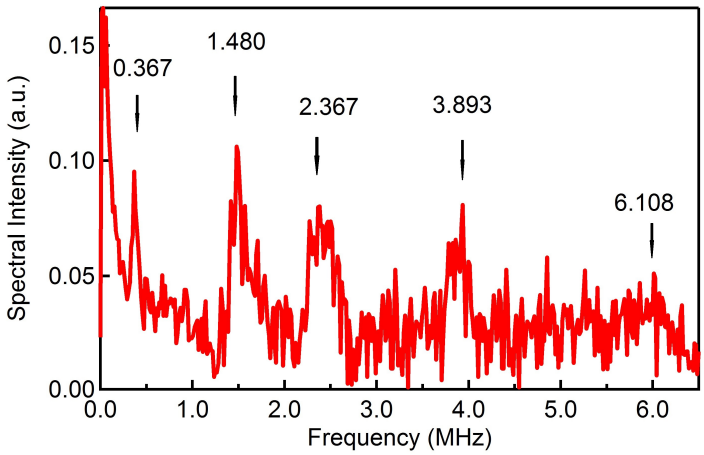

Figure 5.4: The Fourier transform of the spectrum measured at 0.3 K.

where A_F, A_G and A_{BG} are the asymmetries of the muons sitting near the formate, the guanidinium and from the background, respectively. P_i, f_i, λ_i and φ_i are the proportion, frequency, exponential relaxation rate and phase of the muon oscillation at the ith site. σ_6 is the Gaussian relaxation rate of the sixth relaxation term. λ_G is the relaxation rate of the muons sitting near the guanidinium. During the data analysis, all the parameters were independent variable fit parameters at the lowest temperature (0.3 K). The quality of the least square fitting is measured by the normalised square deviation χ^2. By adjusting the initial values of the parameters, the fit was improved and χ^2 of the fit was reduced to be close to 1 (it varied from 1.055 to 1.231 below the Néel temperature), which indicates a good fit. A residual analysis was done one the 4.2 K data to show the quality of the data fitting, as shown in Fig. 5.3 (c). The parameters P_i, A_F, A_G, A_{BG} and φ_i were kept fixed and only λ_i, f_i, σ_6 and λ_G were fitted at other temperatures. Details of the fit parameters are shown in Table 5.1.

The first five terms in Eq. 5.2 are the sum of the five damped oscillations. The oscillation frequencies of these oscillatory terms are shown in Fig. 5.3 (e). It is worth mentioning that among the five oscillations, those with frequencies above 1 MHz are of a very small proportion and the 0.4 MHz oscillation has P_1 that is much higher than the rest of the oscillations' P_is. This means that the low 0.4 MHz one is the dominant

Table 5.1: Details of the fit parameters. P_i, A_F, A_G, A_{BG}, f_i and φ_i are parameters from the fitting function Eq. 5.2.

Components	Values	f_i(0.3K) (MHz)	φ_i
P_1	13.0(± 0.43)%	0.396 (± 0.0067)	111.1 (± 2.5)
P_2	4.1(± 0.28)%	1.435 (± 0.0062)	23.9 (± 1.4)
P_3	4.9(± 0.32)%	2.259 (± 0.0073)	14.1 (± 1.5)
P_4	3.7(± 0.29)%	3.815 (± 0.0091)	397.0 (± 3.7)
P_5	3.8(± 0.38)%	6.177 (± 0.0921)	337.3 (± 4.2)
P_6	70.5%	N/A	N/A
A_F $(\sum_{i=1}^{n=6} A_i)$	11.506 (± 0.021)	N/A	N/A
A_G	11.061 (± 0.022)	N/A	N/A
A_{BG}	0.005 (± 0.0008)	N/A	N/A

oscillation. The sixth term is a Gaussian relaxation term coming from the muons sitting at a site where the relaxation rate is high. This high relaxation rate indicates a slow spin fluctuation. The relaxation mechanism may be of a quasi-static nature. In this case, this Gaussian relaxation probably comes from muons sensing an internal field instead of dynamics in the system. They may sit very close to the copper ions where the internal field is too large for muons to precess. When a large longitudinal field is applied, this Gaussian relaxation is quenched. This confirms that the sixth component has a static nature and describes muons sensing an internal magnetic field. A_G has two possible sources: 1. the signal comes from muons located far away from the copper ions so that they can only sense the dynamics in the system; 2. the signal from muons with spins aligned parallel to the internal fields, then only the dynamics from them can be sensed by the muons. These two dynamic sources result in an exponential relaxation with a relaxation rate of λ_G (Fig. 5.3 (d)). A_{BG} is a temperature and field independent term, which comes from muons stopping in the silver sample holder and cryostat around the sample. The background signal is very small ($A_{BG} = 0.5\%$) in the measurement.

Dr. Anthony E. Phillips performed a DFT+μ calculation to calculate the possible muon sites in CuGF. His result shows that there are six muon sites near the formate and several muon sites near guanidinium which are far away from the copper ions. Among

the six sites near the formate, one is particularly close to the copper ions. This indicates that the five oscillating components corresponds to the precessions from muons sitting near the formate and the sixth Gaussian relaxation comes from muons sitting very close to the copper ions. The A_G term, as discussed, comes from muons far away from the copper ions (probably locate near the guanidinium) or sensing a internal magnetic field that is parallel to their spins. According to the fitting, as shown in Table 5.1, about 51% (A_F) of the implanted muons sit near the formate and about 49% (A_G) of the muons sit near the guanidinium.

The five oscillation frequencies corresponding to muons stopped in at least five different sites with different internal magnetic fields are fitted with the power law:

$$f_i(T) = f_i(0.3\text{K}) \left(1 - \left(\frac{T}{T_N}\right)^n\right)^\beta , \tag{5.3}$$

where β is the critical exponent describing the critical behaviour of the magnetisation near the phase transition temperature and n is a factor that modifies the fit at low temperatures (not close to the transition temperature). β was globally fitted in all of the five oscillations and has a value of 0.365 ± 0.038 with $n = 3.287 \pm 0.321$. The fit is shown in Fig. 5.3 (e). Details of critical behaviour will be discussed in the next section.

The longitudinal field measurements also confirm that the sixth Gaussian relaxation term comes from muons sensing a quasi-static magnetic moment in the sample. Representative spectra at 2.5 K with different applied LFs are shown in Fig. 5.5 (a). All five oscillations and the Gaussian relaxation can be quenched when LF $>$ 1000 Oe. The muon polarisation recovers with increasing LF, as shown in Fig. 5.5 (b). This suggests that the muons can be totally decoupled from the magnetism in the sample at LF $>$ 750 Oe below the Néel temperature. As spin dynamics cannot be quenched by a longitudinal field, this result rules out the possibility that the Gaussian relaxation comes from a dynamic nature.

As muons are local probes sensitive to the local magnetic field, they provide a

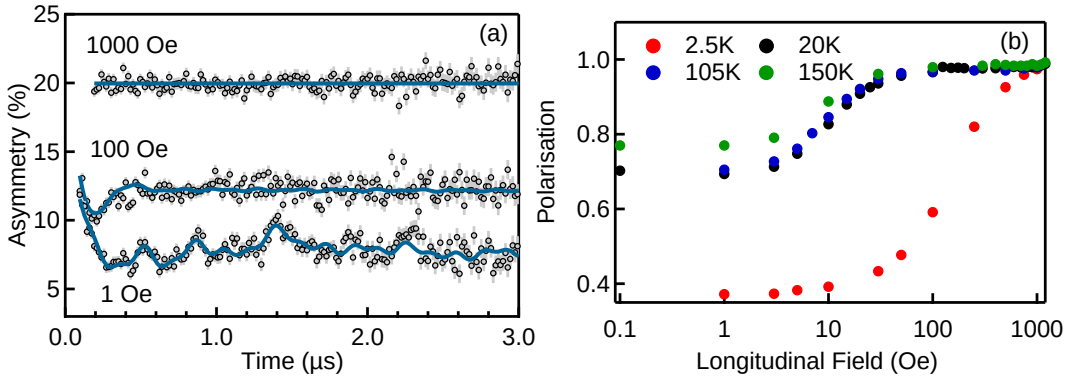

Figure 5.5: (a) The LF μSR spectra at 2.5 K for different applied longitudinal fields: the grey symbols correspond to the raw data, the blue curves are the fit (χ^2 = 1.081 (1 Oe), 1.184 (100 Oe), 1.016 (1000Oe)), showing that all five oscillations and the sixth relaxation term can be quenched under a high LF field. (b) Muon polarisation as a function of the applied longitudinal field. The muon polarisation is completely decoupled from the internal magnetic field at about 750 Oe.

powerful tool to study dynamics in magnetic materials. The longitudinal muon spin relaxation in ZF measurement offers information about spin dynamics at the muon sites. The fit parameters λ_is from Eq. 5.2 are shown in Fig. 5.3 (f). λ_3, λ_4 and λ_5 exhibit a divergent behaviour at the Néel temperature, which describes critical fluctuations at the critical temperature [152]. However, λ_1 follows the opposite trend compared with λ_3, λ_4 and λ_5. λ_1 decrease when it approaches T_N from low temperatures. This phenomenon has also been observed before in Ref. [199–201], where the muon spin relaxation may be governed by the change of the magnetic field width Δ at the corresponding muon site. A similar phenomenon is also observed in this work at high temperatures, as shown in Fig. 5.10 (e). Above the Néel temperature, the fast exponential relaxing component, which describes muons sensing a randomly oriented local magnetic field, follows exactly the same trend as the internal magnetic field width Δ. This indicates that λ_1, which describes the dynamics of the muon site that is far away from the Cu chain, is less sensitive to the critical fluctuations of the system than the relaxation parameters λ_3, λ_4 and λ_5.

The TF measurements provide information about the phase transition that is men-

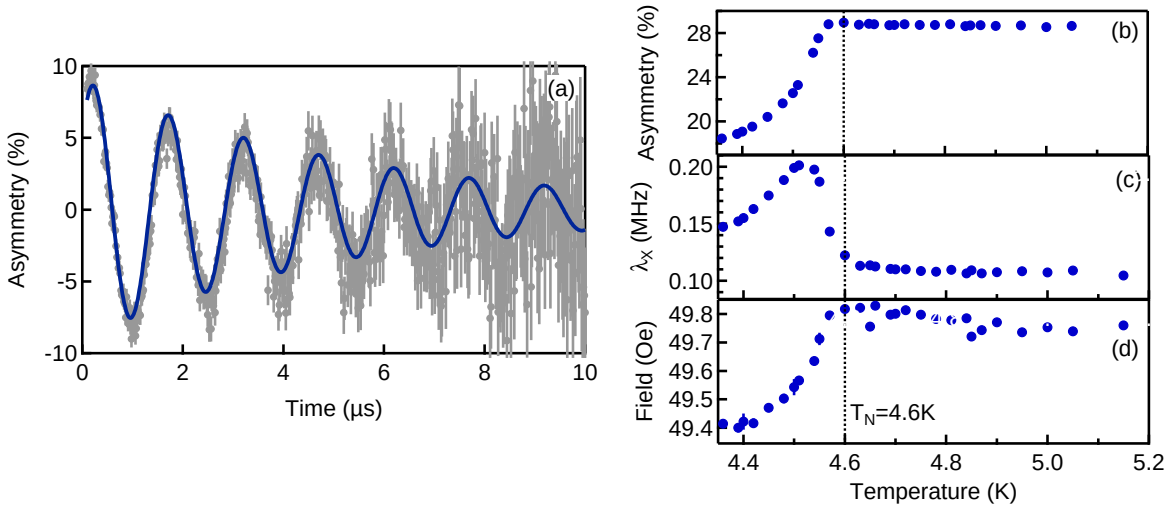

Figure 5.6: The transverse field (50 Oe) muon spin rotation measurement also exhibits a phase transition at 4.55 K. (a) The TF μSR spectrum at 4.3 K, where the grey symbols are the measured data and the blue line is the fit ($\chi^2 = 1.205$). (b) The total muon spin asymmetry decreases with the temperature decreasing below the Néel temperature. (c) The relaxation rate shifts as a function of temperature. (d) The measured field shifts as the temperature goes up.

tioned above and dynamics. A typical TF spectrum is shown in Fig. 5.6 (a). With an applied external TF field, the spectra can be described by a damped oscillation and can be fitted with:

$$A_X(t) = A_X \exp\left(-\lambda_X t\right) \cos\left(\gamma_\mu B t\right), \tag{5.4}$$

where λ_X is the relaxation rate of the oscillating envelope. The fit parameters, including the total asymmetry A_X, the transverse relaxation rate λ_X and the internal field B are shown in Fig. 5.6. The relaxation rate provides information about the spin dynamics in the measured system. Small anomalies are shown in all these parameters at 4.6 K, which indicates a magnetic phase transition at this temperature.

According Ref. [202],

$$\lambda_X = \Delta^2/v, \tag{5.5}$$

λ_X describes the spin fluctuation of the whole system. It can be seen from T is just above the critical temperature, Δ shows little variation with temperature, as shown in

Table 5.2: Theoretical and experimental values of critical exponents β, ν and γ.

Exponents	Quantities described	Techniques	CuGF	3D Heisenberg
β	Magnetisation	μSR ZF	0.365 ($\pm$ 0.038)	0.36
		DC Magnetometer	0.353 ($\pm$ 0.018)	
ν'	Correlation length	μSR ZF dynamics	0.574 ($\pm$ 0.016)	0.70
γ	Susceptibility	μSR TF shift	0	1.39
		DC susceptibility	0.680 ($\pm$ 0.012)	
γ'	Susceptibility	μSR TF shift	-0.639 ($\pm$ 0.068)	1.39
		DC susceptibility	-0.453 ($\pm$ 0.021)	

Fig. 5.10 (e). According to Eq. 5.5, the critical fluctuation decreases sharply as λ_X goes up dramatically when approaching the critical temperature from high temperatures, as shown in Fig. 5.6(c). Thus, the transverse relaxation rate λ_X also describes the critical fluctuation in CuGF.

5.4.2 Critical exponents

In order to understand more about the critical behaviour in CuGF, the critical exponents β, γ and ν of the system were attempted to be investigated by magnetometry and μSR measurements. However, there are two challenges that render this study difficult but important - 1. Due to the 1D chain in the system, the phase transition might be different from a typical paramagnetic-antiferromagnetic transition; 2. Canted spins complicate the measurement of the antiferromagnetic susceptibility and it may be challenging to obtain the value of the exponent γ. In this section, the bulk magnetisation measurements and local μSR measurements are combined in a hope that more information about the critical behaviour of this complicated system can be obtained. This is helpful to understand the magnetism in CuGF.

As discussed in Section 3.1.4, the net magnetisation and antiferromagnetic suscepti-

bility, which are macroscopic, cannot describe the order parameter and its susceptibility in an antiferromagnet. Therefore, the critical behaviour of an antiferromagnet cannot be investigated by simply measuring the net magnetisation and magnetic susceptibility with a magnetometer. However, in CuGF, which is a spin-canted antiferromagnet, there is more than one order parameter to describe the magnetic transition at 4.6 K - the staggered magnetisation (defined in Eq. 3.40) and the magnetisation resulting from the canted moments. The measured net magnetisation originates from the canted moments and can therefore be used to describe the critical behaviour of the order parameter. Thus, the critical exponent β can be investigated with the magnetisation measurement. In terms of the exponent γ, the magnetic susceptibility measured with a DC magnetometer is a combination of three factors: 3D antiferromagnetic susceptibility, 1D antiferromagnetic susceptibility and magnetisation from the canted moments [198]. None of these contributions can describe the order parameter susceptibility (staggered susceptibility and magnetic susceptibility owing to the canted moment). Therefore, the susceptibility measured by a magnetometer cannot be used to determine the exponent γ.

However, the μSR technique is sensitive to the local magnetisation [143] and can give information about the behaviour of the order parameter and its susceptibility around the magnetic transition [151], as discussed in Section 3.1.4. By measuring the local magnetic moment at a specific (or several specific) site(s) in the material, the staggered magnetisation in an antiferromagnet can be investigated. The internal field measured by muons drops when it approaches the critical temperature, as a result of the order parameter [143]. This is just like the internal field of a ferromagnet, which results in a net magnetisation, decreases as temperature increases to its Curie temperature. Moreover, the local susceptibility of CuGF measured by μSR contains the contributions from the staggered susceptibility and the magnetisation resulting from the canted moments. The second term will complete the analysis of the exponent γ.

Critical exponents of different magnetic systems were investigated by the μSR tech-

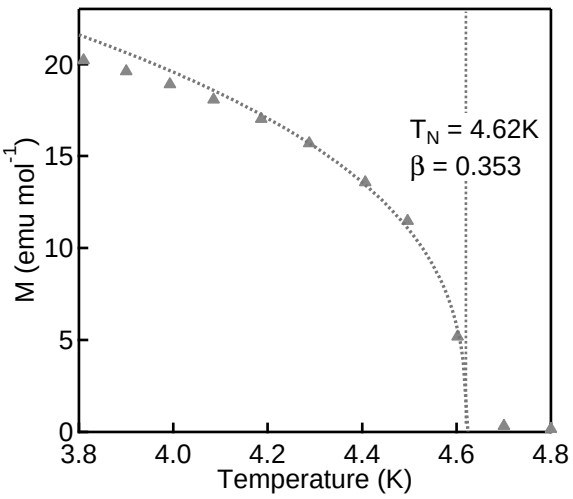

Figure 5.7: The critical exponent β obtained from fits to the magnetisation data (4.2 K to 4.6 K) measured using a SQUID. The fit has the quality $\chi^2 = 1.075$ and $\beta = 0.353$.

nique [151, 152]. The critical exponent β, which describes how order parameters vary with temperature near the critical point, is obtained using zero-field μSR measurements. Without any applied field, muon procession comes purely from the internal magnetic field, which correlates with the order parameter by $B \sim \Phi$. Thus, the muon precession frequency under zero field, which is a measure of the internal field, can be used to study the exponent β using $B \sim \Phi \sim (\frac{T_N - T}{T_N})^{-\beta}$ [151]. By global fitting five muon precession frequencies as a function of temperature near the critical point with the power law above, β was fitted to be 0.365 ± 0.038, as shown in Fig. 5.3 (e).

In CuGF, the net magnetisation is a measure of the magnetisation from the canted moments. Therefore, the exponent β can be obtained from magnetisation data directly. Similar to the μSR data, the magnetisation as a function of temperature is fitted according to the power law $M \sim (\frac{T_N - T}{T_N})^{-\beta}$ [151]. Fig. 5.7 shows the magnetisation near the Néel temperature and fitting provides a β of 0.353 ± 0.018, which is in good agreement with the value obtained from the μSR data. Taking $\beta = 0.36$ from a 3D Heisenberg model, β values obtained from the ZF μSR and magnetisation measurements confirm that CuGF is a 3D Heisenberg antiferromagnet below $T_N = 4.6$ K.

γ describes the behaviour of the susceptibility near the transition temperature.

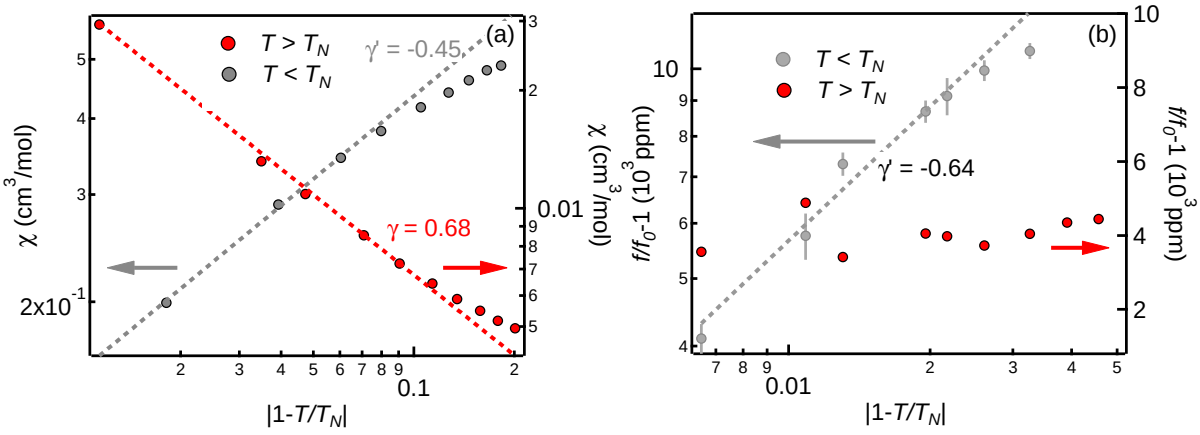

Figure 5.8: (a) The critical exponent γ obtained from fits to the the DC magnetic susceptibility data (4.2 K to 4.6 K) measured under a 50 Oe applied field (fit quality $\chi^2 = 0.998$ (γ), 1.001 (γ')). (b) The critical exponent γ determined by fitting the μSR data (4.2 K to 4.6 K) with an applied 50 Oe transverse field ($\chi^2 = 1.048$). γ and γ' from both techniques are found to have different signs and the values do not agree with the theory.

Even though neither the DC magnetic susceptibility nor the local susceptibility from the μSR measurement can describe the susceptibility of the order parameter of CuGF, γ is attempted to be estimated using these measurements. This could provide some extra information about the magnetism in the system.

By applying a reasonable transverse field, the local susceptibility can be measured using $\chi \sim \left|\frac{\vec{B}}{\vec{H}} - 1\right|$. In TF measurements, B, which is the magnetic induction, can be measured by the muon procession frequency $f(T)$ at any given temperature T. The applied magnetic field H can be represented by its correlated procession frequency $f(0)$. Hence, γ can be described by the field shift employing $\chi \sim \left|\frac{\vec{B}}{\vec{H}} - 1\right| \sim \left|\frac{f(T)}{f(0)} - 1\right|$ $\sim (\frac{T}{T_N}\text{-}1)^{-\gamma}$ [151]. The change of the internal field is measured and shown in Fig. 5.6 (c). The field shift in the transverse field muon spin rotation measurements, $\frac{f(T)}{f(0)}$-1 vs. $\left|(\frac{T}{T_N} - 1)\right|$, is plotted in Fig. 5.8 (b). Using fitting, γ' = -0.639 $\pm$ 0.068 was obtained and γ is nearly zero. These values are significantly different from the theoretical value of any three dimensional magnetic models.

The critical component γ is also fitted directly using the temperature dependent

magnetic susceptibility data, as shown in Fig. 5.8 (a). According to the power law, γ was determined with fitting and is 0.680 $\pm$ 0.012 and γ' is -0.453 $\pm$0.021, accordingly. These values are not in agreement with the 3D Heisenberg antiferromagnetic model.

It is not surprising that the critical exponent γ obtained by fitting the magnetic susceptibility data or μSR data of CuGF is not consistent with the exponent γ of a pure 3D Heisenberg antiferromagnet. Below the critical temperature, the magnetisation resulting from the canted moments, which vanishes when reaching the critical point from low temperatures, makes a big contribution, so a negative γ' was obtained. γ, which is the exponent describing susceptibility above the critical temperature, is much smaller than the theoretical value of the 3D Heisenberg model ($\gamma = \gamma' = 1.39$). This can be explained by the contribution from the one-dimensional magnetic chain. Due to the existence of 1D magnetic correlations, in which case the entropy in the system is released gradually, the magnetic susceptibility would change less dramatically during the phase transition which means that γ should have a smaller value. It is worth mentioning that values of the exponents γ and γ' are not identical using different techniques. This is because the susceptibilities measured by the magnetometry and μSR technique was different. The local probe (μSR) has a better sensitivity to low-dimensional and local magnetism in CuGF.

Exponent ν is measured with zero-field spin fluctuations because the relaxation rate λ_i is a measure of the correlation time τ and $\tau \sim (\frac{T-T_N}{T})^{-\nu}$ [151]. As previously mentioned, λ_3, λ_4 and λ_5 all describe the critical fluctuations near the transition temperature. The dynamics of the oscillation with a largest frequency is studied as an example and the result is shown in Fig. 5.9. The critical exponent ν was obtained by fitting: $\nu = 0.574$ ($\pm$ 0.016). This is smaller than the theoretical value of a 3D Heisenberg antiferromagnet. A possible explanation may be that the muon spin relaxation rate λ can also be affected by the change of local field width. Therefore, the measurement of ν may be influenced by this factor. It is also important to mention here that due to the complexity of the six-term μSR model and the small proportions of the oscillatory

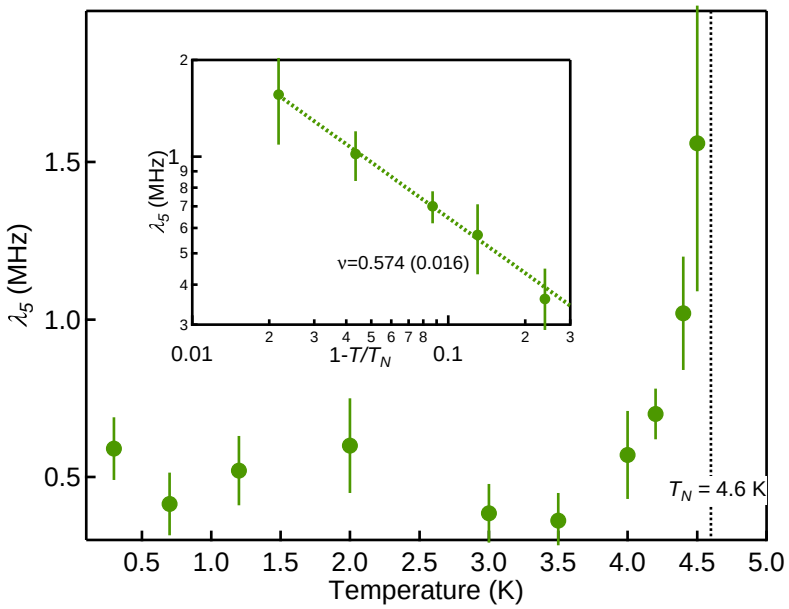

Figure 5.9: The dynamic muon spin relaxation critical behaviour of f_5. The relaxation rate as a function of temperature clearly diverges at the Néel temperature. The inset shows the fitting of the dynamic critical exponent ν, which is fitted to be 0.574 ($\pm$ 0.016) with a fit quality $\chi^2 = 0.988$.

terms out of total implanted muons, the fitted λ_i may not be sufficiently accurate for a precise analysis of the critical exponent ν.

All theoretical and experimental values of the critical exponents are summarised in Table 5.2. The exponent β matches the theoretical value of a 3D Heisenberg antiferromagnet. γ of the spin-canted antiferromagnetic system using the magnetometry and μSR measurement is different from the 3D Heisenberg antiferromagnetic model. Below the Néel temperature, the strong influence from the ferrimagnetism originating from canted spins renders γ a negative value, while above the Néel temperature, the existence of a 1D magnetic chain alters the susceptibility of CuGF from a typical paramagnet. Exponent ν derived from the ZF μSR data is slightly smaller than the theoretical value because the μSR technique measures not only critical fluctuations but also other dynamics in the system. Even though these critical exponents are not consistent with the phase transition theory, they are helpful to understand the magnetism and to obtain more details of the μSR measurements on CuGF.

5.4.3 One-dimensional magnetism in CuGF

Along the *c*-axis of the CuGF crystal, the copper ions are connected via two short Cu-O bonds while in the other two dimensions the copper ions are connected via longer Cu-O bonds. This makes the exchange energy along the copper chains linked via short bonds much stronger than between these chains [17]. Therefore, CuGF shows one-dimensional magnetism and the 1D magnetic chains are along the *c*-axis of the crystal.

The DC susceptibility measurement, as shown in Fig. 5.2, confirms the low-dimensional magnetic correlation in CuGF. Apart from the sharp increase at low temperatures, which corresponds to the 3D spin canted antiferromagnetic order below the Néel temperature, there is a broad peak at about 45 K. This broad peak is a signature of the one-dimensional antiferromagnetism. According to the Bonner and Fisher's model of a 1D Heisenberg antiferromagnetic chain [73], the interchain and intrachain exchange energy were fitted as described in Ref. [17] using this model's numerical solution and modification [80, 81]:

$$\chi_{chain} = \frac{Ng^2\mu_B^2}{k_BT}\frac{0.25 + 0.074975x + 0.075235x^2}{1.0 + 0.9931x + 0.172135x^2 + 0.757825x^3}, \tag{5.6}$$

with

$$x = \frac{|J|}{k_BT}, \tag{5.7}$$

and the interchain exchange energy is modified as follows [81]:

$$\chi = \frac{\chi_{chain}}{1 - \frac{2zJ'}{Ng^2\mu_B^2}\chi_{chain}}. \tag{5.8}$$

In CuGF, the copper ions have four neighbours, so z = 4. The best fit parameters are g = 2.421 ± 0.003, J = -47.3 ± 0.1 cm^{-1} and J' = -5.7 ± 0.2 cm^{-1} [17]. Here, the interchain interaction is much stronger than the intrachain interaction confirming that CuGF indeed has a one-dimensional magnetic correlation.

Above the Néel temperature, μSR measurements were carried out to investigate

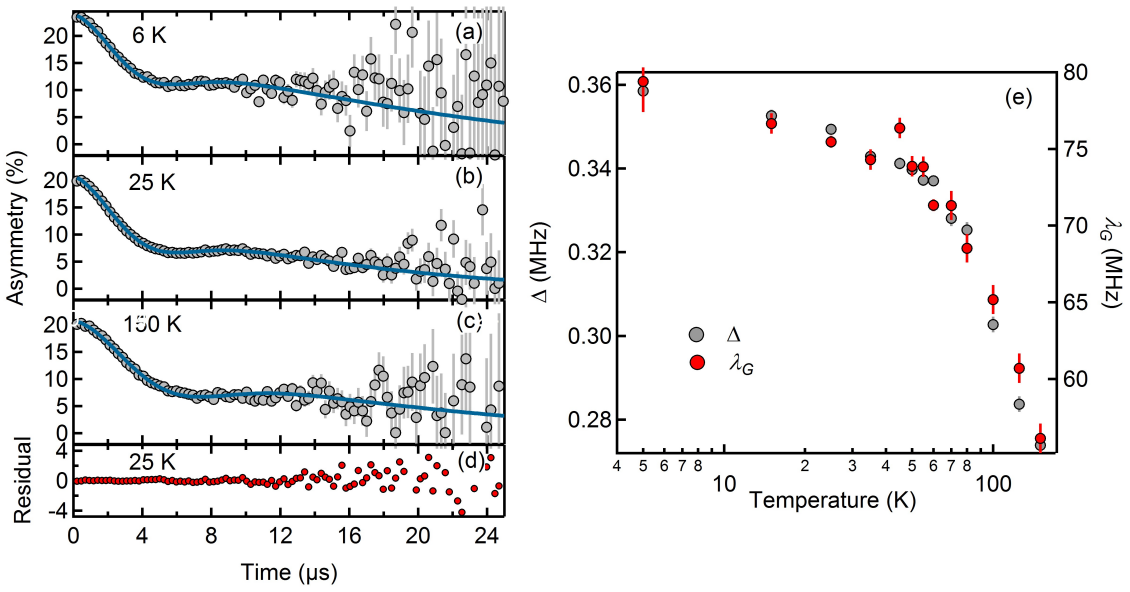

Figure 5.10: The ZF μSR spectra at (a) 6 K, (b) 25 K and (c) 150 K. A static Kubo-Toyabe function and an exponential relaxation are fitted to the data ($\chi^2 = 1.091$ (6 K), 1.115 (25K), 1.351 (150K)). The raw data and the fitting are shown by the grey symbols and blue curves, respectively. (d) The residual analysis on a typical μSR data above the Néel temperature (25 K). (e) The width of the dipole field distribution Δ and the relaxation rate λ_G as a function of temperature ($T > T_N$).

the low-dimensional magnetism in CuGF. As a local probe, muons are probably more sensitive to the short-range correlations resulting from the 1D magnetic chain. The data (the spectra are shown in Fig. 5.10 (a), (b) and (c)) was initially fitted with a static Kubo-Toyabe function and an exponential relaxation term:

$$A(t) = A_F \left(\frac{1}{3} + \frac{2}{3} \left(1 - \gamma_\mu^2 \Delta^2 t^2\right) \exp\left(-\frac{\gamma_\mu^2 \Delta^2 t^2}{2}\right)\right) + A_G \exp(-\lambda_G t) + A_{BG}, \tag{5.9}$$

where the first term is the Kubo-Toyabe function with a local field characterised by Δ and the second term is the exponential relaxation term with a relaxation rate of λ_G. A residual analysis was performed and shows in Fig. 5.10 (d). It has reasonable good fit quality within 20 μs and the residual becomes larger as the measurement errors increase after 20 μs. The Kubo-Toyabe function is a typical polarisation function for disordered

spins. When $T > T_N$, the nuclear spins in the system are randomly orientated so that muons will relax in agreement with a Kubo-Toyabe polarisation function. During the data fitting, A_F, A_G and A_{BG} were kept fixed and only the field variance $\Delta = \sqrt{\langle B^2 \rangle - \langle B \rangle^2}$ and the relaxation rate λ_G are allowed to vary. It is found that the ratio $A_F : A_G = 51 : 49$ is the same above and below the Néel temperature. This suggests that all the implanted muons still sit in the same positions as they did below the Néel temperature. Considering the muon sites, muons sitting near formate sense the randomly oriented nuclear moments having a Kubo-Toyabe relaxation function and muons sitting near guanidinium still sense dynamics in the system.

The Kubo-Toyabe function is valid only in the case that the magnetic moments within the material are randomly oriented and there is no long-range magnetic order in the system. However, the temperature dependence of the dipolar field variance Δ exhibits that there is a sharp decrease between 50 K to about 100 K, as shown in Fig. 5.10 (e). The field distribution should not be temperature dependent if the internal field comes from the nuclear moments. Moreover, λ_G follows the same trend as Δ. This means muons sitting near the formate and the guanidinium experience similar processes of probably the same origin. Hence, whatever drives λ_G to change also drives Δ to vary. λ_G is the relaxation rate resulting from the electron spin dynamics in the system. Therefore, Δ from the Kubo-Toyabe term, which describes the behaviour of muons sitting near formate, may also sense the electron spins. This suggests that muons can still sense the spin correlations, which is probably within the 1D magnetic chain, above the Néel temperature.

When a longitudinal field is applied, the internal field can be quenched with the magnetic field $H > 50$ Oe at 20 K, as shown in Fig. 5.11 (a). This rules out the possibility that the magnetic field that the muons sense above the Néel temperature comes from the nuclear spins. Fig. 5.11 (a) also shows modelled static Kubo-Toyabe functions as a function of field (red curves). It is clear that the model, which describes a system with randomly oriented nuclear moments without any electronic dynamic process,

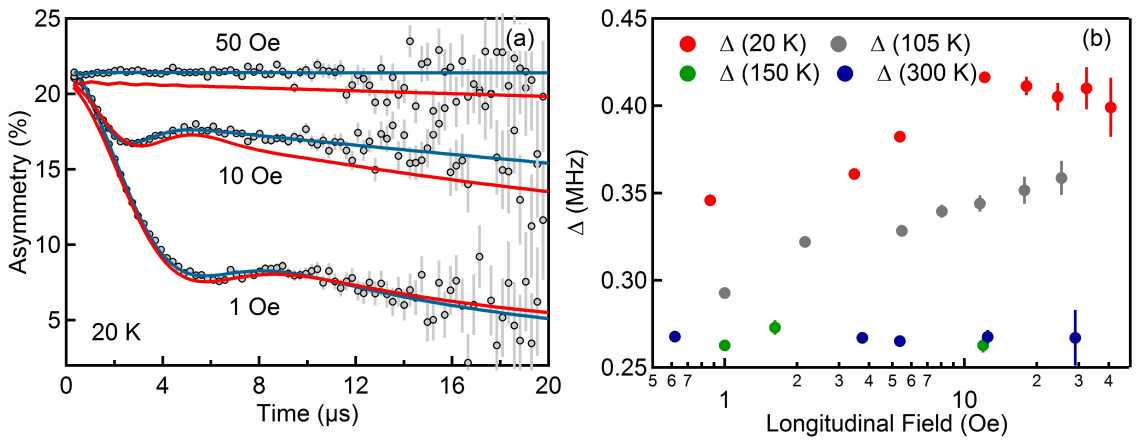

Figure 5.11: (a) The longitudinal field muon spin relaxation measurement shows that the internal field can be decoupled with LF > 50 Oe at 20 K. The grey symbols are raw data, blue curves are the fitting and red curves show the model of static Kubo-Toyabe function with an applied magnetic field. (b) The field dependence of the Gaussian field variance Δ at different temperatures.

cannot fit the data. Therefore, it is impossible to draw the conclusion that muons can only sense nuclear moments at high temperatures. The Gaussian field variance is also found to have a field dependence below 105 K, as shown in Fig. 5.11 (b). At 20 K, Δ increases at small fields and changes little from about 20 Oe onwards. However, at the temperature T_{para} (somewhere between 105 K and 150 K), Δ is independent of the applied field, which indicates that the origin of the field dependence of Δ below 105 K vanishes when $T > T_{para}$. This is the temperature where the one-dimensional magnetic effects start to disappear in the susceptibility measurements. It is suggestive that muons probably sense the short-range correlations arising from 1D magnetic chains in CuGF.

As discussed in Section 3.1.2, Yaouanc [13] showed the influence of short-range correlations to the μSR relaxation function. Short-range correlations result in a damped oscillation relaxation function, which looks like a damped Kubo-Toyabe function, as shown in Fig. 3.9. Owing to the variance of the correlation length, the relaxation function looks like a damped Kubo-Toyabe function with a changing "Δ". That is exactly what was observed in the ZF μSR measurements on CuGF. Therefore, the muons' re-

laxation have three origins above the Néel temperature, the short-range correlations arising from 1D Heisenberg antiferromagnetic chain, the randomly oriented nuclear moments and dynamics in CuGF.

As a consequence, the fitting function is modified as following:

$$A(t) = A_F \left(P_{osc} \cos\left(ft + \psi\right) \exp\left(-\frac{\Delta_{osc}^2 t^2}{2}\right) + \left(1 - P_{osc}\right) K_{GR} \right) + A_G \exp\left(-\lambda_G t\right) + A_{BG} \tag{5.10}$$

where

$$K_{GR} = \frac{1}{3} + \frac{2}{3}\left(1 - \gamma_\mu^2 \Delta_{KT}^2 t^2\right) \exp\left(-\frac{\gamma_\mu^2 \Delta_{KT}^2 t^2}{2}\right) \tag{5.11}$$

is a standard Kubo-Toyabe function describing a field from randomly orientated moments with a Gaussian distribution. In this fitting function, all three processes are included. The guanidinium dynamic term is still described by an exponential relaxation, while the formate term consists of two contributions, one Gaussian damped oscillation from the short-range correlations and one standard Kubo-Toyabe relaxation from the randomly orientated nuclear moments. The background term A_{BG} and the proportions of muons sitting near the guanidinium and the formate (A_G and A_F) are kept the same as in the model represented by Eq. 5.9. During the data fitting, A_{BG}, A_F, A_G are kept fixed, while parameters, including the oscillating frequency f, field deviation of the oscillatory term Δ_{osc}, field distribution due to the nuclear spins Δ_{KT}, fractions of oscillatory part P_{osc} and Kubo-Toyabe part (1-P_{osc}) and exponential relaxation rate of the guanidinium dynamic term λ_G, are floating.

P_{osc}, as shown in Fig. 5.12, describes the volume fraction of the muons experiencing precessions due to short-range correlations ($T > T_N$) or long-range magnetic order ($T < T_N$) of all the muons sitting near the formate. Below the Néel temperature, nearly all of the muons sitting near the formate sense the magnetic correlations, while above the Néel temperature, this fraction drops to about 30% and decreases with increasing temperature. The oscillatory term completely vanishes at about 100 K, which suggests

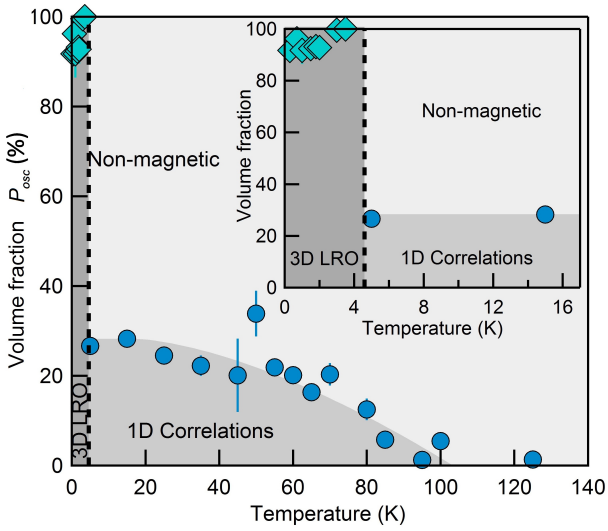

Figure 5.12: The fraction of the oscillatory term of the muons sitting near the formate. The inset shows the details near the transition temperature.

that the magnetic short-range correlations become very small and muons could not sense it when $T > 100$ K. It is also worth mentioning that below the Néel temperature, 30% of the muons sit near the formate experiencing an oscillation and the other 70% relax in a Gaussian relaxation as they sit very close to copper ions. Just above the Néel temperature, 30% of the formate muons experience an oscillation and 70% lead to a Kubo-Toyabe relaxation originating from the nuclear moments. It is possible that the part of muons having a Gaussian relaxation below T_N sense the randomly orientated nuclear spins beyond T_N and exhibit a Kubo-Toyabe relaxation. Muons sitting at the other five sites near the formate exhibiting oscillations below the Néel temperature sense the short-range correlations when $T > T_N$.

Using the fitting function Eq. 5.9, the mean field B_0 and the field variance Δ_{osc} can be obtained from fits to the μSR experimental data. The short-range correlation length can be calculated using the method discussed in Section 3.1.2. The Δ_{osc}/B_0 ratio from the experimental data is shown in Fig. 5.13. Theoretically, the correlation length diverges at the Néel temperature and follows the critical behaviour $\xi \sim \left|1 - \frac{T}{T_N}\right|^{-\nu}$, where $\nu = 0.7$ in a 3D Heisenberg antiferromagnet. It will then decrease with increasing

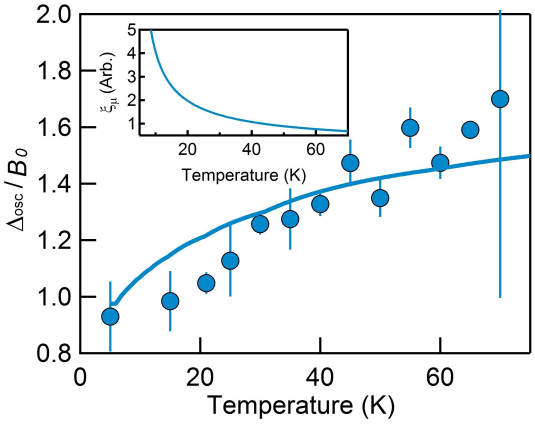

Figure 5.13: The Δ_{osc}/B_0 ratio as a function of temperature is shown by the blue solid circles. The model based on a simple temperature correlation length treatment and Δ/B vs. correlation length relationship discussed in Section 3.1.2 is shown by the blue curve. The inset is a simple temperature correlation length treatment that diverges at the Néel temperature due to the phase transition.

temperature with an inverse proportionality: T^{-1} [82]. This process is shown in Fig. 5.13 (inset). When this theoretical model is applied to the Δ/B vs. ξ relationship in Section 3.1.2, Δ/B from the theoretical model is obtained. It is shown by the blue curve in Fig. 5.13. Even though the theoretical model and the experimental data do not have the same shape, they all show the same general downward trend and have a similar size. The data is a fair description of the theoretical model.

Having established that we are able to estimate the correlation length with the μSR measurements, we are now in a position to interpret the magnetic field dependence data. As shown in Fig. 5.11 (b), Δ shows a field dependence at small applied fields (< 50 Oe). This effect indicates that the correlation length of the 1D magnetic chain may also be field dependent in a small field range. By substituting the Δ_{osc}/B_0 ratio into the Δ/B vs. correlation length relationship discussed above, the short-range correlation length as a function of the longitudinal magnetic field can be derived. Fig. 5.14 shows the calculated correlation length at 20 K. It obeys a power law, where the fitted exponent is -1.19 ($\pm$ 0.07).

In principle, an external magnetic field leads to qualitatively new phenomena in spin chains when the Zeeman energy becomes comparable to the scale set by the exchange

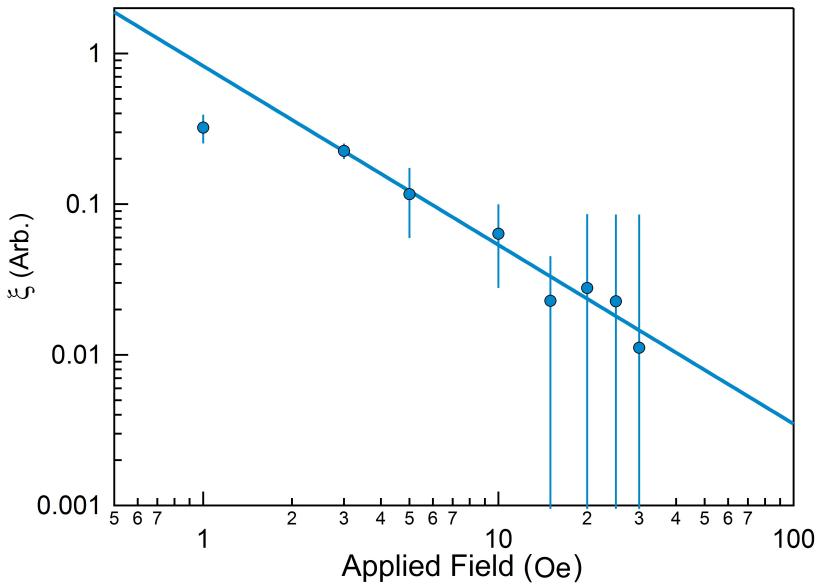

Figure 5.14: The correlation length at 20 K as a function of the applied magnetic field using a power law as a fit function shown by the blue solid line ($\chi^2 = 0.971$). The correlation length is in an arbitrary unit because the data is based on a model that describes short-range correlations in ferromagnetic materials. This approach may not be very precise for a CuGF 1D chain but the trend can be qualitatively reproduced.

energies. However, in our μSR experiments, the magnetic field is applied along the chain direction. One should not observe a field dependence of the correlation length, since the temperature is approximately $J/2$ and the applied fields are equivalent to $J/1000$ to $J/10000$. It is thought that below the bulk 3D T_N that CuGF is a canted antiferromagnet [17]. One potential explanation could be that the 1D fluctuations are canted due to local anisotropy or exchange coupling between the x-components of the adjacent spins on the chain. If this is the case, then the field dependence can be explained by the removal of the transverse correlations from the canted spins.

5.5 Magnetoelectric Coupling

CuGF is a potential multiferroic material because it has a polar space group of $Pna2_1$. The inverse magnetoelectric effect in CuGF, with other words the electric field can control the magnetisation, has been reported in Ref. [58]. By applying an electric field

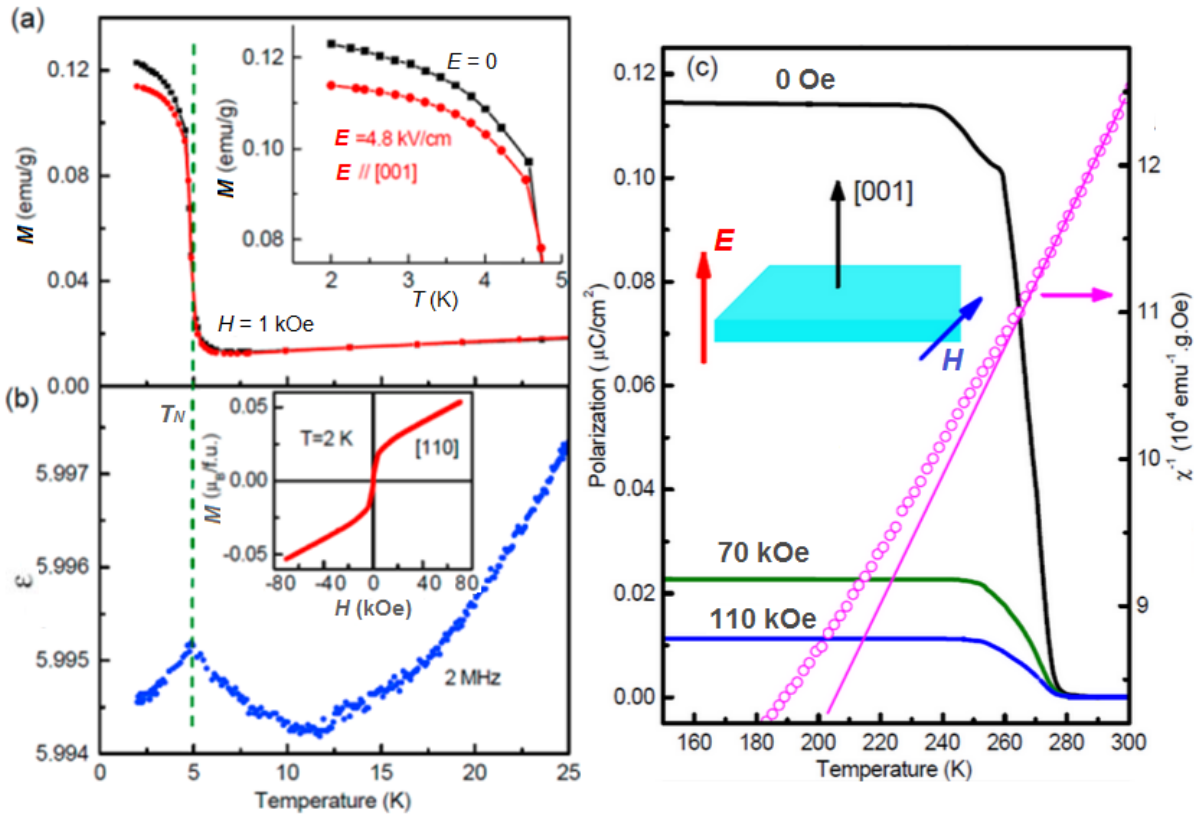

Figure 5.15: (a) The temperature dependence of the *ab*-plane magnetisation along the [110] direction with and without applied electric fields along *c*-axis. The inset shows an enlarged view at low temperatures. (b) The dielectric constant along [110] as a function of temperature. The inset shows the M-H loop along [110] at 2 K. (c) The electric polarisation (left) and the reciprocal of magnetic susceptibility (right) along the *c*-axis as a function of temperature. The straight solid line is a fit to the Curie-Weiss law. The inset shows the measurement configuration [58].

of 4.8 kV/cm along the [001] direction of the CuGF single crystal, a decrease of the magnetisation under 1000 Oe along the [110] crystal direction was observed below the Néel temperature, as shown in Fig. 5.15 (a). The dielectric constant ε as a function of temperature is shown in Fig. 5.15 (b). It decreases when cooled in the paramagnetic state down to about 12 K where it starts to increase and reaches a maximum at around 5 K. This small dielectric constant anomaly occurs at the temperature that is very close to the Néel temperature. Similar dielectric anomalies were also reported in many inorganic multiferromagnetic materials and were believed to be due to the magnetoelectric coupling in the material [3, 4].

In addition to the magnetic ordering below the Néel temperature, a strong magne-

toelectric coupling was shown at high temperatures where CuGF was in a paramagnetic state, as shown in Fig. 5.15 (c). This improper ferroelectricity is due to the Jahn-Teller distortion and the tilting of the organic cations in this perovskite MOF [58].

In this work, the magnetoelectric coupling in CuGF was also studied with the μSR technique at 0.7 K, below T_N, in early 2009 when the magnetoelectric coupling in CuGF was not reported yet. During the μSR experiment, electric fields are applied, which is the same geometry as Tian's experiment [58], along the c-axis of the single crystal. However, the fields applied in this μSR experiment (up to 40 kV/cm) were much larger than the field under which the magnetoelectric coupling was detected (4.8 kV/cm). In the experiment, electric fields were applied to the sample while measuring the internal magnetic field of CuGF at 0.7 K. If the applied electric field affects the magnetism in CuGF, the internal magnetic field, or the muon precession frequencies should change. The electric field dependence of the muon oscillation frequencies, the sixth Gaussian relaxation rate and the five oscillation relaxation rates are shown in Fig. 5.16 (a), (c) and (d1-d5), respectively. There seems to be no change in the precession frequencies or the sixth Gaussian relaxation rate. The variance of the frequencies are shown in Fig. 5.16 (b1-b5). Judging from the unchanged frequency, the magnetoelectric coupling in CuGF is not detected in the μSR experiment. However, the relaxation rates of the damped precessions may exhibit a small kink, centred around zero electric field. λ_1 still assumes the opposite trend as other relaxation rates. This shows the magnetic fluctuations increase if an electric field is applied. It is possible that the glue used to attach the crystals onto the silver plate influenced or even isolated the electric fields so that only a very small field was applied to the real crystals. And it was not enough to observe the magnetoelectric coupling in CuGF.

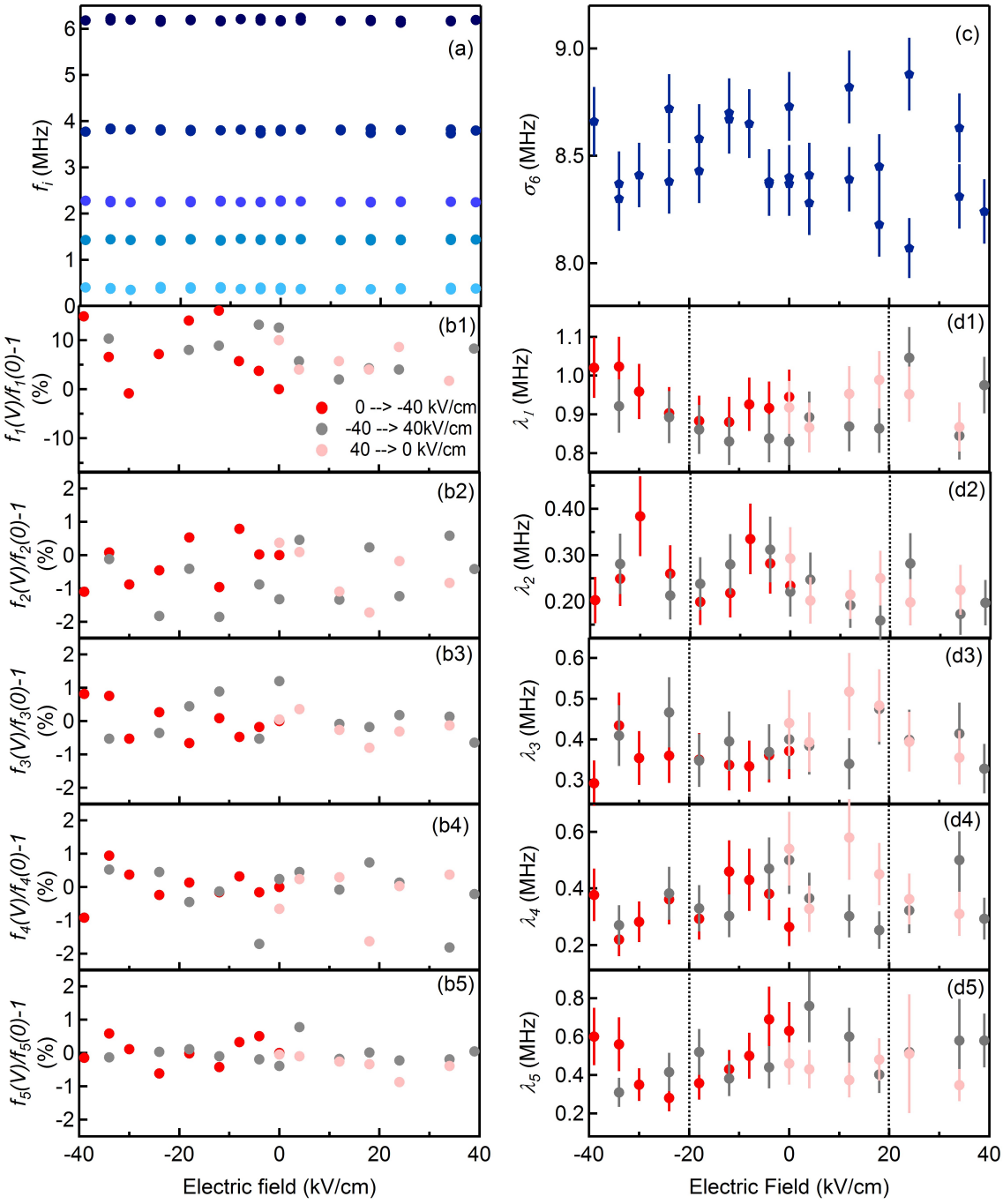

Figure 5.16: (a) Five muon precession frequencies as a function of the applied electric field. (b 1-5) The shift of the five oscillation frequencies at 0.7 K as a function of the applied electrical field. (c) The relaxation rate of the sixth Gaussian term as a function of the applied electric field. (d 1-5) Relaxation rates of the five damped oscillations as a function of electric field. There seems to be a small kink or feature centred around zero electric field (the region between the two dashed lines). These data were measured at a fixed temperature of 0.7 K and error bars are all included but some of them are too small to show up.

5.6 Discussion and Conclusion

This chapter discusses the study of the magnetic properties and low-dimensional magnetism of CuGF using magnetometry and the μSR technique. A spin-canted antiferromagnetic order with a Néel temperature of 4.6 K was observed. The critical phenomena are also investigated, which indicate that CuGF possesses a 3D Heisenberg long-range magnetic order below the critical temperature. Above the Néel temperature, a broad peak at about 45 K was observed in the magnetic susceptibility data, which is a signature of one-dimensional chains in the system. This confirms the earlier study in Ref. [17].

A muon acts as a local probe and is sensitive to one-dimensional magnetic correlations in a system. Muons could measure the correlation length in a low-dimensional magnet. The field and temperature dependence correlation length in CuGF is studied using the μSR technique. The temperature evolution of the short-range correlation has a similar downward trend and the same size to the theoretical model. The field dependence of the correlation length is found to obey a power law $\xi \sim H^{-1}$, which may be a result of the field influence on the transverse correlations from the canted spins.

It is also interesting to compare the μSR study in CuGF with the case of CuDMF ($(CH_3)_2NH_2[Cu(HCOO)_3]$), which has a similar ABX_3 structure to CuGF. In CuDMF, the copper ions are also linked by formate chains but with different cations, $[(CH_3)_2NH_2]^+$, which sit in the cavities of the framework. μSR measurements on CuDMF showed two oscillations with frequencies of 2.34 MHz and 0.85 MHz below the transition temperature corresponding to muons sitting near the formate and near the $[(CH_3)_2NH_2]^+$ cation, respectively. The percentage of muons sitting at these two sites are also 50% and 50% [96], which is similar to the case of CuGF. Therefore, the μSR studies on these two similar-structured magnetic MOFs are likely comparable below their magnetic transition temperatures. However, they behave differently above the transition temperatures. In CuDMF, where the one-dimensional copper chains also exists, μSR only measured

an exponential relaxation polarisation function [96] rather than a damped oscillation reported in this work. This may be reasonable because the spin dynamics or the spin correlations in these two MOFs are likely different due to the different but similar organic frameworks. Thus, how the structure of a multiferroic MOF couples to the properties of the one-dimensional chain in it is also an interesting topic for the future work.

Magnetoelectric coupling in CuGF was observed by the authors in Ref. [58], below and above the Néel temperature. However, the μSR measurements in this work do not detect any magnetoelectric coupling in the sample, although there is some evidence for a small change in the magnetic fluctuations. Using a sample mounted using a conducting glue and measuring it again would be an interesting project for the future work.

Chapter 6

Single Molecule Magnets - CP*-RE-COT

Low-dimensional magnetic structures provide valuable models for understanding fundamental quantum magnetisation phenomena [10–12]. In this chapter, the magnetisation relaxation mechanism of "zero-dimensional" magnets, namely the single molecule magnets, are investigated. As nano-scaled magnets, these SMMs have various applications, including quantum computing [25], high-density data storage [23] and magnetic refrigeration [31]. Since the first report of single molecule magnet in 1980s [32], this area has received extensive research interest.

Unfortunately, the magnetic blocking temperature of SMMs is often far below room temperature and magnetisation relaxations in these systems are not slow enough for applications [30, 33]. Improving the overall uniaxial anisotropy is the key for SMMs systems to generating large energy barriers that lead to slow magnetisation relaxations and high blocking temperatures [103, 106]. However, the anisotropy of SMMs is usually small and difficult to control due to the complexity of the coupling between individual paramagnetic centres in SMMs. This complexity hinders studies of the underlying mechanisms that determine the anisotropy and zero-field splitting properties of SMMs [103].

Therefore, the SMMs with single spin carriers, which are also called single-ion magnets, provide an ideal platform to study the anisotropy in SMM systems. Since the first reported SIM system $[Pc_2Ln]^- \cdot TBA^+$ (Ln = lanthanide) in 2003 [21], this new method of creating single molecule magnets has attracted a lot of attention. All of the reported SIMs are lanthanide-based as lanthanide has a strong spin-orbit coupling that offers a large magnetic anisotropy [119–122]. These simplified one-spin-carrier systems reduce the dimensionality in understanding the nature of the electronic structure in SMMs. This may be helpful to design new systems with higher blocking temperatures and slow magnetisation relaxations. More importantly, studies of SIMs, which are mesoscopic materials, could provide valuable experimental data to validate physical models of quantum effects in magnetism.

The magnetic relaxation mechanisms, discussed in Section 2.2.3, have never been thoroughly studied within a single material over a large temperature range, or perhaps more importantly, how they differ has not been studied in a series of closely related materials. Obtaining the information of all relaxation processes using a single technique is practically impossible, since the relaxation rate often ranges from Hz to $\sim$ GHz. Current reports were mainly focused on the magnetisation relaxation at low temperatures (below 50 K) when the relaxation is slow. Hence, comprehensive measurements of the relaxations in a series of related materials, over a large range of temperature and magnetic field values, are required.

Therefore, a series of SIMs, CP*-RE-COT (RE = Tm, Dy and Tb) was chosen to comprehensively study their magnetisation relaxation mechanism. They possess relatively simple sandwiched structures with a lanthanide ion in the centre, as shown in Fig. 6.1 (a). This series of SIMs have asymmetric molecular structures with a bending angle α and the magnetisation relaxations were found to be related to this angle [103]. This is different from the most studied SIMs system - $[Pc_2Ln]^- \cdot TBA^+$, which has a symmetric molecular structure (Fig. 2.7) [21]. The asymmetric structure of CP*-RE-COT may provide extra information about the coupling between the structure and

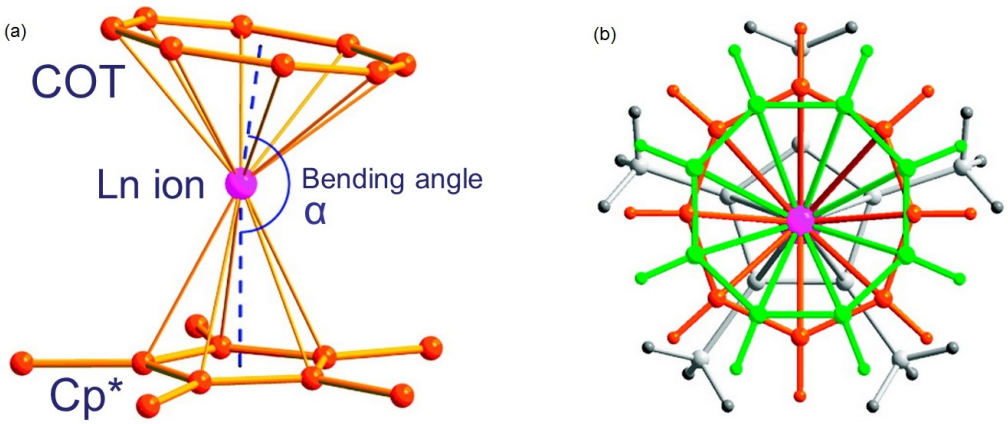

Figure 6.1: (a) The molecular structure of CP*-RE-COT, where the pink balls represent the lanthanide atom, orange balls represent carbon atoms and hydrogen atoms are not shown. Blue dash lines are connections between the lanthanide and the centre of the CP* and the COT rings. The angle between these two lines is defined as the bending angle α. (b) The disorder of the COT ring in CP*-RE-COT. Green ring corresponds to the staggered conformer and the orange ring corresponds to the eclipsed conformer compared with the CP* represented by grey ring. The molecular structure was reported by Ref. [103].

magnetic properties in SIMs.

In this work, an AC magnetometer (a system with a frequency response of 1 Hz to 10 kHz) and the μSR technique (with a frequency response of 0.1 MHz to 100 MHz) were utilised to extend the study of magnetisation relaxations in CP*-RE-COT. Magnetic relaxations were measured in a large temperature range to access different relaxation processes in these SIMs.

6.1 Introduction to A Series of Single-Ion Magnets CP*-RE-COT

As shown in Fig. 6.1 (a), CP*-RE-COT has a simple structure with a rare-earth ion sandwiched between two carbon rings: a cyclooctatetraene dianion ($C_8H_8^-$, COT) and a pentamethyl cyclopentadiene anion ($C_5Me_5^-$, CP*). These two carbon rings are not parallel to each other. The bending angle α is defined as the centroid-lanthanide-centroid angle for different lanthanide ions. Details of the bending angle and the dis-

Table 6.1: Crystallographic data of CP*-RE-COT from Ref. [103]. Data were taken at 293 K.

Formula	$C_{18}H_{23}Tb$	$C_{18}H_{23}Dy$	$C_{18}H_{23}Tm$
α (degrees)	170.4	171.9	173.9
Average Ln-(CP)* length (Å)	2.624(2)	2.594(7)	2.548(4)
Average Ln-(COT) length (Å)	2.546 (6)	2.511(1)	2.477(7)
Ln to (CP)* plane distance (Å)	2.3424(2)	2.3096(2)	2.2639(3)
Ln to (CP)* centroid distance (Å)	2.3326(2)	2.2995(2)	2.2438(3)
Ln to (COT) plane distance (Å)	1.8260(2)	1.7741(2)	1.7019(3)
Ln to (COT) centroid distance (Å)	1.8250(2)	1.7728(2)	1.7653(4)
Space group	*Pnma*	*Pnma*	*Pnma*
a (Å)	10.3609(2)	10.3073(2)	10.2420(3)
b (Å)	13.2089(3)	13.2464(3)	13.2770(3)
c (Å)	11.9129(6)	11.8674(2)	11.8191(3)
V (Å^3)	1630.35(6)	1620.31(5)	1611.82(8)

tance between the lanthanide and the two carbon rings are listed in Table 6.1 (a).

In the series of CP*-RE-COT, all the compounds crystallise with a orthorhombic *Pnma* space group. The crystallographic data are listed in Table 6.1. The unit cell volume decreases with increasing atomic number as the lanthanide ion radius affects the length of the metal-ligand bond due to the lanthanide contraction [203]. According to Ref. [103], the COT ring in CP*-RE-COT crystallises in two configurations - a staggered conformer and a slightly rotated eclipsed conformer, as shown in Fig. 6.1 (b). In the eclipsed conformer, one carbon ion in the COT ring is aligned with a carbon ion in the CP* ring, while in the staggered conformer, no carbon ions in these two rings are aligned with each other. The molar ratio between the two conformers is roughly $W_{eclipsed} : W_{staggered} = 62.4 : 37.6$ [103]. More importantly, the bending angles α in these two conformers are not identical. Taking the Er complex as an example, $\alpha_{Eclipsed}$ is 171.023(6)° whereas $\alpha_{Staggered}$ is 171.133(6)°. These two conformers coexist from 2 K up to room temperature suggesting that they have a static origin instead of a dynamic one from thermal fluctuations.

When the interactions between molecules are considered, the neighbouring molecules

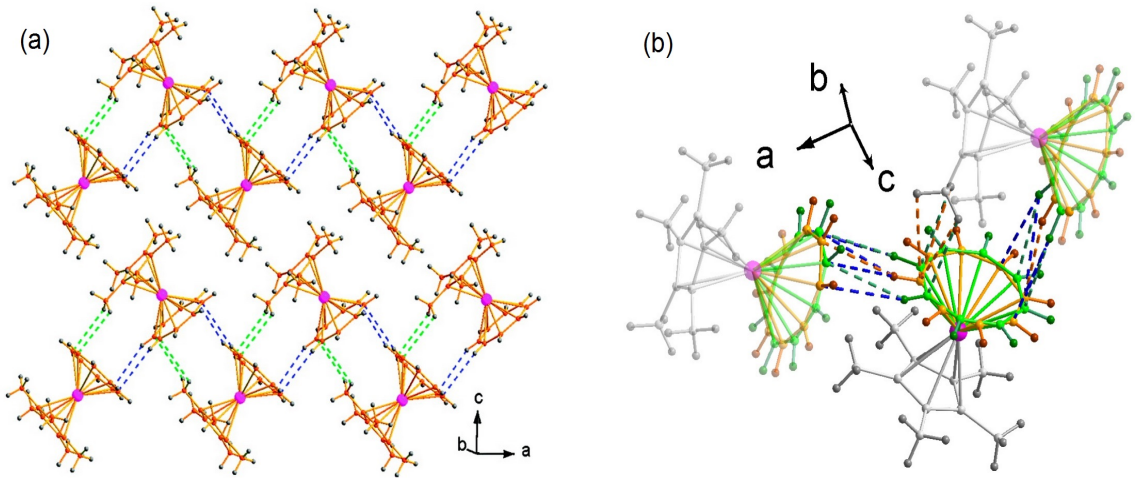

Figure 6.2: (a) Interactions between molecules of CP*-RE-COT within the *ac*-plane of the crystal. The edge to face π-π stacking interactions between COT rings are shown by the blue dashed lines and the C-H$\cdots\pi$ interactions between the CP* and the COT rings are shown by the green dashed lines. (b) Details of the two interaction types in the CP*-RE-COT *ac*-plane for the eclipsed (golden) and staggered (green) COT conformers. The interactions relevant to eclipsed and staggered conformers are also represented by the golden and green dashed lines. The blue dashed lines are interactions between these two conformers [103].

within the *ac*-plane of the crystal are far away from each other and there is no strong interaction between them. There are two different types of intermolecular interaction within the *ac*-plane, as shown in Fig. 6.2 (a): 1. the edge to face π-π stacking interactions between the COT rings (blue dashed lines in Fig. 6.2 (a)); 2. the C-H$\cdots$ π interactions between the methyl group of the CP* and the COT rings (green dashed lines in Fig. 6.2 (b)). In the case of the edge to face π-π stacking interaction, a stack via the shortest C$\cdots$H bond in the adjacent molecules is preferred. For the C-H$\cdots$ π interaction between the CP* and COT rings, the connections between the CP* rings and the eclipsed COT rings were found to be 1.5 times more than the connections between the CP* rings and the staggered COT rings [103]. The asymmetric interactions between the molecules discussed above result in titling of the molecules depicted in Fig. 6.1 (a). Moreover, the magnetic interactions between the lanthanide ions are normally negligible as the distance between two adjacent paramagnetic centres is relatively long. For instance, the distance between two nearest Tm ions in the Tm complex, which has the smallest

unit cell, is about 7.19 Å . Therefore, every CP*-RE-COT molecule can be regarded as being isolated and work as a single molecule magnet.

6.2 Magnetisation Relaxations in CP*-RE-COT

Magnetisation relaxation describes how long a magnet can hold its magnetisation. It is critical to reduce the fluctuations or enhance the capacity to maintain magnetisation in a magnet, thereby slowing down the relaxation process. As discussed in Chapter 2, magnetisation relaxations are usually measured with an AC magnetometer. By measuring the resonance between the magnetic energy absorption of the system and the external field energy, magnetisation relaxations are determined by the external field frequency at which the resonance occurs at a certain temperature. However, the majority of AC susceptibility measurement systems only have a frequency response of up to 10 kHz. Our research group do not have access to any system with higher frequency responses. As magnetisation relaxations in some members of CP*-RE-COT are much faster than 0.1 ms at high temperatures ($T > 50$ K), a probe with a higher frequency response is needed to study the magnetisation relaxations in the CP*-RE-COT series in a comprehensive temperature range. The μSR technique can partially fill this frequency gap by offering responses between 0.1 MHz and 1 GHz.

6.2.1 Experiment details

The polycrystalline samples in the experiments were synthesized using a recrystallisation method by a collaborating group at Peking University. In their synthesis, CP*K dissolved in tetrahydrofuran (THF) solvent was added dropwise to a suspension of equimolar [(COT)LnCl(THFx)] in THF. The solvent was then removed after 24 hours of stirring, and the residue was extracted using toluene and filtration. The filtrate was finally cooled to -30 °C overnight before the crystals were harvested.

Fast magnetisation relaxations at relative high temperatures ($T > 100$ K) in CP*-

RE-COT were investigated using the EMU spectrometer at ISIS and slow magnetisation relaxations of CP*-Dy-COT at low temperatures ($T < 100$ K) were measured using the GPS and LTF spectrometers at PSI. Before the experiments, CP*-RE-COT samples were sealed in silver envelopes in a glove box with a He or N_2 environment. The envelopes were then covered by another two layers of 25 μm silver foil to slow down muons during the experiments. After having taken the samples out of the glove box, they were kept in a sealed bag with an argon atmosphere until they were loaded into the cryostat. Thus, during the whole sample preparation process, the measured samples were protected against oxygen and water that would have caused the deterioration of the sample.

Before the μSR measurements, transverse field measurements were carried out to determine α, which is the asymmetry constant determined by the inequivalence of the forward and backward detectors in a μSR experiment (for more details, see in Chapter 3). These measurements can also verify whether muonium has formed in the sample. A muonium consists of an implanted muon and an electron. It behaves differently from a diamagnetic muon in condensed matter systems. Therefore, it is important to check whether the muonium exists. The existence of muonium affects the data analysis and interpretation. At room temperature, the TF measurement of CP*-RE-COT provided an asymmetry of $\sim 23\%$ for the EMU (ISIS) spectrometer, which has a maximum asymmetry of $\sim 24\%$. The TF results confirm that there is no or little muonium formed in this series of materials during the μSR experiments.

Among all members of CP*-RE-COT, the Dy complex is the most comprehensively studied in this project. It was initially measured from 50 K to room temperature using the EMU spectrometer at ISIS. The measured initial asymmetry decreases below 125 K. Since there is no muonium formed in the sample, the loss of the asymmetry can most likely be attributed to the fast relaxations of the muon spins. According to Eq. 3.35, the muon spin relaxation rate in the fast limit is inversely proportional to the spin fluctuation rate in the sample. The fast muon spin relaxation rate indicates that the

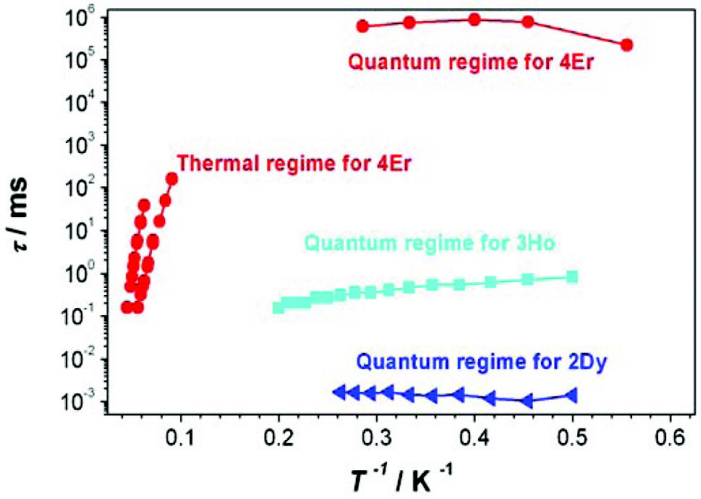

Figure 6.3: The magnetisation relaxation time of the Dy (5% concentration in CP*-Y-COT), Ho and Er compounds at low temperatures. The relaxation time in the quantum regime varies by several orders of magnitude from the Dy to the Er compounds [103].

magnetisation relaxation rate below 125 K is too slow and out of the frequency response range at ISIS (but still too fast to be measured using an AC magnetometer [103]). Thus, the magnetisation relaxation rate of the Dy complex below 100 K were then measured using the LTF and GPS spectrometers at PSI, since they have the capability to measure faster muon spin relaxation rates of up to several hundred MHz.

6.2.2 AC susceptibility measurements on magnetisation relaxations in CP*-RE-COT

The slow magnetisation relaxations in CP*-RE-COT were at first investigated by Jiang [103]. In the Ho and the Er compounds, the magnetisation relaxation is relatively slow and below 5 K it can be measured with an AC magnetometer. Temperature independent magnetisation relaxation rates at low temperatures were observed in these two compounds and in the diluted Dy compound, as shown in Fig. 6.3. Among the four possible relaxation processes in these compounds, the temperature independent relaxations can be explained with quantum tunnelling between the two degenerate ground states. It is also clear that the magnetisation relaxation rates in this series

of single molecule magnets change by several orders of magnitude, from 10^6 ms to less than 0.1 ms. The magnetisation relaxations in the Tm and Tb compounds at low temperatures and thermal relaxations of the whole series of compounds at high temperatures are too fast to be accessible with an AC magnetometer with a frequency response between 1 Hz and 10 kHz.

Detailed AC susceptibility measurements were performed on the Dy, Ho and Er compounds [103]. Taking the Dy complex as an example, without an applied magnetic DC field, the results are shown in Fig. 6.4 (a). There was no detectable peak in the imaginary susceptibility χ'' down to 2 K. This means that the magnetisation relaxation in the Dy complex is too fast for the 10 kHz AC magnetometer used here.

As discussed in Section 2.2.3, small perturbations in the Hamiltonian (Eq. 2.25) results in the entanglement of the two ground states (or higher states but more difficult in SIMs). Thus, the dipole-dipole interaction and the axial asymmetry of the molecule resulting from the intermolecular interactions are believed to be the potential cause for the small perturbations mentioned above [121]. Hence, by limiting the dipolar and intermolecular interactions, the quantum tunnelling process in CP*-RE-COT can be suppressed and the magnetisation relaxation can be slowed down to be detectable with a 10 kHz AC magnetometer. A diluted sample with 5% CP*-Dy-COT concentration in the diamagnetic CP*-Y-COT compound, in which both the dipolar and the intermolecular interactions are limited, was measured. Fig. 6.4 (b) shows the AC susceptibility measurement of the diluted Dy compound. It is clear in Fig. 6.4 (b) that peaks in the χ'' data, which can be used to determine the magnetisation relaxation time in the sample, appear within the temperature range of 2 to 4.5 K. Using the equation $\tau = 1/2\pi f$, the relaxation time of the system can be calculated, as shown in Fig. 6.4 (c). It suggests that the relaxation between 2 and 4.5 K has two processes. Below 3.5 K, τ is a constant at about 0.7 ms and decreases rapidly above this temperature. Moreover, the relaxation at a constant rate at low temperatures can be quenched by an applied magnetic field. The relaxation rates vs. inverse temperature of the process above 3.5 K and the pro-

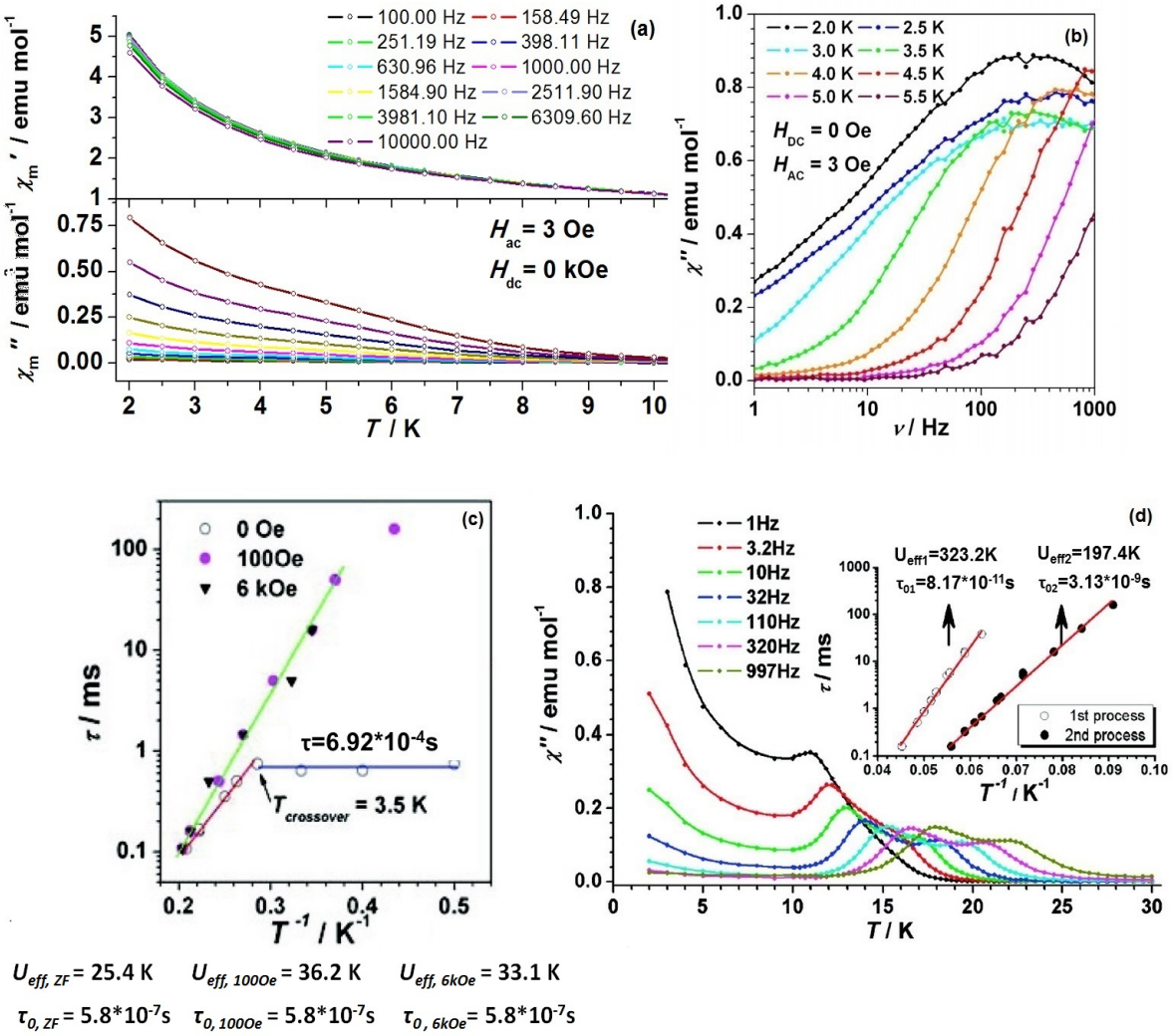

Figure 6.4: (a) AC susceptibility measurements of the pure Dy complex. (b) χ'' as a function of AC field frequency for the 5% CP*-Dy-COT doped in CP*-Y-COT without an applied DC field [103]. (c) The magnetisation relaxation time of CP*-$Y_{0.95}Dy_{0.05}$-COT at 0, 100 Oe and 6 kOe from 2 to 4.5 K [103]. (d) χ'' for the Er complex exhibits two relaxation processes [121].

cess below 3.5 K with applied fields all follow an exponential trend. The temperature dependence of the magnetisation relaxation time indicates that the relaxation have a thermally activated origin. The effective energy barrier of the thermally activated relaxation, $U_{eff} = 25.4$ K [103], is obtained by fitting τ to $\tau = \tau_0 \exp(U_{eff}/k_B T)$. On the other hand, the field dependent and temperature independent relaxation below 3.5 K is governed by quantum tunnelling. With an applied field, the two ground states split and the tunnelling process is completely suppressed. Only the thermal process can be measured. In summary, thermally activated relaxation and quantum tunnelling coexist in CP*-Dy-COT between 2 and 4.5 K. Above 3.5 K, the thermal effects dominate.

The magnetisation relaxations in the Ho and Er compounds, which are slower than in the Dy compound, were also measured at low temperatures. It is worth mentioning that thermally activated relaxations in this series of SIMs exhibited two relaxation processes. In the Er complex, which has the slowest magnetisation relaxation among all the members of this series, two peaks in the χ'' data were observed (Fig. 6.4 (d)), indicating two different relaxation processes [121]. By studying these two relaxation times τ_1 and τ_2, as plotted in Fig. 6.4 (d inset), the two thermally activated processes were described by two different energy barriers $U_{eff1} = 323.2$ K and $U_{eff2} = 197.4$ K, respectively. Moreover, in Ref. [121], the AC susceptibility data were fitted to a linear combination of the two relaxations processes with a modified Debye model:

$$\chi_{total} = \chi_S + (\chi_T - \chi_S) \left(\frac{F_1}{1 + (i\omega\tau_1)^{1-\alpha_1}} + \frac{F_2}{1 + (i\omega\tau_2)^{1-\alpha_2}} \right), \tag{6.1}$$

where F_1, F_2 are fractions. τ_1, τ_2 are the relaxation times and α_1, α_2 are the distribution widths of each relaxation. The fractions F_1 and F_2 are constraint by $F_1 + F_2 = 1$ and the values were assumed to be 0.623 and 0.377. This is consistence with the weight ratio of the two conformers indicating that the two relaxation processes in CP*-RE-COT stem from the two conformers and that these conformers involve different characteristic energy barriers U_{eff}.

In summary, AC susceptibility measurements of CP*-Dy, Ho, Er-COT exhibit slow magnetisation relaxations. The quantum tunnelling and thermally activated relaxation processes were characterised in these materials but only at very low temperatures. In the Er complex, two thermally activated relaxations owing to the two conformers in the structure was observed. It might be similar in other members of this series of SIMs, which all have the same structure as the Er complex. Details of the magnetisation relaxations in pure Tm, Dy, and Tb complexes, however, have not been investigated yet as they are faster than the limit of the AC susceptibility measurements. Therefore, a comprehensive study on magnetisation relaxations in the Dy complex and brief investigations on the Tm and Tb complexes were done in this project.

6.2.3 ZF μSR measurements of magnetisation relaxations in CP*-RE-COT

Three sets of zero-field μSR measurements were carried out on the Dy compound at 20 and 800 mK using the LTF spectrometer, from 1.8 to 150 K using the GPS spectrometer and from 75 K to room temperature using the EMU spectrometer. Below 1.8 K, an oscillatory signal is observed, which will be discussed in detail in the next section. Typical μSR spectra of CP*-Dy-COT above 1.8 K are shown in Fig. 6.5 (a). It is clear the muon spin relaxation rates vary with temperature. It is also seen in Fig. 6.5 (a inset) that there is no asymmetry loss as the initial asymmetries of 25% is identical for all spectra, which is nearly the maximum of the GPS spectrometer. Judging from the spectra, more than one relaxation is present. It was initially attempted to fit the data to two exponential relaxation functions. However, it did not work for all the data at different temperatures indicating that two relaxations were insufficient to describe these spectra. Hence, a third relaxation process was added and all these data at different

temperatures were fitted successfully to three exponential relaxations:

$$A(t) = A_{relax} \sum_{i=1}^{n=3} F_i \exp\left(-\lambda_i t\right) + A_{BG}. \tag{6.2}$$

A residual analysis was done on the 100 K data. It is shown in Fig. 6.5 (b) that the residual is relatively small. In Eq. 6.2, A_{relax} and A_{BG} are constant and $F_1 = 41\%$, $F_2 = 28\%$ and $F_3 = 31\%$ were fixed during the fitting process for every set of the measurements. A_{BG} is a background signal from muons missing the sample and sitting in the silver package or cryostat nearby. $F_3 = 31\%$ is roughly 1/3 of the total implanted muons and has the slowest relaxation rate with temperature independent $\lambda_3 \sim 0.1$ MHz. This suggests that the third term comes from muons experiencing a magnetic field that is parallel to muons' spins. Also, a small proportion of the total muons hit the cryostat, the sample holder or the silver package with the sample inside. The other two components are much faster than the third one and $F_1 : F_2 \sim 60 : 40$. As mentioned earlier, there are two thermally activated relaxation processes resulting from two different conformers with a ratio of 60 : 40 in the Er complex. It is likely that these two muon sites correspond to the two conformers in CP*-Dy-COT, where the first term describes the magnetisation relaxation of the eclipsed conformer and the second term giving information about the relaxation of the staggered conformer.

The muon spin relaxation rates of the first and second components, λ_1 and λ_2 are shown in Fig. 6.6. The two data sets measured at the EMU and GPS spectrometers match perfectly. The first relaxation term, which has the fastest muon spin relaxation rate λ_1 increases as the sample is cooled down. According to Section 3.1.3, the muon spin relaxation following an exponential form indicates that the spin fluctuation in the sample is in the fast limit. Therefore, the magnetisation relaxation rate of the measured sample ν_1 can be calculated using Eq. 3.35: $\lambda_1 = \frac{2\Delta_1^2}{\nu_1}$ if the field distribution Δ_1 is known.

λ_2 for the second muon spin relaxation term, however behaves differently from λ_1

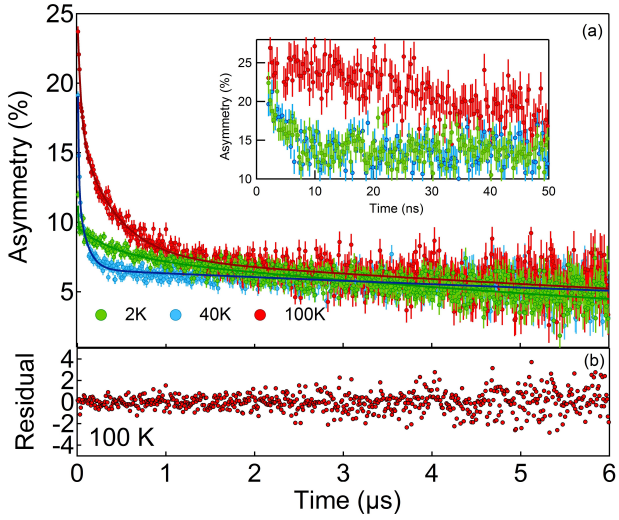

Figure 6.5: (a) Typical μSR spectra of CP*-Dy-COT at different temperatures with three fitted exponential relaxations. The normalised least square were $\chi^2 = 1.012$ (2 K), 1.006 (40 K) and 0.999 (100 K). Data are shown by the solid circles and the fit is shown by the curve with the same colour. The inset shows the zoom-in of the data up to 50 ns. (b) The residual analysis of the 100 K data.

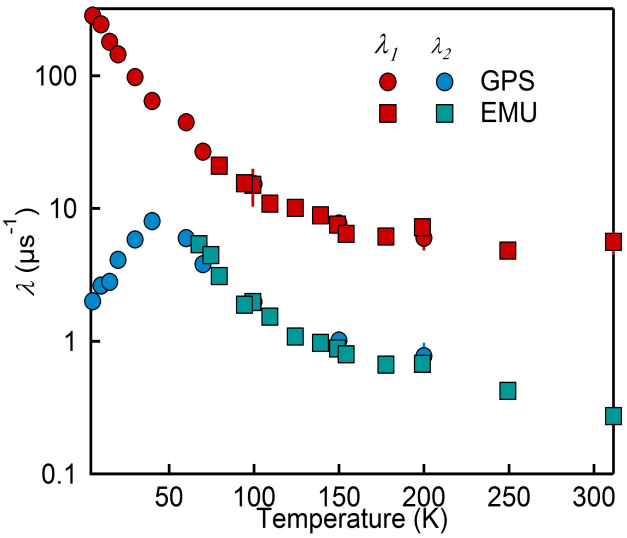

Figure 6.6: The muon spin relaxation rates of the first and second relaxation components λ_1 and λ_2 as a function of temperature under zero field measured with the EMU (square symbols) and GPS (circle symbols) spectrometers.

and has a peak at 40 K. Above 40 K, λ_2 behaves similarly to λ_1 that describes a spin fluctuation in the fast limit. Below 40 K, it cannot be described by an exponential relaxation function in the fast limit any more. Therefore, between 2 and 40 K, μSR data were described using the model:

$$A(t) = A_{relax}\left(F_1 \exp\left(-\lambda_1 t\right) + F_2 Y(t) + F_3 \exp\left(-\lambda_3 t\right)\right) + A_{BG}, \tag{6.3}$$

where the second relaxation component is fitted using the polarisation function $Y(t)$ as discussed in Section 3.1.3:

$$Y(t) = \exp\left(-\frac{2\Delta^2 t}{\nu^2}\left(\exp\left(-\nu t\right) - 1 + \nu t\right)\right), \tag{6.4}$$

which represents the spin fluctuations in the measured sample in an intermediate limit. The sample's magnetisation relaxation (spin fluctuation) rate ν_2 is calculated via $Y(t)$ between 2 and 40 K and in the fast limit employing $\lambda_2 = \frac{2\Delta^2}{\nu_2}$ above 40 K. However, to calculate ν_2 the local field distribution Δ_2 at the corresponding muon site is also needed. Thus, in order to obtain the magnetisation relaxation time in this material, the field distributions at the two muon sites need to be known.

6.2.4 Long-range magnetic ordering in CP*-Dy-COT

In order to estimate the field distributions of the two muon sites in the Dy complex, ZF μSR measurements were performed at very low temperatures. Below 2 K, the thermally activated relaxation processes in this SIM are suppressed and the relaxation process via quantum tunnelling dominates. Therefore, muons should sense a nearly quasi-static field distribution. The ZF μSR measurements of CP*-Dy-COT shows an oscillatory asymmetry signal at low temperatures. This is a signature of long-range magnetic ordering in the sample. As the dipolar or exchange interactions between every molecule in SMMs are normally weak, it is not common to observe long-range magnetic

order in these systems. There have been reports on long-range magnetic ordering in some cluster-based SMMs, including Mn_{12}-acetate [128–130], Mn_4 cluster [127], Mn_6 clusters [131] and Fe_{17} cluster [132]. In SIMs, however, no long-range magnetic order has been reported so far. A possible explanation of the lack of reports of long-range magnetic ordering in SIMs is that the characterisation of those systems most likely did not reach sufficiently low temperature to investigate the ordered state. To our knowledge, this is the first experimental observation of the long-range magnetic order in SIMs.

Fig. 6.7 (a) and (c) show μSR spectra at 0.02 and 0.8 K. The Fourier transform of the spectra was taken but the peak in the frequency domain is suppressed by the fast relaxation signal. Giving that there are two muon sites, two oscillatory terms are expected in the muon spin polarisation function. Hence, the spectra are described by two damped oscillations and three exponential relaxations (one or two cannot fit). Therefore, all the data exhibiting an oscillatory signal (< 2 K) are fitted with five components:

$$A(t) = A_{relax}\left(\sum_{i=1}^{n=2} F_i \cos\left(f_i t + \varphi_i\right) \exp\left(-\lambda_i t\right) + \sum_{j=1}^{n=3} F_j \exp\left(-\lambda_j t\right)\right) + A_{BG}, \quad (6.5)$$

where A_{relax} and A_{BG} are the asymmetries for the relaxing terms and background term. F_i are the volume fractions of the two damped oscillation components with the frequencies f_i, phases φ_i and relaxation rates λ_i. F_j is the volume fraction of the relaxing terms characterised by the relaxation rates λ_j. During the data fitting, A_{relax}, A_{BG} and all F_i and F_j were kept fixed and only the frequencies f_i, λ_i and λ_j were allowed to vary. The data were fitted well both at the early 150 ns indicating a good description of the oscillatory terms and on the whole spectrum, as shown in Fig. 6.7 (a inset). The residual analysis was taken on the data measured at the lowest temperature, as shown in Fig. 6.7 (b). All fit parameters for the 0.8 K data are listed in Table 6.2.

The long-range magnetic order probably arises from the dipolar interaction between

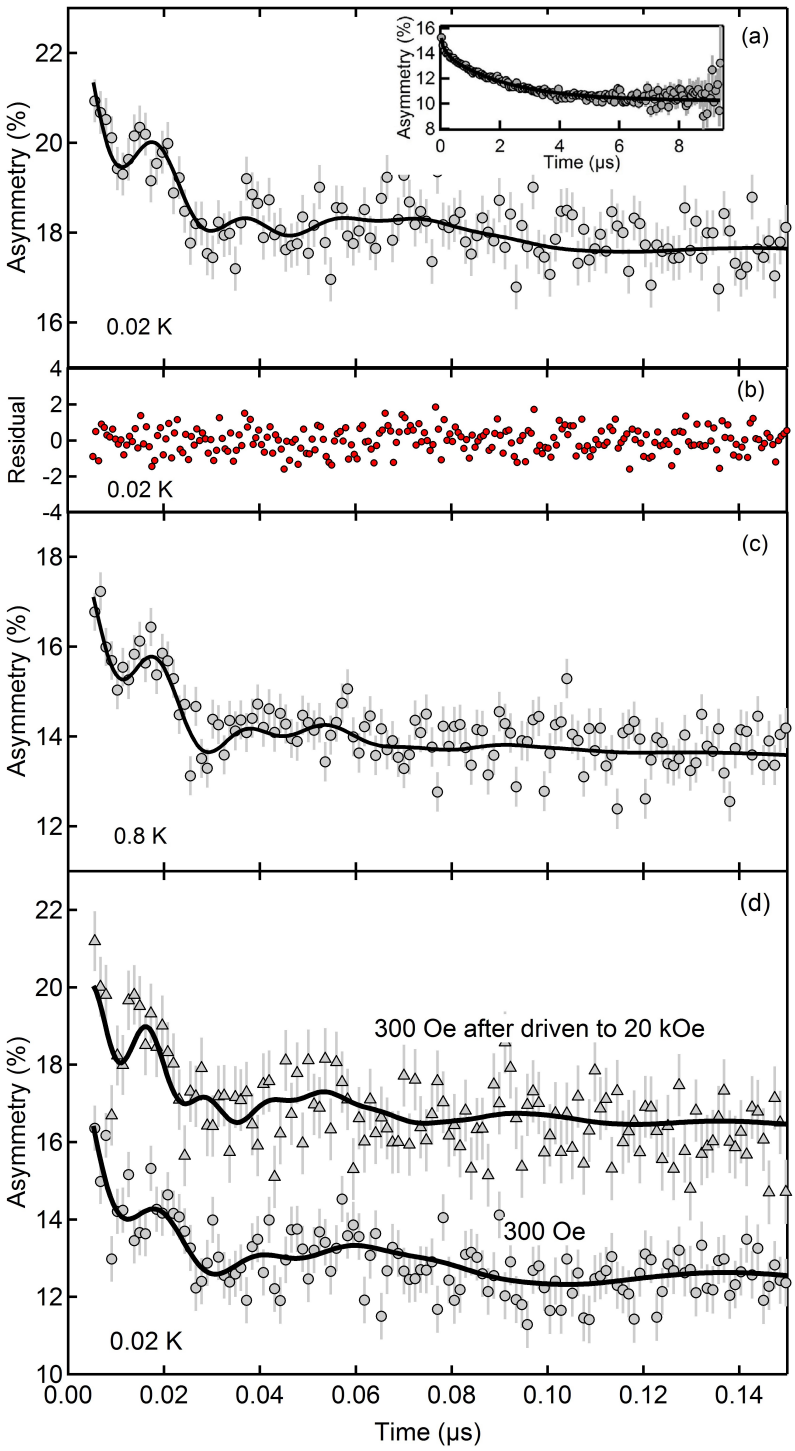

Figure 6.7: (a) μSR spectra and fit of CP*-Dy-COT under zero magnetic field at 0.02 K (fit quality $\chi^2 = 1.058$). The inset shows the same spectrum up to 9 μs (fit quality $\chi^2 = 0.996$). (b) The residual analysis on the data at 0.02 K. (c) ZF μSR spectrum at 0.8 K (fit quality $\chi^2 = 1.020$). (d) LF μSR spectra with a 300 Oe applied longitudinal field driven from zero field and with a 300 Oe field after having been driven to 20 kOe at 0.02 K (fit quality $\chi^2 = 1.076$ for 300 Oe before 20 kOe and $\chi^2 = 1.094$ for 300 Oe after 20 kOe). The grey symbols represent the raw data and the black curves are for the fit to Eq. 6.5.

Table 6.2: Details of the fit parameters for the 0.8 K data.

Components	F_i (F_j)(%)	f_i (f_j) (0.8 K) (MHz)	λ (MHz)
F_1	32.6 (± 4.8)%	24.3 (± 1.6)	82.1 (± 7.9)
F_2	22.2 (± 2.0)%	53.5 (± 1.3)	66.4 (± 7.6)
F_3	9.2 (± 0.9)%	N/A	62.3 (± 17.7)
F_4	7.2 (± 0.8)%	N/A	9.2 (± 0.9)
F_5	29.0%	N/A	0.5 (± 0.0052)
A_{relax}	13.5 (± 0.025)	N/A	N/A
A_{BG}	10.4 (± 0.026)	N/A	N/A

the molecules, similar to the cluster-based SMMs [127–132]. The transition temperature of the Dy complex is between 0.8 and 1.8 K as muon precession was observed at 0.8 K but not at 1.8 K. A calculation was executed by Dr. Francis Pratt from ISIS whose result suggests that the dipolar energy between molecules in CP*-Dy-COT is no more than 0.6 K. This indicates that long-range magnetic order is possible below this temperature. However, the long-range magnetic order is still observed at 0.8 K in this material. The dipolar energy seems to be insufficient for a pure dipolar ordering above 0.8 K. It is possible that some other factors, such as weak exchange interactions, enhance the long-range magnetic order in CP*-Dy-COT.

According to the high temperature data, where CP*-Dy-COT is in its paramagnetic state, it is likely that there are two muon sites in the sample that correspond to two conformers of this Dy based SIM. Among the five components shown in Table 6.2, the fifth component with $F_5 \sim 30\%$ is consistent with F_3 in Eq. 6.2 at high temperatures. It has a relatively small relaxation rate λ_5 of approximately 0.5 MHz. This indicates that the fifth component at low temperatures also corresponds to muons experiencing a field that is parallel to their spins so that they can only relax when the internal field fluctuates. The two oscillatory terms describe the muons sitting at the two sites and probing two different internal magnetic field, B_1 = 24.3 MHz ($\frac{f_1}{\gamma_\mu}$ = 1793 Oe) and B_2 = 53.5 MHz ($\frac{f_2}{\gamma_\mu}$ = 3948 Oe). The ratio of these two oscillatory terms is also roughly 60 : 40 indicating that the muon sites at low temperatures are identical to the high

temperature case, which have two muon sites corresponding to the two conformers in the structure. For the third and fourth components, which are two exponential relaxation terms, the volume fractions are much smaller than F_1 and F_2. The ratio of F_3 and F_4 is again roughly 60 : 40 and can again be attributed to the same muon sites as F_1 and F_2 but without experiencing the long-range order. Although there are five components at low temperatures as described by Eq. 6.5, there are only two muon sites corresponding to the muons sitting at the two different conformers. The dipolar and exchange interactions, which enables long-range ordering in CP*-Dy-COT, are very weak such that the state may not be completely ordered. The disorder may give rise to the third and fourth terms, which are relaxation terms for muons probing internal field dynamics.

The magnetic hysteretic behaviour was investigating using applied longitudinal fields during the μSR measurements. In these measurements, a μSR spectrum was first measured with an applied field of LF = 300 Oe. The field was then driven to 20 kOe and kept for 2 minutes followed by the same measurement with LF = 300 Oe. Fig. 6.7 (d) shows the spectra before and after 20 kOe. It can be seen that they are significantly different. The spectrum after 20 kOe has a higher baseline and muon spin precession frequency. This can be attributed to the magnetic moments becoming more aligned along the field direction after the 20 kOe field. This is indicative of a hysteretic behaviour in CP*-Dy-COT.

In this section, it was shown that long-range magnetic order in CP*-Dy-COT can be observed. Further evidence of this behaviour using other techniques, such as heat capacity measurements below 1 K, have been planned. If confirmed, this is the first report of long-range magnetic ordering in SIMs. Furthermore, the internal field distributions at the two muon sites were approximated and the relaxation times for the Dy complex discussed in Section 6.2.3 were calculated.

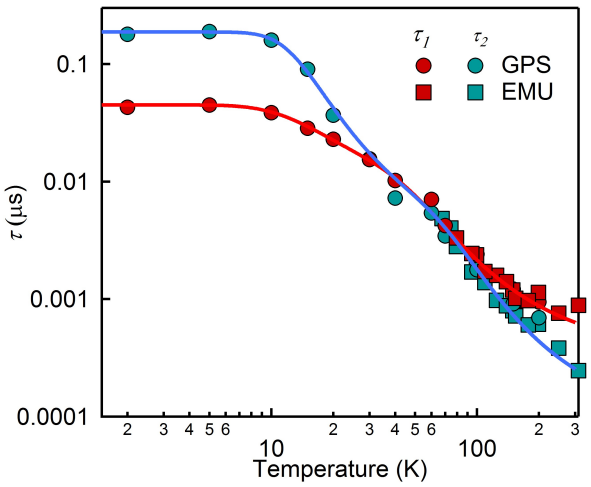

Figure 6.8: The calculated zero-field magnetisation relaxation time ($\tau = 1/\nu$) corresponding to two conformers (τ_1 for the eclipsed conformer and τ_2 for the staggered conformer) in the structure from 2 K to room temperature. The red and blue symbols are data points and curves are fit to Eq. 6.6 (fit quality $\chi^2 = 0.966$ (τ_1), 0.945 (τ_2)).

6.2.5 Magnetisation relaxations and relaxation mechanism in CP*-Dy-COT

It is now possible to use the measured internal field distributions of the two muon sites to calculate the magnetisation relaxation time of the sample $\tau = 1/\nu$ given the measured muon spin relaxation rate λ reported in Section 6.2.3. Fig. 6.8 shows the magnetisation relaxation time τ of the two conformers as a function of temperature. Below 10 K, τ_1 and τ_2 are constant indicating that the thermal process is negligible and the quantum tunnelling is dominant. In this quantum tunnelling regime, the magnetisation relaxation time of the sample is approximately 0.1 μs. This is three orders of magnitude smaller than the value obtained from the AC susceptibility measurements for a diluted sample, as shown in Fig. 6.3 [103]. Above 10 K, the thermal process plays a significant role in the magnetisation relaxation and consequently τ_1 and τ_2 decrease rapidly with increasing temperature.

As discussed in Section 2.2.3, the magnetisation relaxation in an SIM is believed to be composed of four processes: direct, quantum tunnelling, Orbach and Raman

Table 6.3: Fit parameters using Eq. 6.6 for CP*-Dy-COT.

	QT	Orbach Process 1		Orbach Process 2	
Conformer	B_1 (μs^{-1})	τ_0^{-1} (μs^{-1})	U_{eff} (meV)	τ_0^{-1} (μs^{-1})	U_{eff} (meV)
Eclipsed	22.8 ($\pm$ 0.2)	2985 ($\pm$ 800)	19.5 ($\pm$ 2)	149 ($\pm$ 16)	3.3 ($\pm$ 0.2)
Staggered	5.34 ($\pm$ 0.05)	11832 ($\pm$ 2340)	30.9 ($\pm$ 15)	420 ($\pm$ 53)	5.4 ($\pm$ 0.2)

processes. These processes are described by the following equation:

$$\nu = AH^2T + \frac{B_1}{1 + B_2H^2} + CT^n + \tau_0^{-1} \exp\left(-\frac{U_{eff}}{k_BT}\right). \tag{6.6}$$

In order to study the magnetisation relaxation mechanisms in CP*-Dy-COT, τ_1 and τ_2 shown in Fig. 6.8 are independently fitted using the equation above. It is found that τ_1 and τ_2 are well described by the same model consisting of a single quantum tunnelling (QT) process and two Orbach processes. The fit parameters are listed in Table 6.3. It can be seen from Fig. 6.8 that τ_1 is smaller below 40 K, however, τ_2 decreases more rapidly. This is consistent with the fit parameters. Below 10 K, where the quantum tunnelling process is dominant, τ_1 is longer in the eclipsed conformer, whereas when T $>$ 10 K, the effective energy barriers of both Orbach processes in the eclipsed conformer are smaller than those in the staggered one.

The different relaxation pathways can be analysed by studying the electronic structure of CP*-Dy-COT. The crystal field in this material has been previously calculated by Jiang in Ref. [103]. Their results are shown in Fig. 6.9 (a). In the calculation, the temperature dependent magnetic susceptibilities, which reflect the thermal population of the split ground multiplets, were fitted with the CONDON program. This method of calculating the electronic fine structure in SIMs using the magnetic susceptibility data was initially developed by Ishikawa [204].

Details of the ground and the lowest four excited states in the Dy complex are shown in Fig. 6.9 (b). The quantum tunnelling process occurs between the ground doublet states, whereas the thermally activated relaxation is described by two Orbach processes. It can be seen in Table 6.3 that the effective energy barriers of the eclipsed conformer

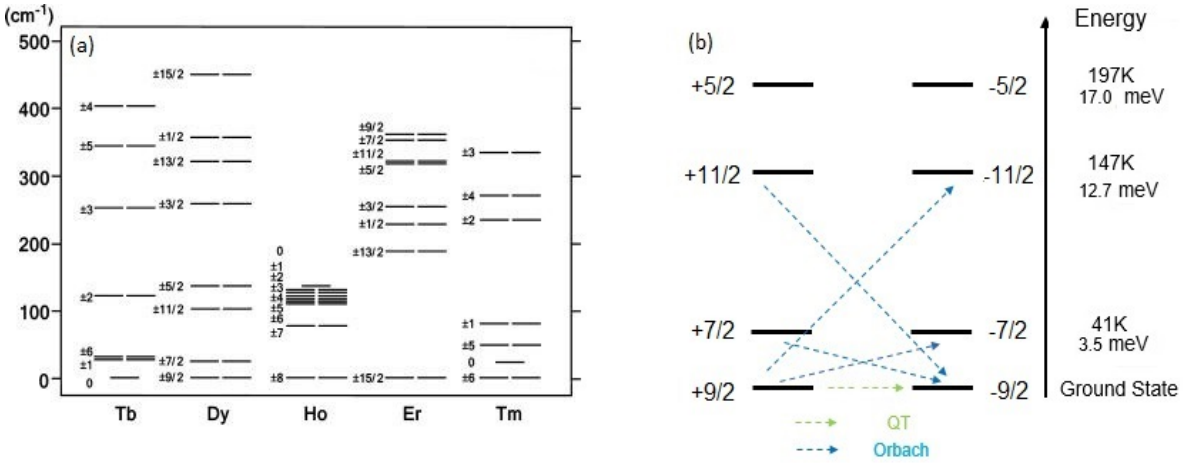

Figure 6.9: (a) The electronic structure of CP*-Dy-COT calculated by Jiang in Ref. [103]. (b) Various magnetisation relaxation pathways in the Dy complex.

match the electronic structure of the Dy complex very well.

In the second Orbach process of the eclipsed conformer, $U_{eff2} = 3.3$ ($\pm$ 0.2) meV. This is comparable with the energy barrier between the first excited state and the ground state. Therefore, this Orbach process may describe a magnetisation relaxation via the first excited state. Similarly, $U_{eff1} = 19.5$ ($\pm$ 0.2) meV is consistent with the energy barrier between the third excited state and the ground states, thus can describe a magnetic relaxation via the third excited state. Therefore, two Orbach processes are measured. The relaxation via the second excited state is absent here. This may be due to the fact that the first Orbach process is dominant when $T > 150$ K. However, there are only four data points consequently the fit parameters may not precise enough to describe the relaxation. The reason why the second excited state is absent requires further investigations.

In the case of the staggered conformer, the measured energy barriers are much higher than those of the eclipsed conformer. The fitted values do not match the calculated values shown in Fig. 6.9 (b). This may be due to the structure as well as the bending angle being different and the crystal field most likely varies in the two conformers. This has a large impact on the magnetisation relaxation. As the electronic structure in Fig. 6.9 is based on the magnetic susceptibility whose dominant component is that of the

eclipsed conformer, it is unlikely to model the magnetisation relaxation accurately in the staggered conformer.

6.2.6 Longitudinal field dependence of the magnetisation relaxation in CP*-RE-COT

Longitudinal magnetic fields were also applied in the μSR measurements, in order to extract essential information about the direct relaxation. This term is expected to vary quadratically with the magnetic field. Fig. 6.10 (a) and (b) show the field dependence of λ_1 and λ_2 for several temperatures. It is immediately clear that at all temperatures, λ_1 and λ_2 are relatively field independent at low fields, but in the region of 1000 Oe, a clear peak in the relaxation rate is evident at all temperatures. The lower the temperature, the more pronounced is the peak. The relaxation rate's increment at 1000 Oe can be directly observed in the raw (time-resolved) data, as shown in Fig. 6.10 (c). It is clear that at 1000 Oe, the muon spin relaxation is faster than in the zero field case. Thus, according to Eq. 3.35, where muon spin relaxation rate is inversely proportional to the spin fluctuation rate in the system, it is obvious that the magnetisation relaxation slows down dramatically at around 1000 Oe.

This 1000 Oe peak has also been observed in the Tm and Tb compounds of the CP*-RE-COT series. This is shown in Fig. 6.11. AC susceptibility measurements of the Tb and Tm compounds also exhibit 1000 Oe peaks in the χ'' data at 2.5 K, as shown in Fig. 6.12. Since we verified the peaks with two independent instruments, a possible instrument related artefact as explanation for the peaks at 1000 Oe can be clearly ruled out. These results suggests that the magnetisation relaxation in these materials slows down dramatically in an applied magnetic field of 1000 Oe.

In the Hamiltonian of a single-ion magnet, there are two terms, the spin-spin inter-

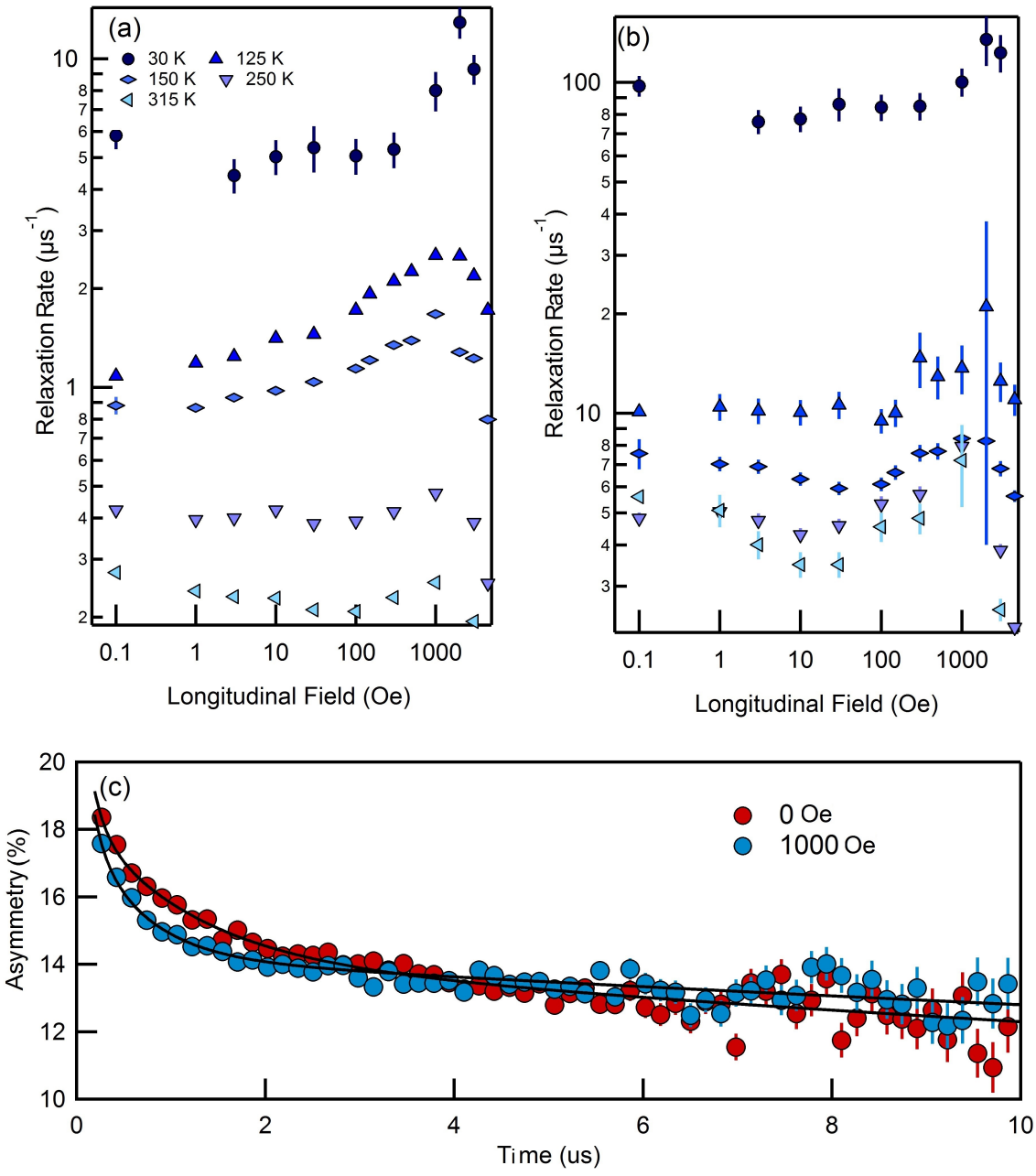

Figure 6.10: (a) The field dependence of the muon spin relaxation rate λ_1 at 30, 100, 125, 150, 250 and 315 K. (b) The field dependence of the muon spin relaxation rate λ_2 at 30, 100, 125, 150, 250 and 315 K. (c) Comparison of μSR spectra at zero field and using a longitudinal field of 1000 Oe at 250 K (with fit quality $\chi^2 = 1.196$ (0 Oe), 1.142 (1000 Oe)).

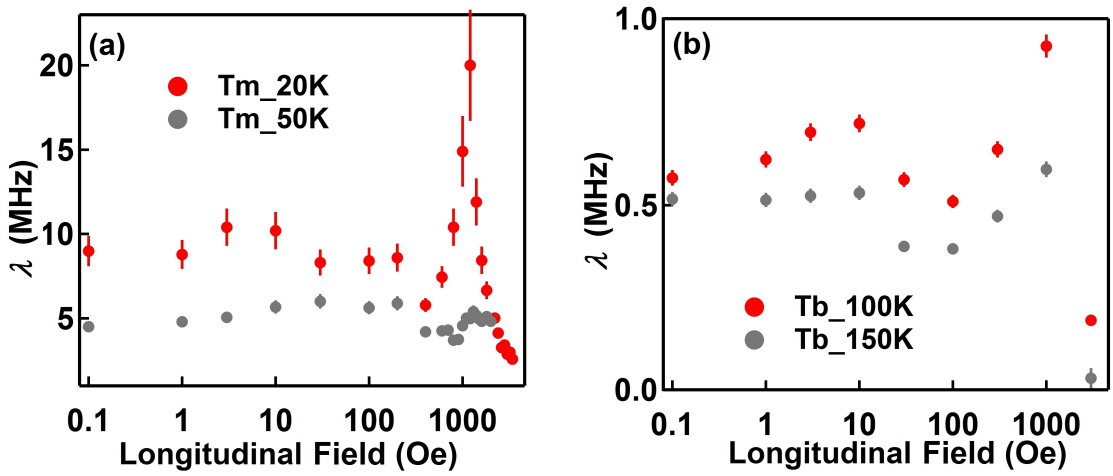

Figure 6.11: (a) The field dependence of the muon spin relaxation rate λ_1 of the Tm compound at different temperatures. (b) The muon spin relaxation rate λ_1 as a function of field of the Tb compound at different temperatures.

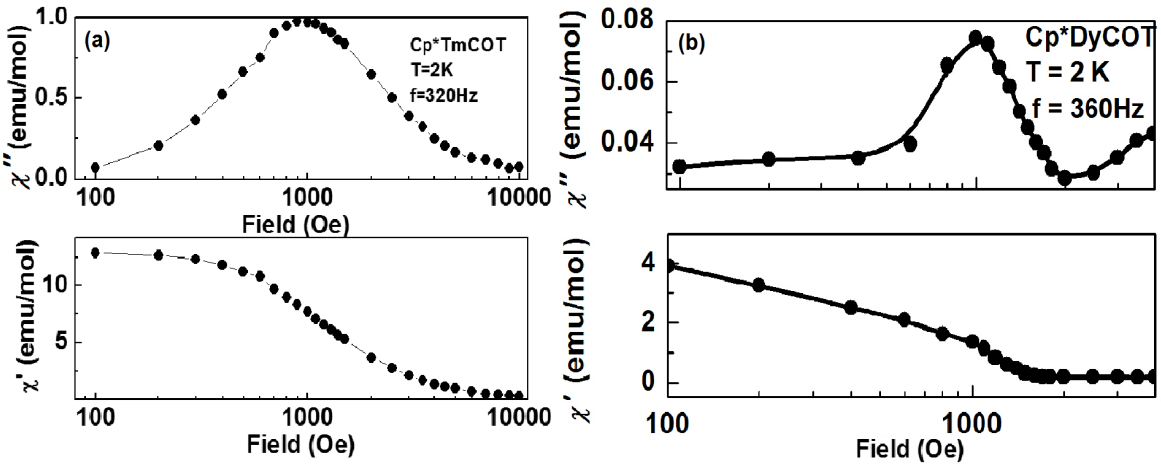

Figure 6.12: AC susceptibility data of CP*-RE-COT. The peaks near 1000 Oe also appear using this instrument. (a) The AC susceptibility data for the Tm complex at 2.5 K. (b) The AC susceptibility data for the Dy complex at 2.5 K.

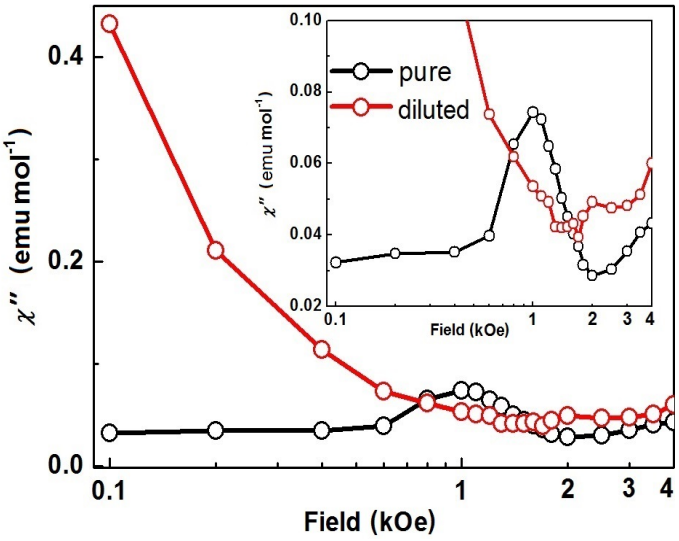

Figure 6.13: The field dependence of χ'' for pure CP*-Dy-COT and CP*-$Dy_{0.05}Y_{0.95}$-COT employing an AC field amplitude of 3 Oe and a frequency of 360 Hz. The inset shows the same data as the main figure but with an emphasis on the maximum near 1000 Oe.

action term and the Zeeman term:

$$H = -\sum_{i<j} J_{ij}\vec{S}_i \cdot \vec{S}_j + g\mu_B \sum_i \vec{B} \cdot \vec{S}_i, \tag{6.7}$$

where J_{ij} is the exchange energy between two nearest single ions, $g = 10$ is the g-factor of the lanthanide ion. When the exchange energy matches the Zeeman interaction energy, the quantum tunnelling the two entangled degenerated ground states is suppressed. Hence, there would be a significant slow down of the magnetisation relaxation. In an applied field $B = \frac{J_{exchange}}{g\mu_B} \sim 1$ kOe ($J_{exchange} \sim 0.7$ K), the Zeeman energy matches with the exchange interaction in Eq. 6.7. Therefore, the slow down of the magnetisation relaxation at about 1000 Oe is the consequence of the suppression of quantum tunnelling.

Field dependent AC susceptibility measurements of a diluted Dy complex were carried out to verify these results. In a diamagnetic Y complex sample with a 5% concentration of the Dy complex, the dipolar interaction as well as the intermolecular interactions between the CP*-Dy-COT molecules is reduced. Fig. 6.13 shows the re-

sults for the pure and diluted samples. It is clear that for the diluted sample the 1000 Oe peak disappears. Since the average intermolecular distance is linked to a decrease of the exchange interaction, we can conclude that the maximum near 1000 Oe has its origin in the exchange interaction between magnetic moments of the Dy complex.

The exchange energy ($\sim$ 0.7 K) may be a possible source of the enhanced long-range magnetic order in CP*-Dy-COT. If the exchange energy contributes additively, the critical temperature increases to approximately 1.3 K. This temperature is in the correct temperature window (between 0.8 and 1.8 K), in which the μSR results are indicative of a magnetic transition. Further investigations are still needed to confirm these findings.

6.3 Conclusion

In conclusion, the magnetisation relaxation mechanisms of a series of single molecule magnets CP*-RE-COT were investigated using the μSR technique. Between 2 K and room temperature, the Dy compounds exhibited three possible relaxation pathways, one quantum tunnelling process and two Orbach processes. The energy barriers obtained from the magnetisation relaxation analysis matched the calculated electronic structure of the Dy complex. This potentially opens an avenue to experimentally measure the electronic structure of SMMs, which is complicated to be calculated when $4f$ lanthanide ions are included.

Long-range magnetic order in the Dy complex was indicated by the μSR measurements. If confirmed in a future experiment, this would be the first long-range magnetic order observed in an SIM system. It has a transition temperature between 0.8 and 1.8 K. However, the dipolar energy seems to be insufficient for a pure dipolar ordering above 0.8 K, which may suggest that hte exchange interaction contributes. To confirm long-range magnetic order, further investigations are needed.

The existence of exchange interaction in this series of materials was also indicative in

the measurements of magnetisation relaxations. In an applied longitudinal fields, a peak around 1000 Oe was observed in the relaxation data obtained with the μSR technique and χ'' from AC susceptibility measurements for all Tm, Dy and Tb compounds. This is probably a result of the suppression of quantum tunnelling between the entangled ground states. The prevention of this quantum mechanical tunnelling process is caused by the applied magnetic field that quenches the exchange interaction.

In order to fully understand the relaxation mechanisms in this series of SIMs, a more precise calculation of the electronic structure of all series members as well as thorough investigations of the Tb and Tm complexes are required.

Chapter 7

Conclusion and Future Work

In this thesis, the magnetism of $BiFeO_3$, multiferroic MOFs CuGF and a series of single molecule magnets CP*-RE-COT were discussed. The exotic magnetic properties in these systems, namely the magnetoelectric coupling in multiferroic $BiFeO_3$ and copper guanidinium formate, the magnetisation relaxation mechanisms in CP*-RE-COT as well as their magnetic structures were investigated.

In the case of $BiFeO_3$, which is a room temperature multiferroic material, an RF thin film deposition system was built. However, due to the compatibility problem of the substrate heater, no high-quality epitaxial $BiFeO_3$ thin film was successfully deposited. With a self-developed ferroelectric characterisation system, the ferroelectricity in the epitaxial $BiFeO_3$ thin films from the Bouyanfif's group at the Université de Picardie Jules Verne was studied. Unfortunately, the large leakage current in these films hindered the investigation of the ferroelectricity and any further study on magnetoelectric coupling in the thin film structure. Investigations on spin cycloid in these $BiFeO_3$ thin films were carried out by the grazing-incidence small angle neutron scattering. Two satellites were observed at around $Q = 0.01$ Å^{-1}. However, the data were of low quality and further measurements are needed.

The multiferroic MOF, $[C(NH_2)_3][Cu(HCOO)_3]$, was studied with magnetometry and the μSR technique. Spin-canted antiferromagnetic order with a Néel temperature

of 4.6 K was detected. Critical phenomena were also investigated, which indicate that CuGF possesses 3D Heisenberg long-range magnetic order below the critical temperature. Above the Néel temperature, a broad peak at about 45 K was observed in the magnetic susceptibility data, which is a signature of one-dimensional magnetic chain in the system. The magnetic correlations in this one-dimensional system was also studied with the locally probing μSR technique. The correlation length was determined and its field dependence exhibits an inverse proportionality: $\xi \sim H^{-1}$. This may be caused by the field's influence on the transverse correlations from the spin-canting effect.

In single molecule magnets CP*-RE-COT, magnetisation relaxations were measured with an AC magnetometer and the μSR technique. The Dy compound exhibits three possible relaxation pathways, including a quantum tunnelling process and two Orbach relaxation processes. When a magnetic field was applied, a peak around 1000 Oe was observed in all of the Tm, Dy and Tb compounds, for both μSR and AC susceptibility measurements. Due to the exchange interactions in CP*-RE-COT, the quantum tunnelling effect was suppressed by a certain applied magnetic field that matched the exchange interactions. Moreover, the μSR data suggest long-range magnetic ordering in CP*-Dy-COT. If confirmed, this is the first report of long-range magnetic ordering in an SIM system, even though it has been reported in several cluster-based SMMs.

There are still some open issues left that requires further investigations:

- Spin cycloid and magnetoelectric coupling in $BiFeO_3$: due to the relatively poor data quality, the study of the spin cycloidal structure in $BiFeO_3$ thin film is not conclusive. It is planned to use an instrument with a more appropriate Q range and to count for a longer time for a better data quality. If the existence of the spin cycloid is confirmed in thin films, both temperature and magnetic field dependence measurements will be performed to study the evolution of this cycloidal structure as a function of temperature and magnetic field.

  Efforts shall be made to reduce the leakage current in $BiFeO_3$ epitaxial films. With a smaller leakage current, the ferroelectric properties can be investigated and a

further study of the magnetoelectric coupling in $BiFeO_3$ with neutron scattering and ferroelectric characterisation will be carried out.

- One-dimensional magnetic chains: it was discussed in Chapter 5 that CuGF and CuDMF behaved differently in the μSR measurements even though they have similar molecular structures with one-dimensional copper chains. This may originate from the fact that spin dynamics, or the spin correlations are different in these two MOFs; they may possess different but similar organic frameworks. It is possible to study more MOFs with one-dimensional magnetic chains to investigate how the structures of the MOFs couples with the properties of the one-dimensional magnetic chains.

- CP*-RE-COT: the measurements on this whole series of single ion magnets have not been completed. Further investigations of the other members (the Tb and Tm complexes) within the series have been proposed. Moreover, the measurements on the magnetisation relaxations can also be improved by extending the temperature range. With a thorough study of the whole series of magnets, it may be possible to understand what determines the anisotropy and zero-field splitting properties. This is crucial to understanding the nature of local anisotropy in SIMs.

  The behaviour consistent with long-range magnetic order was detected in CP*-Dy-COT using the μSR technique. Further measurements, e.g. heat-capacity or susceptibility measurements at low temperatures (< 2 K) are planned in order to confirm the long-range magnetic order in this material.

  It was shown that the electronic energy levels can be measured by analysing the magnetisation relaxations in these lanthanide-based single ion magnets. This could provide experimental data to validate existing models of lanthanide-based complexes. Calculation of the electronic structures of these single ion magnets is also planed in order to fully understand the relaxation mechanisms in these materials.

Bibliography

[1] N. A. Spaldin, S.-W. Cheong, and R. Ramesh. Multiferroics: Past, present, and future. *Physics Today.*, 63:38, 2010.

[2] N. A. Hill. Why are there so few magnetic ferroelectrics? *J. Phys. Chem. B.*, 104:6694, 2000.

[3] T. Kimura, T. Goto, H. Shintani, K. Ishikawa, T. Arima, and Y. Tokura. Magnetic control of ferroelectric polarization. *Nature*, 426:55, 2003.

[4] N. Hur, S. Park, P. A. Sharma, J. S. Ahn, S. Guha, and S-W. Cheong. Electric polarization reversal and memory in a multiferroic material induced by magnetic fields. *Nature*, 429:392, 2004.

[5] M. Kurmoo. Magnetic metal-organic frameworks. *Chem. Soc. Rev.*, 38:1353, 2009.

[6] X. Y. Wang, Z. M. Wang, and S. Gao. Constructing magnetic molecular solids by employing three-atom ligands as bridges. *Chem. Commun.*, 3:281, 2008.

[7] R. Sessoli, D. Gatteschi, A. Caneschi, and M. A. Novak. Magnetic bistability in a metal-ion cluster. *Nature*, 365:141, 1993.

[8] R. Lescouezec, L. M. Toma, J. Vaissermann, M. Verdaguer, F. S. Delgado, C. Ruiz-Perez, F. Lloret, and M. Julve. Design of single chain magnets through cyanide-bearing six-coordinate complexes. *Coord. Chem. Rev.*, 249:2691, 2005.

[9] X. Y. Wang, L. Wang, Z. M. Wang, G. Su, and S. Gao. Coexistence of spin-canting, metamagnetism, and spin-flop in a (4,4) layered manganese azide polymer. *Chem. Mater.*, 17:6369, 2005.

[10] Y. Imry, P. Oincus, and D. Scalapino. Phase transition in quasi-one-dimensional magnetic structures: quantum effects. *Phys. Rev. B.*, 12:1978, 1975.

[11] M. Azzouz. Field-induced quantum criticality in low-dimensional heisenberg spin systems. *Phys. Rev. B.*, 74:174422, 2006.

[12] W. Wernsdorfer and R. Sessoli. Quantum phase interference and parity effects in magnetic molecular clusters. *Science*, 284:133, 1999.

[13] A. Yaouanc, A. Maisuradze, and P. Dalmas De Reotier. Influence of short-range spin correlations on the sr polarization functions in the slow dynamic limit: Application to the quantum spin-liquid system $Yb_2Ti_2O_7$. *Phys. Rev. B.*, 87:134405, 2013.

[14] J. Herrero-Albillos, G. Catalan, J. Alberto Rodriguez-Velamazan, M. Viret, D. Colson, and J. F. Scott. Neutron diffraction study of the $BiFeO_3$ spin cycloid at low temperature. *J. Phys. Condens, Mat.*, 22:256001, 2010.

[15] G. Catalan and J. F. Scott. Physics and applications of bismuth ferrite. *Adv. Mater.*, 21:2463, 2009.

[16] P. Jain, V. Ramachandran, R. J. Clark, H. Zhou, B. H. Toby, N. S. Dala, H. W. Kroto, and A. K. Cheetham. Multiferroic behavior associated with an order-disorder hydrogen bonding transition in MetalOrganic Frameworks (MOFs) with the perovskite ABX_3 architecture. *J. Am. Chen. Soc.*, 131:13625, 2009.

[17] K. Hu, M. Kurmoo, Z. Wang, and S. Gao. Metal-organic perovskites: Synthesis, structures, and magnetic properties of $[C(NH_2)_3][M^{II}(HCOO)_3]$ (M=Mn, Fe, Co, Ni, Cu, and Zn; $C(NH_2)_3$= Guanidinium). *Chem. Eur. J*, 15:12050, 2009.

[18] G. Xu, W. Zhang, Z. Ma, Y. Chen, L. Zhang, H. Cai, Z. Wang, R. Xiong, and S. Gao. Coexistence of magnetic and electric orderings in the metal-formate frameworks of $[NH_4][M(HCOO)_3]$. *J. Am. Chem. Soc.*, 133:14948, 2011.

[19] L. Canadillas-Delgado, O. Fabelo, J. Alberto, M. Lemee-Cailleau, S. A. Mason, E. Pardo, F. Lloret, J. Zhao, X. Bu, V. Simonet, C. V. Colin, and J Rodriguez-Carvajal. The role of order-disorder transitions in the quest for molecular multiferroics: Structural and magnetic neutron studies of a mixed valence iron(II)-iron(III) formate framework. *J. Am. Chem. Soc.*, 134:19772, 2012.

[20] X. Y. Wang, L. Wang, Z. M. Wang, and S. Gao. Solvent-tuned azido-bridged Co^{2+} layers: Square, honeycomb, and kagomé. *J. Am. Chem. Soc.*, 128:674, 2006.

[21] N. Ishikawa, M. Sugita, T. Ishikawa, S.-Y. Koshihara, and Y. Kaizu. Lanthanide double-decker complexes functioning as magnets at the single-molecular level. *J. Am. Chem. Soc.*, 125:8694, 2003.

[22] M. Bibes and A. Barthelemy. Multiferroics: Towards a magnetoelectric memory. *Nature*, 7:425, 2008.

[23] M. Mannini, F. Pineider, P. Sainctavit, C. Danieli, E. Otero, C. Sciancalepore, A. M. Talarico, M. Arrio, A. Cornia, D. Gatteschi, and R. Sessoli. Magnetic memory of a single-molecule quantum magnet wired to a gold surface. *Nat. Mater.*, 8:194, 2009.

[24] H. Bea, M Gajek, and M. Barthelemy. Spintronics with multiferroics. *J. Phys. Condens. Matter.*, 20:434221, 2008.

[25] M. N. Leuenberger and D. Loss. Quantum computing in molecular magnets. *Nature*, 410:789, 2009.

[26] K. M. L. Taylor, W. J. Rieter, and W. Lin. Manganese-based nanoscale metal-organic frameworks for magnetic resonance imaging. *J. Am. Chem. Soc.*, 130:14358, 2008.

[27] G. Lu and J. T. Hupp. Metalorganic frameworks as sensors: A zif-8 based fabry-pérot device as a selective sensor for chemical vapors and gases. *J. Am. Chem. Soc.*, 132:7832, 2010.

[28] D. Buso, J. Jasieniak, M. D. H. Lay, P. Schiavuta, P. Scopece, J. Laird, H. Amenitsch, A. J. Hill, and P. Falcaro. Highly luminescent metal-organic frameworks through quantum dot doping. *Small*, 8:80, 2012.

[29] S. Jiang, B. Wang, G. Su, Z. Wang, and S. Gao. A mononuclear dysprosium complex featuring single-molecule-magnet behavior. *Angew. Chem. Int. Ed.*, 49:7448, 2010.

[30] G. Christou, D. Gatteschi, S. D. Hendrickson, and R. Sessoli. Single-molecule magnets. *MRS. BULLETIN*, 25:66, 2000.

[31] F. Torres, J. M. Hernandez, X. Bohigas, and J. Tejada. Giant and time-dependent magnetocaloric effect in high-spin molecular magnets. *J. Appl. Phys. Lett.*, 77:3248, 2000.

[32] A. Caneschi, D. Gatteschi, R. Sessol, A. L. Barra, L. C. Brunel, and M. Guilloti. Alternating current susceptibility, high field magnetization, and millimeter band EPR evidence for a ground S = 10 state in $[Mn_{12}O_{12}(Ch_3COO)_{16}(H_2O)_4]\cdot 2CH_3COOH\cdot 4H_2O$. *J. Am. Chem. Soc.*, 113:5873, 1991.

[33] L. Ungur, J. J. Le Roy, L. Korobkov, and M. Murugesu. Fine-tuning the local symmetry to attain record blocking temperature and magnetic remanence single-ion magnet. *Angew. Chem.*, 126:4502, 2014.

[34] H. C. Orsted. *Experimenta Circa Effectum Conflictus Electrici in Acum Magneticam.* Hafniae: Typis Schultzianis, 1820.

[35] P. Curie. Sur la symètrie dans les phénomènes physiques, symétrie d'un champ électrique et d'un champ magnétique. *J. Phys. Theor. Appl.*, 3:393, 1894.

[36] I. E. Dzyaloshinskii. On the magneto-electrical effect in antiferromagnets. *Sov. Phys. JETP*, 10:628, 1959.

[37] D. N. Astrov. The magnetoelectric effect in antiferromagnetics. *Sov. Phys. JETP*, 11:708, 1960.

[38] J. Wang, J. B. Neaton, H. Zheng, V. Nagarajan, S. B. Ogale, B. Liu, D. Viehland, V. Vaithyanathan abd D. G. Schlom, U. V. Waghmare, N. A. Spaldin, K. M. Rabe, M. Wuttig, and R. Ramesh. Epitaxial $BiFeO_3$ multiferroic thin film heterostructures. *Science.*, 299:1719, 2003.

[39] W. Eerenstein, N. D. Mathur, and J. F. Scott. Multiferroic and magnetoelectric materials. *Nature*, 442:759, 2006.

[40] N. A. Spaldin and M. Fiebig. The renaissance of magnetoelectric multiferroics. *Science.*, 309:391, 2005.

[41] C. F. Fennie and K. M. Rabe. Ferroelectric transition in $YMno_3$ from first principles. *Phys. Rev. B.*, 72:100103, 2005.

[42] N. Ikeda, H. Ohsumi, K. Ohwada, K. Ishii, T. Inami, Kazuhisa Kakurai, Y. Murakami, K. Yoshii, S. Mori, Y. Horibe5, and H. Kito. Ferroelectricity from iron valence ordering in the charge-frustrated system $LuFe_2O_4$. *Nature*, 436:1136, 2005.

[43] L. V. Shuvalov and N. V. Belov. Symmetry of crystals in which ferromagnetic and ferroelectric properties appear simultaneously. *Science.*, 309:391, 2005.

[44] J. M. Rondinelli, A. S. Eidelson, and N. A. Spaldin. Non-d^0 Mn-driven ferroelectricity in antiferromagnetic $BaMnO_3$. *Phys. Rev. B.*, 79:205119, 2009.

[45] G. T. Rado. Observation and possible mechanisms of magnetoelectric effects in a ferromagnet. *Phys. Rev. Lett.*, 13:335, 1964.

[46] B. Kundys, M. Viret, D. Colson, and D. O. Kundys. Light-linduced size changes in $BiFeO_3$ crystals. *Nat. Mater*, 9:803, 2010.

[47] O. M. Yaghi and H. L. Li. Hydrothermal synthesis of a metal-organic framework containing large rectangular channels. *L. Am. Chen. Soc.*, 117:10401, 1995.

[48] M. Eddaoudi, J. Kim, N. Rosi, D. Vodak, J. Wachter, M. O'Keeffe, and O. M. Yaghi. Systematic design of pore size and functionality in isoreticular MOFs and their application in methane storage. *Science*, 295:469, 2002.

[49] J. L. Rowsell and O. M. Yaghi. Strategies for hydrogen storage in metal-organic frameworks. *Angew. Chem, Int.Ed.*, 44:4670, 2005.

[50] J. S. Seo, D. Whang, H. Lee, S. I. Jun, J. Oh, Y. J. Jeon, and K. Kim. A homochiral metal-organic porous material for enantioselective separation and catalysis. *Nature*, 404:982, 2000.

[51] C. A. Kent, B. P. Mehl, L. Ma, J. M. Papanikolas, T. J. Meyer, and W. Lin. Energy transfer dynamics in metal-organic frameworks. *J. Am. Chem. Soc.*, 132:12767, 2010.

[52] W. Zhang and R. Xiong. Ferroelectric metal-organic frameworks. *Chem. Rev.*, 112:1163, 2012.

[53] A. Stroppa, P. Barone, P. Jain, J. M. Perez-Mato, and S. Picozzi. Hybrid improper ferroelectricity in a multiferroic and magnetoelectric Metal-Organic Framework. *Adv. Mater.*, 25:2284, 2013.

[54] A. Stroppa, P. Jain, P. Barone, M. Marsman, J. M. Perez-Mato, A. K. Cheetham, H. W. Kroto, and S. Picozzi. Electric control of magnetization and interplay between orbital ordering and ferroelectricity in a multiferroic Metal-Organic Framework. *Angew. Chem.*, 123:5969, 2011.

[55] F. Kagawa, S. Horiuchi, M. Tokunaga, J. Fujioka, and Y. Tokura. Ferroelectricity in a one-dimensional organic quantum magnet. *Nature Physics*, 5:169, 2010.

[56] Y. Tian, J. Cong, S. Shen, Y. Chai, L. Yan, S. Wang, and Y. Sun. Electric control of magnetism in a multiferroic metalorganic framework. *Phys. Status. Solidi.*, 8:91, 2014.

[57] Y. Tian, A. Stroppa, Y. Chai, L. Yan, S. Wang, P. Barone, S. Picozzi, and Y. Sun.

[58] Y. Tian, A. Stroppa, Y. Chai, P. Barone, M. Perez-Mato, S. Picozzi, and Y. Sun. High-temperature ferroelectricity and strong magnetoelectric effects in a hybrid organic-inorganic perovskite framework. *Phys. Status Solid*, 9(1):62, 2014.

[59] A. K. Cheetham and C. N. R. Rao. There's room in the middle. *Science*, 378(5847):58, 2007.

[60] G. Férey. Hybrid porous solids: past, present, future. *Chem. Soc. Rev.*, 37:191, 2008.

[61] C. J. Kepert. Advanced functional properties in nanoporous coordination framework materials. *Chem. Commun.*, 7:695, 2006.

[62] R. A. Fischer and C. Wôll. Functionalized coordination space in metal-organic frameworks. *Angew. Chem.*, 47:8164, 2008.

[63] M. J. Zaworotko. Materials science: Designer pores made easy. *Nature*, 451:410, 2008.

[64] C. N. R. Rao, A. K. Cheetham, and A. Thirumurugan. Hybrid inorganic-organic materials: a new family in condensed matter physics. *J. Phys. Condens. Matter.*, 20:083202, 2008.

[65] D. Maspoch, D. Ruiz-Molina, and J. Veciana. Old materials with new tricks: multifunctional open-framework materials. *Chem. Soc. Rev.*, 36:770, 2007.

[66] H. Miyasaka and R. Clorac. Synthetic strategy for rational design of single-chain magnets. *Bull. Chem. Soc. Jpn.*, 78:1725, 2005.

[67] L. Bogani, A. Vindigni, R. Sessolia, and D. Getteschi. Single chain magnets: where to from here? *J. Mater. Chem.*, 18:4750, 2005.

[68] L. M. C. Beltran and J. R. Long. Directed assembly of metal-cyanide cluster magnets. *Acc. Chem. Res.*, 38:325, 2005.

[69] S.I. Ohkoshi, K.-I. Arai, Y. Sato, and K. Hashimoto. Humidity-induced magnetization and magnetic pole inversion in a cyano-bridged metal assembly. *Nat. Mater.*, 3:857, 2004.

[70] O. Sato. Optically switchable molecular solids: photoinduced spin-crossover, photochromism, and photoinduced magnetization. *Acc. Chem. Res*, 36:692, 2003.

[71] S. J. Blundell and F. L. Pratt. Organic and molecular magnets. *J. Phys.: Condens. Matter*, 16:R771, 2004.

[72] E. Ising. Beitrag zur theorie des ferromagnetismus. *Z. Physik*, 31:253, 1925.

[73] J. C. Bonner and M. R. Fisher. Linear magnetic chains with anisotropic coupling. *Phys. Rev.*, 135(3A):A640, 1964.

[74] M. T. Hutchings, G. Shirane, R. J. Birgeneau, and S. L. Holt. Spin dynamics in the one-dimensional antiferromagnet $(CD_3)_4NMnCl_3$. *Phys. Rev. B.*, 5:1999, 1972.

[75] M. T. Hutchings, E. L. Samuelsen, G. Shirane, and K. HIRAKAWA. Neutron-diffraction determination of the antiferromagnetic structure of $KCuF_3$. *Phys. Rev.*, 188:919, 1969.

[76] I.U. Heilmann, G. Shirane, Y. Endoh, R. J. Birgeneau, and S. L. Holt. Neutron study of the line-shape and field dependence of magnetic excitations in $CuCl_2 \cdot 2N(C_5D_5)$. *Phys. Rev. B.*, 18:3530, 1978.

[77] M. Steiner, J. Villain, and C. G. Windsor. Theoretical and experimental studies on one-dimensional magnetic systems. *Advances in Physics*, 25:87, 1976.

[78] W.-X. Zhang, R. Ishikawa, B. Breedlove, and M. Yamashita. Single-chain magnets: beyond the glauber model. *RSC Adv.*, 3:3772, 2013.

[79] M. E. Fisher. Magnetism in one-dimensional systems-the heisenberg model for infinite spin. *Am. J. Phys.*, 32:343, 1964.

[80] Olivier Kahn. *Molecular Magnetism*. Wiley-VCH Publishers, New York, Weinheim, Cambridge, 1993.

[81] R. L. Carlin. *Magnetochemistry*. Springer, Berlin, 1986.

[82] A. Klumper. The spin -1/2 heisenberg chain: thermodynamics, quantum criticality and spin-Peierls exponents. *Eur. Phys. J. B*, 5:677, 1998.

[83] J. Bernasconi and T. Schneiderl. *Dynamics Correlations in Classical Heisenberg chain*. Springer-Verlag Berlin Heidelberg.

[84] S. K. Satija, J. D. Axe, and G. Shirane. Neutron scattering study of spin waves in one-dimensional antiferromagnet $KCuF_3$. *Phys. Rev. B.*, 21:2001, 1980.

[85] J. M. Law, H.-J. Koo, M.-H. Whangbo, E. Brücher, V. Pomjakushin, and R. K. Kremer. Strongly correlated one-dimensional magnetic behavior of $NiTa_2O_6$. *Phys. Rev. B.*, 89:014423, 2014.

[86] E. Ressouche, J. Boucherle, B. Gillon, P. Rey, and J. Schweizer. Spin density maps in nitroxide-copper(ii) complexes. a polarized neutron diffraction determination. *J. Am. Chem. Soc.*, 115:3610, 1993.

[87] G. Nenert, Hyun-Joo Koo, C. V. Colin, E. M. Bauer, C. Bellitto, C. Ritter, G. Righini, and M.-H. Whangbo. Magnetic order through super-superexchanges in the polar magnetoelectric organic-inorganic hybrid Cr[(D_3N-$(CH_2)_2$-PO_3)(Cl)(D_2O)]. *Inorg. Chem.*, 52:753, 2013.

[88] P. J. Saines, J. H.-M. Yeuong, J. R. Hester, A. R. Lennie, and A. K. Cheetham. Detailed investigations of phase transitions and magnetic structure in Fe(III), Mn(II), Co(II) and Ni(II) 3,4,5-trihydroxybenzoate (gallate) dihydrates by neutron and X-ray diffraction. *Dalton Transactions*, 40:6401, 2011.

[89] R. A. Mole, J. A. Stride, P. F. Henry, M. Hoeizel, A. Senyshyn, A. Alberola, C. J. Gomez-Garcia, P. R. Raithby, and P. T. Wood. Two stage magnetic ordering and spin idle behavior of the coordination polymer $Co_3(OH)_2(C_4O_4)_2 \cdot 3H_2O$ determined using neutron diffraction. *Inorg. Chem.*, 50:2246, 2011.

[90] A. Mesban, R. Sibille, T. Mazet, B. Malaman, S. Lebegue, and M. Francois. Magnetism in the $(Co_{1-x}Fe_x)_2(OH)_2(C_8H_4O_4)$ solid solutions: a combined neutron diffraction and magnetic measurements study. *J. Mater. Chem.*, 20:9386, 2010.

[91] P. J. Saines, J. R. Hester, and A. K. Cheetham. Neutron diffraction study of the magnetic structures of manganese succinate $Mn(C_4H_4O_4)$: A complex inorganic-organic framework. *Phys. Rev. B.*, 82:144435, 2010.

[92] R. A. Mole, J. A. Stride, T. Unruh, and P. T. Wood. Non-classical behaviour in an S = 5/2 chain with next nearest neighbour interactions observed from the inelastic neutron scattering of $Mn_2(OD)_2(C_4O_4)$. *J. Phys,: Condens. Matter.*, 21:076003, 2009.

[93] E. Lhotel, V. Simonet, E. Ressouche, B. Canals, D. B. Amabilino, C. Sporer, D. Luneau, J. Veciana, and C. Paulsen. Subtle competition between ferromagnetic and antiferromagnetic order in a Mn(II)-free radical ferrimagnetic chain. *Phys. Rev. B.*, 75:104429, 2007.

[94] R. Sibille, E. Lhotel, T. Mazet, B. Malaman, C. Ritter, V. Ban, and M. Francois. Magnetic structure and dynamics of a strongly one-dimensional cobalt^{II} metal-organic framework. *Phys. Rev. B.*, 89:104413, 2014.

[95] Z. Wang, P. Jain, K.-Y. Choi, J. van Tol, A. K. Cheetham, H. W. Kroto, H.-J. Koo, H. Zhou, J. Hwang, E. S. Choi, M.-H. Whangbo, and N. S. Dalal. Dimethylammonium copper formate $[(CH_3)_2NH_2]Cu(HCOO)_3$: A metal-organic framework with quasi-one-dimensional antiferromagnetism and magnetostriction. *Phys. Rev. B.*, 87:224406, 2013.

[96] P. J. Baker, T. Lancaster, I. Franke, W. Hayes, S. J. Blundell, F. L. Pratt, P. Jain, Z.-M. Wang, and M. Kurmoo. Muon spin relaxation investigation of magnetic ordering in the hybrid organic-inorganic perovskites $[(CH_3)_2(NH)_2]M(HCOO)_3$ (M=Ni,Co,Mn,Cu). *Phys. Rev. B.*, 82:012407, 2010.

[97] L. Nèel. Thèorie du trainage magnètique des ferromagnètiques au grains fins avec applications aux terres cuites. *Ann. Geophys.*, 5:99, 1949.

[98] Superparamagnetism. `https://en.wikipedia.org/wiki/Superparamagnetism`.

[99] A. Mishra, W. Wernsdorfer, K. A. Abbound, and G. Christou. Initial observation of magnetization hysteresis and quantum tunneling in mixed manganeselanthanide single-molecule magnets. *J. Am. Chem. Soc.*, 126:15648, 2004.

[100] N. Ishikawa, M. Sugita, and W. Wernsdorfer. Nuclear spin driven quantum tunneling of magnetization in a new lanthanide single-molecule magnet: Bis(phthalocyaninato)holmium anion. *J. Am. Chem. Soc.*, 127:3650, 2005.

[101] N. Ishikawa, M. Sugita, and W. Wernsdorfer. Nuclear spin driven quantum tunneling of magnetization in a new lanthanide single-molecule magnet: Bis(phthalocyaninato)holmium anion. *J. Am. Chem. Soc.*, 127:3650, 2005.

[102] C. J. Milios, A. Vinslava, W. Wernsdorfer, S. Moggach, S. Parsons, S. P. Perlepes, G. Christou, and E. K. Brechin. A record anisotropy barrier for a single-molecule magnet. *J. Am. Chem. Soc.*, 129:2754, 2007.

[103] S. Jiang, S. Liu, L. Zhou, B. Wang, Z. Wang, and S. Gao. Series of lanthanide organometallic single-ion magnets. *Inorg. Chem.*, 51:3079, 2012.

[104] L. Thomas, F. Lionti, R. Ballou, D. Gatteschi, R. Sessoli, and B. Barbara. Macroscopic quantum tunnelling of magnetization in a single crystal of nanomagnets. *Nature*, 383:145, 1996.

[105] J. R. Friedman, M. P. Sarachik, J. Tejada, and R. Ziolo. Macroscopic measurement of resonant magnetization tunneling in high-spin molecules. *Phys. Rev. Lett.*, 76:3830, 1996.

[106] R. Sessoli and A. K. Powell. Strategies towards single molecule magnets based on lanthanide ions. *Coordination Chemistry Reviews*, 253:2328, 2009.

[107] P. D. W. Boyd, Q. Li, J. B. Vincent, K. Folting, H.-R. Chang, W. E. Strein, J. C. Huffman, G. Christou, and D. N. Hendrickson. Potential building blocks for molecular ferromagnets: $[Mn_{12}O_{12}(O_2CPh)_{16}(H_2O)_4]$ with a S = 14 ground state. *J. Am. Chem. Soc.*, 110:8537, 1988.

[108] J. R. Friedman and M. P. Sarachik. Single-molecule nanomagnets. *Annu. Tev. Condens. Matter. Phys.*, 1:109, 2010.

[109] G. Chaboussant, A. Sieber, S. Ochsenbein, H.-U. Gudel, M. Murrie, A. Honecker, N. Fukushima, and B. Normand. Exchange interactions and high-energy spin states in Mn_{12}-acetate. *Phys. Rev. B.*, 70:104422, 2000.

[110] R. A. Robinson, P. J. Brown, D. N. Argyriou, D. N. Hendrickson, and S. M. Aubin. Internal magnetic structure of Mn_{12} acetate by polarized neutron diffraction. *J. Phys.:Condens. Matter.*, 12:2805, 2000.

[111] A. Cornia, R. Sessoli, L. Sorace, D. Gatteschi, A. L. Barra, and C. Daiguebonne. Origin of second-order transverse magnetic anisotropy in Mn_{12}-acetate. *Phys. Rev. Lett.*, 89:257201, 2002.

[112] M. N. Leuenberger and D. Loss. Spin relaxation in Mn_{12}-acetate. *Europhys. Lett.*, 46:692, 1999.

[113] E. K. Brechin, J. Yoo, M. Nakano, J. C. Huffman, D. N. Hendrickson, and G. Christou. A new class of single-molecule magnets: mixed-valent $[Mn_4(O_2CMe)_2(Hpdm)_6][ClO_4]_2$ with an S = 8 ground state. *Chem. Commun.*, 1999:783, 1999.

[114] H. J. Eppley, H.-L. Tsai, N. de Vries, K. Folting, G. Christou, and D. N. Hendrickson. High-spin molecules: Unusual magnetic susceptibility relaxation effects in $[Mn_{12}O_{12}(O_2CEt)_{16}(H_2O)_3]$ (S = 9) and the one-electron reduction product $(pph_4)[Mn_{12}O_{12}(O_2CEt)_{16}(H_2O)_4]$ (S = 19/2). *J. Am. Chem. Soc.*, 117:301, 1995.

[115] C. Sangregorio, T. Ohm, C. Paulsen, R. Sessoli, and D. Gatteschi. Quantum tunneling of the magnetization in an iron cluster nanomagnet. *Phys. Rev. Lett.*, 78:4645, 1997.

[116] H. Oshio, N. Hoshino, T. Ito, and M. Nakano. Single-molecule magnets of ferrous cubes: Structurally controlled magnetic anisotropy. *J. Am. Chem. Soc.*, 126:8805, 2004.

[117] M. McCaig. *Permanent magnets in theory and practice.* John Wiley and Sons Inc., New York, 1987.

[118] A. M. Ako, I. J. Hewitt, V. Mereacreand R. Clerac, W. Wernsdorfer, C. E. Anson, and A. K. Powell. A ferromagnetic coupled Mn_{19} aggregate with a record S=83/2 ground spin state. *Angew. Chem. Int. Ed.*, 45:4926, 2006.

[119] M. A. AlDamen, J. M. Clemente-Juan, E. Coronado, C. Marti-Gastaldo, and A. Gaita-Arino. Mononuclear lanthanide single-molecule magnets based on polyoxometalates. *J. Am. Chem. Soc.*, 130:8874, 2008.

[120] J. D. Rinehart and J. R. Long. Slow magnetic relaxation in a trigonal prismatic uranium(III) complex. *J. Am. Chem. Soc.*, 131:12558, 2009.

[121] S. Jiang, B. Wang, H. Sun, Z. Wang, and S. Gao. An organometallic single-ion magnet. *J. Am. Chem. Soc*, 133:4730, 2011.

[122] K. S. Pedersen, J. Bendix, and R. Clerac. Single-molecule magnet engineering: building-block approaches. *Chem. Commun*, 50:4396, 2014.

[123] N. Ishikawa, M. Sugita, T. Ishikawa, S.-Y. Koshihara, and Y. Kaizu. Mononuclear lanthanide complexes with a long magnetization relaxation time at high temperatures: a new category of magnets at the single-molecular level. *J. Phys. Chem. B.*, 108:11256, 2004.

[124] R. A. Layfield, J. J. W. McDouall, S. A. Sulway, F. Tuna, D. Collison, and R. E. P. Winpenny. Influence of the n-bridging ligand on magnetic relaxation in an organometallic dysprosium single-molecule magnet. *Chem. Eur. J.*, 16:4442, 2010.

[125] S. Wang, H.-L. Tsai, E. Libby, K. Folting, W. E. Streib, D. N. Hendrickson, and G. Christou. Modeling the photosynthetic water oxidation center: Chloride/bromide incorporation and reversible redox processes in the complexes $Mn_4O_3X(OAc)_3(dbm)_3$ (X) Cl, Br) and $(pyH)_3[Mn_4O_3Cl_7(OAc)_3]$. *Inorg. Chem.*, 35:7578, 1996.

[126] X. Marinez-Hidalgo, E. M. Chudnovsky, and A. Aharony. Dipolar ordering in Fe_8? *europhys. Lett.*, 55:273, 2001.

[127] M. Evangelisti, F. Luis, F. L. Mettes, N. Aliaga, G. Aromi, J. J. Alonso, G. Christou, and L. J. de Jongh. Magnetic long-range order induced by quantum relaxation in single-molecule magnets. *Phys. Rev. Lett*, 93:117202, 2004.

[128] F. Luis, J. Campo, J. Gomez, G. J. McIntyre, J. Luzon, and D. Ruiz-Molina. Long-range ferromagnetism of Mn_{12} acetate single-molecule magnets under a transverse magnetic field. *Phys. Rev. Lett*, 95:227202, 2005.

[129] A. J. Millis, A. D. Ken, M. O. Sarachik, and Y. Yeshurun. Pure and random-field quantum criticality in the dipolar ising model: Theory of Mn_{12} acetates. *Phys. Rev. B.*, 81:024423, 2010.

[130] D. A. Garanin and E. M. Chudnovsky. Dipolar ordering and quantum dynamics of domain walls in Mn_{12} acetate. *Phys. Rev. B.*, 78:174425, 2008.

[131] A. Morello, F. L. Mettes, F. Luis, J. F. Fernandez, J. Krzystek, G. Aromi, G. Christou, and L. J. de Jongh. Long-range ferromagnetic dipolar ordering of high-spin molecular clusters. *Phys. Rev. Lett.*, 90:017206, 2003.

[132] M. Evangelisti, A. Candini, A. Ghirri, M. Affronte, G. W. Powell, I. A. Gass, P. A. Wood, S. Parsons, E. K. Brechin, D. Collison, and S. L. Heath. Tunable dipolar magnetism in high-spin molecular clusters. *Phys. Rev. Lett*, 97:167202, 2006.

[133] D. Gattesch and R. Sessoli. Quantum tunnelling of magnetization and related phenomena in molecular materials. *Angew. Chem. Int. Ed.*, 42:268, 2003.

[134] J. Tang and P. Zhang. *Lanthanide Single Molecule Magnets.* Springer-Verlag Berlin Heidelberg, 2015.

[135] S.-D. Jiang. *Design, Syntheses and Magnetic Properties of Single-Ion Magnets Based on Lanthanide*. Ph.D. thesis, Peking University, 06 2011.

[136] R. Orbach. On the theory of spin-lattice relaxation in paramagnetic salts. *Proc. Phys. Soc.*, 77:821, 1961.

[137] J. H. Van Vleck. Paramagnetic relaxation times for titanium and chrome alum. *Phys. Rev.*, 57:426, 1940.

[138] J. M. Zadrozny, M. Atanasov, A. M. Bryan, C.-Y. Lin, B. D. Rekken, P. P. Power, F. Neese, and J. R. Long. Slow magnetization dynamics in a series of twocoordinate iron(II) complexes. *Chem. Sci.*, 4:125, 2013.

[139] F. Branzoli, M. Filibian, P.Carretta, S. Klyatskaya, and M. Ruben. Spin dynamics in the neutral rare-earth single-molecule magnets $[TbPc_2]^0$ and $[DyPc_2]^0$ from μsr and nmr spectroscopies. *Phys. Rev. B.*, 79:220404, 2009.

[140] F. Branzoli, P. Carretta, M. Filibian, M. J. Graf, S. Klyatskaya, M. Ruben, F. Coneri, and P. Dhakal. Spin and charge dynamics in $[TbPc_2]^0$ and $[DyPc_2]^0$ single-molecule magnets. *Phys. Rev. B.*, 82:134401, 2010.

[141] Moun spin spectroscopy. `https://en.wikipedia.org/wiki/Muon_spin_spectroscopy`.

[142] L. Nuccio, L. Schulz, and A. J. Drew. Muon spin spectroscopy: magnetism, soft matter and the bridge between the two. *J. Phys. D: Appl. Phys*, 47:473001, 2014.

[143] A. Yaouanc and P. Dalmas. *Muon Spin Rotation, Relaxation, and Resonance*. Oxford University Press, New York, 2011.

[144] D. A. Bryman and E. T. H. Clifford. Exotic muon decay $\mu \rightarrow e+x$. *Phys. Rev. Lett.*, 57:2787, 1986.

[145] A. Yaouanc, P. Dalmas de Reotier, Y. Chapuis, C. Marin, G. Lapertot, A. Cervellino, and A. Amato. Short-range magnetic ordering process for the triangular-lattice compound $NiGa_2S_4$: A positive muon spin rotation and relaxation study. *Phys. Rev. B.*, 77:092403, 2008.

[146] R. Akiyama, Y. Ikedo, M. Mansson, T. Goko, J. Sugiyama, D. Andreica, A. Amato, K. Matan, and T. J. Sato. Short-range spin correlations in β''-$LiFeO_2$ from bulk magnetization, neutron diffraction, and μsr experiments. *Phys. Rev. B.*, 81:024404, 2010.

[147] R. S. Hayano, Y. J. Uemura, J. Imazato, N. Nishida, T. Yamazaki, and R. Kubo. Zero-and low-field spin relaxation studied by positive muons. *Phys. Rev. B.*, 20:850, 1979.

[148] A. Abragam. *The principles of nuclear magnetism.* Oxford University Press, Oxford, 1961.

[149] H. E. Stanley. *Introduction to phase transitions and critical phenomena.* Oxford Science Publications, 1987.

[150] J. D. Reger and A. P. Young. Monte Carlo simulation of the spin 1/2 Heisenberg antiferromagnet on a square lattice. *Phys. Rev. B.*, 37:5978(R), 1988.

[151] F. L. Pratt, P. Baker, S. Blundell, , T. Lancaster, M. Green, and M. Kurmoo. Chiral-lime critical behaviour in the antiferromagnet cobalt glycerolate. *Phys. Rev. Lett.*, 99:017202, 2007.

[152] F. L. Pratt, T. Lancaster, P. Baker, S. Blundell, W. Kaneko, M. Ohba, S. Kitagawa, and S. Ohira-Kawamura nad S. Takagi. Muon spin relaxation studies of critical fluctuations and diffusive spin dynamics in molecular magnets. *Physica B.*, 404:58, 2009.

[153] Strphen. W. Lovesey. *Theory of neutron scattering from condensed matter*. Oxford University Press, New York, 1984.

[154] A. Wildes. Neutron magnetic scattering. Oxford School on Neutron Scattering, 2013.

[155] I. Sosnowska, T. P. Neumaier, and E. Streichele. Spiral magnetic ordering in bismuth ferrite. *J. Phys. C.*, 15:4835, 1982.

[156] T. Choi, S. Lee, Y.J. Choi, V. Kiryukhin, and S.-W. Cheong. Switchable ferroelectric diode and photovoltaic effect in $BiFeO_3$. *Science*, 324:63, 2009.

[157] A. M. Kadomtseva, Y. F. Popov, A. P. Pyatakov, G. P. Vorob'ev, A. K. Zvezdin, and D. Viehland. Phase transitions in multiferroic $BiFeO_3$ crystals, thin-layers, and ceramics: Enduring potential for a single phase, room-temperature magnetoelectric 'holy grail'. *Phase Transitions.*, 79:1019, 2008.

[158] F. Bai, J. Wang, M. Wutting, J. Li, N. Wang, A. P. Pyatakov, A. K. Zvezdin, L. E. Cross, and D. Viehland. Destruction of spin cycloid in $(111)_c$-oriented $BiFeO_3$ thin films by epitiaxial constraint: Enhanced polarization and release of latent magnetization. *Appl. Phys. Lett.*, 86:032511, 2005.

[159] J. F. Scott, M. K. Singh, and R. S. Katiyar. Critical phenomena at the 140 and 200 k magnetic phase transitions in $BiFeO_3$. *J. Phys.: Condens. Matter.*, 20:252203, 2008.

[160] D. Rout, K. Moon, and S. L. Kang. Temperature-dependent raman scattering studies of polycrystalline $BiFeO_3$ bulk ceramics. *J. Raman Spectrosc.*, 40:618, 2009.

[161] Z. Zhang, Z. Jin, Q. Pan, Y. Xu, X. Lin, G. Ma, and Z. Cheng. Temperature dependent photoexcited carrier dynamics in multiferroic $BiFeO_3$ film: A hidden phase transition.

[162] C. A. Aristizabal, L. Nuccio, N. A. Morley, D. C. Arnold, F. Morrison, and A. J. Drew. Magnetism in $BiFeO_3$ as revealed by muon spin rotation. In preparation.

[163] S. A. T. Redfern, C. Wang, J. W. Hong, G. Catalan, and J. F. Scott. Elastic and electrical anomalies at low-temperature phase transitions in $BiFeO_3$. *J. Phys.: Condens. Matter.*, 20:452205, 2008.

[164] P. Ren, P. Liu, B. Xia, X. Zou, L. You, J. Wang, and L. Wang. Dielectric dynamics of epitaxial $BiFeO_3$ thin films. *AIP Advances*, 2:022133, 2012.

[165] J. Herrero-Albillos R. Jarrier, X. Marti, R. Haumont, P. Gemeiner abd G. Geneste, P. Berthet, T. Schulli, P. Cevc, R. Blinc, Stanislaus S. Wong, Tae-Jin Park, M. Alexe, M. A. Carpenter, J. F. Scott, G. Catalan, , and B. Dkhil. Surface phase transitions in $BiFeO_3$ below room temperature. *Phys. Rev. B.*, 85:184104, 2012.

[166] D. Sando, A. Agbelele, D. Rahmedov, J. Liu, P. Rovillain, C. Toulouse, I. C. Infante, A. P. Pyatakov, S. Fusil, E. Jacquet, C. Carretero, C. Deranlot, S. Lisenkov, D. Wang, J-M. Le Breton, M. Cazayous, A. Sacuto, J. Juraszek, A. K. Zvezdin, L. Bellaiche, B. Dkhil, A. Barthelemy, and M. Bibes. Crafting the magnonic and spintronic response of $BiFeO_3$ films by epitaxial strain. *Nat. Mater.*, 12:641, 2013.

[167] S. V. Kiselev, R. P. Ozerov, and G. S. Zhdanov. Detection of magnetic order in ferroelectric $BiFeO_3$ by neutron diffraction. *Sov. Phys.-Dokl.*, 7:724, 1963.

[168] J. R. Teague, R. Gerson, and W. J. James. Dielectric hysteresis in single crystal $BiFeO_3$. *Solid State Commun.*, 8:1073, 1970.

[169] F. Kubel and H. Schmid. Structure of a ferroelectric and ferroelastic monodomain crystal of the perovskite $BiFeO_3$. *Acta. Cryst. B.*, 46:698, 1990.

[170] P. Ravindran, R. Vidya, A. Kjekshus, and H. Fjellvag. Theoretical investigation of magnetoelectric behavior in $BiFeO_3$. *Phys. Rev. B.*, 74:224412, 2006.

[171] D. C. Arnold, K. S. Knight, F. D. Morrison, and P. Lightfoot. Ferroelectric-paraelectric transition in $BiFeO_3$: Crystal structure of the orthorhombic β phase. *Phys. Rev. Lett.*, 102:027602, 2009.

[172] I. A. Kornev, S. Lisenkov, R. Haumont, B. Dkhil, and L. Bellaiche. Finite-temperature properties of multiferroic $BiFeO_3$. *Phys. Rev. Lett.*, 99:227602, 2007.

[173] R. Haumont, P. Bouvier, A. Pashkin, K. Rabia, S. Frank, B. Dkhil, W. A. Crichton, C. A. Kuntscher, and J. Kreisel. Effect of high pressure on multiferroic $BiFeO_3$. *Phys. Rev. B.*, 79:184110, 2008.

[174] C. Ederer and N. A. Spaldin. Effect of epitaxial strain on the spontaneous polarization of thin film ferroelectrics. *Phys. Rev. Lett.*, 95:257601, 2005.

[175] D. Lebeugle, D. Colson, A. Forget, and M. Viret. Very large spontaneous electric polarization in $BiFeO_3$ single crystals at room temperature and its evolution under cycling fields. *Appl. Phys. Lett.*, 91:022907, 2007.

[176] D.-H. Kim, H.-N. Lee, M. D. Biegalski, and H. M. Christen. Effect of epitaxial strain on ferroelectric polarization in multiferroic $BiFeO_3$ films. *Appl. Phys. Lett*, 92:012911, 2008.

[177] H. W. Jang, S. H. Baek, D. Ortiz, C. M. Folkman, R. R. Das, Y. H. Chu, P. Shafer, J. X. Zhang, S. Choudhury, V. Vaithyanathan, Y. B. Chen, D. A. Felker, M. D. Biegalski, M. S. Rzchowski, X. Q. Pan, D. G. Schlom, L. Q. Chen, R. Ramesh, and C. B. Eom. Strain-induced polarization rotation in epitaxial (001) $BiFeO_3$ thin films. *Phys. Rev.Lett.*, 101:107602, 2008.

[178] G. Xu, H. Hiraka, G. Shirane, J. Li, J. Wang, and D. Vieland. Low symmetry phase in (001) $BiFeO_3$ epitaxial constrained thin films. *Appl. Phys. Lett.*, 86:182905, 2005.

[179] J. Li, J. Wang, M. Witting, R. Ramesh, N. Wang ans B. Ruette, A. P. Pyatakov, A. K. Zvezdin, and D. Viehland. Dramatically enhanced polarization in (001), (101), and (111) $BiFeO_3$ thin films due to epitiaxial-induced transitions. *Appl.Phys.Lett*, 84:5261, 2004.

[180] Y. Shuai, S. Zhou, S. Streit, H. Reuther, D. Burger, S. Slesazeck, T. Mikolajick, M. Helm, and H. Schmidt. Reduced leakage current in $BiFeO_3$ thin films with rectifying contacts. *Appl. Phys. Lett.*, 98:232901, 2011.

[181] Z. Zhong and H. Ishiwara. Variation of leakage current mechanisms by ion substitution in $BiFeO_3$ thin films. *Appl. Phys. Lett.*, 95:112902, 2009.

[182] G. W. Pabst, L. W. Martin, Ying-Hao Chu, and R. Ramesh. Leakage mechanisms in $BiFeO_3$ thin films. *Appl. Phys. Lett.*, 90:072902, 2007.

[183] R. Palai, R. S. Katiyar, H. Schmid, P. Tissot, S. J. Clark, J. Robertson, S. A. T. Redfern, G. Catalan, and J. F. Scott. β phase and γ-β metal-insulator transition in multiferroic $BiFeO_3$. *Phys. Rev. B.*, 77:014110, 2008.

[184] D. Lebeugle, D. Colson, A. Forget, M. Viret, A. M. Bataille, and A. Gukasov. Electric-field-induced spin flop in $BiFeO_3$ single crystals at room temperature. *Phys. Rev. Lett.*, 100:227602, 2008.

[185] A. N. Kalikin and V. M. Skorikov. $BiFeO_3$ films and single crystals as a promising inorganic material for spintronics. *Russian Journal of Inorganic Chemistry.*, 55:1794, 2010.

[186] A. V. Zalesski, A. K. Zvezdin, A. A. Frolov, and A. A. Bush. 57fe NMR study of a spatially modulated magnetic structure in $BiFeO_3$. *JETP.*, 71:465, 2000.

[187] V. S. Pokatilov and A. S. Sigov. ^{57}Fe NMR study of multiferroic $BiFeO_3$. *Journal of Experimental and Theoretical Physics*, 110:440, 2010.

[188] M. K. Singh, R. S. Katiyar, and J. F. Scott. New magnetic phase transitions in $BiFeO_3$. *J. Phys. Condens, Mat.*, 20:252203, 2008.

[189] A. Razumnaya, Y. Gagoub, H. Bouyanfif, B. Carcanb, B. Alloucheb, J. Wolfmanc, C. Autret-Lambertc, M. El Marssib, D. Mezzaned, and I. Luk'yanchuk. Resistive switching hysteresis in thin films of bismuth ferrite. *Ferroelectrics*, 444:183, 2013.

[190] J. Wu and J. Wang. Orientation dependence of ferroelectric behavior of $BiFeO_3$ thin films. *J. Appl. Phys.*, 106:104111, 2009.

[191] S.-J. Chiu, Y.-T. Liu, H.-T. Lee, G.-P. Yua, and J.-H. Huang. Growth of $BiFeO_3/SrTiO_3$ artificial superlattice structure by RF sputtering. *Journal of Crystal Growth*, 334:90, 2011.

[192] F. Yan, T. J. Zhu, M. O. Lai, and L. Lu. Influence of oxygen pressure on the ferroelectric properties of $BiFeO_3$ thin films on $LaNiO_3$/Si substates via laser ablation. *Appl. Phys. A.*, 101:651, 2010.

[193] M. Stewart and M. G. Cain. Ferroelectric hysteresis-measurement and analysis. `https://physlab.lums.edu.pk/images/e/eb/Reframay4.pdf`, 1999.

[194] X. Qi, J. Dho, R. Tomov, M. G. Blamire, and J. L. MacManus-Driscoll. Greatly reduced leakage current and conduction mechanism in aliovalent-ion-doped $BiFeO_3$. *Appl. Phys. Lett.*, 86:062903, 2005.

[195] H. Yang, M. Jain, N. A. Suvorova, H. Zhou, H. M. Luo, D. M. Feldmann, P. C. Dowden, R. F. DePaula, S. R. Foltyn, and Q. X. Jia. Temperature-dependent leakage mechanisms of $Pt/BiFeO_3/SrRuO_3$ thin film capacitors. *Appl. Phys. Lett*, 91:072911, 2007.

[196] N. D. Mathur and J. F. Scott. Magnetoelectric phenomena and devices. *Philos. Trans. A. Math. Phys. Eng. Sci.*, 372:2009, 2014.

[197] F. L. Pratt. WIMDA: a muon data analysis program for the Windows PC. *Physica D.*, 710:289, 2000.

[198] M. Deumal, J. M. Rawson, A. E. Goeta, J. A. K. Howard, R. C. B. Copley, M. A. Robb, and J. J. Novoa. Studying the origin of the antiferromagnetic to spin-canting transition in the β-*p*-$NCC_6F_4CNSSNC$ molecular magnet. *Chem. Eur. J.*, 16:2741, 2010.

[199] A. J. Steele, T. Lancaster, S. J. Blundell, F. L. Pratt, C. Baines, M. M. Conner, H. I. Southerland, J. L. Manson, and J. A. Schlueter. Magnetic order in quasi-two-dimensional molecular magnets investigated with muon-spin relaxation. *Phys. Rev. B.*, 84:064412, 2011.

[200] T. Lancaster, S. J. Blundell, D. Andreica, M. Janoschek, B. Roessli, S. N. Gvasaliya, K. Conder, E. Pomjakushina, M. L. Brooks, P. J. Baker, D. Prabhakaran, W. Hayes, and F. L. Pratt. Magnetism in geometrically frustrated $YMno_3$ under hydrostatic pressure studied with muon spin relaxation. *Phys. Rev. Lett*, 98:197203, 2007.

[201] T. Lancaster, S. J. Blundell, F. L. Pratt, C. H. Gardiner, W. Hayes, and A. T. Boothroyd. A μSR study of the rare earth antiferromagnet PrO_2. *J. Phys.: Condens. Matter.*, 15:8407, 2003.

[202] P. Dalmas de Reotier and A. Yaouanc. Muon spin rotation and relaxation in magnetic materials. *J. Phys.: Condens. Matter*, 9:9113, 1997.

[203] D. Aguila, L. Barrios, V. Velasco, L. Arnedo, N. Aliaga-Alcalde, M. Menelaou, S. J. Teat, O. Roubeau, F. Luis, and G. Aromi. Lanthanide contraction within a series of asymmetric dinuclear [Ln_2] complexes. *Chem. Eur. J.*, 19:5881, 2013.

[204] N. Ishikawa, T. Okubo, and Y. Kaizu. of hetero-dinuclear phthalocyanine complexes with a diamagnetic Yttrium(III) and a paramagnetic trivalent Lanthanide ion. *J. Phys. Chem. A.*, 106:9543, 2002.